

Advanced Test Mass Suspensions and Electrostatic Control for AIGO

Benjamin H. Lee, B.Sc (Hons.)

This thesis is presented for the degree of

Doctor of Philosophy

at the

School of Physics

University of Western Australia

2007

ABSTRACT

This thesis presents the research done towards the development of the final mirror suspension stage for the high power test facility at AIGO, Western Australia. One of the goals of the facility is to test advanced suspension methods that may be useful in future gravitational wave detectors.

An in depth study of current mirror suspension techniques is presented and areas of possible improvement are highlighted. The extension of an existing suspension modelling toolkit written in Mathematica is also presented, where added functions allow one to include the violin modes of a suspension into their analysis. Through this tool, new suspension geometries boasting a lower number of violin modes with lower Q factors were developed. The orthogonal ribbon suspension and the thin tube suspension boast a lower number of lower Q violin modes compared to typical ribbon suspensions. For the latter, a reduction in the number of violin modes below 5kHz down to 5 and peak thermal noise amplitude by approximately 30dB is predicted. Presented also is the affect that such suspension geometries have on pendulum mode dilution factor and overall suspension thermal noise. It is seen that the violin mode improvement comes at a cost of a small increase in thermal noise above approximately 50Hz.

A theoretical analysis of the AIGO cavity locking control scheme is also given. Issues of sensor noise and dynamic range are considered to produce a possible hierarchical locking method that would be compatible with advanced detectors. The resulting actuator force range requirements for AIGO at each actuation location on the vibration isolation system are given. Requirements of local controls before achieving cavity lock are also discussed.

Finally, the suspension of a dummy sapphire mirror using removable modular niobium ribbons is presented. The design and performance of an electrostatic actuator and sensor for suspended mirror control is given. Initial experimental results of positioning and control of the final stage suspension through a digital interface is also included.

ACKNOWLEDGEMENTS

I would like to acknowledge my principle supervisor, Professor David Blair, for his support and helpful suggestions during the time of my research. In particular, his words of encouragement during difficult times proved influential into the eventual submission of this thesis. To my other supervisors, Dr Li Ju and Dr Chunnong Zhao, I thank you for your willingness to share your wealth of knowledge.

To the other students in the group, in particular Eu-Jeen, Jean-Charles, Jerome, Sascha, Pablo, Slawek, Andrew, Andrew, Yan and Fan, thanks for the good times both here and abroad. Without you all, it would have seemed like a struggle.

I will also thank the workshop staff, lead capably by Peter Hay, for not only your workmanship, but your invaluable ideas.

Thankyou also to Dr Alberto Gennai for helping to make my stay in Pisa as comfortable as possible. My acknowledgments also go to Dr Mark Barton, for his teaching, support and enthusiastic approach with regards to the Mathematica suspension modelling toolkit.

Finally, I will mention my family, who not only had to put up with me during this time, but understood that my research was time consuming and an important part of my studies. Without your support, this would not have happened.

PREFACE

This section provides a summary of the thesis layout. Its purpose is to aid the reader in understanding the research events that took place.

The introduction to this thesis is an extract of a review paper that was written early in 2005. It provides a broad overview of gravitational wave physics. Due to its length, sections concerning gravitational wave sources were not included, leaving mainly those sections involving experimental gravitational wave detection. As such, the introduction relates more closely to the research that was conducted. In section 1.3.1, some mentions of strain sensitivity achieved by various detectors are out of date. Currently the LIGO detectors are operating very close to their design sensitivities, while steady progress has been made at VIRGO towards their design sensitivity.

The following chapter provides a more detailed overview of the current status of test mass suspensions. Four suspension materials (fused silica, silicon, sapphire and niobium) are studied in depth and estimated thermal noise performance at both room temperature and cryogenic temperatures are given. The effects of dissipation dilution, surface loss and coupling to other directions of motion are also considered in order to determine optimum and limiting suspension ribbon thicknesses.

In Chapter 3, extensions to an existing suspension toolkit written in Mathematica by Mark Barton are presented. The extensions allow the user to simulate the suspension violin modes in an analysis. A comparison of the results generated by the program and those generated by finite elements modelling techniques are also given.

Applications of the modelling program are given next. Presented in this chapter is the study of two different triple section suspension geometries termed the orthogonal ribbon suspension and the thin tube suspension. These results have been published as papers and are directly included into the body of the thesis. The effect of triple section suspension elements on pendulum mode dilution factor is also discussed as well as a new concept of involving removable modular suspensions.

Requirements on the local control of the AIGO vibration isolation system is presented in Chapter 4. A theoretical hierarchical control scheme that can be applied at AIGO in order to lock a suspended optical cavity is also discussed. The required force range at each actuator location has been calculated and the expected control noise at the final stage mirror resulting from actuation noise is plotted. In this study, we have assumed a sensitivity requirement equivalent to that needed by an advanced detector.

Finally the design and calibration of the electrostatic actuator and sensor that acts directly on the test mass is presented. We demonstrate the electrostatic control of a dummy mass currently suspended by $25\mu\text{m}$ niobium ribbons at the bottom of the AIGO vibration isolation system.

Appendix A highlights some of the work done towards electrostatic modelling using finite element modelling techniques. Due to a change of research direction, this area of study was not completed. For this reason, it has been included as an Appendix rather than a chapter. Appendix B illustrates the electronic circuits that have been discussed while Appendix C provides a list of publication.

CONTENTS

Abstract	i
Acknowledgements	iii
Preface	v
1 Introduction	1
1.1 Simple conceptual foundations for gravitational wave physics	1
1.1.1 The Einstein equation	1
1.1.2 The weak field approximation	2
1.1.3 Gravitational Wave Emission	4
1.1.4 Gravitational Wave Detection	5
1.2 Resonant Mass Gravitational Wave Detectors	8
1.2.1 Introduction	8
1.2.2 Gravitational Wave Burst Source Energy	9
1.2.3 Resonant Detector Noise Sources	10
1.2.4 Transducers	13
1.2.5 Impedance Matching	15
1.2.6 Suspension Systems	16
1.2.7 Advanced Detectors	17
1.3 Interferometric Gravitational Wave Detectors	19
1.3.1 Introduction	19
1.3.2 Optical Configurations	19
1.3.3 Optical Spring Effect	24
1.3.4 Vibration Isolation	24
1.3.5 Thermal Noise	26
1.3.6 Advanced Interferometers	28
1.3.7 Australian International Gravitational Observatory	29

2	Mirror Suspension Thermal Noise	31
2.1	Introduction	31
2.2	Suspension thermal noise in interferometric GW detectors	32
2.3	Suspension Materials	35
2.3.1	Standard Material Properties	35
2.3.2	Surface Loss	36
2.3.3	Thermoelastic Loss	38
2.3.4	Total Material Loss	39
2.4	Dissipation Dilution	44
2.5	Coupled Suspension Thermal Noise	48
2.6	Suspensions for AIGO	52
3	Mirror Suspension Modelling	55
3.1	Introduction	55
3.2	Violin Mode Modelling Procedure	58
3.2.1	Solving for Frequency and Mode Function	60
3.2.2	Violin Mode Dilution Factor	63
3.2.3	Violin Mode Thermal Noise	63
3.3	Model Comparison	64
3.4	Extension to Triple Sectioned Suspension Elements	69
3.4.1	Solving Triple Sectioned Suspension Element Violin Modes	70
3.4.2	Altering Calculation of Pendulum Mode Dilution Factor	72
3.4.3	Comparison to Finite Element Model	73
4	Advanced Geometry Suspensions	77
4.1	Preface	77
4.2	Pendulum Mode Dilution Factor	77
4.2.1	Introduction	77
4.2.2	Suspensions Supporting 30kg Test Masses	78
4.2.3	Suspension for AIGO Size Masses	81
4.2.4	Summary and Conclusion	83
4.3	Orthogonal Ribbon Physics Letters A Paper	84
4.3.1	Introduction	84
4.3.2	The Orthogonal Ribbon	86

4.3.3	First Violin mode frequency	88
4.3.4	First Violin mode dilution factor	90
4.3.5	Comparison of thermal noise spectrums	91
4.3.6	Conclusion	95
4.3.7	Acknowledgments	96
4.3.8	Postscript	97
4.4	Thin walled Nb tubes Physics Letters A Paper	99
4.4.1	Introduction	99
4.4.2	Suspension Modelling	101
4.4.3	Violin modes and the Orthogonal Ribbon	101
4.4.4	Improving the Orthogonal Ribbon	102
4.4.5	Nb Tube suspension	103
4.4.6	Thermal noise spectrums	106
4.4.7	Conclusion	108
4.4.8	Acknowledgments	109
4.4.9	Postscript	110
4.5	Removable Modular Suspension Elements for AIGO	113
5	Isolation System Control	119
5.1	Introduction	119
5.2	AIGO Isolation system requirements	120
5.2.1	Within the detection band	121
5.2.2	Below the detection band	122
5.2.3	Requirement Summary	123
5.3	Local Control Systems	123
5.3.1	Remote Mirror Positioning and Alignment	127
5.3.2	Low Frequency Torsion Mode	128
5.3.3	Low Frequency Pitch Mode	130
5.3.4	Minimisation of Horizontal RMS Residual Velocity	132
5.3.5	Vertical RMS Residual Velocity	141
5.4	Global Control Systems	143
5.4.1	Initial Cavity Locking	144
5.4.2	Switching to Hierarchical Control - General Case	152

5.4.3	Switching to Hierarchical Control - AIGO	153
5.4.4	Noise Improvement through Emphasis Filtering	160
5.5	Noise Analysis and Comparison	163
5.6	Summary	166
6	AIGO Test Mass Control	169
6.1	Introduction	169
6.2	The Suspension	169
6.3	The Electrostatic Actuator	174
6.3.1	Basic Design	174
6.3.2	Pitch Mode Coupling	177
6.3.3	Sensor Calibration	179
6.3.4	Actuator Calibration	180
6.4	Local Test Mass Positioning	183
6.4.1	Basic Layout	183
6.4.2	Initial Tuning	185
6.4.3	Results	185
6.4.4	Discussion	192
7	Conclusions	193
7.1	Thesis Summary	193
7.2	Future Work	195
A	Electrostatic Modelling	197
A.1	Introduction	197
A.2	Orthogonal Direction Actuation	202
A.3	Electrode Spacing Optimisation	202
B	Electronic Circuits	205
	Bibliography	219
C	List Of Publications	221

LIST OF FIGURES

1.1	Lines of gravitational tidal force...	3
1.2	Two polarisations of the quadrupole...	4
1.3	(a) A resonant bar detector...	6
1.4	A rough comparison of earth based detector and space based...	6
1.5	Representation of the state of the antenna...	11
1.6	Noise sources and quantities used to characterise a transducer...	12
1.7	Mechanical model of a secondary resonator...	15
1.8	Secondary resonators designs...	16
1.9	A basic Michelson interferometer.	20
1.10	Laser frequency stabilisation.	21
1.11	Dual recycled interferometer.	23
1.12	Fundamental noise sources expected in Advanced LIGO generated using Bench62.	28
2.1	Total loss angle as a function of frequency...	40
2.2	Total loss angle as a function of frequency...	41
2.3	Total loss angle of sapphire and silicon suspension...	43
2.4	Total loss angle versus frequency of niobium suspension fibers...	44
2.5	Ribbon suspension loss as a function of ribbon thickness...	47
2.6	Ribbon suspension thermal noise as a function of ribbon thickness...	49
2.7	x-direction thermal noise, 0.1% of y-direction thermal noise...	52
3.1	AIGO suspension chain model.	56
3.2	A Comparison of the thermal noise due to the entire AIGO suspension chain compared to the thermal noise due to only the final suspension stage. 0.1% coupling has been assumed.	56
3.3	Flow diagram of violin mode modelling procedure.	59

3.4	The mechanical model being analysed by the violin mode modelling procedure.	59
3.5	A function to calculate the sum of forces at end 1.	62
3.6	A comparison of the first three violin modeshapes...	65
3.7	A comparison of the first three violin modeshapes...	67
3.8	A comparison of the first three violin modeshapes...	68
3.9	A triple section suspension element in its simplest form.	70
3.10	The boundary and interface requirements of a triple section suspension element.	71
3.11	Pendulum mode bending of a suspension under no tension.	72
3.12	A fused silica triple section suspension used for model result comparison.	73
3.13	A comparison of the first three violin modeshapes...	74
4.1	a) Bending of the suspension when under no load, and when under load.	78
4.2	The pendulum mode dilution factor of a fused silica bar/flexure suspension...	79
4.3	Pendulum mode dilution factor as a function of flexure length for several bar thicknesses.	80
4.4	Pendulum mode dilution factor as a function of flexure length for several bar thicknesses.	81
4.5	Pendulum mode dilution factor as a function of flexure length for several bar thicknesses.	82
4.6	(a) A normal ribbon fixed between two mounting blocks...	87
4.7	The first violin mode frequency of a fused silica and a niobium orthogonal ribbon...	88
4.8	First violin mode dilution factor for a fused silica and a niobium orthogonal ribbon...	90
4.9	Thermal noise spectrum for a 300mm long, 100 μ m thick, 6mm wide niobium ribbon...	93
4.10	Thermal noise spectrum for a 300mm long, 100 μ m thick, 5.5mm wide fused silica ribbon...	94
4.11	A comparison of the fused silica orthogonal ribbon suspension thermal noise...	95

4.12 Violin modes of a fused silica bar/flexure suspension versus central section bar thickness.	97
4.13 Orthogonal ribbon suspension.	101
4.14 Tube suspension.	104
4.15 A comparison between expected suspension thermal noise...	107
4.16 A comparison between expected suspension thermal noise...	108
4.17 A comparison between expected suspension thermal noise...	111
4.18 A comparison between expected suspension thermal noise...	111
4.19 a) Removable modular hook suspension. b) Removable modular peg suspension.	113
4.20 3mm diameter, 6mm deep equatorial holes required in the test mass to support the pin-in-hole interface.	114
4.21 Force diagram for pin-in-hole interface supporting the 4.2kg sapphire test mass.	115
4.22 A contour plot of the displacement of a contact pin...	116
4.23 A contour plot of the total stress intensity of a Nb contact pin...	117
5.1 Seismic noise measured at the AIGO site...	120
5.2 Principal noise sources for Advanced LIGO...	121
5.3 There are four horizontal direction control loops...	126
5.4 There are two vertical direction control loops...	126
5.5 A simple block diagram representation of the isolation chain torsion mode...	129
5.6 Pitch mode actuation at the...	131
5.7 The expected horizontal transfer function of the AIGO...	133
5.8 The expected horizontal seismic noise...	133
5.9 The RMS residual motion...	134
5.10 The RMS residual velocity...	134
5.11 A simple block diagram representation of the isolation chain local horizontal control...	135
5.12 Loop gain bode plot of the local control loop...	136
5.13 The horizontal seismic noise with the local control loop closed.	139

5.14	The RMS residual motion of the mirror with the local control system closed...	140
5.15	The RMS residual velocity of the mirror with the local control system closed...	140
5.16	A comparison between the expected horizontal and vertical...	142
5.17	A comparison between the horizontal and vertical RMS residual motion...	142
5.18	A comparison between the horizontal and vertical RMS residual velocity...	143
5.19	A simulated mirror stop...	145
5.20	Feedback loop of the initial cavity locking strategy.	146
5.21	A comparison between the closed loop and open loop...	147
5.22	A block diagram illustrating the feedback loop...	147
5.23	The loop gain transfer function...	148
5.24	A comparison between the closed loop and open loop...	149
5.25	The feedback force spectrum...	150
5.26	A comparison of actuation noise...	151
5.27	A block diagram illustrating a simple control system.	152
5.28	A block diagram illustrating a general process of splitting the error signal	153
5.29	Block diagram of the proposed hierarchical...	154
5.30	Rearranged block diagram of the proposed hierarchical...	154
5.31	Seismic induced cavity length spectrum...	155
5.32	The open loop gain and phase plots...	156
5.33	Seismic induced cavity length spectrum...	157
5.34	Closed loop actuation force spectrum...	157
5.35	Closed loop actuation residual force...	158
5.36	Feedback gain that is contributed to each of the...	159
5.37	A comparison of actuation noise during hierarchical feedback...	159
5.38	A block diagram showing the source of the dominant electrostatic actuation noise.	161
5.39	A block diagram showing the inclusion of preemphasis...	161
5.40	Magnitude response of the Preemphasis and Deemphasis filters.	162
5.41	The improvement in sensitivity that can be achieved...	163
5.42	Actuation noise sources in comparison...	164
5.43	Actuation noise sources in comparison...	165

6.1	a) AIGO control mass drawing. b) A Photo of the suspended AIGO control mass.	170
6.2	a) The brass/niobium suspension currently being used...	171
6.3	Expected suspension thermal noise from the AIGO four ribbon niobium suspension.	172
6.4	Expected contribution of suspension thermal noise at 100Hz as a function of laser spot position...	173
6.5	A comparison of expected AIGO suspension thermal noise for a centred laser spot...	173
6.6	The electrode layout for the four quadrant capacitor used at AIGO. . .	174
6.7	Basic circuit constructed around the electrode capacitor used to allow both actuation and position sensing.	175
6.8	a) Coupling of test mass translation to pitch when a force is applied by the electrostatic actuator.	178
6.9	Capacitive position sensor calibration for the four quadrants.	180
6.10	The noise floor of the capacitive sensor...	181
6.11	A measurement of the capacitance of one electrode quadrant vs test mass distance.	182
6.12	Force calibration of the electrostatic plate using a magnetic actuator with known calibration...	183
6.13	Electrostatic force vs electrode voltage up to 2.5kV for the AIGO electrode array layout acting on an aluminium test mass.	184
6.14	Electrostatic force vs electrode voltage up to 1kV for the AIGO electrode array layout acting on an aluminium test mass.	185
6.15	The experimental layout used to initially control the suspended dummy test mass...	186
6.16	Measured displacement spectrum of the suspended dummy mass.. . . .	187
6.17	Time domain response of both the undamped and damped x direction motion of the suspended mirror	188
6.18	Dummy mass position control using the electrostatic actuator.	188
6.19	Measured yaw spectrum of the suspended dummy mass.	189
6.20	Time domain response of both the undamped and damped yaw direction motion of the suspended mirror.	190

6.21	Dummy mass yaw position control using the electrostatic actuator.	190
6.22	Measured pitch spectrum of the suspended dummy mass.	191
6.23	Time domain response of both the undamped and damped pitch direction motion of the suspended mirror.	191
6.24	Dummy mass pitch position control using the electrostatic actuator.	192
A.1	a) Comb electrode array for electrostatic actuation of a suspended dielectric.	197
A.2	a) The mesh generated from the model of a sapphire sample located 1mm...	198
A.3	The total area of the model must be much larger than the actuator in order to obtain reasonable results.	199
A.4	Modelled capacitance of 8 a=3mm, b=3mm electrodes on a FR4 substrate for sapphire test mass separated from the actuator by 1mm.	200
A.5	Modelled capacitance vs distance plots of 8 a=3mm, b=3mm electrodes on a FR4 substrate...	201
A.6	Modelled capacitance vs distance plots of 20 a=3.2mm, b=4mm electrodes on a vetronite substrate...	201
A.7	a) The mesh generated from the model of a 150mm diameter sapphire mirror located 1mm...	202
A.8	Modelled electrostatic force vs electrode width a	204
B.1	Printed circuit board design of the electrostatic plate.	206
B.2	Schematic of the electrostatic sensing circuit for the north quadrants.	207
B.3	Schematic of the electrostatic sensing circuit for the south quadrants.	208
B.4	Schematic of the bias voltage supply circuit.	209
B.5	Schematic of the high voltage amplifier.	210

CHAPTER 1

INTRODUCTION

1.1 Simple conceptual foundations for gravitational wave physics

The detection of gravitational waves (GWs) will open a new window to astrophysical processes, revolutionizing our understanding of the cosmos. Our present view of the Universe is provided predominantly by the different regions of the electromagnetic spectrum – from radio to gamma-ray we are able to view a host of different astrophysical sources. In contrast to electromagnetic waves, which can be absorbed and scattered, GWs are not blocked by stars and debris as they emanate undisturbed from the regions of their origins. Therefore, if cosmic gravitational radiation can be detected and studied in addition to electromagnetic radiation, astronomers will be able to detect both bright objects, such as exploding stars, and dark objects such as black-holes. This introductory section sets out to provide an overview of the key concepts of gravitational wave physics, as well as providing a flavour for the topics in subsequent sections.

1.1.1 The Einstein equation

General Relativity predicts GWs as ripples in the curvature of spacetime that propagate at the speed of light [1, 2]. They are emitted by bulk motions of matter such as collapsing stellar cores, or by coherent vibrations of spacetime curvature such as those caused by black holes.

In Newtonian physics, spacetime is modelled as an infinitely rigid metric. In such a medium, gravitational waves require infinite velocity and energy density to propagate. General relativity introduces a weak coupling between the curvature of spacetime, described by the Einstein curvature tensor \mathbf{G} , and the source of the curvature — the

distribution of matter and energy — described by the stress-energy tensor \mathbf{T} . The coupling is expressed in the Einstein equation:

$$\mathbf{T} = \frac{c^4}{8\pi G} \mathbf{G}, \quad (1.1)$$

where c the speed of light and G is Newton's gravitational constant. The constant $c^4/8\pi G$ determines how effectively the energy-mass distribution distorts spacetime. Its large value expresses the extreme stiffness of space, explaining why GWs have such small amplitudes.

1.1.2 The weak field approximation

Gravitational radiation at distances far away from sources may be described in the weak field approximation, in which we express the metric of spacetime, $g_{\alpha\beta}$, as a small perturbation, $h_{\alpha\beta}$, of a flat Minkowski spacetime time, $\mu_{\alpha\beta}$:

$$g_{\alpha\beta} = \mu_{\alpha\beta} + h_{\alpha\beta} \quad |h_{\alpha\beta}| \ll 1. \quad (1.2)$$

To obtain an explicit statement of the metric perturbation it is necessary to make a gauge (coordinate system) choice. The most useful gauge in this context is the 'transverse traceless' (TT) gauge, in which the coordinates are defined by the geodesics of freely falling test bodies. For a cartesian frame x , y and z , with z the direction of wave propagation, $h_{\mu 0} = 0$; i.e. only the spatial components are nonzero. Also the transverse condition implies $h_{zz} = 0$ and $h_{xx} = -h_{yy}$ satisfying the traceless condition. In this gauge, the field equations in the absence of matter and electromagnetic fields ($\mathbf{T} = 0$) can be expressed as a system of standard linear wave equations:

$$g_{\alpha\beta} = \left(\nabla^2 - \frac{1}{c^2} \frac{\partial^2}{\partial t^2} \right) h_{\alpha\beta}, \quad (1.3)$$

This is the three-dimensional wave equation for GWs and it implies that gravitational waves travel at the vacuum speed of light c . The metric perturbation has the effect of inducing an oscillation in the distances between test masses (geodesic oscillation) as a function of time. The GW tensor \mathbf{h} can be considered as the GW field, and for waves

travelling in the z -direction may be expressed as:

$$\mathbf{h} = \begin{pmatrix} 0 & 0 & 0 & 0 \\ 0 & h_{xx} & h_{xy} & 0 \\ 0 & h_{yx} & h_{yy} & 0 \\ 0 & 0 & 0 & 0 \end{pmatrix}. \quad (1.4)$$

It follows that a plane monochromatic wave propagating in the z direction, as described in the TT gauge, has only two independent non-vanishing components $h_{\alpha\beta}$ [2] :

$$\begin{aligned} h_{xx}^{TT} &= -h_{yy}^{TT} = \Re[h_+ e^{-i\omega(t-z/c)}], \\ h_{xy}^{TT} &= h_{yx}^{TT} = \Re[h_\times e^{-i\omega(t-z/c)}], \end{aligned} \quad (1.5)$$

where the two independent modes of polarization are pronounced ‘plus’ and ‘cross’ and have (dimensionless) amplitudes h_+ and h_\times . Figure 1.1 shows the direction of the tidal force from a GW travelling in the z direction over a single cycle for the two polarizations. This figure illustrates how a GW travelling in the z direction will alternatively expand and shrink the space between two free masses in the x and y directions at the frequency of the GW. We can express the strength of a GW as a dimension-less quantity, strain h , which measures the relative length change $\Delta L/L$ between the masses.

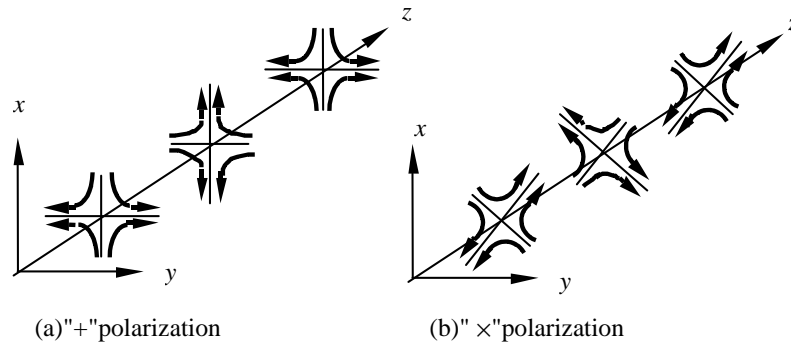


Fig. 1.1: Lines of gravitational tidal force for a complete GW cycle for the two polarizations. (Reproduced from [3].)

The weak-field approximation is valid so long as the background spacetime curvature is small. However, for dynamic strong fields, as occur in the coalescence of a

binary black hole system, non-linear effects become important. These include gravitational redshift, refraction and backscattering. Unfortunately this non-linear regime is expected to contain the most readily detectable GW sources. It is difficult for theorists to accurately model GW emission from a source of extreme curvature, such as the formation of a black hole. Currently, there is a world-wide effort to develop numerical relativity techniques to address this deficiency.

1.1.3 Gravitational Wave Emission

The emission of GWs can be most easily understood if one considers the dynamic motion of a system of distributed mass. Conservation of momentum requires that the centre of mass of the system remain unchanged. Any spherically symmetric changes in mass distribution will not effect the external gravitational field, hence no emission of gravitational radiation. It is only non-spherically symmetric changes that permit the propagation of GWs. Since the simplest form of non-spherically symmetric deformation is the quadrupole moment, it follows that the GW is a quadrupole wave.

Figure 1.2 shows the distortion of a ring of points resulting from the gravitational tidal force illustrated in Fig. 1.1. Considering the h_+ polarisation, it can be seen that the motion involves instantaneous inward movements of the side and outward movement of the top and bottom. This alternating stretching and shrinking motion of the ring continues as the cycle completes.

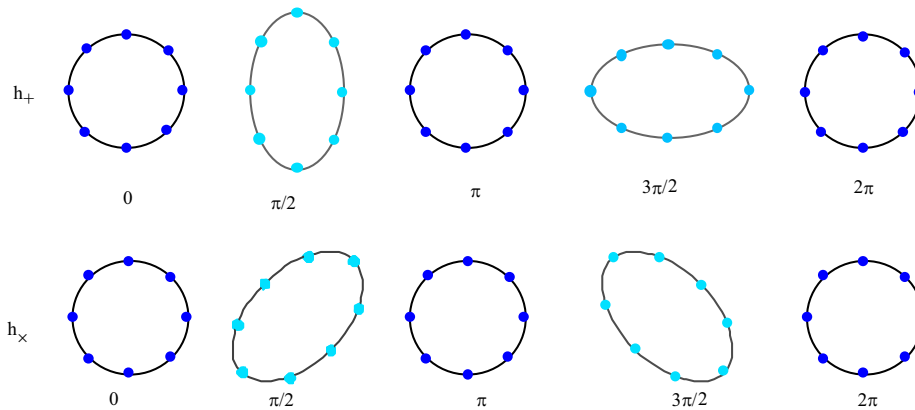


Fig. 1.2: Two polarisations of the quadrupole moment deformation of a ring of points during one cycle of a passing gravitational wave. The gravitational wave travels in a direction normal to the page. (Reproduced from [3])

1.1.4 Gravitational Wave Detection

The symmetry between GW detectors and sources allows one to predict the motion that will be induced by a passing GW. A ring of masses will be distorted in exactly the same manner as the distortion of a ring of masses will emit gravitational waves. GW detectors are therefore designed specifically to be extremely sensitive to these motions.

Earth Based Detectors

There are two main types of GW detectors, a resonant mass detector and an interferometric detector. The concept of these are illustrated in Fig. 1.3, where an interferometric detector, and two forms of resonant mass detectors are shown. The bar detector is a resonant mass detector that essentially requires a measure of the change in length of the bar as a GW passes. The fundamental resonant frequency of the bar is designed to be close to the frequency of the gravitational wave to be detected. The GW induces motion which is resonantly enhanced and can be detected by a suitable transducer. An interferometric detector is based on laser interferometry and measures the relative difference between two arm lengths. These arm lengths are the distance between the orthogonally spaced masses and the center when illustrated on a ring of masses as in Fig. 1.3b. The alternate stretching and shrinking of the ring as a gravitational wave passes presents an ideal situation for measuring the displacement using an interferometer. Detection can also be achieved through a particular type of torsion resonator. The time varying quadrupole distortion illustrated in Fig. 1.3c is equivalent to a time varying gravity gradient. The masses that are not displaced during the stretching and shrinking cycle (the diagonal masses) experience a component of alternating forces in the tangential direction. Thus by designing a quadrant torsion resonator with a resonant frequency equal to that of the target gravitational wave, induced motion can be mechanically amplified.

The gravitational wave spectrum ranges from 10^{-6}Hz to 10^4Hz , however as apparent from Fig. 1.4, the detection frequency for terrestrial detectors is limited to between 10Hz and several thousand Hz. Noise sources such as seismic noise, earth tides, thermal expansion and gravity gradient noise (changes in gravity gradient due to air density fluctuations, seismic waves, ocean tides, etc.) set the low frequency limit.

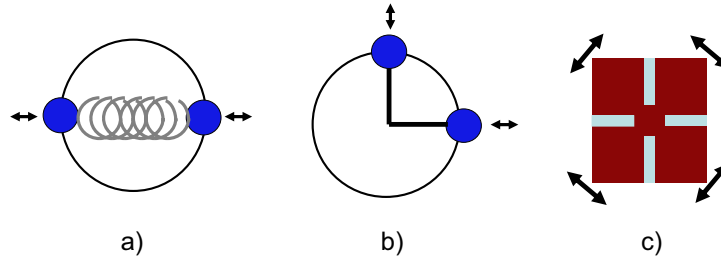


Fig. 1.3: (a) A resonant bar detector. (b) An interferometric detector. (c) A torsional resonant detector

Space Based Detectors

The Laser Interferometer Space Antenna (LISA) is a proposed NASA/ESA project aimed at developing and operating a space based detector ¹. LISA is designed for a lower detection band of 10^{-4} Hz to 10^{-1} Hz as shown in Fig. 1.4. Such low frequencies

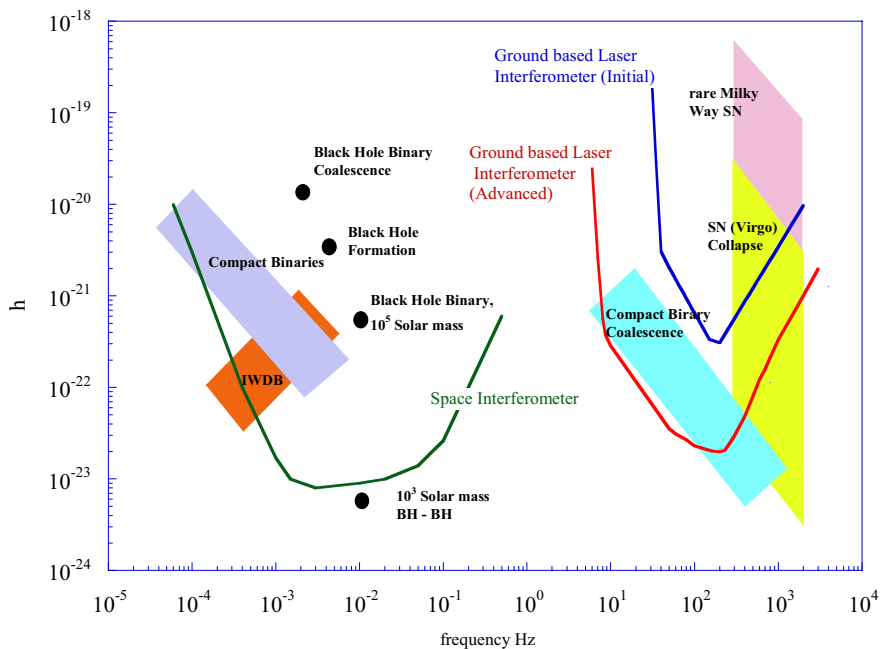


Fig. 1.4: A rough comparison of earth based detector and space based detector sensitivity and some sources. (Reproduced from [3])

are possible because unlike earth based detectors, noise sources in this frequency band are much less significant. LISA monitors the motion of three test masses free falling in space through the use of sophisticated interferometry. At the location of each of the test masses, an outgoing laser signal is phase locked to an incoming laser signal—

¹For further information on LISA visit <http://lisa.jpl.nasa.gov/>

essentially forming an active mirror. Each test mass is located relative to the others in this manner. The test masses are also shielded from solar wind which would otherwise disturb the test mass free fall. External forces exerted on the shield are compensated by ion drive thrusters. Unlike earth based interferometers, large interferometer arm lengths are possible (5×10^6 km). This increases the relative motion between the masses (ΔL) for a gravitational wave of fixed amplitude, h .

1.2 Resonant Mass Gravitational Wave Detectors

This section discusses the major issues and principles behind gravitational wave detection using resonant mass detectors. Typical sources of detector noise are briefly discussed along with some methods of analysing data from multiple detectors. Finally, we mention some of the advanced detectors being proposed in this field.

1.2.1 Introduction

Gravitational wave detection began in the 1960s with research conducted by Joseph Weber [4]. The detector designed by Weber consisted of a large aluminium bar sufficiently isolated from the environment that a gravitational wave excitation of its mechanical quadrupole modes could be discerned as a transient excitation. Piezoelectric crystals were located on the surface of the bar. A low noise amplifier and a lock in amplifier (for synchronous detection) allowed monitoring of the energy of the fundamental longitudinal resonance. Detection of the acoustic signal induced by coupling between the gravitational wave and the resonant bar is the basis behind the concept of resonant mass gravitational wave detectors.

One of the key issues involved with resonant mass detectors is the method of extracting a signal with an amplitude that is many times smaller than the thermal vibrations of the bar. It was shown that the effective thermal noise energy can be reduced by a factor of $\sim \tau_i/\tau_a$ for bars with low acoustic loss (or high Q), where τ_i is the measurement integration time and τ_a , the ring down time of the bar. A reduction in the effective thermal noise energy through the use of a high Q antenna (large value of τ_a) can be shown from the fluctuation-dissipation theorem [5], where a larger ring down time implies lower dissipation and hence a lower level of noise coupled through the thermal reservoir.

Current bar detectors have peak sensitivities in a narrow frequency band (a few 10s of Hz) at a frequency of 700–900Hz, defined by the fundamental longitudinal resonance. The bar material and mass is chosen such that the absorption cross section of the fundamental mode is greatest. The absorption cross section indicates the amount of coupling between the gravitational wave and the bar. Development of resonant mass detectors continued after Weber's pioneering work and have resulted in the use of cryogenic and superconducting techniques in current generation bar detectors. The first detec-

tors to achieve long term operation under cryogenic conditions were EXPLORER [6] at CERN (Geneva), ALLEGRO [7] at Baton Rouge (Louisiana) and NIOBE [8] at Perth (Australia). In the mid 1990s, the detectors NAUTILUS [9] at Frascati (Italy) and AURIGA [10] at Legnaro (Italy) began operation at ultracryogenic temperatures. Table 1.1 summarizes the five detectors. EXPLORER, ALLEGRO, NAUTILUS and AURIGA are currently either operational or being upgraded. NIOBE made its final run during 2001.

Antenna	Material	Temperature	Frequency (Hz)	Mass (kg)
EXPLORER	Al	4K	900	2270
ALLEGRO	Al	2K	900	2300
NIOBE	Nb	5K	700	1500
NAUTILUS	Al	100mK	900	2260
AURIGA	Al	100mK	900	2230

Tab. 1.1: Basic properties of five cryogenic resonant bar detectors

1.2.2 Gravitational Wave Burst Source Energy

It is possible to determine the feasibility of using resonant mass detectors for gravitational wave burst source detection. To achieve this, the amount of energy that will be deposited into a resonant bar from a burst source needs to be approximated. The energy flux carried by a gravitational wave is given by S in $\text{Jm}^{-2}\text{s}^{-1}$:

$$S = \frac{c^3}{16\pi G} \langle \dot{h}_+^2 + \dot{h}_\times^2 \rangle. \quad (1.6)$$

The values h_+ and h_\times are the two polarisations of the dimensionless strain amplitude of the wave. Assuming that the pulse is a single cycle and of duration $\sim 10^{-3}\text{s}$, S can be rewritten as:

$$S = \frac{c^3}{16\pi G} \frac{4h^2}{\tau_g^2}. \quad (1.7)$$

The assumption that $dh/dt \sim 2h/\tau_g$ has been made and is reasonable given our knowledge of τ_g . The total pulse energy, E_G in units Jm^{-2} :

$$E_G = S \cdot \tau_g = \frac{c^3}{16\pi G} \frac{4h^2}{\tau_g}. \quad (1.8)$$

To determine the flux spectral density for short bursts, two assumptions are made. Firstly, the bandwidth of the short pulse is given by $\Delta\omega \sim 1/\tau_g$ and secondly, the pulse

energy $F(\omega)$ is uniform over this bandwidth. Thus $F(\omega) \sim E_G/\Delta\omega$. By replacing $\Delta\omega$ with $1/\tau_g$ and using equation (1.8) the flux spectral density in units of $\text{Jm}^{-2}\text{Hz}^{-1}$ can be expressed by:

$$F(\omega) = \frac{c^3 h^2}{4\pi G} \sim 20 \times 10^{34} h^2. \quad (1.9)$$

Only a fraction of the energy of a passing gravitational wave is coupled into the bar as acoustic energy. The value of this fraction indicates the efficiency of the antenna. Clearly, the larger the fraction of energy that is coupled the greater the efficiency. The amount of coupling is termed the *antenna cross section* and is denoted by $\sigma(\omega)$. The energy deposited in the bar by a gravitational wave with flux spectral density $F(\omega)$ can be expressed by E as:

$$E = \int \sigma(\omega) F(\omega) d\omega. \quad (1.10)$$

When integrated over the frequency band, the cross section can be expressed in terms of physical properties of the bar [11], namely mass, M , and velocity of sound, v_s :

$$\int \sigma(\omega) d\omega = \frac{8GM}{\pi c} \left(\frac{v_s}{c}\right)^2. \quad (1.11)$$

Finally, by combining equations (1.9), (1.10) and (1.11), the energy deposited in the antenna is given by:

$$U_s \sim F(\omega) \sin^2(\theta) \cos^2(2\phi) \frac{8G}{\pi c} \left(\frac{v_s}{c}\right)^2 M. \quad (1.12)$$

The coordinates θ and ϕ describe the orientation of the incoming wave relative to the bar. The expression U_s in equation (1.12) provides an approximation to the amount of induced energy that could be expected during a burst event. Clearly, the condition for detection is that the detectable signal energy, U_s , is greater than the noise energy, U_n . A brief analysis of the noise contributions to the total noise energy, U_n , in bar detectors is given in the following section.

1.2.3 Resonant Detector Noise Sources

In general there are three classes of noise that affect resonant mass detectors. The first that will be considered is Brownian motion noise. To understand this source of noise and the effect it has on the bar, it is convenient to use an approach first presented by Gibbons and Hawking [12]. The state of the bar is represented by symmetrical harmonic oscillator coordinates, X_1 and X_2 , which differ in phase by 90 degrees. Thus,

any point on the (X_1, X_2) plane represents a state of the bar. When a gravitational wave couples acoustic energy into the bar, its state will change from an initial state, P_1 , to a final state, P_2 . This is illustrated in Fig. 1.5. In an ideal detector, the change

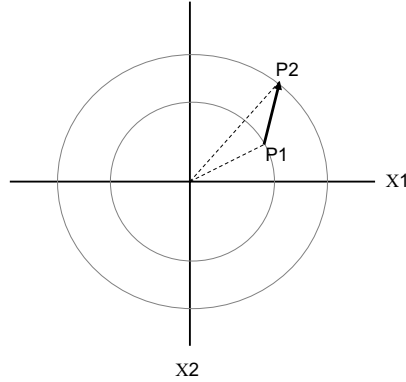


Fig. 1.5: Representation of the state of the antenna in X1-X2 coordinates.

in state, $\Delta|P_1 - P_2| = (\Delta X_1^2 - \Delta X_2^2)^{1/2}$, will be due solely to a gravitational wave. However in reality, thermal fluctuations cause the state vector P to undergo a random walk in the (X_1, X_2) plane. Thus unless methods to reduce the effective thermal noise are employed, it is likely that the change in the state vector, $\Delta|P_1 - P_2|$, will be hidden by thermal fluctuations. This is indeed Brownian motion noise.

The second source of noise is series electronic noise. This includes all the contribution towards electronic noise through the amplifier that sum at the output signal. In parametric transducers, the pump signal phase noise also contributes to this broadband source.

The final major class of noise is termed back action noise and is caused by currents in the amplifier that act back through the transducer inducing forces on the bar. This noise is indistinguishable from Brownian motion noise and is unavoidable according to quantum mechanics – the state of a system cannot be measured without being disturbed. However, because this noise may be of classical origin, there is a classical uncertainty principle limit which may greatly exceed the true quantum limit.

The three major sources of noise can be expressed in a single equation, U_n , which expresses the total system noise.

$$U_n = 2k_B T_a \frac{\tau_i}{\tau_a} + \frac{|Z_{12}|^2}{2M} S_i(\omega) \tau_i + \frac{2M}{|Z_{21}|^2} \frac{S_e(\omega)}{\tau_i} \quad (1.13)$$

The first term in equation (1.13) describes the Brownian motion noise in the antenna. The second term represents the contribution from back action noise while the third

term describes the contribution from series electronic noise. Figure 1.6 illustrates the location of the noise sources as described by the noise equation, U_n . To reduce the total

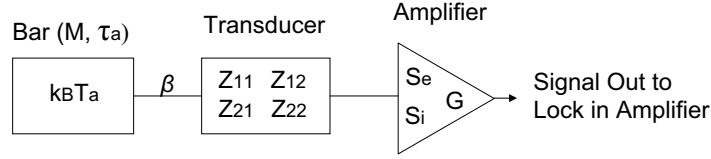


Fig. 1.6: Noise sources and quantities used to characterise a transducer and amplifier.

system noise, it is intuitive and supported by equation (1.13) that $S_e(\omega)$ and $S_n(\omega)$ should be minimised. As Brownian motion noise is shown to reduce proportionally with bar temperature, we can see the advantage of cryogenics. It also changes proportionally with the inverse of the antenna relaxation time, τ_a^{-1} , resulting from the fluctuation-dissipation theorem [5]. The total noise also depends on elements of a Z_{ij} matrix, which is a matrix used to conveniently model the transducer. This will be discussed in the next section.

By analysing the noise sources, it is possible to obtain the minimum detectable strain amplitude of a resonant bar detector that has reached its fundamental limits. These limits are the thermal noise limit of the bar, and the quantum limit set by the readout system. The thermal noise, or Brownian motion noise that limits the detectable strain amplitude, is given by [13]:

$$h_{th} = \left(\frac{k_B T \tau_i \omega_a}{M \pi^2 v_s^2 Q} \right)^{\frac{1}{2}} \sim 10^{-21} \left[\left(\frac{f}{1 \text{ kHz}} \right) \left(\frac{10^{10} \text{ J}}{M v_s^2} \right) \left(\frac{10^9}{Q} \right) \left(\frac{T}{0.1 \text{ K}} \right) \left(\frac{\tau_i}{10^{-2} \text{ s}} \right) \right]^{\frac{1}{2}}. \quad (1.14)$$

The total of the series electronic noise and the back action noise cannot be reduced below a level given by $\hbar \omega_a$. This is the quantum limit. The minimum detectable strain amplitude allowed by a quantum limited amplifier can be expressed as [13]:

$$h_{SQL} = \left(\frac{2 \hbar \omega_a}{M \pi^2 v_s^2} \right)^{\frac{1}{2}} \sim 1.1 \times 10^{-22} \left[\left(\frac{f}{1 \text{ kHz}} \right) \left(\frac{10^5 \text{ kg}}{M} \right) \left(\frac{10^4 \text{ ms}^{-1}}{v_s^2} \right) \right]^{\frac{1}{2}}. \quad (1.15)$$

Thus, a detector with parameters equivalent to those implied in the above two numerical equations can obtain a burst strain sensitivity of approximately $\Delta L/L = 10^{-21}$, limited by the thermal noise. These parameters are likely for advanced detectors, where 100 tonne masses could be implemented.

Reduction of the effective thermal noise is very important in resonant gravitational wave detectors. The term ‘effective thermal noise’ has been used since it is possible to monitor the longitudinal mode resonance of the bar as if it has a lower thermal noise level than that expected from its mean temperature. This is achieved by lowering the ratio of integration time to antenna relaxation time, τ_i/τ_a . A large value of τ_a indicates a low level of coupling between the thermal reservoir and the resonant mode. A small value of τ_i provides little time for the thermal fluctuations to significantly contaminate the resonant state of the bar. This sensitivity dependence on τ_a and τ_i is reflected in equations (1.13) and (1.14) where τ_a is represented by the Q value ($Q \sim \tau_a^{-1}$) in equation (1.14). It is interesting to note that the back action and series noise terms (second and third terms) in equation (1.13) also exhibit dependence on τ_i . However the total amplifier noise (sum of back action and series noise) cannot be reduced beyond the quantum limit by choice of τ_i . In the case of back action noise, reduced integration time is advantageous since there is a smaller amount of time for the fluctuations to build up and affect the mass. Conversely for series noise, it is advantageous to increase the integration time in order to reduce the bandwidth of the noise and hence the noise energy that will sum at the output.

1.2.4 Transducers

Following excitation from a gravitational wave, a transducer is necessary to convert the acoustic energy of the resonant bar into an electrical signal. The transducers used for resonant bar detectors fall into two categories, the passive and the parametric transducer. The passive transducer has no external power source. An inductive or capacitive system is used to detect motion, which is then coupled to a superconducting quantum interference device (SQUID) amplifier. The parametric transducer however, makes use of an external power source in the form of a pump oscillator at frequency ω_p , where ω_p is greater than the antenna frequency ω_a . The transducer is arranged such that the oscillation of the bar at frequency ω_a creates modulation sidebands on the output signal. An example of a relatively simple parametric transducer is the active capacitive transducer. Motion of the bar changes the capacitance of a capacitor which is part of a low loss resonant circuit. This motion therefore modulates a pump frequency electrical signal, adding modulation sidebands.

All linear transducers can be modeled by a two port network. This is conveniently expressed in the following matrix equation, where the Z_{ij} matrix represents the transducer itself, the (F, v) vector represents the force and velocity inputs from the bar and the (V, i) vector represents the voltage and current output from the transducer.

$$\begin{pmatrix} V \\ I \end{pmatrix} = \begin{bmatrix} Z_{11} & Z_{12} \\ Z_{21} & Z_{22} \end{bmatrix} \begin{pmatrix} F \\ v \end{pmatrix} \quad (1.16)$$

The mechanical input impedance of the transducer is given by Z_{11} in kgs^{-1} and the electrical output impedance by Z_{22} in ohms. The forward transductance is given by Z_{21} in Vm^{-1}s and indicates the transducer sensitivity. The larger the value of Z_{21} , the lower the series noise in the total noise U_n (equation (1.13)). The reverse transductance, Z_{12} in kgA^{-1} , determines the level of back action force that drives the antenna. Clearly this value should be minimal, however it can never be made zero.

In principle, it is possible for both types of transducers to approach quantum limited noise levels. The active nature of parametric transducers means that stored energy can induce forces on the bar that vary strongly with position. This effective spring constant, which may be very large, can cause stability problems. However, the parametric transducer is advantageous in comparison to a passive transducer when considering the coupling factor, β .

The parameter β was introduced by Gibbons and Hawking [12] and indicates the level of coupling between the transducer and the bar. It is defined as the ratio of acoustic energy that is converted to electrical energy in one cycle. From a thermodynamic point of view, the bar will be ‘heated’ by a passing gravitational wave before energy flow through β eventually brings the transducer and bar into equilibrium. The value of β will determine the time taken to reach equilibrium. For a passive capacitive transducer, the coupling factor β_{pass} can be expressed as:

$$\beta_{\text{pass}} = \frac{1}{2} \frac{CV^2}{M\omega_a^2 x^2}, \quad (1.17)$$

where C is the capacitance, V the electric potential, M the mass of the bar and x the capacitance separation. For a parametric capacitive transducer, the coupling factor is given by:

$$\beta_{\text{par}} = \frac{\omega_p}{\omega_a} \frac{1}{2} \frac{CV^2}{M\omega_a^2 x^2} \quad (1.18)$$

in the limit that the electric Q factor, Q_e , is greater than the ratio of the pump frequency to the antenna frequency, ω_p/ω_a . The advantage that a large β provides is

that a smaller integration time, τ_i , is needed to extract the same amount of acoustic energy. The benefit of using a small value of τ_i was discussed in the previous section, being that the effective Brownian motion noise can be reduced beyond the fundamental limit.

1.2.5 Impedance Matching

Impedance matching is one of the reasons why gravitational wave detection is extremely inefficient. To achieve a large energy flow from the gravitational wave to the detector involves matching the mechanical output impedance of space time ($c^3/G \sim 10^{33}$ ohms) to molecular matter ($\omega_{\text{bar}}M_{\text{bar}} \sim 10^7$ ohms) or electromagnetic waves (~ 377 ohms). Similarly obtaining a high coupling factor, β , requires a match between the output impedance of the bar and the input impedance of the transducer. This is a relatively difficult task since the mechanical output impedance of the bar is very high compared to that of an electric or magnetic field that couples to the transducer. The requirement is an acoustic transformer at the interface. This can be achieved through the use of a secondary low mass resonator with an oscillation frequency tuned to that of the bar.

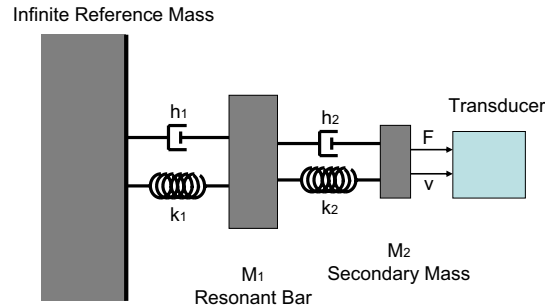


Fig. 1.7: Mechanical model of a secondary resonator used for impedance matching between the bar and the transducer.

A mechanical model illustrating the use of a secondary resonator for the purpose of impedance matching is shown in Fig. 1.7. The secondary mass is much smaller than the resonant mass allowing reasonable coupling to the transducer. Three specific secondary resonator designs are the diaphragm [14], the mushroom [15] and the bending flap [16]. The concept of these designs are illustrated in Fig. 1.8. It is possible for the secondary resonator to be replaced by multiple resonators, in effect creating a multimode acoustic

transformer. With several resonators coupled to the bar, the progressive reduction of mass in each stage can be more gradual, allowing a better overall impedance match.

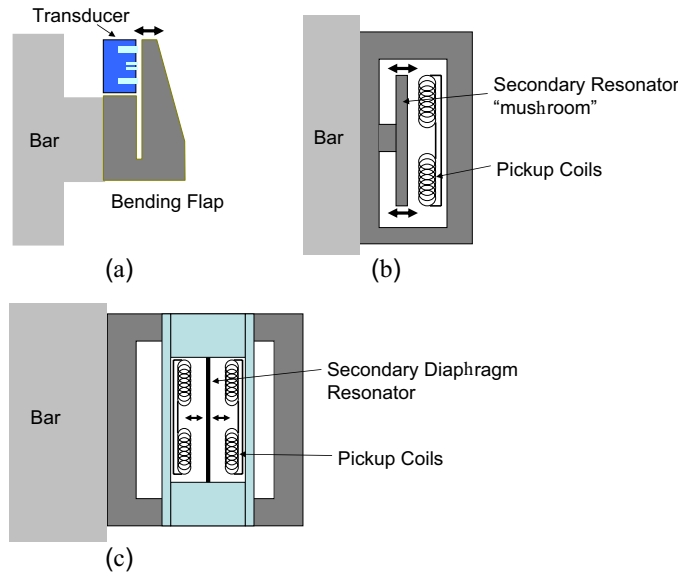


Fig. 1.8: Secondary resonator designs. (a) Bending flap; (b) mushroom; (c) diaphragm.

1.2.6 Suspension Systems

Another important consideration in the design of a resonant mass gravitational wave detector is the suspension of the bar. One purpose of the suspension system is to isolate the resonant mass from seismic noise. Seismic noise typically has a spectrum of the form $\alpha f^{-2} \text{m Hz}^{-1/2}$, where α may range from 10^{-6} to 10^{-9} . Therefore, it is essential that vibration is heavily attenuated at the fundamental resonance of the antenna. Attenuation of approximately 10^{10} at the frequencies of interest can be achieved with mechanical isolators [17, 18]. The normal modes of the suspension define low frequency resonance, whilst for higher frequencies, vibration is heavily attenuated. However, in designing such isolation systems, one must be wary of the high frequency internal modes of the individual suspension elements and masses. These modes can cause severe degradation of the performance of the isolator. Ideally the system should be designed such that the normal modes are as low as possible while keeping all the higher order modes above the antenna frequency.

The suspension must also be constructed from a low loss material, particularly at the point of contact, in order to preserve the high Q factor of the bar. For the same

reason the point of contact should be at a vibrational node [19]. In fact the method of contact is an important issue, since additional vibration can be induced if one is not careful. The traditional use of a cable slung around the bar for suspension results in a mechanism known as the slip–stick phenomena. This occurs due to the poorly defined boundary conditions at the tangential points, and is a source of additional noise. A better solution is to use a well defined method of attachment, i.e. welding suspension rods to the bar, or through the use of high pressure well defined contact points.

Finally in ultracryogenic detectors (below 100mK) the suspension must be an adequate thermal conductor. In such a system ultracryogenic cooling is achieved through a conduction path from the antenna to the dilution refrigerator. Since the dilution refrigerator is likely to be a large source of vibration, this conductive requirement needs to be carefully integrated with the vibration isolation requirement.

1.2.7 Advanced Detectors

Spherical detectors possess certain properties that make them advantageous in comparison to current cylindrical resonant mass detectors. Through the use of five or more transducers to monitor the quadrupole modes, gravitational waves of all polarisations and from all directions can be detected using a single sphere. Also, for a sphere of diameter equal to the length of a cylindrical bar, the cross section (amount of coupled gravitational wave energy) is greater by a factor equal to the ratio of the masses, ~ 20 . Recent studies have analysed methods of overcoming technical difficulties that may be associated with spherical detectors. Thus the realisation of spherical detectors is underway with development of small 65cm diameter detectors, MiniGRAIL [20] at Leiden University (Holland) and Schenberg [21] at São José Campos INPE (Brazil).

Very large spherical detectors have been proposed with masses ~ 100 tonnes. One of the difficulties with large spherical detectors is the problem of impedance matching the transducer to the spherical quadrupole mode. Using a single stage additional resonator as an acoustic transformer is not sufficient, since the resonator mass will be smaller than the effective quadrupole mass of a 100 tonne sphere by a factor of about 10^5 . In order to achieve a reasonable antenna bandwidth, it is desirable that the mass ratios between adjacent resonators are no more than 30:1. This, therefore, requires a four stage impedance matching oscillator.

For the small spherical detectors being developed, efficient impedance matching and bandwidth can be achieved with less resonant stages. Such devices have been designed for MiniGRAIL [22], and the Schenberg detector [23].

The dual detector [24] has been recently proposed as a promising new design for an acoustic gravitational wave detector. The scheme basically comprises of two nested resonant masses, designed such that their response to a gravitational wave is 180 degrees out of phase. Sensors measure the relative displacement between the surfaces of the two oscillators. In such a detector, the bandwidth can be made quite large, approximately equal to the difference between the two resonant modes. Back action noise also tends to subtract, leading to a flat response within the detector bandwidth. Proposed schemes, such as the dual cylindrical molybdenum detector described in [25] boast extremely high sensitivity in the kHz range. With an optimised readout system, sensitivity approaching $2 \times 10^{-23} \text{mHz}^{-1/2}$ over a bandwidth from 2kHz to 5kHz can be achieved. Detectors with such high sensitivities in the kHz range would nicely compliment interferometric gravitational wave detectors.

1.3 Interferometric Gravitational Wave Detectors

1.3.1 Introduction

An interferometer is a sensitive device for measuring length changes. In a simple Michelson interferometer, relative differences in the length of two orthogonal arms can be measured to a sensitivity of a fraction of the wavelength of the incident light. The maximum sensitivity is achieved when the two arms change length out of phase, i.e. one arm stretches while the other shrinks. This describes a quadrupole distortion of the plane of the interferometer, making it ideally suited as a gravitational wave detector.

The idea of using an interferometer as a gravitational wave detector was suggested as early as the 1960s, and in the 1970s the first sensitive interferometer was constructed [26]. A strain sensitivity of $2 \times 10^{-16} \text{ Hz}^{-1/2}$ was achieved. To date, several long baseline interferometers have been constructed and are in operation or being commissioned. LIGO [27] located in the USA includes two 4km interferometers and one 2km interferometer and has reached its design sensitivity, corresponding to a peak sensitivity of $3 \times 10^{-23} \text{ Hz}^{-1/2}$ at approximately 150Hz. The GEO600 detector [28] in Germany is a 600m interferometer reaching a peak sensitivity of $7 \times 10^{-22} \text{ Hz}^{-1/2}$ at 1kHz. TAMA300 [29, 30] is a 300m interferometer located in Japan with a peak sensitivity of $3 \times 10^{-21} \text{ Hz}^{-1/2}$ at 1.3kHz. The VIRGO interferometer [31] is a 3km interferometer which is currently being commissioned. Interferometers with such high sensitivity required the development of new optical schemes, low noise lasers, high quality optics and advanced vibration isolation systems. Their high sensitivity goals in a low frequency band (few 10s of Hz to kHz) is likely to complement the array of existing and developing resonant mass detectors. Finally with the launch of LISA in the near future, a powerful gravitational wave detection network can be achieved over a vast frequency range.

1.3.2 Optical Configurations

Simple Michelson Interferometer

The layout of a simple Michelson interferometer is illustrated in Fig. 1.9. As a gravitational wave passes perpendicular to the plane of the interferometer, one arm will contract while the other arm elongates. The change in length, ΔL , where $\Delta L = L_2 - L_1$

will change the relative phase between the light that recombines at the beam splitter. This change in phase can be expressed as $\Delta\phi$, where

$$\Delta\phi = 2\pi\Delta L/\lambda. \quad (1.19)$$

for incident light of wavelength λ .

The interferometer is most sensitive at a ‘dark fringe’. This occurs when the relative phase between the recombined light signals are 180 degrees out of phase. In this situation, no light is seen at the photodetector. An interferometric gravitational wave detector is designed such that the output is always dark. Control systems keep the recombining light 180 degrees out of phase, and it is the error signals in the servo loops that contain the information about the distortion due to a passing gravitational wave.

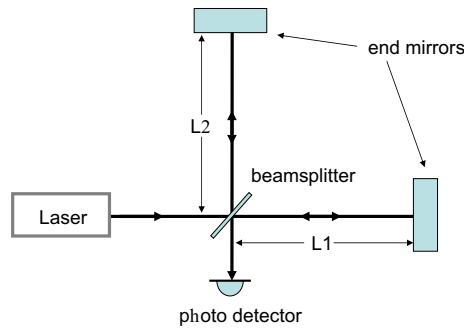


Fig. 1.9: A basic Michelson interferometer.

Ideally, an interferometer is immune from frequency and intensity fluctuations at the input laser. These cause common mode fluctuations in the arms to which the output of the interferometer is insensitive. However in reality, asymmetries in the arms and small differences in the optics will cause the fluctuations to unavoidably couple to the output signal. Intensity noise can be suppressed using an active control loop. The output intensity of the laser is monitored directly through the use of an intensity photodetector. This is used to generate an intensity error signal which can be fed back through an amplifier to modulate the current running through the laser diodes, or through a current shunt circuit located in parallel with the diodes. The bandwidth of the servo loop must be large enough to reduce the relative intensity fluctuations, $\Delta P/P$, to less than $10^{-8}\text{Hz}^{-1/2}$ between 40Hz to 100Hz. A laser intensity noise level of $2 \times 10^{-8}\text{Hz}^{-1/2}$ in this frequency region has been achieved [32].

The laser frequency stabilisation technique that is used in current interferometric detectors was proposed by Drever and Hall et. al. [33], and is based on a technique used in microwave systems proposed by Pound [34]. Figure 1.10 illustrates the essential components of this method. The purpose of radio frequency (RF) modulation and demodulation of the light enables the frequency fluctuations of the laser to be measured relative to a frequency reference provided by the reference cavity. A frequency error signal can then be fed back to the laser or a Pockel cell modulator. Frequency fluctuations have been suppressed to a level of almost $1\text{mHz Hz}^{-1/2}$ at 100Hz using this method [35]. Further frequency stabilisation can be attained through the use of a large suspended reference cavity, where frequency noise of $10\mu\text{Hz Hz}^{-1/2}$ at 100Hz has been achieved [35].

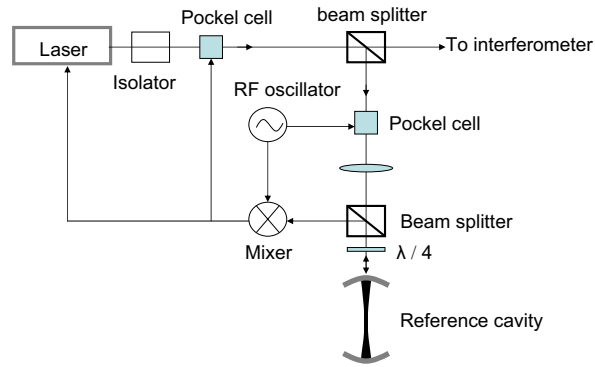


Fig. 1.10: Laser frequency stabilisation.

Another source of noise that is related to the input laser is beam jitter, the result of vibrations of the laser cavity. If the interferometer is not perfectly symmetric, vibrations of the incident beam can couple to the output signal. This is solved in interferometric detectors using a mode cleaner. The mode cleaner is an optical cavity through which the incident light is passed before reaching the interferometer. Higher order modes that are present in the incident beam can be suppressed by a long, high finesse optical cavity, designed such that all modes except the fundamental mode are strongly suppressed. Vibration coupling due particularly to seismic noise through to all optical components (including mode cleaner optics) can also affect the output signal. This is solved through the use of advanced vibration isolation techniques, which is discussed in a later section.

The standard quantum limit defines the highest sensitivity that can be achieved with an interferometer, without the use of quantum-non-demolition techniques. Photon

counting error and radiation pressure fluctuations both contribute to the quantum noise [36, 37]. Photon counting error (shot noise) is a result of $N^{1/2}$ fluctuations in the number of photons read by the photodetector. This noise is reduced when the interferometer operates around a dark fringe. The minimum detectable strain sensitivity limited by shot noise expressed in terms of laser power, P , for a perfect photodetector is given by:

$$h_{SN} = \frac{c}{2\omega} \sqrt{\frac{\hbar\omega}{P\tau}} \quad (1.20)$$

where ω is the laser frequency and τ the light storage time. Radiation pressure noise, however, occurs as a result of radiation pressure forces acting on the mirrors. It is a back action effect and sets a minimum detectable strain described by:

$$h_{RP} = \frac{2\hbar\omega\tau}{cM} \sqrt{\frac{P\tau}{\hbar\omega}} \quad (1.21)$$

where M is the mirror mass. Since photon shot noise scales as $P^{-1/2}$ and radiation pressure noise scales as $P^{1/2}$, then clearly there will be an optimal value for P . This value can be expressed as

$$P_{opt} = \frac{\lambda Mc}{8\pi\tau^2}. \quad (1.22)$$

For a reasonable set of parameters, $M \sim 10^2\text{kg}$, $\tau \sim 10^{-3}\text{s}$ and $\lambda \sim 1\mu\text{m}$, the optimum laser power is given by $P_{opt} \sim 6 \times 10^7\text{W}$. Despite the practical issues concerned with constructing a low noise laser of such high power, it is possible to approach the standard quantum limit using interferometer parameters similar to those above. These methods are mentioned below.

Fabry-Perot Cavity Interferometer

The Fabry-Perot cavity interferometric detector was first proposed by Drever et. al. [38]. In such a device, two extra mirrors are added in the interferometer to create resonant cavities in the arms. These cavities are illustrated in Fig. 1.11. The storage time of the light in a Fabry-Perot interferometer can be increased to $\sim 0.5 \times 10^{-3}\text{s}$ for arm lengths of a few km. This optimum storage time for gravitational wave detection of $\sim 1\text{kHz}$ would otherwise require Michelson interferometer arm lengths of 150km. One advantage of using a Fabry-Perot cavity over a delay line cavity is the reduction in the required mirror size and vacuum tube diameter. The optical resonance also increases the effective light power in the arms, reducing the shot noise and approaching closer to the optimum power required to reach the standard quantum limit.

Power Recycling Interferometer

While an interferometer operates around a dark fringe, almost all of the incident light—except that which is lost due to imperfections in the optics—is reflected back towards the laser. Thus, the interferometer acts like a mirror. Using this property, the power incident on the interferometer can be increased by a technique termed power recycling [39]. By placing a recycling mirror between the laser and interferometer, as illustrated in Fig. 1.11, a large resonant optical cavity that includes the interferometer can be realised. Using this technique, the effective laser power within the power recycling cavity can be made 1000 times larger than the incident laser.

Dual Recycling Interferometer

A dual recycling interferometer [39] involves both a power recycling mirror and a mirror located between the output of the interferometer and the photodetector. This is known as the signal recycling mirror and the arrangement of this type of interferometer is illustrated in Fig. 1.11. The purpose of the signal recycling mirror is to reflect the signal sidebands induced by gravitational waves back into the interferometer. With correct positioning of this mirror, the signal power and thus the interferometer sensitivity can be increased. The increase in sensitivity comes at a cost of a reduced bandwidth, due to the increase in storage time of the signal sideband. Dual recycling has been demonstrated on the Garching 30m prototype interferometer [40, 41] and is used in the GEO600 detector [42].

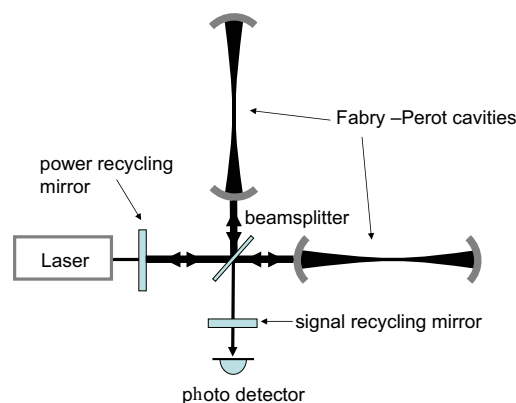


Fig. 1.11: Dual recycled interferometer.

1.3.3 Optical Spring Effect

For cavities with sufficiently large circulating optical power, radiation pressure can induce significant forces on the mirrors. These forces have a magnitude of $\sim 70\text{mN}$ in cavities with 1MW circulating power. The dependence of the resonating light intensity on the cavity length results in a radiation force that is dependent on the mirror positions. Therefore, the cavity acts like an optical spring.

Correlation between intensity fluctuations and radiation pressure fluctuations allows the standard quantum limit (SQL) as described for free masses, to be suppressed in a narrow frequency band. This is possible because the cavity mirrors are no longer free. Instead they act as a simple harmonic oscillator, with a resonant frequency dependent on both the optical spring constant and the mechanical spring constant of the suspensions. A reduction in the SQL for free mirrors can be achieved since the SQL for a harmonic oscillator is lower in a frequency band around the resonance. Using this technique, it is possible to increase the sensitivity of large scale quantum limited interferometers [43]. For this reason, there has been a significant amount of research in this area and experimental demonstration of this effect using table top optics [44] and high powered optics [45].

1.3.4 Vibration Isolation

The optics in a gravitational wave detector must be isolated from the earth which vibrates with a spectrum given approximately by $\alpha f^{-2}\text{m Hz}^{-1/2}$, for $\alpha \sim 10^{-6} - 10^{-9}$. Suitable isolation has been achieved using sophisticated mechanical isolators that incorporate both active and passive techniques. The VIRGO Superattenuator provides sufficient vibration isolation to increase the detection bandwidth down to a few Hz [46]. It is inevitable that seismic noise will limit detector sensitivity at low frequency, since larger amplitude low frequency vibrations become increasingly difficult to suppress. However, it is not only the performance of the isolation system in the detection bandwidth that is important. Any residual motion below the isolator cutoff frequency affects the ability to lock mirrors to various optical schemes as discussed above. Thus, an ideal isolation system for interferometer optics will attenuate vibration within the detector pass band as well as frequencies below. For the remainder of this section we discuss some methods to achieve this.

The design of passive mechanical isolators used in current interferometric gravitational wave detectors, is based on a series of cascaded pendulums. Each pendulum acts as a horizontal isolator of frequency, f_N , where the total attenuation for frequencies higher than the highest resonant mode is given by $(f_1 f_2 \dots f_N / f^N)^2$. Ideally, only horizontal isolation would be required, however due to the curvature of the earth and other mechanical imperfections, there is minimum coupling from vertical to horizontal vibration of 10^{-3} . At present, developments in vertical isolation are achieved through the use of tapered metal cantilever springs developed at both UWA [47] and VIRGO [48], or Euler springs [49] developed at UWA.

Active methods can also be used for vibration isolation. Such methods include monitoring the relative test mass motion and feeding an error signal back to an actuator. This can act either at the suspension point, or directly on the test mass in order to apply a corrective force. For a suspension with a transfer function, G , and a feedback amplifier with transfer function, H , the closed loop transfer function can be expressed as:

$$\frac{x_o}{x_i} = \frac{G}{1 + HG} . \quad (1.23)$$

Thus, it can be seen that the level of isolation improves with increasing value of H . In reality however, H is limited by instabilities caused by the excess feedback of internal mechanical mode oscillations. H must be chosen such that all closed loop poles appear in the left half of the complex plane. Active isolation techniques have been studied at Glasgow University [50] and an active hydraulic pre-isolator has been developed at Stanford University [51, 52]. Active hydraulic pre-isolators that provide isolation from approximately 0.1Hz up to 10Hz have been installed at the Livingston LIGO site [27].

The result of cascading several pendulum and vertical stages to form an isolation chain is amplified motion at the mode frequencies. Although this motion is at frequencies below the detection band, high amplitude residual motion makes locking the optical components to within a fraction of the laser wavelength extremely difficult. Reducing the residual motion can be achieved through the use of a pre-isolator. The pre-isolator is a suspension stage with very low resonant frequency (10mHz–50mHz) and thus a low cutoff frequency. Used in conjunction with an isolation chain, the pre-isolator filters the motion due to the isolation chain resonant modes, that would

otherwise increase residual motion. At the same time, the internal mechanical resonances of the pre-isolator that would normally degrade isolation performance is filtered by the isolation chain. The very low frequency oscillation of the pre-isolator can easily be suppressed using active techniques. There are several methods of creating ultra low frequency suspension stages suitable for use as a pre-isolator. One such method is through the use of an inverted pendulum [53, 54]. This has led to the development of the 6m pre-isolator for the VIRGO superattenuator [55], and a much more compact stage with comparable performance at UWA [56].

1.3.5 Thermal Noise

Above the frequency region where seismic noise is sufficiently suppressed (above 10Hz), thermal fluctuations may contribute a significant amount of noise. This is termed thermal noise and in gravitational wave interferometers, is normally divided into two categories: Suspension thermal noise and test mass thermal noise.

Suspension thermal noise comprises of the thermal fluctuations of the suspension system that is seen at the optic. Since this involves filtering of the thermal noise through the suspension itself, it is the final suspension stage that will dominate this source of noise. For a simple resonant system with spring constant, k , mass, m and loss angle, ϕ , the thermal noise displacement power spectrum as seen at the test mass can be given as [57]:

$$x_p^2 = \frac{4k_B T k \phi}{\omega[(k - m\omega^2)^2 + k^2 \phi^2]} . \quad (1.24)$$

By replacing the spring constant with $k = \omega_0^2 m$ and expressing the loss angle ϕ with $Q_p = \gamma/\phi$, the thermal noise power spectrum of a single stage suspension can be approximated by:

$$x_p^2 = \frac{4k_B T \omega_0^2}{Q_p m \omega^5} , \quad (1.25)$$

for $\omega \gg \omega_0$. It can be seen that the suspension Q-factor, Q_p , can be made high depending on the enhancement factor γ . In pendulum suspensions, this factor can be large (several hundred) if the majority of the energy is stored in the loss-less gravitational field and not in the bending of the suspension element. From equation (1.25), it is clear that minimising suspension thermal noise is achieved by increasing the mirror size or suspension Q. Very high pendulum Q factors ($> 10^7$) have been achieved using

fused silica fibres [58]. Thus there has been extensive research into the use of low loss materials such as fused silica for test mass suspensions [59, 60].

Test mass thermal noise involves the thermal fluctuations of the optic. The thermal noise displacement power spectrum of the surface of the test mass can be expressed as a function of the internal resonances [57]:

$$x_{int}^2 = \frac{4k_B T}{\omega} \sum_i \frac{\omega_i^2 \phi_i}{m_i [(\omega_i^2 - \omega^2)^2 + \omega_i^4 \phi_i^2]} . \quad (1.26)$$

Here, i denotes the i th mode and m_i is the effective mass associated with that mode. Typically, the internal resonances are several kHz and thus at the high end of the detection band. The displacement power spectrum can then be simplified by assuming that $\omega \ll \omega_i$, and that the loss angle is constant for all modes:

$$x_{int}^2 = \frac{4k_B T \phi}{\omega} \sum_i \frac{1}{m_i \omega_i^2} . \quad (1.27)$$

This result presents a guide towards choosing a test mass material that will exhibit low internal thermal noise within the detection band. A low ϕ (or high Q) is critical, and the internal resonances (defined by the test mass geometry and velocity of sound) must be as high as possible. These issues are satisfied in both sapphire and fused silica test masses. For sapphire, the intrinsic Q, where $Q \sim 1/\phi$, is 3×10^8 [58] and velocity of sound 10^4ms^{-1} while for fused silica 6×10^7 [61] and $6 \times 10^3 \text{ms}^{-1}$ respectively. Additionally, analysis of the dependence of the internal loss, ϕ , for silica on both frequency and surface to volume ratio has been reported by Penn et al [62]. These two materials, sapphire and fused silica, also exhibit favourable optical properties needed in high power interferometers such as low optical absorption.

The normal-mode decomposition approach described above to estimate test mass thermal noise is no longer accurate if inhomogeneous losses are considered. A direct application of the Fluctuation-Dissipation theorem was first developed by Levin to address this problem [63]. An example of an inhomogeneous loss is that due to the optical coating on one face of the test mass in order to provide the required reflectivity for interferometer operation. Test mass thermal noise due to the mechanical loss of the coating substrate, or coating losses, are expected to limit sensitivities of advanced detectors in the mid frequency range. As a result, a significant amount of study addressing coating losses has been done [64, 65, 66].

1.3.6 Advanced Interferometers

Future interferometric detectors such as Advanced LIGO [67] and LCGT [68] may boast extremely high sensitivity in a reasonably high bandwidth around 100Hz. Capable of detecting strain amplitudes of a few $\times 10^{-24} \text{Hz}^{-1/2}$ in this frequency region, a neutron star inspiral reach of $\sim 200 \text{Mpc}$ is possible. With this reach, several events per year can be expected.

To achieve this sensitivity, the interferometer must be quantum limited. This requires a reduction of other noise sources such as seismic noise and thermal noise. In the case of Advanced LIGO, a four stage fused silica suspension is being developed that will provide adequate vibration isolation, as well as very low thermal noise performance. A dual recycling optical scheme with Fabry-Perot cavities allows high optical power in the arms in order to reduce shot noise. The signal recycling mirror provides some degree of tunability, where it may be possible to optimise the interferometer for a particular astrophysical source. The fundamental noise sources expected in Advanced LIGO was generated using the default values of Bench62², and plotted in Fig. 1.12 below.

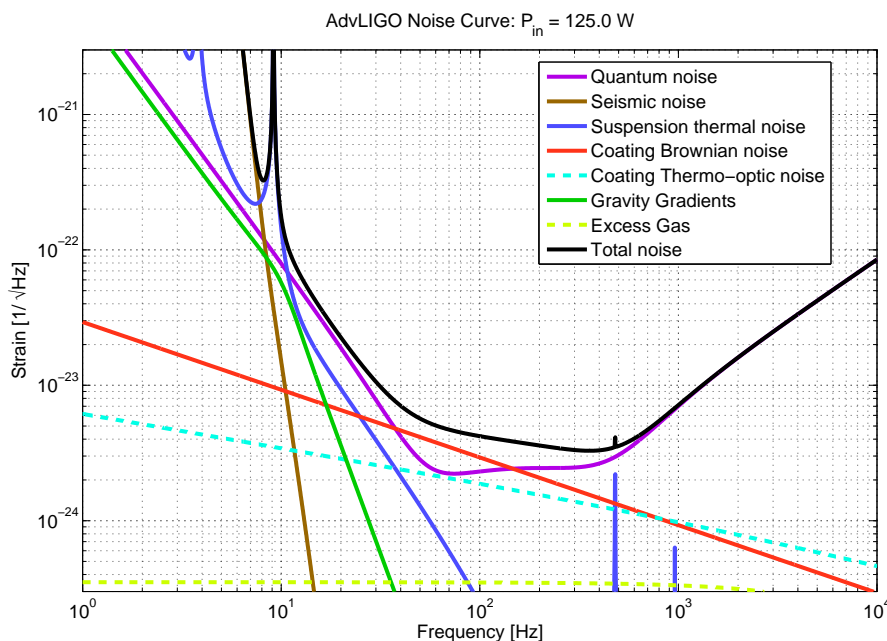


Fig. 1.12: Fundamental noise sources expected in Advanced LIGO generated using Bench62.

²See <http://ilog.ligo-wa.caltech.edu:7285/advligo/Bench>

The LCGT is a proposed cryogenic interferometer that will be developed in Japan. The major difference with this interferometer is the method of reducing thermal noise. Reduction of the thermal noise towards the quantum limit is realised by cooling the mirrors down to 20K. Since thermal noise will be reduced due to the cryogenic environment, the choice of suspension material is based on both cryogenic compatibility, as well as the intrinsic Q factor.

With such high sensitivity over a large bandwidth, the finalisation of these advanced interferometric gravitational wave detectors should signal the start of gravitational wave astronomy. Like the development of resonant mass detectors, improvements in suspended interferometric techniques are rapidly increasing detector sensitivities. It seems likely that we will witness successful operation of advanced interferometric detectors in the near future.

1.3.7 Australian International Gravitational Observatory

The Australian International Gravitational Observatory (AIGO) [69] is located in Gingin, Western Australia and is the facility to which all of the work presented in this thesis aimed. This high optical power research facility currently aims to investigate problems that high optical power may pose in advanced detectors. Such problems include thermal lensing and parametric instabilities. Advanced isolators supporting sapphire optics are also being built for further experimentation. The test mass suspension designs and global control methods presented in this thesis are to be implemented in this part of the observatory.

CHAPTER 2

MIRROR SUSPENSION THERMAL NOISE

2.1 Introduction

In order to achieve the high sensitivity proposed for advanced interferometric gravitational wave detectors, suspension thermal noise must be reduced below the standard quantum limit in the frequency range above approximately 10Hz. For Advanced LIGO, the displacement sensitivity is expected to be $8 \times 10^{-21} \text{m}/\sqrt{\text{Hz}}$ at 100Hz [67] thus setting a level below which the suspension thermal noise observed at the suspended optic should exist.

A mechanical system that is in equilibrium with a thermal reservoir will exhibit modes each with average energy $k_B T$. Randomly fluctuating thermal forces drive the mechanical system and through its mechanical resistance, a random displacement, analogous to Brownian motion, results. It is this thermally induced displacement noise at the location of observation that is known as thermal noise. For a low loss mode (or a mechanical oscillation with a high Q factor), most of the thermally induced energy exists within a small frequency band centered around the mechanical mode frequency. As a result, the thermal noise power is lower in other possibly more important frequency regions. For an internally damped mechanical oscillator, non-zero loss implies energy dissipation, which according to the fluctuation dissipation theorem [70] guarantees mechanical noise. The resulting thermal noise power of the oscillating object is given by [57]:

$$x^2(\omega) = 4k_B T \frac{k\phi(\omega)}{\omega((k - m\omega^2)^2 + k^2\phi^2(\omega))} \quad (2.1)$$

Here, k_B is the Boltzmann constant, T the temperature, k the oscillator spring constant, m the oscillator mass, ϕ the loss angle and ω is the frequency in rad/s. Equation 2.1

can be rewritten in terms of the resonant frequency ω_0 :

$$x^2(\omega) = \frac{4k_B T}{m} \frac{\omega_0^2 \phi(\omega)}{\omega((\omega_0^2 - \omega^2)^2 + \omega_0^4 \phi^2(\omega))} \quad (2.2)$$

It is through this equation that the design requirements for an oscillator with minimal thermal noise can be obtained:

1. Minimise the temperature, T , of the oscillator.
2. Maximise m without changing the resonant frequency.
3. Minimise the loss, $\phi(\omega)$.
4. Assuming ϕ is constant, for $\omega \gg \omega_0$, the thermal noise power $x^2(\omega)$ goes as $\frac{1}{\omega^5}$. Thus it is desirable to have the resonant frequency of the oscillator as far below the important frequency band as possible. The problem however is that higher order mode frequencies will also decrease with a reduction in primary mode frequency. These higher order modes will also contribute thermal noise which must be considered.

In this chapter, the minimisation of suspension thermal noise in interferometric gravitational wave detectors will be discussed. A study of several suspension materials will also be presented, with the aim of the research being to select the material with which the suspensions for AIGO will be constructed.

2.2 Suspension thermal noise in interferometric GW detectors

When considering interferometric gravitational wave detectors, suspension thermal noise is often classified in a slightly broader heading of noise sources termed thermal noise. This includes suspension thermal noise and test mass thermal noise, where the only significant difference is the source of the dissipation and hence thermal fluctuations. Test mass thermal noise considers the mechanical dissipation and material properties in the mirror substrate itself as well as the reflective coatings, where thermal energy excites test mass internal modes. Motion at the surface of the mirror is integrated over the laser spot, and it is this integrated motion that is observed as test mass thermal noise. The lowest internal mode of the mirrors are generally around 10kHz

for typical interferometer size test masses. Therefore the thermal noise power that is contributed from the test mass has mainly a $1/\omega$ response within the detection band.

Suspension thermal noise however considers the dissipation within the suspension element. Thus thermal energy excites suspension modes which result in mirror motion. The primary suspension modes usually have frequencies close to 1Hz and are therefore lower than the observation frequencies. The higher order modes of the suspension however begin at a few hundred Hz, and thus lie within the detection band where it is expected that photon shot noise will limit the sensitivity. The focus of my research has been on the suspension thermal noise and thus the following sections relate to the issue of minimising suspension thermal noise.

Thermal noise can be reduced by lowering the temperature of the suspension. The use of cryogenics in resonant mass gravitational wave detectors is common and necessary to reduce thermal noise to required levels. The principle is the same for interferometric gravitational wave detectors where each suspended optic of the main detector needs to be cooled. This is the motivation behind the LCGT project [71], which differs from the current detectors of LIGO, VIRGO, GEO600 and TAMA since the final stages of the suspension system are to be kept at temperatures below 20K. Suspension materials with high conductivity providing a path for heat flow must be used. For LCGT, it is proposed that sapphire fibres will suspend the optic while high purity aluminium also provide heat extraction paths. The cryogenic part of the system must also be integrated with the vibration isolation system which operates at room temperature. Although a reduction in temperature to 20K will only reduce the thermal noise power directly by about one order of magnitude, the reduction in temperature may also affect certain material properties resulting in a smaller loss value ϕ . This is discussed in more detail in the following sections. Operating the interferometer at cryogenic temperatures also has other advantages, such as a reduction in thermal lensing [72].

Currently the test masses to be used at AIGO are approximately 4kg, compared to the largest test masses used at VIRGO of approximately 20kg. For advanced detectors, masses in excess of 30kg are planned. Larger masses imply more inertia, and thus more resistance to spurious thermal acceleration forces. However larger masses also require stronger suspension elements and control forces, placing a practical limit on the maximum test mass size. Other considerations such as cost and optical properties often take precedence when selecting test mass sizes, and therefore many consequences

must be considered before test mass dimensions are changed in order to reduce thermal noise. Larger test masses however, also provide the advantage of less susceptibility to radiation pressure noise. Since radiation pressure noise is the quantum limit of an interferometric gravitational wave detector at low frequencies, future detectors that are made specially for low frequency operation may consider the use of test masses in the order of 100kg.

The largest amount of research however has been devoted to the minimisation of the suspension internal loss, $\phi(\omega)$. The choice of material has a large influence on the level of suspension thermal noise. Steel (LIGO, VIRGO and TAMA) and fused silica (GEO600) suspensions are currently in use, with serious research having recently been invested into the possibility of advanced suspensions constructed from Silicon [73], Sapphire [74, 75] and Niobium [76] on top of the research having already been conducted for current suspensions [77, 78, 79]. These materials possess properties that, when treated properly, exhibit low levels of internal loss and thus are likely to provide suspensions for advanced detectors. Sapphire, Silicon and Niobium are also compatible with cryogenic temperature interferometers. Changing the aspect ratio of the suspension element by using ribbons [80] rather than fibers can also result in an effective reduction in ϕ through an improvement in the level of dissipation dilution.

Finally, the thermal noise contributed from the violin string modes of the suspension must be considered. The frequency band between the pendulum mode and first violin mode of the suspension is unlikely to exceed three orders of magnitude, and thus for a pendulum mode frequency of 1Hz, the violin modes are going to exist well within the detection band. Fortunately, the high Q factors exhibited by the violin string modes mean that the thermal noise will be observed as high amplitude spikes piercing the shot noise sensitivity limit. A readout scheme has been proposed to monitor the suspension thermal noise in LIGO and thus remove the violin mode thermal noise [81]. The method however requires accurate sensing for each suspension fiber and a sensor noise lower than $2 \times 10^{-11} \text{m}/\sqrt{\text{Hz}}$ to apply to second generation detectors. We have also studied violin mode thermal noise and come up with a suspension design that boasts a lower number of violin modes with lower peak amplitude. These results are presented in Chapter 4.

2.3 Suspension Materials

2.3.1 Standard Material Properties

Except for the GEO600 detector pioneering fused silica suspensions [82, 83], the use of steel or tungsten wires to suspend mirrors in first generation detectors were considered sufficient. The need for lower thermal noise however has led to the proposal of several other materials as possible candidates for advanced interferometers. Currently, the most likely suspension material (coinciding with the largest amount of suspension material research) is fused silica. Monocrystalline silicon and sapphire also show promise particularly at cryogenic temperatures, whilst niobium exhibits the best properties of all metals.

There are several desirable properties when considering the use of a material for mirror suspension. Firstly, the internal loss factor of the material, ϕ should be as low as possible. From Equation 2.2, it can be seen that at high frequencies, the thermal noise power is proportional to ϕ . Although other factors such as surface loss and dissipation dilution (discussed later) can change the effective value of ϕ , generally speaking, materials that boast favourable values of ϕ will provide lower loss suspensions.

Secondly, a high tensile strength allows the support of a larger mass, or equivalently, less suspension material to suspend the same mass. This results in higher frequency and further spaced suspension violin modes, and thus less thermal noise contamination within the detection band. For a thin suspension element with negligible bending stiffness compared to the tensile restoring force, the violin mode frequencies are given by;

$$f_n = \frac{n}{2L} \sqrt{\frac{F_T}{\rho_L}} \quad (2.3)$$

where f_n is the n th violin mode frequency, L is the suspension length, F_T is the tension and ρ_L is the linear mass density of the suspension element. Thus by maximising the tension to density ratio, $\frac{F_T}{\rho_L}$, a lower number of more widely spaced violin modes will exist.

Equation 2.3 also illustrates the desire for lower material mass density, ρ_v . A lower suspension mass also results in a lower level of coupling to the test mass. For the same thin suspension element as considered above, the violin mode squared displacement

amplitude at the suspended mass is [57];

$$\Psi_n^2(L) = \frac{2\rho_L L}{n^2\pi^2 M^2} \quad (2.4)$$

where Ψ_n is the n th mode shape. Therefore to minimise the level of violin mode displacement coupling to the test mass, a low linear density and hence volume density, ρ_v is desired.

Material	Loss Angle ϕ	Tensile Strength	Density ρ_v (kg/m^3)
Steel	$\phi \simeq 2 \times 10^{-4}$ [84, 85]	3GPa[84]	7800
Niobium	$\phi \simeq 1 \times 10^{-5}$ [86]	0.4GPa[87]	8570
Fused Silica	$\phi_{bulk} \simeq 6 \times 10^{-8}$ [59]	4GPa[84]	2200
Silicon	$\phi_{bulk} \simeq 3 \times 10^{-8}$ [79]	1GPa[79]	2330
Sapphire	$\phi_{bulk} \simeq 3 \times 10^{-9}$ [88]	2GPa[89]	4000

Tab. 2.1: Table of suspension material properties. The source of the values are referenced. The loss angles given above are bulk losses where indicated. Otherwise they are internal losses for suspension element size samples.

Using these three properties, we compare five different suspension materials, C85 steel, niobium, fused silica, crystalline silicon and sapphire. The resulting values for loss angle, tensile strength and density are given in Table 2.1. The obvious standout is fused silica, with the highest tensile strength, lowest volume density and very low loss angle. The value for tensile strength however is an average value, where the actual strength of the fiber is highly dependant on its handling during production. For this reason, a larger safety margin is required and hence a working stress of about 25%, or 1Gp is approximately the largest loading that should be applied. Similar sorts of safety margins would be required for silicon and sapphire suspensions. For the metallic suspensions of steel and niobium however, the tensile strength fluctuates less from sample to sample and hence a higher working stress of approximately 50% can be used.

2.3.2 Surface Loss

The bulk loss angle of a material, ϕ_{bulk} , however, is not sufficient to indicate the loss angle for a sample of typical suspension element dimensions. Surface loss is one

phenomena that must be considered, particularly since long thin suspension filaments have significant surface area compared to its volume. Gretarsson et. al. have studied the surface induced loss of fused silica fibers, characterising the loss as follows [90]:

$$\phi = \phi_{bulk} \left(1 + \mu \frac{d_s}{V/S} \right) \quad (2.5)$$

Here ϕ_{bulk} is the loss angle of the bulk material, d_s the dissipation depth, V/S the volume to surface ratio and μ a geometrical factor relating to the geometry of the suspension element and the mode of oscillation. For transverse oscillations, μ is given by;

$$\mu = \begin{cases} 2 & \text{fibers} \\ (3+a)/(1+a) & \text{ribbons} \end{cases} \quad (2.6)$$

where a is the aspect ratio (thickness to width) of the combined suspension elements. As a function of suspension dimensions, ϕ can be expressed;

$$\phi = \begin{cases} \phi_{bulk} \left(1 + 4 \frac{d_s}{r} \right) & \text{fibers} \\ \phi_{bulk} \left(1 + \left(\frac{3Nw+t}{Nw+t} \right) \left(\frac{2d_s(w+t)}{wt} \right) \right) & \text{ribbons} \end{cases} \quad (2.7)$$

where r is the radius or the ribbon, w and t are the width and thickness of the ribbon respectively and N is the number of ribbon suspensions. A more recent study by Penn et al has shown that the surface loss equation for fused silica can be extended to include a frequency dependant term [62]. However, for thin ribbon or fiber suspensions (with thickness or radius in the order of $100\mu\text{m}$), the surface loss dominates the contribution due to the frequency dependant term by more than two orders of magnitude for frequencies up to 10kHz. As such, the frequency dependant term is ignored for this study.

From Equation 2.7 it can be seen that for fiber suspensions (suspensions with circular profile), surface loss becomes significant when r approaches d_s . For ribbon suspensions (suspensions with rectangular profile), the surface loss will become significant when the smallest dimension of w or t (i.e. t) approaches d_s . In [80], it is given that d_s for fused silica is approximately $100\mu\text{m}$, although it may range between $30\mu\text{m}$ to $200\mu\text{m}$. Given that mirror masses to be supported by these suspensions may be close to 30kg, fused silica suspensions will likely have dimensions in the order of $100\mu\text{m}$, and thus the relevant loss angle of the material may be several tens of times higher than the bulk loss.

A similar study for thin single crystal silicon cantilevers was conducted by Yasumura et. al. [91], resulting in a similar characterisation of surface loss. Thus it is likely that for small dimension silicon suspensions, an increase in the material loss angle of larger than ten times could be expected, when compared to the bulk loss value of 3×10^{-8} . Although the bulk loss for niobium is in the order of 3×10^{-7} at room temperature [92], surface loss can result in a minimum loss angle of $\phi = 10^{-5}$ [86]. This is for thin niobium suspensions in the order of $100\mu\text{m}$ and given correct treatment. This also results from the geometry dependant Q factor of niobium, $Q_{Nb} \simeq 10^7(V/S)^{1/2}$ [76]. Finally, the surface loss properties for sapphire are not as well known as fused silica, however similar results would be a safe assumption.

2.3.3 Thermoelastic Loss

Another contribution to material loss ϕ is the frequency dependant phenomena known as thermoelastic loss [93, 94]. This loss results from the coupling of strain to temperature due to the non-zero thermal expansion coefficient of the suspension material. As the suspension element bends due to pendulum mode or violin mode oscillation, one side of the suspension element is slightly compressed whilst the other is slightly stretched. Consequently, the compressed side is heated while the stretched side is cooled and the resulting temperature gradient causes heat to flow. Given sufficient time for the heat flow to reduce the temperature gradient (depending on the oscillation frequency), the magnitude of the restoring force is reduced to a smaller value. This effect is observed as a frequency dependant mechanical loss.

The thermoelastic loss can be characterised as follows;

$$\phi_{th}(\omega) = \Delta \frac{\omega\tau}{1 + (\omega\tau)^2} \quad (2.8)$$

where Δ is related to the Young's modulus E , thermal expansion coefficient α , temperature T , volume density ρ_v and volume specific heat C_v by:

$$\Delta = \frac{E\alpha^2 T}{\rho_v C_v} \quad (2.9)$$

The value τ is related to the geometry of the suspension by;

$$\tau = \begin{cases} \frac{\rho_v C_v r^2}{1.08\pi\kappa} & \text{fibers} \\ \frac{\rho_v C_v t^2}{\pi^2\kappa} & \text{ribbons} \end{cases} \quad (2.10)$$

where r and t are the radius and thickness of the suspension element respectively and κ is the thermal conductivity.

From the above equations, it can be seen that the thermoelastic loss peak occurs when $\omega\tau = 1$. Thus the frequency where the peak occurs increases for larger values of thermal conductivity κ or smaller suspension element radius r or thickness t . Generally, the thermoelastic loss at its peak is larger than any other internal loss, and thus it is desirable to locate the peak as far from the detection band as possible.

Material	Th. Expansion Coeff. α (K^{-1})	Th. Conductivity κ ($W/m/K$)	Specific Heat C_v ($J/kg/K$)	Peak Thermoelastic Loss Frequency (Hz)
Steel	1.2×10^{-5}	49	486	8122
Niobium	7.3×10^{-6}	53.7	265	3714
Fused Silica	5.1×10^{-7}	1.38	772	511
Silicon	2.6×10^{-6}	149	710	56592
Sapphire	5.4×10^{-6}	46	770	9384

Tab. 2.2: Table of suspension material thermophysical properties at 300K. The thermoelastic loss peak frequencies were obtained for ribbon thicknesses of $50\mu\text{m}$ in all except niobium, where a thickness of $100\mu\text{m}$ was used, due to its lower tensile strength.

A table of thermophysical properties at room temperature along with the thermoelastic peak frequency is given in Table 2.2. It is observed that the largest variation between materials occurs for the value of thermal conductivity, κ . Consequently, it is the high thermal conductivity of silicon and the low thermal conductivity of fused silica that accounts for the highest and lowest thermoelastic peak frequency in silicon and fused silica respectively. The width of the thermoelastic peak however means that thermoelastic loss is significant, particularly for the violin modes, in all materials except for silicon. The low thermal expansion coefficient, α of fused silica will also result in a lower level of thermoelastic loss. The level of thermoelastic loss for each material type is compared graphically as a function of frequency in the following section.

2.3.4 Total Material Loss

The total material loss can be reasonably approximated by summing the contributions from bulk material loss, surface loss and thermoelastic loss, i.e. $\phi = \phi_{bulk} + \phi_{surface} + \phi_{thermoelastic}$. The resulting loss angle for steel, niobium, fused silica, silicon and sapphire versus frequency is illustrated in Figure 2.1. In this plot, a circular profile is

assumed for each suspensions element. The steel and niobium fibers are loaded at 50% of their breaking strength as indicated in Table 2.1, while the fused silica, silicon and sapphire fibers are loaded at 25%. We also assume that a 30kg test mass is being supported by four suspension elements.

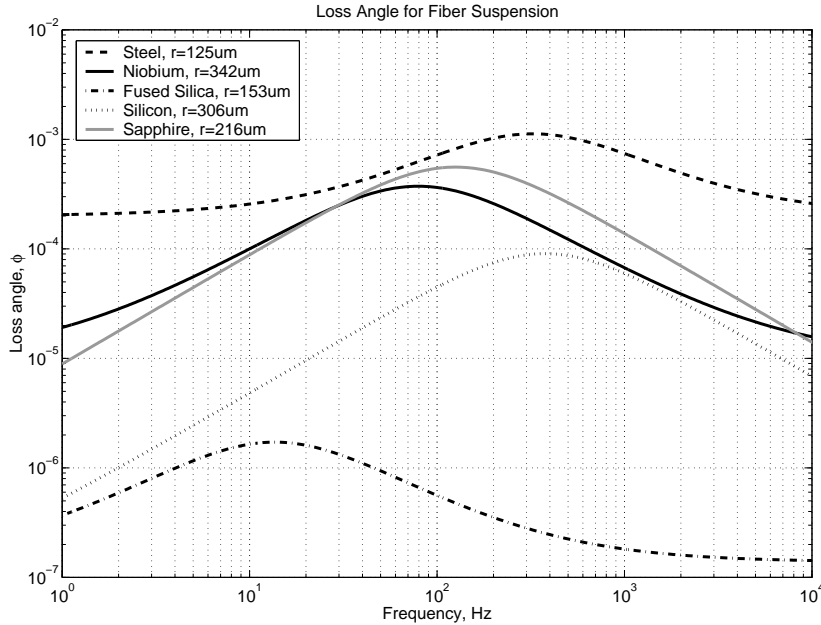


Fig. 2.1: Total loss angle as a function of frequency for various suspension materials. Fiber suspensions loaded at 50% of breaking stress are assumed with the steel and niobium fibers, while a 25% loading is assumed for fused silica, silicon and sapphire suspensions. A 30kg test mass supported by 4 suspensions is also assumed.

It can be observed that the pendulum mode thermal noise (close to 1Hz) is limited by thermoelastic loss for all the non-metallic suspensions, whereas the violin modes ($> 100\text{Hz}$) are affected by thermoelastic loss in all suspension materials. This provides reasonable argument for increasing the peak thermoelastic loss frequency by using suspensions that are thin in the critical direction (i.e. ribbons). It is also observed that the very low material loss of sapphire is completely overshadowed by the large thermoelastic contribution, giving it a poor room temperature loss angle at frequencies of interest. Fused silica and silicon display the lowest loss at the pendulum mode frequency, making these two materials the best candidates for room temperature fiber suspensions. The higher violin mode loss likely to be exhibited by the silicon fiber may be overlooked since photon shot noise is likely to dominate the detector noise at these frequencies.

In Figure 2.2, the total material loss for ribbon suspensions are illustrated. Again, the non-metallic suspensions are loaded at 25% of breaking stress while the metallic suspensions are loaded at 50%. A ribbon thickness of $50\mu\text{m}$ is assumed for all materials except niobium, where a $100\mu\text{m}$ thickness is assumed, due to its lower tensile strength.

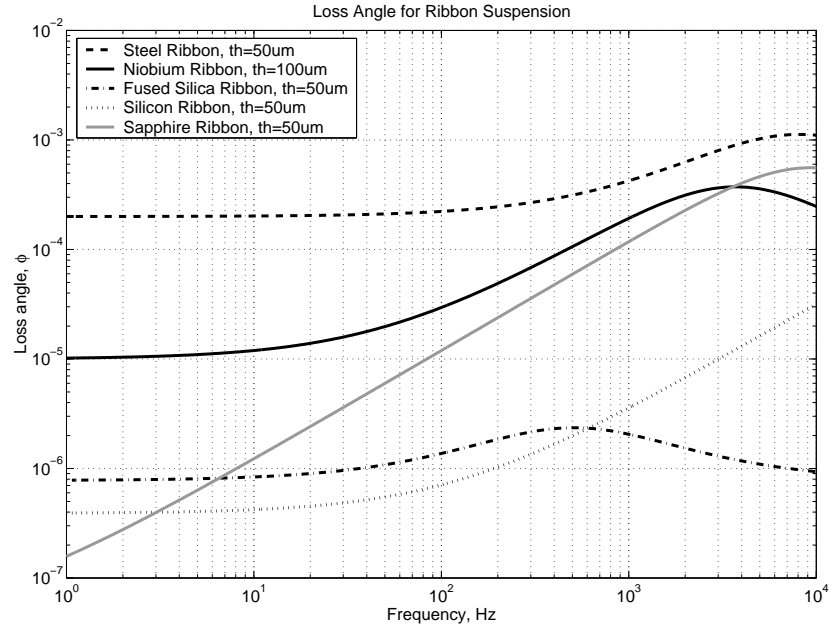


Fig. 2.2: Total loss angle as a function of frequency for various suspension materials. Ribbon suspensions loaded at 50% of breaking stress are assumed with the steel and niobium fibers, while a 25% loading is assumed for fused silica, silicon and sapphire suspensions. A 30kg test mass supported by 4 suspensions is also assumed.

The thinner dimension in the bending direction results in an increase in peak thermoelastic loss frequency for all materials. At these thicknesses, the pendulum mode loss is no longer limited by thermoelastic loss for all of the materials except sapphire, however the pendulum mode loss for sapphire is still very low. It seems that silicon and fused silica provide the best room temperature ribbon suspensions, with silicon showing slightly higher loss than fused silica at frequencies larger than 1kHz, due to the thermoelastic effect. Pulling of fused silica suspensions are still being improved [95, 59], while the pulling of monocrystalline silicon suspensions are being developed [60]. In the plots generated above, the assumption has been made that $50\mu\text{m}$ ribbons of each material can be created. Thin metallic foil of these dimensions are readily available and easy to obtain.

Another interesting comparison between the various material losses is made at cryogenic temperatures. At 20K, there are significant favourable changes in the bulk

loss angle, thermal expansion coefficient and thermal conductivity of three materials. These three materials are sapphire, silicon and niobium, and the changes in these values are summarised in Table 2.3.

Material (20K)	Loss Angle ϕ	Th. Expansion Coeff. α (K^{-1})	Th. Conductivity κ ($W/m/K$)
Sapphire	$\phi_{bulk} \simeq 2 \times 10^{-10}$ [96]	1.2×10^{-8}	15700
Silicon	$\phi_{bulk} \simeq 6 \times 10^{-10}$ [60]	3.7×10^{-9}	4940
Niobium	$\phi_{bulk} \simeq 2 \times 10^{-8}$ [97]	2.4×10^{-7}	229

Tab. 2.3: Table of suspension material loss angle, thermal expansion coefficient and thermal conductivity at 20K. The values for α and κ are obtained from [98]

Not only does a reduction in suspension temperature directly reduce the thermal noise, but a reduction in ϕ also results due to changes in some physical properties. For sapphire and silicon, the very large thermal conductivity at 20K of $\kappa = 15700W/m/K$ and $\kappa = 4940W/m/K$ pushes the thermoelastic peak to a high enough frequency that the thermoelastic loss within the detection band can be ignored. Similarly, the reduction in the thermal expansion coefficient of niobium results in a very small thermoelastic peak.

For a cryogenic suspension, the suspension elements must also supply a conduction path for heat to flow in order to keep the mirror cooled at the desired temperature, normally around 10K. Thus the suspension diameter will depend on the thermal conductivity of the material. The relationship between mirror temperature and suspension cross sectional area can be approximated by [99];

$$T_m - T_0 = \frac{P}{\kappa(T_0)\frac{A}{L} + 4\sigma T_0^3 A_{mirror}} \quad (2.11)$$

where T_m is the mirror temperature, T_0 the cryostat temperature, P the laser power absorbed by the mirror, $\kappa(T_0)$ the thermal conductivity of the suspension element at temperature T_0 , A the suspension element cross sectional area, L the suspension element length, σ the Stefan Boltzmann constant and A_{mirror} the surface area of the mirror. By reasonably assuming $T_m = 20K$, $T_0 = 4K$, $L = 0.25m$, $P \simeq 0.5W$ and a mirror radius of 0.14m and thickness 0.12m, a suspension cross sectional area for each suspension material can be assumed. For a four fiber suspension, it is found

that a radius of $120\mu\text{m}$, $220\mu\text{m}$ and 1mm is required for sapphire, silicon and niobium suspensions respectively.

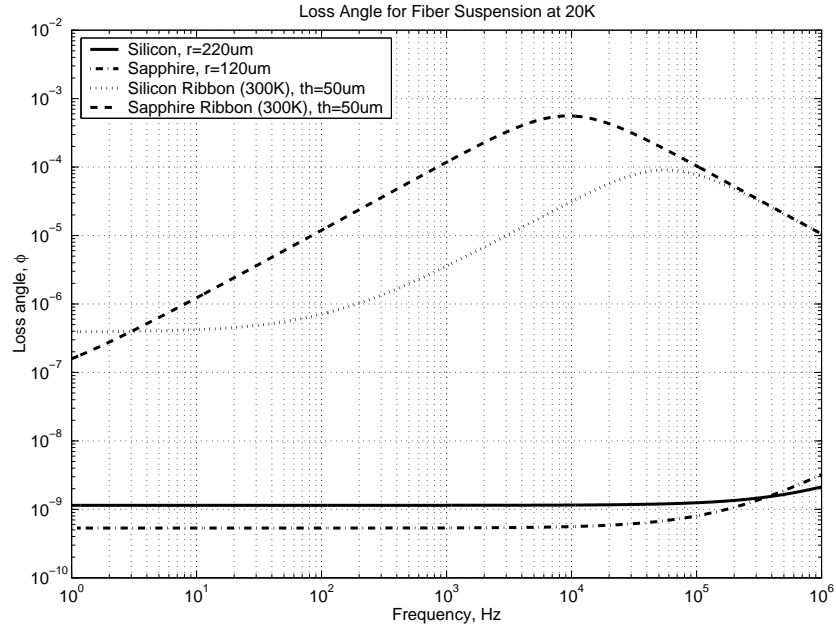


Fig. 2.3: Total loss angle versus frequency of sapphire and silicon suspension fibers at 20K compared to $50\mu\text{m}$ sapphire and silicon suspension ribbons at 300K.

The resulting loss of $120\mu\text{m}$ radius and $220\mu\text{m}$ radius sapphire and silicon fiber suspensions respectively at 20K are illustrated in Figure 2.3. They are compared to sapphire and silicon ribbon suspensions at room temperature. The large difference in loss angle between the cryogenic and room temperature suspensions are due to several factors.

Firstly, there is a reduction in bulk loss, ϕ_{bulk} for both materials. This also combines with a small reduction in surface loss due to the relatively larger fiber radius compared to the room temperature ribbon thickness of $50\mu\text{m}$. Secondly, the reduction in thermal expansion coefficient, α when at 20K reduces the peak thermoelastic loss value. Finally, a larger thermal conductivity value, κ , increases the peak thermoelastic loss frequency. The combination of the last two factors result in virtually no thermoelastic contribution to the loss within the detection band, i.e. up to 10kHz. This result demonstrates the effectiveness of cryogenic suspensions at reducing thermal noise if a sapphire or silicon suspension is chosen, and thus the reason sapphire and silicon are the leading candidates for use in cryogenic interferometric detectors. The cost of this improvement is obviously

the need to incorporate cryogenic methods to the vibration isolation system of each optic.

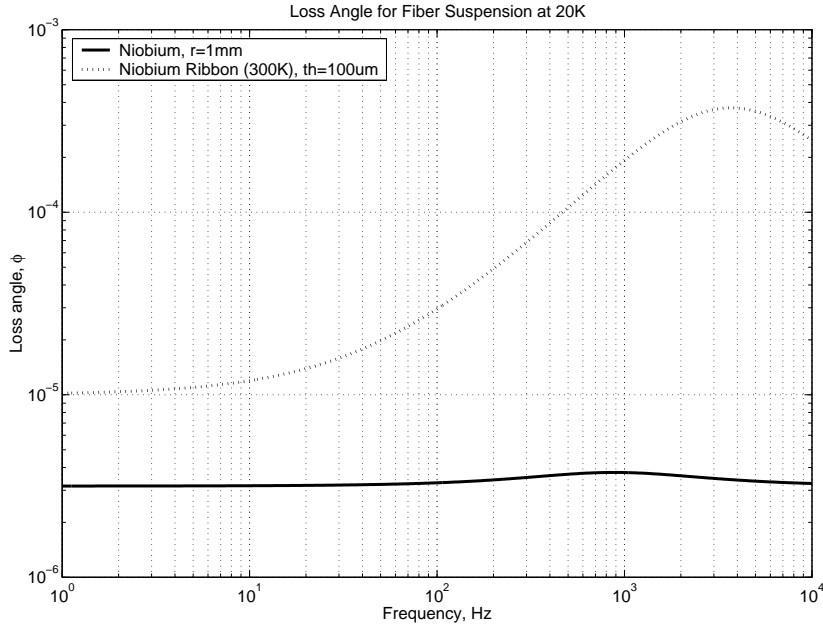


Fig. 2.4: Total loss angle versus frequency of niobium suspension fibers at 20K compared to $100\mu\text{m}$ niobium suspension ribbons at 300K.

Finally, Figure 2.4 demonstrates the improvement when using a cryogenic niobium suspension system. Using Equation 2.11 and similar values as before, the required niobium fiber radius is 1mm. Although the thermal conductivity is greater at 20K, the large fiber radius compared to the ribbon thickness of $100\mu\text{m}$ means that the thermoelastic loss peak occurs at a lower frequency. However the reduction in the coefficient of thermal expansion, α , means that the peak thermoelastic loss value is much lower in the cryogenic system. The bulk loss of niobium is also much lower at 20K, however surface loss still dominates according to $Q \simeq 10^7(V/S)^{1/2}$ [76] as discussed before. Consequently niobium suspensions will not perform as well as sapphire or silicon suspensions at 20K.

2.4 Dissipation Dilution

As discussed earlier, the use of rectangular profile suspensions that are thinner in the direction of the laser beam will result in an increase in the peak thermoelastic loss frequency. However, this is not the primary reason for the use of ribbon suspensions. It is the phenomena termed dissipation dilution and more specifically, the improved

dilution factor when using suspension ribbons that favour the rectangular profile suspension element over the more traditional fiber or wire suspension.

In a typical pendulum suspension, the restoring force is a combination of two; gravitational restoring force and the suspension element restoring force resulting from its bending elasticity. Given that other sources of mechanical losses are suppressed, then the only mechanical loss comes from the loss angle of the suspension element. Since the lossless gravitational restoring force can be made much larger than the lossy elastic restoring force, it is possible to obtain a pendulum mode Q factor much larger than $1/\phi$. The effective pendulum loss factor, ϕ_{pend} can be expressed:

$$\phi_{pend} = \phi \frac{E_{el}}{E_{grav} + E_{el}} \approx \phi \frac{E_{el}}{E_{grav}} \quad (2.12)$$

Here ϕ is the total loss angle of the suspension material and is in fact a function of frequency due to the thermoelastic effect. E_{el} is the maximum amount of stored elastic energy, while E_{grav} is the maximum amount of stored gravitational energy. The term $\frac{E_{el}}{E_{grav}}$ is the dilution factor and can be as small as 10^{-3} for thin ribbons.

Using the equality $\frac{E_{el}}{E_{grav}} = \frac{k_{el}}{k_{grav}}$, the dilution factor can be expressed in terms of physical and geometric quantities [57]:

$$\phi_{pend}(\omega) = \phi(\omega) \frac{N\sqrt{TEI}}{2mgL} \quad (2.13)$$

This results from $k_{grav} = mg/L$ and $k_{el} = n\sqrt{TEI}/2L^2$. Here N is the number of suspension elements, m the suspended mass, g the acceleration due to gravity, L the suspension length, T the tension in the suspension elements, E the Young's modulus of the suspension material and I the cross section moment of inertia of the suspension element. I can be expressed:

$$I = \begin{cases} \frac{\pi}{4}r^4 & \text{fibers} \\ \frac{1}{12}wt^3 & \text{ribbons} \end{cases} \quad (2.14)$$

Combining Equation 2.13 and Equation 2.14 for ribbon suspensions, we obtain:

$$\phi_{pend}(\omega) = \phi(\omega)n\sqrt{\frac{Ewt^3}{48mgL^2}} \quad (2.15)$$

By reducing the thickness of the ribbon, t , the dilution factor can be reduced and hence a reduction in ϕ_{pend} . The ribbon stress can be maintained by appropriately increasing w as t is reduced. This cannot be achieved with a fiber suspension since a reduction

in fiber radius r in order to improve the dilution factor will reduce the load which the suspension can support.

If $\phi(\omega)$ were independent of ribbon thickness t , then it would seem possible from Equation 2.15 that an arbitrarily low $\phi_{pend}(\omega)$ could be obtained so long as a very thin and wide ribbon could be used. In reality however, the existence of surface loss (discussed earlier) results in $\phi(\omega)$ increasing with reducing t . This implies the possibility of an optimum ribbon thickness between the competing factors of increased surface loss and increased dissipation dilution. In the following, we study this scenario for fused silica, silicon, sapphire and niobium ribbons. A similar study for fused silica ribbons has been conducted by Gretarsson et. al. [80].

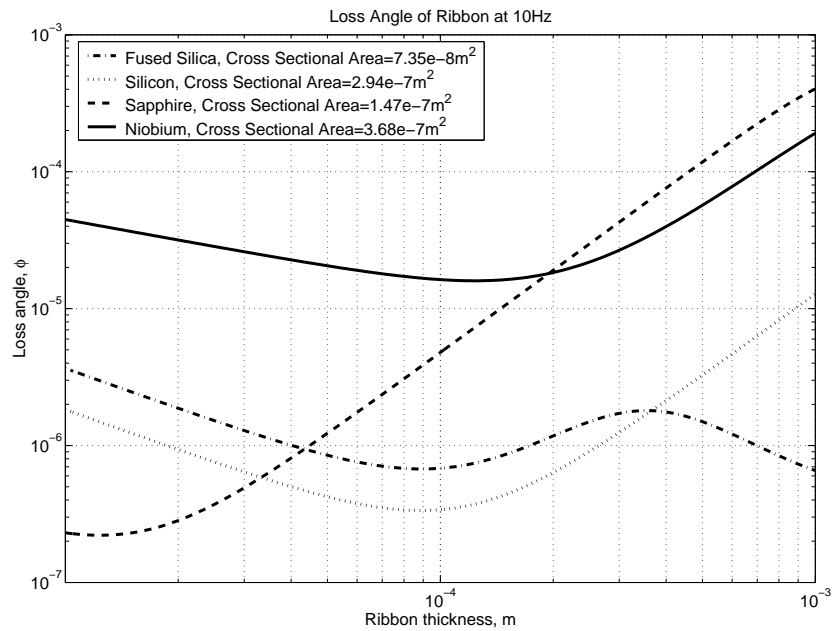
Combining the effects of surface loss and thermoelastic loss using Equations 2.7, 2.8, 2.9 and 2.10, $\phi(\omega)$ can be expressed in terms of ribbon thickness t by:

$$\phi(\omega) = \phi_{bulk} \left(1 + \left(\frac{3Nw + t}{Nw + t} \right) \left(\frac{2d_s(w + t)}{wt} \right) \right) + \left(\frac{E\alpha^2 T}{\rho_v C_v} \right) \left(\frac{\omega \frac{\rho_v C_v t^2}{\pi^2 \kappa}}{1 + \left(\omega \frac{\rho_v C_v t^2}{\pi^2 \kappa} \right)^2} \right) \quad (2.16)$$

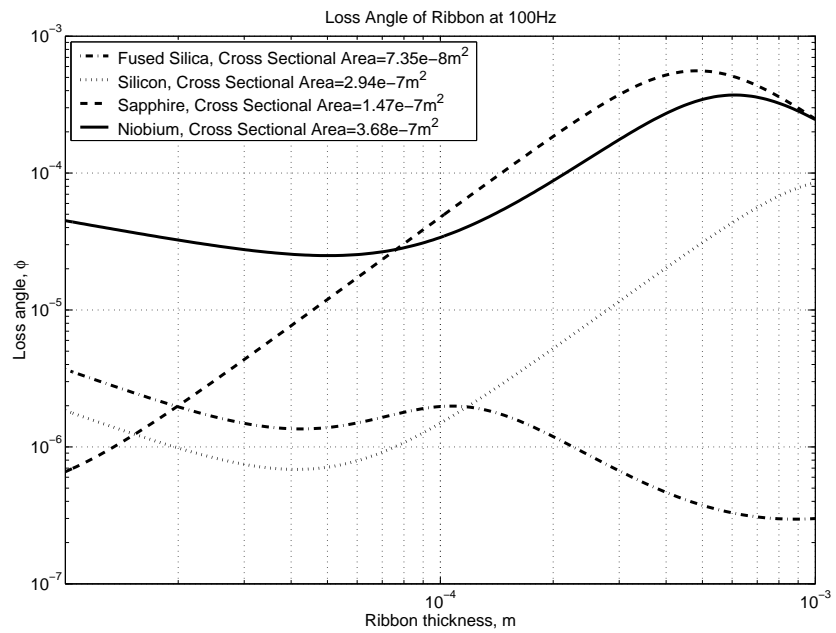
The resulting ribbon loss as a function of ribbon thickness for fused silica, silicon, sapphire and niobium ribbon suspensions are illustrated in Figure 2.5. It is assumed that a four ribbon suspension system is used to support a 30kg test mass. The cross sectional area of the ribbons remains constant with the fused silica, silicon and sapphire ribbons loaded at 25% of their breaking stress (Table 2.1), while the niobium ribbons are loaded at 50%. An increasing loss is noticed at low ribbon thicknesses for fused silica, silicon and niobium ribbons, due to the increased surface loss. The peak losses at higher thicknesses are due to the thermoelastic loss peak. For the sapphire ribbon, thermoelastic loss is seen to dominate for all ribbon thicknesses from $10\mu\text{m}$ to 1mm .

At 10Hz, a minimum loss angle occurs at approximately $100\mu\text{m}$ for fused silica, silicon and niobium ribbons. At 100Hz, the minimum loss shifts to ribbon thicknesses around 40 to $50\mu\text{m}$. This minimum is due to the thermoelastic peak appearing for thicknesses greater than $100\mu\text{m}$. For the sapphire ribbon however, achieving the minimum loss angle would require an unrealistic ribbon thickness of close to $10\mu\text{m}$, due to the dominance of thermoelastic loss for all ribbon thicknesses plotted.

Combining the effects of dissipation dilution, surface loss and thermoelastic effect using Equations 2.15 and 2.16, an approximated expression for suspension thermal



(a)



(b)

Fig. 2.5: Ribbon suspension loss as a function of ribbon thickness. A four ribbon suspension supporting a 30kg mass is assumed. Suspension element cross sectional area remains constant with 25% loading for all materials except niobium, which is loaded at 50% of breaking stress.
 a) Loss at 10Hz b) Loss at 100Hz

noise power $x^2(\omega)$ can be expressed in terms of ribbon thickness t by:

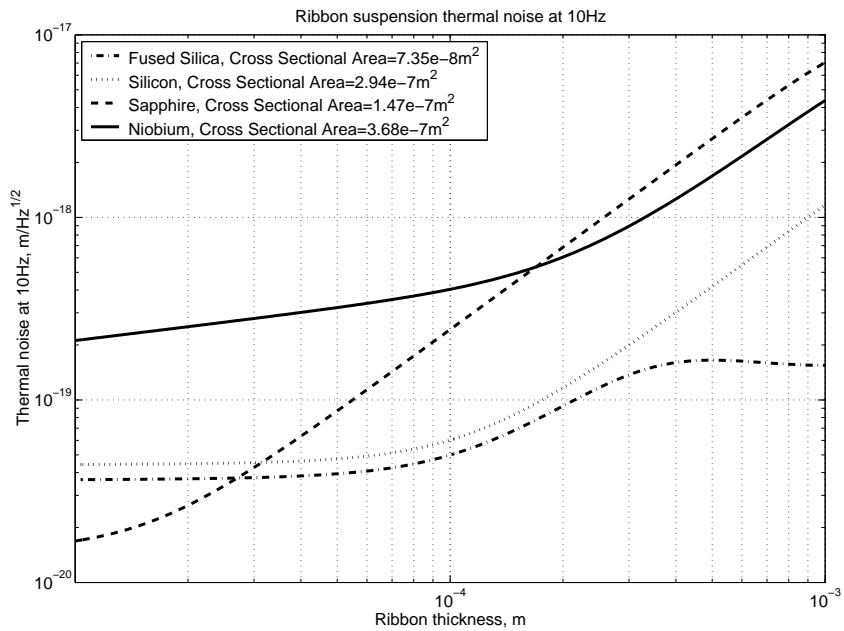
$$x^2(\omega) = \frac{4k_B T g}{m L \omega^5} N \sqrt{\frac{E w t^3}{48 m g L^2}} \left(\phi_{bulk} \left(1 + \left(\frac{3 N w + t}{N w + t} \right) \left(\frac{2 d_s (w + t)}{w t} \right) \right) + \left(\frac{E \alpha^2 T}{\rho_v C_v} \right) \left(\frac{\omega \frac{\rho_v C_v t^2}{\pi^2 \kappa}}{1 + \left(\omega \frac{\rho_v C_v t^2}{\pi^2 \kappa} \right)^2} \right) \right) \quad (2.17)$$

This is only valid for pendulum mode thermal noise at frequencies higher than the pendulum mode frequency of approximately 1Hz, i.e. $> 10\text{Hz}$.

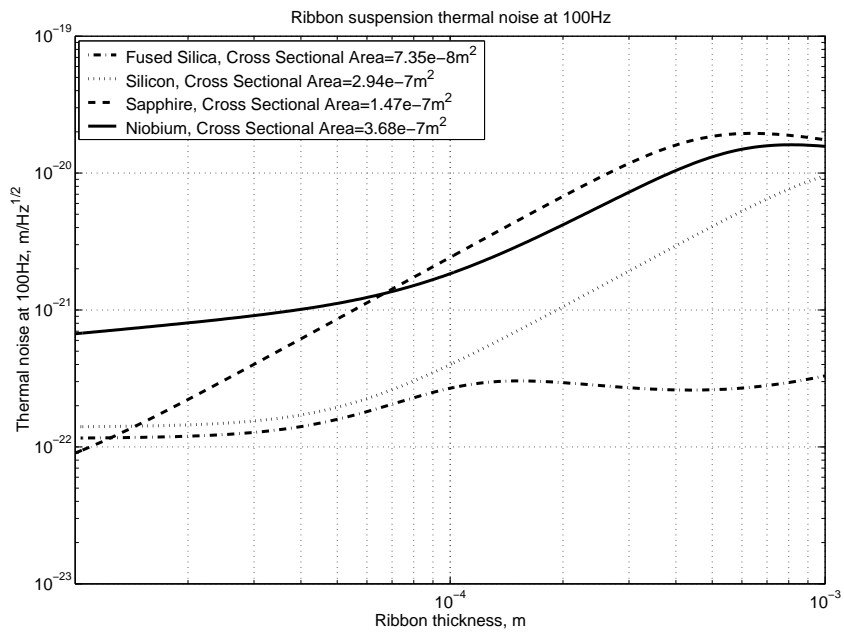
A plot of the expected pendulum mode thermal noise amplitude at 10Hz and 100Hz is shown in Figure 2.6. Again, a four ribbon, 30kg suspension is assumed with 25% loading for all materials except niobium, which is loaded at 50% of breaking stress. The inclusion of surface loss results in a flattening of the thermal noise amplitude curve at low thicknesses for fused silica, silicon and sapphire. The flattening results from the cancellation between improved dilution factor and increased surface loss at low thickness. The key result is that for fused silica and silicon ribbons, a thickness less than $50\mu\text{m}$ results in almost no improvement in pendulum mode thermal noise, and thus a ribbon thickness of approximately $50\mu\text{m}$ is suitable. For niobium ribbons, a reduction in pendulum mode thermal noise at both 10Hz and 100Hz can still be achieved by using a thinner ribbon, however the improvement is not as great beyond about $100\mu\text{m}$. The limitation in this case is likely to involve the practicality of obtaining and using niobium ribbons less than $50\mu\text{m}$ thick. For the sapphire ribbons, the flattening of the curve occurs at thicknesses less than $10\mu\text{m}$ since surface loss only begins to dominate at these thicknesses due to the large amount of thermoelastic loss. Thus for sapphire ribbons, the practical limitation of producing very thin ribbons will be reached before the minimum level of pendulum mode thermal noise can be achieved.

2.5 Coupled Suspension Thermal Noise

Another interesting comparison to be made is the level of thermal noise in the two other perpendicular directions. Here, we will define the direction of the laser as the x-direction, the y-direction being the direction perpendicular to the laser but in the plane of the interferometer, and the z-direction being the vertical direction. Ideally there will be no coupling of thermal noise from either the y or z directions, but in reality a small amount of coupling will exist. The amount of coupling in advanced



(a)



(b)

Fig. 2.6: Ribbon suspension thermal noise as a function of ribbon thickness. A four ribbon suspension supporting a 30kg mass is assumed. Suspension element cross sectional area remains constant with 25% loading for all materials except niobium, which is loaded at 50% of breaking stress. a) Thermal noise at 10Hz b) Thermal Noise at 100Hz

detectors is expected to be approximately 0.1%, obtained from the expected coupling in the Advanced LIGO suspensions [100]. This minimum amount of coupling arises from expected machining tolerances and the effect of the curvature of the earth. With interferometer arm lengths of approximately 4km and an earth radius approximately 6000km, the mirror faces will have to be tilted up to 1mrad from vertical in order for the 4km arm cavities to correctly align. As a result, vertical motion to horizontal motion coupling of at least 1 in 1000 will be observed.

The use of ribbons allows the reduction of pendulum mode thermal noise in the x-direction, however an improvement in the dilution factor for the x-direction will result simultaneously in a worsening of the dilution factor in the y-direction. This occurs due to the need to increase the ribbon width, w , in order to maintain the suspension strength. Similarly, a worsening of the z-direction thermal noise will result due to an increase in surface loss. There is no dilution factor nor thermoelastic effect for the vertical stretch mode oscillation of the suspension, however there is a dependence on the material loss angle, and hence the V/S ratio. The purpose of this study is to investigate whether a particular ribbon thickness will result in coupled y-direction or z-direction thermal noise becoming dominant. Obviously, there is no point using thinner ribbons to reduce the x-direction thermal noise to a level lower than the contributions from either the y-direction or z-direction.

The contributions to thermal noise from the x, y and z-directions are expressed in Equations 2.18-2.21. Here, the values c_{yx} and c_{zx} represent the coupling factor from the y-direction to the x-direction, and the z-direction to the x-direction respectively. The z-direction thermal noise for niobium shown in Figure 2.21 is included as a separate equation since the surface loss is characterised differently as discussed previously. The material loss angle, $\phi(\omega)$ is given in Equation 2.16. The resulting thermal noise for each of the suspension materials is plotted in Figure 2.7. We have assumed 0.1% coupling and a typical four ribbon suspension supporting a 30kg test mass. The fused silica, silicon and sapphire ribbons are loaded at 25% of breaking stress (Table 2.1), while the niobium ribbons are loaded at 50%.

$$x_x^2(\omega) = \frac{4k_B T g}{mL\omega^5} N \sqrt{\frac{Ewt^3}{48mgL^2}} \phi(\omega) \quad (2.18)$$

$$x_y^2(\omega) = c_{yx} \frac{4k_B T g}{mL\omega^5} N \sqrt{\frac{Ew^3t}{48mgL^2}} \phi(\omega) \quad (2.19)$$

$$x_z^2(\omega) = c_{zx} \frac{4k_B T}{m\omega^5} \frac{NEwt}{ML} \phi_{bulk} \left(1 + \left(\frac{3Nw+t}{Nw+t} \right) \left(\frac{2d_s(w+t)}{wt} \right) \right) \quad (2.20)$$

$$x_{z,Nb}^2(\omega) = c_{zx} \frac{4k_B T}{m\omega^5} \frac{NEwt}{ML} 10^{-7} \left(\frac{2d_s(w+t)}{wt} \right)^{-1/2} \quad (2.21)$$

In general, the observed trends are as expected. For decreasing ribbon thicknesses, the x-direction thermal noise also decreases due to the improving dilution factor, while the y and z-direction thermal noise increases due to the worsening dilution factor and increase in surface loss respectively. The decreasing y-direction thermal noise observed with the sapphire ribbon results from the large thermoelastic loss dominating at 100Hz, where a reduction in thickness reduces the thermoelastic loss. In all cases, it is observed that the z-direction thermal noise is more dominant than the y-direction thermal noise and thus is more likely to become the dominant source of thermal noise given thin enough ribbons.

For the 0.1% coupling assumed in this study, we find that the suspension thermal noise for the silicon and niobium suspension will be made worse if the ribbon thickness is reduced beyond $40\mu\text{m}$, whereas for fused silica and sapphire, a reduction in thickness to less than $25\mu\text{m}$ and $10\mu\text{m}$ respectively would be required before the z-direction thermal noise dominates. For the fused silica and sapphire ribbons, these limiting thicknesses are low enough that it can be safely assumed that these points will not be reached, given, of course, that a coupling level of at least 0.1% is obtained. This result also suggests that a limitation on the thickness of fused silica or sapphire ribbons at $50\mu\text{m}$ will ensure that there is minimal contribution to x-direction thermal noise from either the y or z-directions. For the niobium and silicon ribbons, $50\mu\text{m}$ thick ribbons could still be used, however thicker ribbons closer to $100\mu\text{m}$ thick would provide a better safety margin for the coupling factor requirements. These values of 0.1% coupling and $50\mu\text{m}$ thick ribbons are already right at the practical limits for current suspension fabrication technologies.

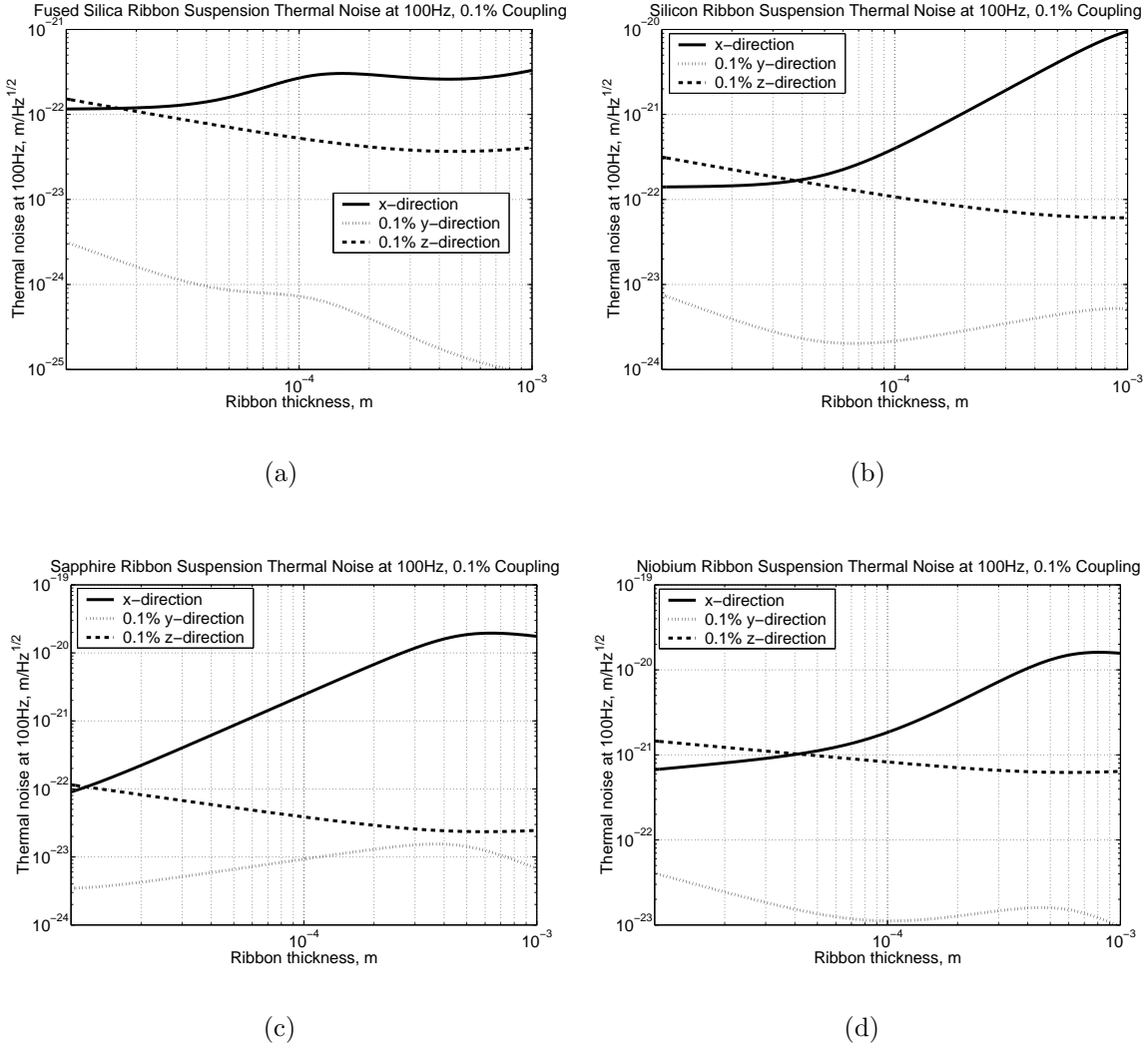


Fig. 2.7: x-direction thermal noise, 0.1% of y-direction thermal noise and 0.1% of z-direction thermal noise for fused silica, silicon, sapphire and niobium ribbons. A four ribbon suspension of a 30kg test mass is assumed. The ribbon cross sectional area is kept constant with the fused silica, silicon and sapphire ribbons loaded at 25% of breaking stress and the niobium ribbon loaded at 50%.

2.6 Suspensions for AIGO

The results given above clearly show that the best materials for a room temperature suspension is the use of fused silica or silicon ribbons. For the high power test facility at AIGO however, our initial suspensions will be constructed from thin niobium ribbons, with plans to upgrade to better performing materials when improved sensitivity is required. The reason for choosing niobium can be outlined as follows.

Niobium foil suitable for use as suspension ribbons is easily obtainable. Our research group and technician staff have experience working with niobium and the ability to machine and bond niobium parts to form intricate suspension elements. In the following chapter, we discuss the concept of removable modular suspensions and present some modelling results of suspensions with a nonhomogeneous cross section profile along its length. Although these ideas can be applied to lower loss materials, the concepts need thorough testing and experimental verification of simulation results before they can be considered useful for advanced interferometric detectors. The use of niobium provides a relatively cheap and convenient way to perform these tests.

CHAPTER 3

MIRROR SUSPENSION MODELLING

3.1 Introduction

Applications capable of accurately modelling test mass suspensions for use in interferometric gravitational wave detectors are an important tool as researchers aim to optimise every aspect of the detector. The result of the simulation program should therefore give an indication of the performance of the system with respect to vibration isolation and suspension thermal noise. Simulation of feedback control loops would also be useful in designing local control systems required by most multistage suspensions.

Currently, the AIGO vibration isolation system and final stage suspension is modelled by two programs. In order to investigate the isolation performance of the system, a transfer matrix approach developed by Winterflood [101] was used. This method is analogous to the study of electrical systems through the use of two port networks. The power of this approach is the large reduction in computation time when used to analyse multi stage mechanical systems, such as the five stage vibration isolation system to be used at AIGO. Calculations involve the multiplication of 2×2 or 4×4 matrices rather than the inversion of a large matrix of size in the order of the number of stages multiplied by the degrees of freedom. The disadvantage however is the limitation of the analysis. Firstly, only one degree of freedom (translation) or two degrees of freedom (translation and tilt) can be efficiently modelled. Secondly, a relationship can only be generated between a single input and a single output and finally, the need for a transfer matrix for every mechanical element of the system means that only standard items (e.g. masses, springs, dashpots, e.t.c) can be modelled. The transfer matrix technique is sufficient to obtain theoretical transfer functions to indicate levels of vibration iso-

lation, however for the final stage suspension, a more elaborate modelling program is required.

The reason for the requirement of a better model for the final suspension stage is the need to accurately predict the level of suspension thermal noise that will drive the test mass. As such, all six degrees of freedom of the suspended mass need to be considered such that the thermal noise that is coupled from all modes can be included. Ideally, suspension thermal noise from the entire suspension chain should be considered. However, for frequencies higher than the final stage pendulum mode ($>5\text{Hz}$) the thermal noise is generally dominated by that of the final stage suspension. This is of course due to the increasing mechanical isolation of the thermal noise for suspension stages located further up the isolation chain. As such, a reasonable estimation of the suspension thermal noise level can be generated by modelling only the final suspension stage. This is illustrated in Figure 3.2, where the thermal noise plots for both a multistage chain and just the final suspension stage are compared. The larger level

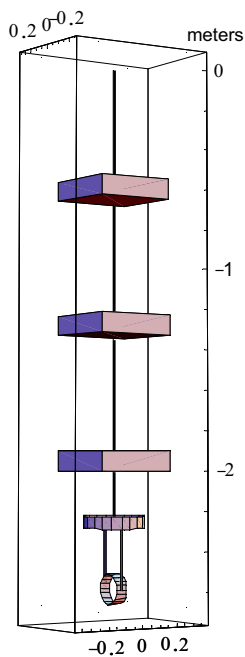


Fig. 3.1: AIGO suspension chain model.

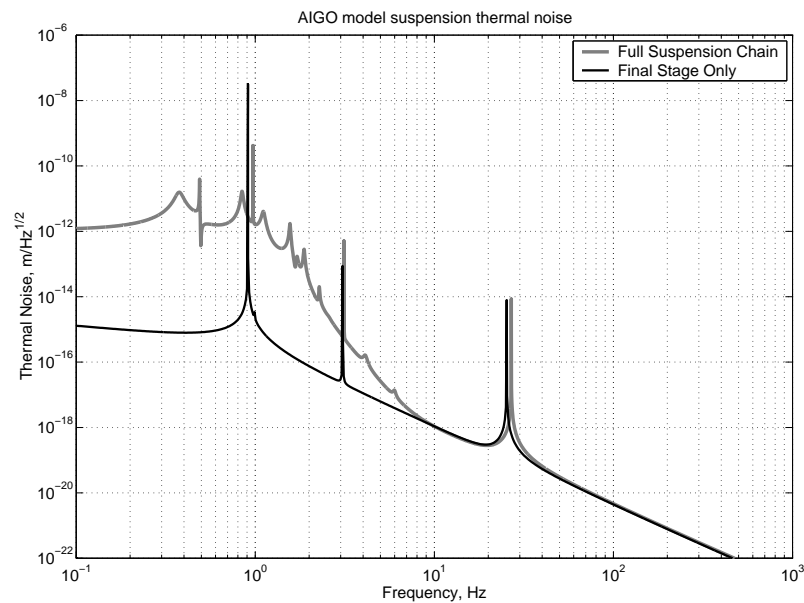


Fig. 3.2: A Comparison of the thermal noise due to the entire AIGO suspension chain compared to the thermal noise due to only the final suspension stage. 0.1% coupling has been assumed.

of suspension thermal noise at lower frequencies is not an issue since seismic noise is expected to dominate at these frequencies.

The final AIGO stage and advanced suspension geometries to be tested at the AIGO facility have been modelled based on a Mathematica toolkit, written by Mark

Barton for modelling of Advanced LIGO suspensions [102]. The program essentially constructs a potential energy matrix (or stiffness matrix) and a kinetic energy matrix (or mass matrix) from a set of user defined inputs which define the specific model and model case to be solved. The set of eigenvalues and eigenvectors that are obtained from the matrices give the internal modes and mode frequencies of the system. User defined damping functions also allow transfer function and thermal noise calculations. Similarly, Matlab and Maple were used to investigate the suspensions for GEO600 [103, 104].

The Mathematica toolkit allows the following physical objects to be modelled:

1. Rigid masses with up to six degrees of freedom.
2. Massless wires with wire bending and longitudinal elasticity and associated frequency dependant loss.
3. Six degree of freedom springs with specified pre-loaded forces and frequency dependant damping.

Thus the program is extremely useful for modelling the low frequency modes of the suspensions and can give a good indication of the level of pendulum mode thermal noise that can be expected. Currently however, there is little allowance for the calculation of higher order violin modes of the suspension wires and their resultant contribution to the suspension thermal noise. The high Q nature of violin modes in low loss suspensions mean that large amplitude oscillations at the violin mode frequencies may exist, resulting in interferometer saturation, non-linearity in output signals and other dynamic range problems. Also, the violin mode thermal noise spikes will pierce the shot noise limit at high frequencies. Therefore there is considerable motivation to characterise and thus optimise the suspension method with respect to the higher order violin modes. Some research towards violin mode damping in order to address some of these problems has been conducted [105].

To model the first three violin modes of a suspension system using the current Mathematica toolkit, a set of beads that are restricted to move in the xy plane (the plane perpendicular to the suspension direction) are defined. These beads approximate the mass distribution of the suspension wire allowing an approximation of higher order modes. However, it is found that a large number of beads is required before a reasonable

calculation of the first three violin mode frequencies is achieved. For a typical four wire suspension of a test mass, the model rapidly becomes complicated. Calculation time also increases due to the large number of degrees of freedom to solve, despite the fact that each bead is restricted to two degrees of freedom each.

We have written a Mathematica package that will solve the x and y direction violin mode frequencies for a given suspension wire or ribbon, and calculate the contribution from each violin mode to the thermal noise. Although it is an entirely different manner of mode calculation, the package is designed to be used in conjunction with the toolkit written by Mark Barton. Extensions of the program to include non-homogenous suspension elements have also been investigated. The purpose of this tool is to model the suspensions proposed for AIGO, as well as investigate some ideas of different suspension element geometries and their implications on violin mode frequencies, Q-factors and suspension thermal noise.

In this chapter, the procedure used for modelling violin modes is discussed, and a comparison of results modelled using FEM techniques is given. We also present some model comparisons for a more elaborate triple section suspension element. It should be mentioned that in the following sections, the word ‘wire’ has been used to represent a general suspension element of any material with circular or rectangular profile, and as such is not restricted to just thin circular metallic wires.

3.2 Violin Mode Modelling Procedure

The violin mode modelling procedure considers just one suspension wire under conditions defined by the overall suspension model. In the general case of multi wire suspensions of a test mass, a symmetrical distribution of the wires will result in groups of violin modes with the same frequency. In most cases, it is a symmetrical system being modelled and hence the results of the single wire analysis will be sufficient to approximate the violin mode dynamics of the entire test mass suspension stage. In the case that a non-symmetric system is to be analysed, for example when investigating the effect of machining imperfections, each wire has to be modelled separately according to its individual condition. The advantage of this manner of modelling is the increased computation speed and the ability to efficiently analyse all violin modes within the detection band. The disadvantage is that a transfer function of the suspension that

includes the violin modes will not be constructed, which could be useful for testing the stability of certain control loops. In most cases however, it is only for thermal noise where the consideration of violin modes is important. Just the knowledge of the likely frequencies and Q-factors is often enough to design control systems in the presence of these violin modes.

The modelling procedure is based on five steps outlined in the flow diagram illustrated in Figure 3.3. Firstly, the model parameters are obtained. The violin mode

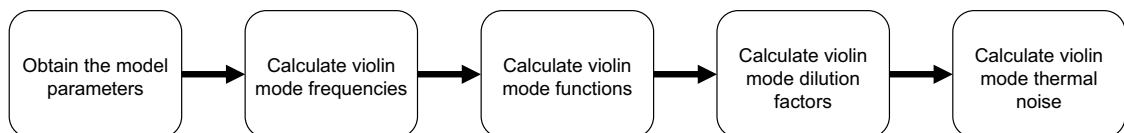


Fig. 3.3: Flow diagram of violin mode modelling procedure.

modelling procedure is designed to run after the suspension has been modelled by the Mark Barton Mathematica toolkit (MB toolkit). Therefore most of the required list of model parameters would already have been defined. However the violin mode modelling procedure can also be called for a stand alone analysis, in which case the parameters have to be calculated by the user. Secondly, the most time consuming part of calculating the violin mode frequencies occurs. The final parts involve calculating violin mode functions, violin mode dilution factors and violin mode thermal noise.

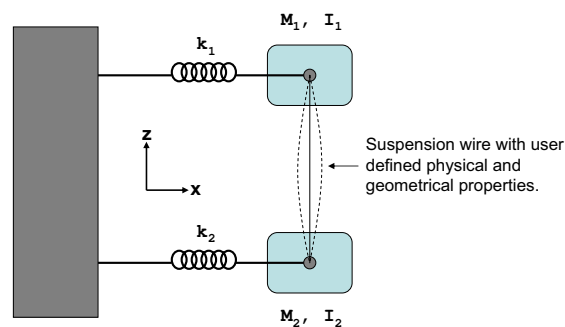


Fig. 3.4: The mechanical model being analysed by the violin mode modelling procedure. All motion is restricted to the x direction, while rotation of the masses in the xz plane can occur.

The wire being analysed has been made general, to allow for as many suspension situations as possible. The wire itself is connected at each end to masses with mass M_1 and M_2 and rotational moment of inertia I_1 and I_2 . These masses are connected to a mechanical ground through springs with spring constant k_1 and k_2 . This is illustrated in Figure 3.4. All motion is restricted to the x direction as indicated in the diagram,

while rotation of the masses within the xz plane can occur. Often the spring stiffnesses to be modelled are negligible compared to the acceleration of the end masses at typical violin mode frequencies.

The 15 parameters required by the procedure are listed in Table 3.1. Although the analysis is essentially only a calculation of the violin modes in a single direction, calculations for the orthogonal direction are done by simply repeating the procedure with the appropriate parameter values. For circular wires, there are usually only minor differences in the end constraints, and hence the x and y direction violin modes are very similar. For ribbon suspensions however, the x and y direction violin modes can be vastly different.

Item	Parameter	Description	Item	Parameter	Description
1.	F_T (N)	Tension	9.	M_1 (kg)	Mass at end 1
2.	ρ_L (kg/m)	Linear mass density	10.	I_1 (kgm ²)	Rotational inertia at end 1
3.	L (m)	Length	11.	k_1 (N/m)	Spring constant at end 1
4.	E (Pa)	Young modulus	12.	T (K)	Temperature of suspension
5.	I_x (m ⁴)	Area moment of inertia in the bending direction	13.	N	Number of suspension elements
6.	M_2 (kg)	Mass at end 2	14.	$\phi(\omega)$	Material Loss
7.	I_2 (kgm ²)	Rotational inertia at end 2	15.	f_{max} (Hz)	Maximum frequency of interest
8.	k_2 (N/m)	Spring constant at end 2			

Tab. 3.1: Model parameters for the violin mode modelling procedure.

3.2.1 Solving for Frequency and Mode Function

For any set of parameters as described above, violin mode frequencies and wavefunctions are determined based on the solution to the dynamic beam equation [106]:

$$F_T \frac{\partial^2 X(z, t)}{\partial z^2} - EI_x \frac{\partial^4 X(z, t)}{\partial z^4} = \rho_L \frac{\partial^2 X(z, t)}{\partial t^2} \quad (3.1)$$

A general solution to this equation consists of sine, cosine, hyperbolic sine and hyperbolic cosine functions as shown below;

$$X_{gen}(z) = A \cos(k_t z) + B \sin(k_t z) + C \cosh(k_e z) + D \sinh(k_e z) \quad (3.2)$$

where;

$$k_t = \sqrt{\frac{-F_T}{2EI_x} + \frac{\sqrt{16\pi^2 f^2 EI \rho_L + F_T^2}}{2EI_x}} \quad (3.3)$$

$$k_e = \sqrt{\frac{F_T}{2EI_x} + \frac{\sqrt{16\pi^2 f^2 EI \rho_L + F_T^2}}{2EI_x}} \quad (3.4)$$

and f is frequency while A , B , C and D are constants. Here we have assumed a sinusoidal function, such that $X_{gen}(z, t) = X_{gen}(z) \sin(\omega t)$. Therefore the goal is to determine $X(z)$ by solving for A , B , C and D for a particular set of parameters and all values of f such that $X(z, t)$ satisfies the beam equation (Equation 3.1).

The usual method to solve for f is to use three boundary condition equations to eliminate three constants, and then the fourth boundary condition equation to solve for f , which is independent of the last constant. The boundary conditions are based on conservation of force and torque and restrictions on displacement and angular displacement at the endpoints of the wire. Since each end is connected to a mass that is free to move and rotate, there are no restrictions on linear or angular displacements. Therefore the four boundary condition equations come from conservation of force and torque at each end. Summing the forces to zero at each end gives;

$$\begin{aligned} EI_x X_{gen}'''(-L/2) + F_T X_{gen}'(-L/2) - M_1(-\omega^2) X_{gen}(-L/2) - k_1 X_{gen}(-L/2) &= 0 \\ -EI_x X_{gen}'''(L/2) + F_T X_{gen}'(L/2) - M_1(-\omega^2) X_{gen}(L/2) - k_1 X_{gen}(L/2) &= 0 \end{aligned}$$

while a summation of the moments at each end requires:

$$\begin{aligned} -EI_x X_{gen}''(-L/2) + I_1(-\omega^2) X_{gen}'(-L/2) &= 0 \\ EI_x X_{gen}''(L/2) + I_1(-\omega^2) X_{gen}'(L/2) &= 0 \end{aligned}$$

The last constant can then be solved by normalising the mode shapes, $X(z)$, to mass, where:

$$\int_{-L/2}^{L/2} \rho_L X_{gen}^2(z) dz + M_2 X_{gen}^2(-L/2) + M_1 X_{gen}^2(L/2) = 1 \quad (3.5)$$

Since we have left the model as general as possible, no simplifications have been made. Therefore the function of f to be used to solve for the violin mode frequencies is very complicated and contains many parameters, making it impractical to solve analytically. Although a completely analytical solution for f that requires only the substitution of parameter values would be elegant, ultimately, the requirement for a

numerical solution has lead to a slightly different method of violin mode calculation. Several methods have been studied, with the following being the most time efficient.

A function is defined that takes as its input a list of numerical parameters and a frequency f . The output of the function is the sum of forces on the wire at end 1. This is achieved by setting one of the four constants (the normalising constant) of the general solution X_{gen} to 1. Requirements on the sum of moments at each end and the sum of forces at end 2 along with the input frequency f are used to solve for the three unknown constants. By substituting in the numerical parameters, the problem becomes a numerical third order simultaneous equation that can easily be solved efficiently. The resultant values are then used to output the sum of forces at end 1. This is summarised in Figure 3.5.

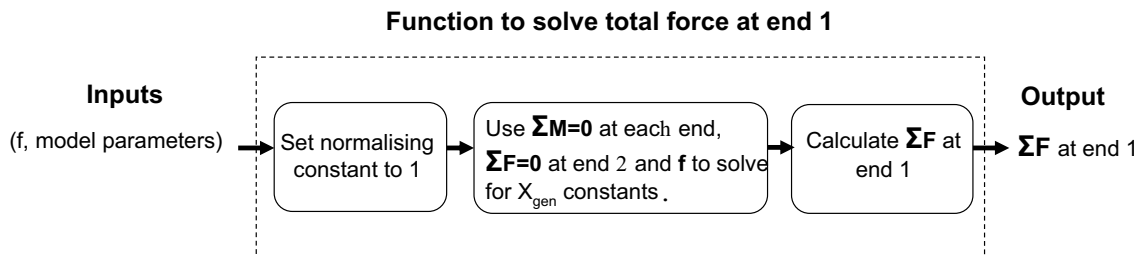


Fig. 3.5: A function to calculate the sum of forces at end 1.

The problem then becomes an issue of finding the roots of the function described above (i.e. the value of f for which the sum of forces at end 1 is zero and hence obeys the fourth boundary condition). This is efficiently achieved with a recursive scanning function that searches broadly over the frequency range of interest at first, whilst zooming in on small frequency ranges that may contain a root. Roots and hence violin mode frequencies are found to at least 5 significant figures. Once a list of violin mode frequencies are obtained, the mode function, $X(z)$, for each frequency is determined by solving numerically for the four constants of $X_{gen}(z)$ using three boundary conditions and the normalising condition described in Equation 3.5. The output is a list of violin mode frequencies, and a list of violin mode amplitude functions, $X(z)$, where z ranges from $-L/2$ to $L/2$.

3.2.2 Violin Mode Dilution Factor

The dilution factor in violin modes result from similar circumstances as those for the pendulum mode. Tension (resulting from the gravitational force applied to the supported mass) and wire elasticity both contribute to restoring force, whilst only the wire bending elasticity contributes significantly to loss. Therefore the violin mode dilution factor is given by:

$$\frac{E_{el}}{E_{tens} + E_{el}} \quad (3.6)$$

Here, E_{el} is the stored elastic energy in the bent wire, while E_{tens} is the stored potential energy resulting from tension. The potential energy due to tension is given by;

$$E_{tens} = \frac{1}{2} \int_{-L/2}^{L/2} T(X'(z))^2 dz \quad (3.7)$$

while the energy due to wire bending elasticity is;

$$E_{el} = \frac{1}{2} \int_{-L/2}^{L/2} EI_x(X''(z))^2 dz \quad (3.8)$$

where again T is the tension in the wire, L the wire length, E the Young's modulus of the wire material and I_x the area moment of inertia of the wire in the bending direction.

Thus given that $X(z)$ and all other required variables are known, the dilution factor for each violin modeshape is simply calculated as shown in Equations 3.6-3.8.

3.2.3 Violin Mode Thermal Noise

The violin mode thermal noise power can be calculated from the dissipation dilution theorem. Thus the total thermal noise power at end 1 of the wire (the optic) is calculated by summing the thermal noise from all violin modes. This is given by Equation 3.9 [57].

$$x_{viol}^2(\omega) = 4k_B T \sum_{n=1}^{\infty} \frac{\psi_n^2(-L/2) \phi_n(\omega) \omega_n^2}{\omega((\omega_n^2 - \omega^2)^2 + \phi_n^2(\omega) \omega_n^4)} \quad (3.9)$$

Here, $\psi_n(-L/2)$ is the wave function of the n th violin mode at position $-L/2$, ω_n the n th violin mode frequency in rad/s and $\phi_n(\omega)$ the effective frequency dependant loss function for the n th mode. The effective loss function also includes the appropriate dilution factor.

The result is a single function of frequency that gives the thermal noise power contributed from the violin modes. This can be combined with existing expressions to approximate the total thermal noise power of the suspension.

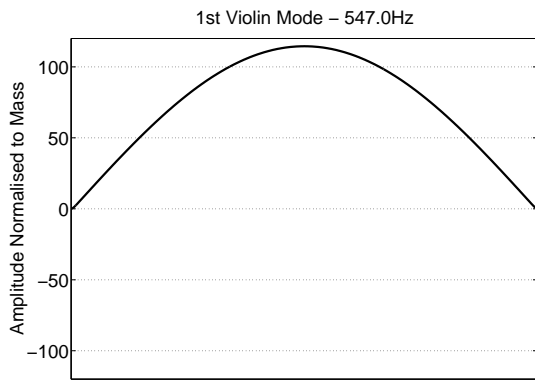
3.3 Model Comparison

A comparison between the violin mode modelling procedure and an ANSYS finite element model has been conducted. The model in question consists of a 40cm long fused silica fiber with a radius of $236\mu\text{m}$ supporting a 7.4kg cylindrical mass. The ANSYS model consists of 523900 SOLID185 3D elements. All violin modes up to 5kHz were modelled.

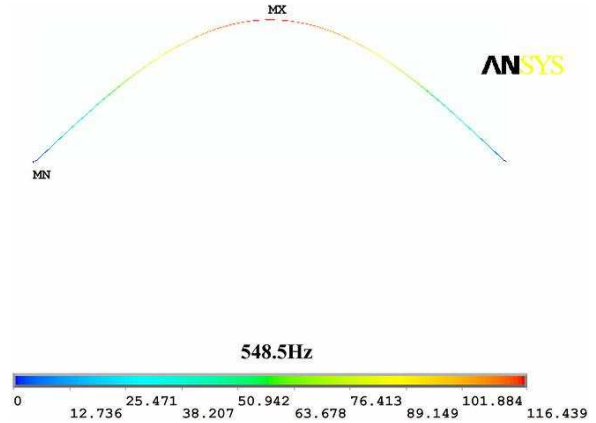
Mode No.	Violin Mode Freq. (Hz)		Difference (%)
	VM Model	ANSYS	
1	547.0	548.5	0.27
2	1094.3	1097.2	0.26
3	1642.0	1646.5	0.27
4	2190.2	2196.6	0.29
5	2739.4	2748.1	0.32
6	3289.5	3300.8	0.34
7	3840.9	3855.1	0.37
8	4393.7	4411.4	0.40
9	4948.2	4969.9	0.44

Tab. 3.2: Comparison of a fused silica fiber violin mode frequencies modelled using two methods. The first method involves the violin mode modelling procedure written in Mathematica as described above, the second makes use of FEM methods using ANSYS.

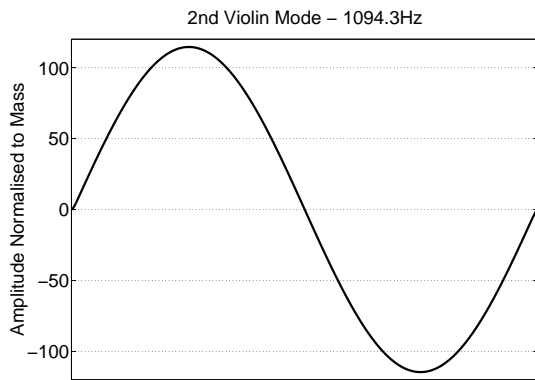
The resulting violin modes of the two models are tabulated in Table 3.3. A percentage difference for each of the modes between the two models is also given, where in all cases the violin mode frequencies agree to better than 0.5%. It was found necessary to approximate the effect of Poisson's ratio in the Mathematica model to achieve this agreement. This was done by accounting for the slight changes in fiber radius and density when placed under load. The change in fiber length is already accounted for, where the specified 0.4m length is the stretched fiber length. A comparison of the violin



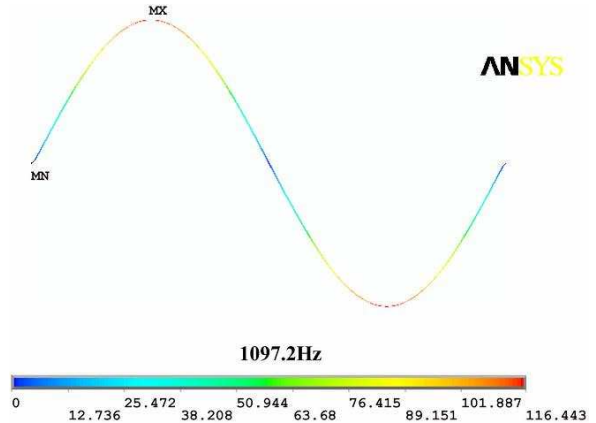
(a)



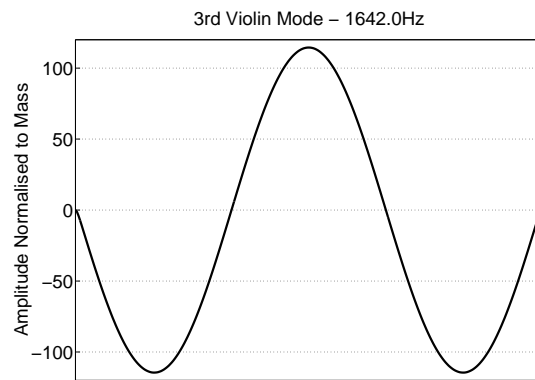
(b)



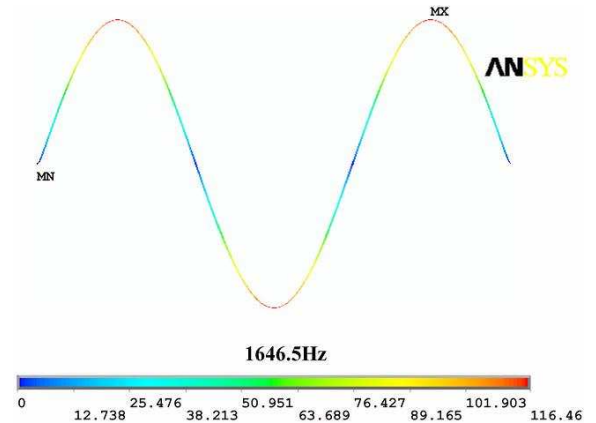
(c)



(d)



(e)



(f)

Fig. 3.6: A comparison of the first three violin modeshapes of a fused silica fiber obtained using the violin mode modelling procedure written in Mathematica, and using a FEM model constructed in ANSYS. a), c) and e) are the 1st, 2nd and 3rd violin modes respectively modelled through the Mathematica program. b), d) and f) are the 1st, 2nd and 3rd violin modes respectively modelled using ANSYS.

modeshapes obtained using the two models is given in Figure 3.6. It can be seen that the amplitude function of the first three violin modes produced by the two modelling techniques agree reasonably closely.

Similarly, a fused silica ribbon was modelled by the two different methods. The model in question consists of a $100\mu\text{m}$ thick, 5.5mm wide fused silica ribbon. The ribbon is fixed at one end while supporting a 7.4kg mass at the other. Again, the effect of Poisson's ratio is accounted for by adjusting the dimensions and density of the ribbon when under load. The resulting frequencies up to 5kHz in both the x and y directions are given in Table 3.3. As usual, we define the x direction as the direction of the thin

Mode No.	Violin Mode Freq. (Hz)			Violin Mode Freq. (Hz)		
	x-direction			y-direction		
	VM Model	ANSYS	Diff. (%)	VM Model	ANSYS	Diff. (%)
1	307.2	303.6	-1.2	386.4	384.4	-0.5
2	614.5	607.2	-1.2	846.8	846.6	-0.0
3	921.8	911.0	-1.2	1429.1	1434.8	0.4
4	1229.2	1215.1	-1.2	2157.6	2170.8	0.6
5	1536.7	1519.6	-1.1	3043.8	3063.5	0.6
6	2152.1	2129.8	-1.0	4093.1	4115.3	0.5
7	2460.0	2435.7	-1.0			
8	2768.1	2742.4	-0.9			
9	3385.0	3365.6	-0.6			
10	3693.8	3667.6	-0.7			
11	4002.9	3978.0	-0.6			
12	4312.3	4289.3	-0.5			
13	4622.1	4601.7	-0.4			
14	4932.2	4915.5	-0.3			

Tab. 3.3: Comparison of a fused silica ribbon violin mode frequencies in the two orthogonal x and y directions modelled using two methods. The first method involves the violin mode modelling procedure written in Mathematica as described above, the second makes use of FEM methods using ANSYS.

dimension of the ribbon, while the y direction is the direction of the wide dimension of the ribbon. Figures 3.7 and 3.8 compare the first three modeshapes of the ribbon

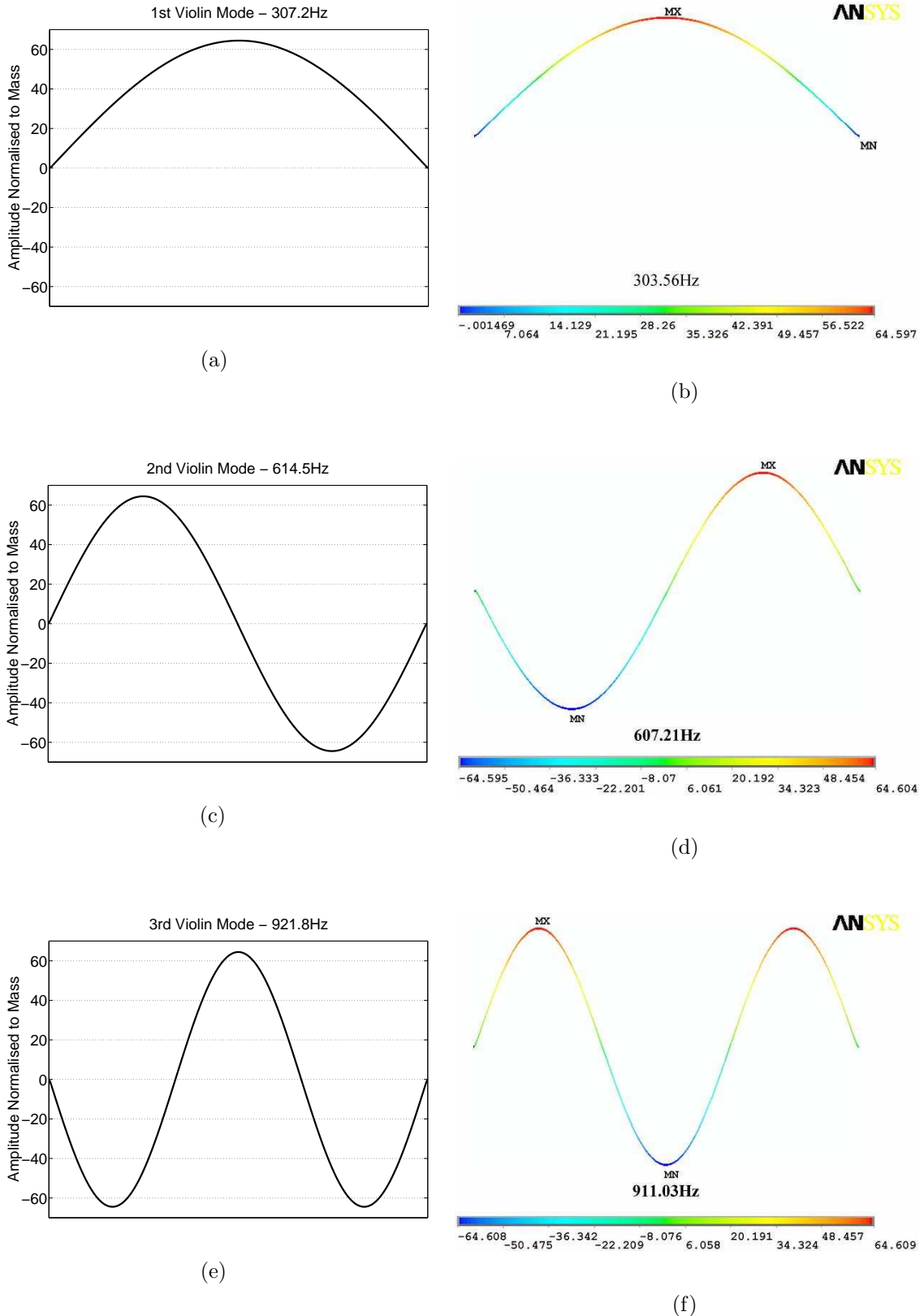


Fig. 3.7: A comparison of the first three y direction violin modeshapes of a fused silica ribbon obtained using the violin mode modelling procedure written in Mathematica, and using a FEM model constructed in ANSYS. a), c) and e) are the 1st, 2nd and 3rd violin modes respectively modelled through the Mathematica program. b), d) and f) are the 1st, 2nd and 3rd violin modes respectively modelled using ANSYS.

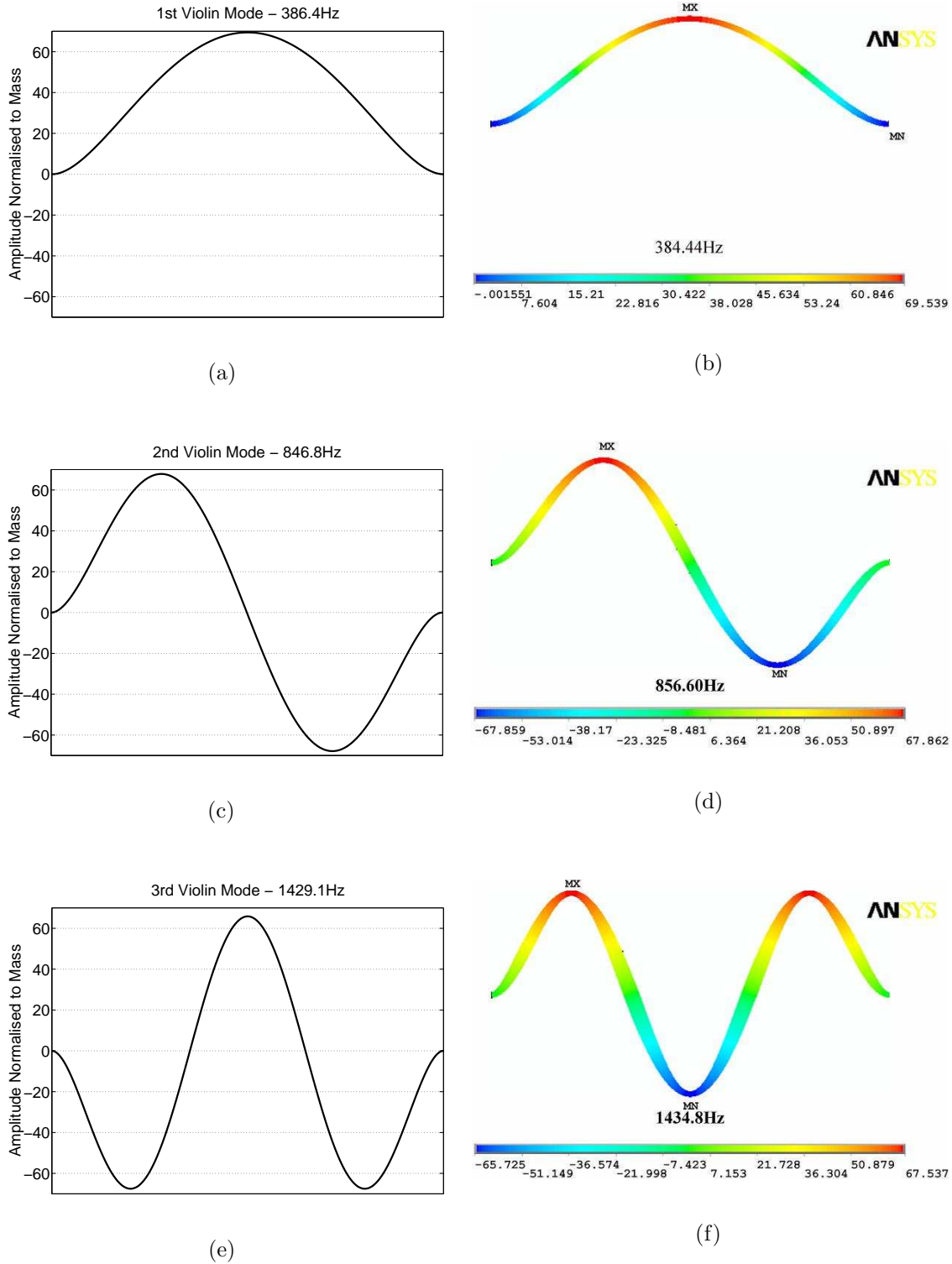


Fig. 3.8: A comparison of the first three x direction violin modeshapes of a fused silica ribbon obtained using the violin mode modelling procedure written in Mathematica, and using a FEM model constructed in ANSYS. a), c) and e) are the 1st, 2nd and 3rd violin modes respectively modelled through the Mathematica program. b), d) and f) are the 1st, 2nd and 3rd violin modes respectively modelled using ANSYS.

in the x and y direction respectively, modelled using the Mathematica procedure and ANSYS. Again it can be seen that the amplitudes of the modeshapes (normalised to mass) agree closely between the Mathematica and ANSYS models. The normalised amplitudes for the ribbon model are smaller than that for the fiber due to the larger linear mass density exhibited by the ribbons.

The slight differences observed between the two modelling techniques may be explained by the approximation of the effect of Poisson's ratio in the Mathematica model. In this case, suspension dimensions have been altered in order to account for the shrinking and stretching effect. The changes however, and hence linear density and area moment of inertia remain constant along the length of the wire. In the ANSYS finite element model, one end of the suspension is constrained in all degrees of freedom, while the other is attached to a sapphire mass with larger young's modulus than fused silica. Consequently, the shrinking of the wire or ribbon dimensions when placed under load is maximum at the center of the suspension and varies along its length. Therefore the values of linear density and area moment of inertia also vary along the suspension length, and thus may produce slightly different results.

3.4 Extension to Triple Sectioned Suspension Elements

By extending the violin mode modelling procedure to allow for the study of triple sectioned suspension elements, the program suddenly becomes a very useful and powerful tool for designing test mass suspensions that could be used in advanced detectors. A triple section suspension element is of the form illustrated in Figure 3.9. As the name suggests, a triple section suspension element is a suspension element that consists of three sections. Usually this involves two end flexures, and a central section of any geometry that is essentially constant along its length. The motivation behind the analysis of such suspension geometries is the possibility of lower Q factor and lower number of suspension violin modes, whilst not significantly compromising the pendulum mode thermal noise. This extension to the violin mode modelling procedure, along with an extension of the Mark Barton Mathematica toolkit, allows one to explore in depth this family of suspension elements.

The parameters involved in modelling the triple section suspension are essentially the same as those required for the suspension wire given in Table 3.1. The main

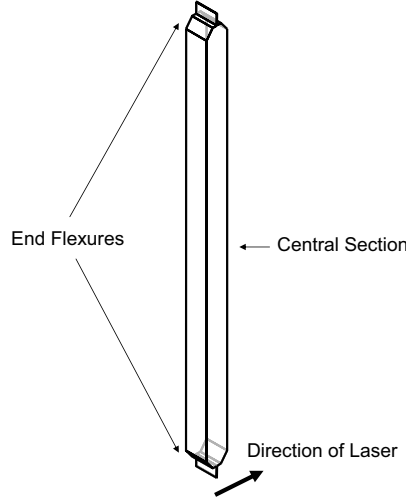


Fig. 3.9: A triple section suspension element in its simplest form. The three sections include two flexures located at each end, and a central section, in this case a solid bar.

difference being that linear mass density, ρ_L , length, L , and area moment of inertia, I_x , are required for each of the three sections denoted by subscripts 1, C and 2 to represent section at end 1, central section, and section at end 2 (e.g. L_1 , L_C and L_2). Currently the assumption has been made that the triple section suspension element is constructed from the same material, however this assumption can easily be abandoned by allowing the input of the values of young's modulus, E_1 , E_C and E_2 .

3.4.1 Solving Triple Sectioned Suspension Element Violin Modes

To solve for the violin modes of such a suspension, the dynamic beam equation (Equation 3.1) must be solved for all three sections. Thus the general solution consists of a piecewise function defined over the total length of the suspension. This is shown in Equation 3.10.

$$X_{gen}(z) = \begin{cases} A_1 \cos(k_t z) + B_1 \sin(k_t z) + C_1 \cosh(k_e z) + D_1 \sinh(k_e z), & -\frac{L_C}{2} - L_1 < z < -\frac{L_C}{2} \\ A_C \cos(k_t z) + B_C \sin(k_t z) + C_C \cosh(k_e z) + D_C \sinh(k_e z), & -\frac{L_C}{2} < z < \frac{L_C}{2} \\ A_2 \cos(k_t z) + B_2 \sin(k_t z) + C_2 \cosh(k_e z) + D_2 \sinh(k_e z), & \frac{L_C}{2} < z < \frac{L_C}{2} + L_2 \end{cases} \quad (3.10)$$

Physical requirements at the two boundaries and the two interfaces between different sections result in 12 simultaneous equations that must be satisfied. These requirements are illustrated in Figure 3.10. These 12 equations along with the normalising requirement shown in Equation 3.11 allow one to solve for the 12 constants and violin

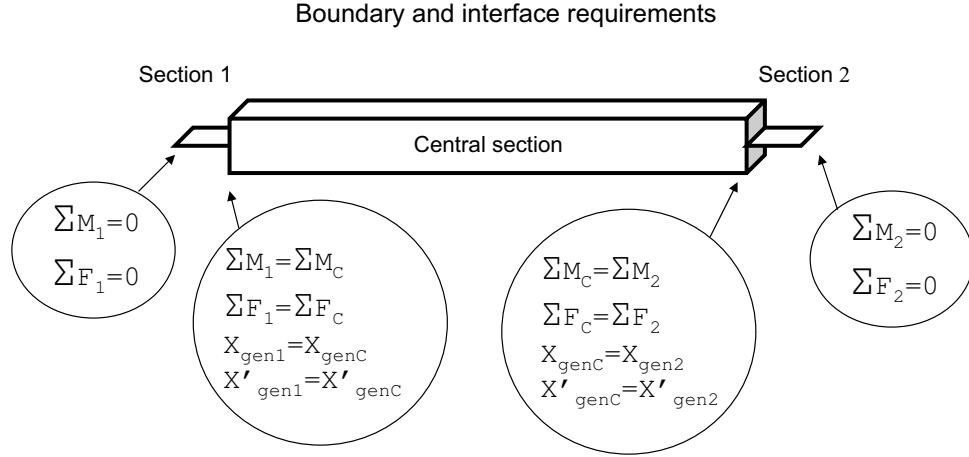


Fig. 3.10: The boundary and interface requirements of a triple section suspension element. The result is 12 simultaneous equations that must be satisfied.

mode frequencies f .

$$\int_{-\frac{L_C}{2}-L_1}^{-\frac{L_C}{2}} \rho_{L1} X_{gen}^2(z) dz + \int_{-\frac{L_C}{2}}^{\frac{L_C}{2}} \rho_{LC} X_{gen}^2(z) dz + \int_{\frac{L_C}{2}}^{\frac{L_C}{2}+L_2} \rho_{L2} X_{gen}^2(z) dz + M_1 X_{gen}^2(-L_C/2 - L_1) + M_2 X_{gen}^2(L_C/2 + L_2) = 1 \quad (3.11)$$

The method used to solve the violin mode frequencies and mode functions is very similar to that described in Section 3.2.1, only extended to solve for the extra number of constants using the extra interface condition equations. Again it was found that this method was the most computationally time efficient.

The dilution factor for each mode is also calculated in a similar manner by determining the stored elastic energy, and the stored potential energy due to tension. The stored elastic energy for the triple section suspension is given by Equation 3.12 while the stored potential energy is given by Equation 3.13.

$$E_{el} = \frac{1}{2} E \left(I_{x1} \int_{-\frac{L_C}{2}-L_1}^{-\frac{L_C}{2}} X''(z)^2 dz + I_{xC} \int_{-\frac{L_C}{2}}^{\frac{L_C}{2}} X''(z)^2 dz + I_{x2} \int_{\frac{L_C}{2}}^{\frac{L_C}{2}+L_2} X''(z)^2 dz \right) \quad (3.12)$$

$$E_{tens} = \frac{1}{2} F_T \left(\int_{-\frac{L_C}{2}-L_1}^{-\frac{L_C}{2}} X'(z)^2 dz + \int_{-\frac{L_C}{2}}^{\frac{L_C}{2}} X'(z)^2 dz + \int_{\frac{L_C}{2}}^{\frac{L_C}{2}+L_2} X'(z)^2 dz \right) \quad (3.13)$$

By calculating E_{el} and E_{tens} for each mode, the dilution factor can be calculated by $\frac{E_{el}}{E_{el}+E_{tens}}$. In this case the approximation $\frac{E_{el}}{E_{el}+E_{tens}} \approx \frac{E_{el}}{E_{tens}}$ cannot be made since the stored elastic energy is not always much smaller than the potential energy due to tension. Violin mode contribution to thermal noise can then be approximated by using the dissipation dilution theorem shown in Equation 3.9.

3.4.2 Altering Calculation of Pendulum Mode Dilution Factor

One part of the calculations involved in the Mark Barton toolkit involves a calculation of the wire bending elasticity, used to determine the dilution factor for various modes of the suspension. This is done in a very similar manner to that described for violin modes in Equation 3.8. In this case however, the bending equation is given by Equation 3.14. It must also be solved for two orthogonal directions of bending.

$$\frac{EI_x}{F_T} \frac{\partial^4 X(z)}{\partial z^4} - \frac{\partial^2 X(z)}{\partial z^2} = 0 \quad (3.14)$$

The bending function $X(z)$ is solved in terms of α and β , the angles at the endpoints of the suspension as illustrated in Figure 3.11. In doing so, the potential energy given

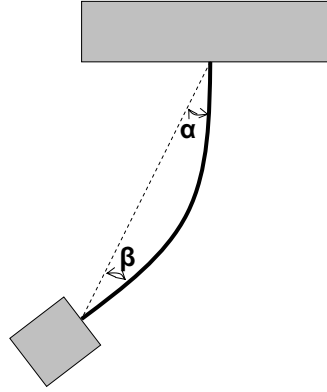


Fig. 3.11: Pendulum mode bending of a suspension wire. The shape of the bending depends on the value of the characteristic bending length, λ , where $\lambda = \sqrt{\frac{EI_x}{F_T}}$.

in Equation 3.15 can also be determined in terms of α and β , and hence as a function of the parameters of the system (i.e. the coordinates of each mass in the model).

$$PE = \frac{1}{2} \int_0^L EI_x (X''(z))^2 dz \quad (3.15)$$

A package has been written to allow for the use of triple section suspension elements by overriding existing functions. The wire bending potential energy function has been recalculated as a function of α and β for a triple section suspension. Similarly, the wire twisting potential energy derived from the torsion stiffness has also been updated with the triple section suspension equivalent. An alteration to the parameters required to describe suspension wires is also necessary, since values such as length, linear mass density, area moment of inertia, polar moment of inertia e.t.c need to be defined for each section.

3.4.3 Comparison to Finite Element Model

To test the triple section suspension modelling procedure as described above, the results of a particular model was compared to those obtained using finite element modelling techniques with ANSYS. The triple section suspension being modelled consists of a 5mm radius fused silica rod of length 0.38m connected to a $236\mu\text{m}$ radius fused silica fiber of length 1cm at each end. This is illustrated in Figure 3.12. The suspension is

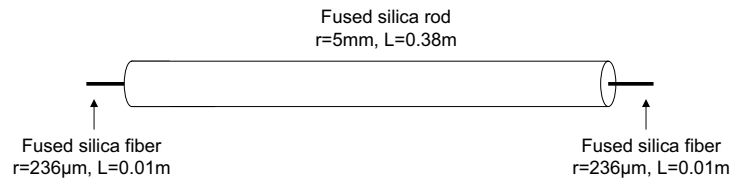


Fig. 3.12: A fused silica triple section suspension used for model result comparison.

fixed at one end, and supporting a 7.4kg mass at the other. The resulting violin modes up to 5kHz obtained using the Mathematica program and an ANSYS FEM model is given in Table 3.4. Obviously this particular suspension would not be beneficial in

	Violin Mode Freq. (Hz)		
Mode No.	VM Model	ANSYS	Difference (%)
1	80.8	81.8	1.2
2	160.1	160.9	0.5
3	409.4	420.7	2.7
4	1006.2	1036.5	2.9
5	1941.3	1991.4	2.5
6	3196.3	3260.7	2.0
7	4768.0	4835.3	1.4

Tab. 3.4: Comparison of a fused silica triple section suspension x direction violin mode frequencies modelled using two methods. The first method involves the violin mode modelling procedure written in Mathematica as described above, the second makes use of FEM methods using ANSYS.

an interferometric gravitational wave detector, due to the low frequency of the first two violin modes. The purpose of this geometry however is solely to compare the results of the two different modelling methods. Figure 3.13 compares the amplitudes

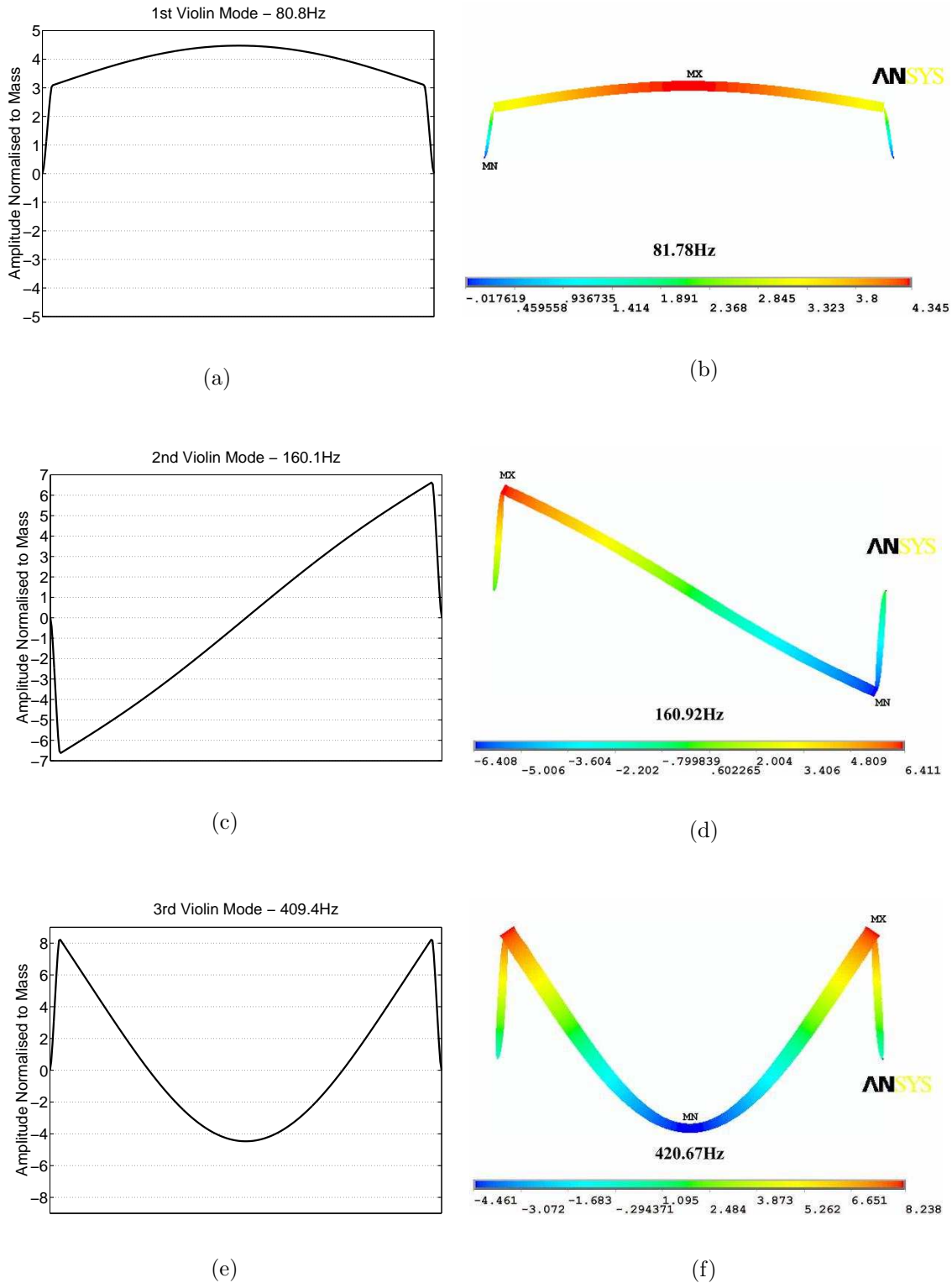


Fig. 3.13: A comparison of the first three x direction violin modeshapes of a fused silica triple section suspension element obtained using the violin mode modelling procedure written in Mathematica, and using a FEM model constructed in ANSYS. a), c) and e) are the 1st, 2nd and 3rd violin modes respectively modelled through the Mathematica program. b), d) and f) are the 1st, 2nd and 3rd violin modes respectively modelled using ANSYS.

(normalised to mass) of the first three violin modes obtained using the two different modelling methods.

It can be seen that the violin modes obtained using the two different methods agree to better than 3%. Similarly, the amplitude functions are also in relatively good agreement. It is likely that the difference between the two methods occurs due to the slight deformation of the suspension element when placed under load. This deformation will only be simulated by the ANSYS FEM model and is not considered in the Mathematica procedure. Despite this minor difference, the comparison still indicates that the Mathematica procedure should produce relatively accurate results, correct to within about 3%.

CHAPTER 4

ADVANCED GEOMETRY SUSPENSIONS

4.1 Preface

In this chapter, the modelling results of various triple section suspension ideas are presented. The modelling results have been obtained from the Mathematica suspension modelling toolkit originally developed by Mark Barton. The extensions of this toolkit to model advanced geometry suspensions has been discussed in detail in the previous chapter. Most of the results presented below are attached in Sections 4.3 and 4.4 in the form of two published papers. These papers give the motivation, violin mode frequencies and expected thermal noise improvements of the orthogonal ribbon and thin tube suspensions. Furthermore, extra work related to these suspension types has been added as postscripts to the papers. This work was done at the same time as the presented results, however was left off the final submission.

In addition to the papers attached, the first section of this chapter presents the work done initially to investigate the effect a likely triple section suspension element would have on pendulum mode thermal noise. Finally, the concept of removable modular suspension elements for integration with advanced suspension types at AIGO are discussed. The design and analysis of a high pressure contact pin required to realise such a system is given.

4.2 Pendulum Mode Dilution Factor

4.2.1 Introduction

The use of a triple section suspension element allows one to manipulate, to some degree, the higher order violin modes in the suspension. The choice of central section

geometry has a significant effect on the violin mode frequencies and Q factors. It is important however that the choice of geometry does not significantly degrade the pendulum mode Q factor, since it is necessary that the suspension exhibits minimum thermal noise. Thus the purpose of this study is to investigate, using the modelling procedure described in Chapter 3, the effect that likely geometrical changes in the suspension will have on the pendulum mode dilution factor.

It is most likely that a useful triple section suspension element will consist of short flexures at each end of a central structure. This is illustrated in Figure 4.1(b) and 4.1(c), where the central structure has been drawn as a solid bar. The idea is that the

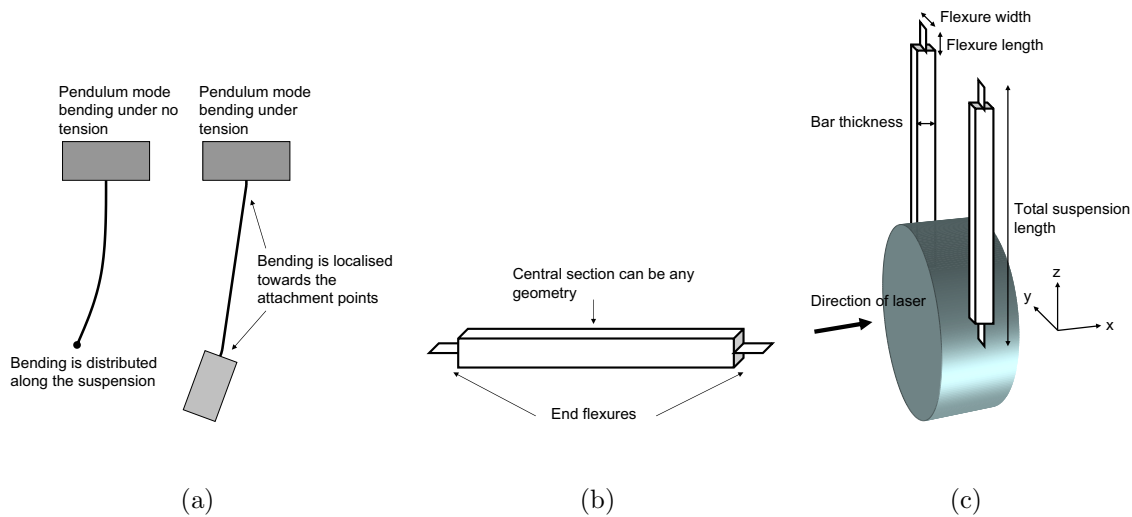


Fig. 4.1: a) Bending of the suspension when under no load, and when under load. b) A likely triple section suspension consisting of end flexures and a central section. c) The suspension element orientation with respect to the suspended mirror.

end flexures will allow for the bending required at each end for pendulum mode motion, while the central structure stiffness increases the frequencies of the violin modes. To observe the effect that various triple section arrangements may have on pendulum mode dilution factor, a bar/flexure suspension with varying bar thickness and flexure length is considered.

4.2.2 Suspensions Supporting 30kg Test Masses

In the first model, we consider four fused silica bar/flexure suspensions supporting a 30kg mass. The end flexures are fixed at 5.5mm width and $100\mu\text{m}$ thickness, while

the central bar has a fixed width of 5.5mm also. The total length of the suspension remains at 30cm, thus an increase in flexure length corresponds to a reduction in bar length. Figure 4.2 illustrates the pendulum mode dilution factor (represented by the level of darkness) as a function of variation in the two parameters; flexure length and bar thickness.

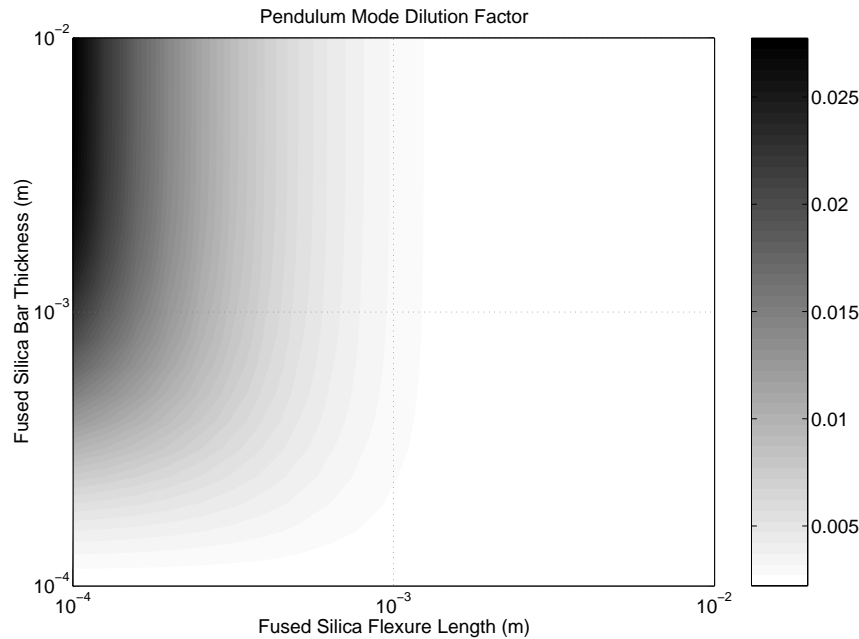


Fig. 4.2: The pendulum mode dilution factor of a fused silica bar/flexure suspension as a function of flexure length and bar thickness. The suspension width is fixed at 5.5mm, while the flexure thickness is fixed at $100\mu\text{m}$. The total suspension length is 30cm.

The plot displays an expected result, that pendulum mode dilution factor increases for large bar thickness at small flexure lengths. At larger flexure lengths, most of the pendulum mode flexing will occur in the end flexures, and hence the dilution factor becomes less and less dependant on the bar thickness. For small flexure lengths however, pendulum motion will involve bending of the central section, and hence the dilution factor will depend on the bending stiffness, i.e. the thickness of the bar. This result implies that there is likely a particular minimum flexure length, for which the pendulum mode bending remains almost independent of the stiffness of the central section. Therefore if the end flexures are constructed to be at least this minimum length, we have the freedom to change the central section to any geometry, knowing that it will not significantly worsen the pendulum mode dilution factor. To find the

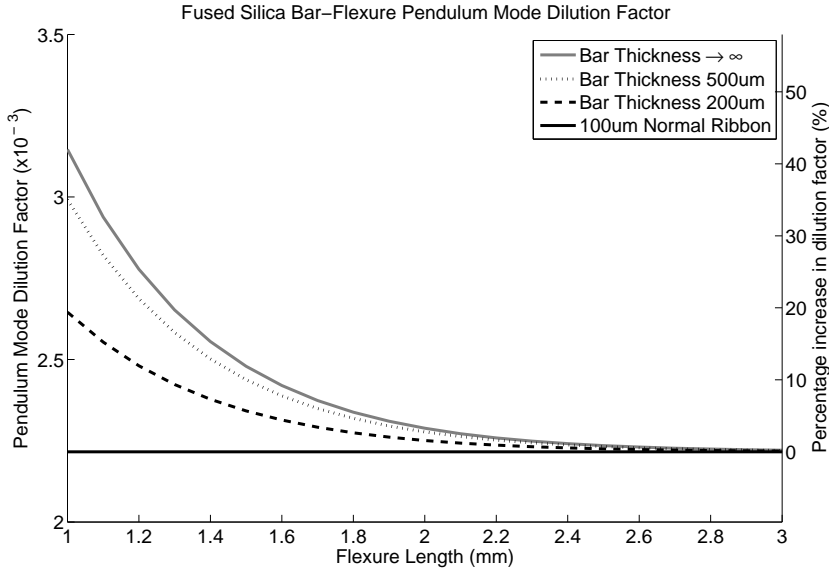


Fig. 4.3: Pendulum mode dilution factor as a function of flexure length for several bar thicknesses. The same model is being considered as that analysed by Figure 4.2.

value of this minimum length, pendulum mode dilution factor is plotted against flexure length for several values of bar thickness in Figure 4.3.

It is important to note that in this modelling procedure, the mass of the suspension itself does not contribute to the tension within the suspension. In most cases, the mass of the suspension is much less than the test mass it is supporting, and hence the approximation is valid. Therefore this allows us to model the unrealistic case where the central bar thickness approaches infinity, without altering the value of tension. Consequently, the result of an infinitely stiff central section on the pendulum mode dilution factor can be easily assessed. Figure 4.3 compares the dilution factor as a function of flexure length for bar thicknesses of $200\mu\text{m}$, $500\mu\text{m}$ and ∞ with that expected from a fused silica ribbon suspension of length 30cm, width 5.5mm and thickness $100\mu\text{m}$. The results show that even for an infinitely stiff central section, flexure lengths as small as 1.5mm will only result in 10% increase in pendulum dilution factor. It is interesting to note that this minimum length of 1.5mm is significantly larger than the characteristic bending length, $\lambda = \sqrt{\frac{EI_x}{F_T}}$, for the flexures, which is approximately 0.66mm.

Similarly, a niobium triple section suspension has been analysed. The characteristic bending length, λ , of a niobium flexure is larger due to the larger value of young's modulus. Thus it is expected that the minimum flexure length to ensure less than 10% increase in pendulum mode dilution factor will also increase. Again, the model

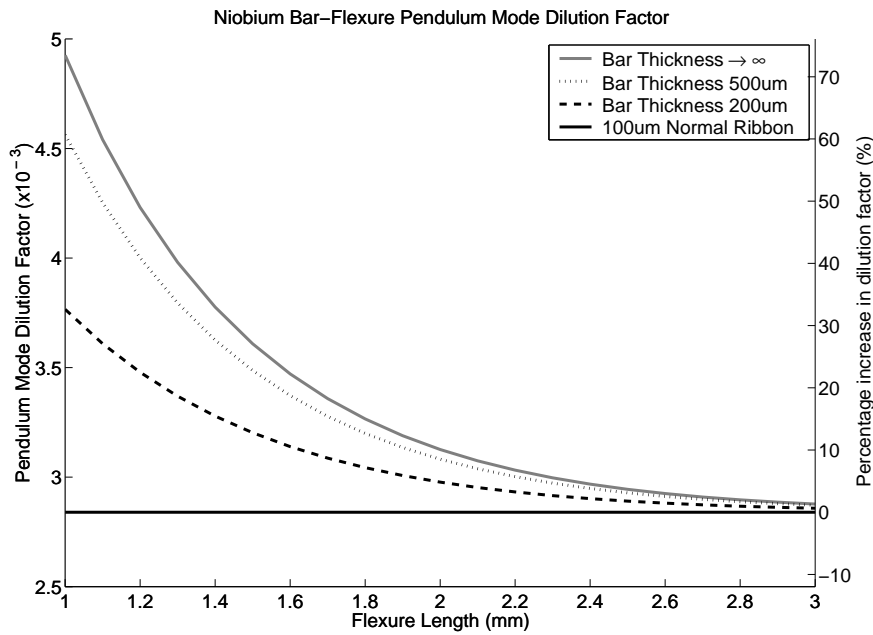


Fig. 4.4: Pendulum mode dilution factor as a function of flexure length for several bar thicknesses. The model consists of four niobium bar/flexure suspensions of width 6mm, with flexure thickness of $100\mu\text{m}$ supporting a 30kg test mass. The total suspension length is 30cm.

being analysed consists of four bar/flexure suspensions supporting a 30kg mass. The flexures are $100\mu\text{m}$ thick and 6mm wide, while the central section bar is 6mm wide. The total length of the suspension is 30cm. A plot of pendulum mode dilution factor versus flexure length for various central section thicknesses is illustrated in Figure 4.4.

In this case, 2mm long flexures will ensure that the pendulum mode dilution factor will not increase by more than 10% over that achieved with a $100\mu\text{m}$ niobium ribbon suspension. The characteristic bending length for niobium flexures of these dimensions is approximately 0.82mm, and thus the minimum required flexure length of 2mm is approximately 2.5 times the characteristic bending length of the flexure.

4.2.3 Suspension for AIGO Size Masses

The test masses to be used at AIGO are 4.2kg. Therefore the end flexures of supporting triple section suspension elements can be made with smaller thickness and smaller width. In turn, this effects the minimum flexure length that is required such that less than a 10% increase in pendulum mode dilution factor will result. Again this 10%

increase is in comparison to a normal ribbon suspension with the same width and thickness as the end flexure.

To compute the increase in pendulum mode dilution factor, four niobium bar/flexure suspensions supporting a 4.2kg mass is modelled. The width of the end flexures and central bar is 3mm, while the flexure thickness is $25\mu\text{m}$. The total suspension length is 30cm. Flexures of these dimensions will support the 4.2kg test mass with a 50% safety margin over the breaking stress of niobium. A plot of pendulum mode dilution factor versus flexure length for various central bar thicknesses is shown in Figure 4.5.

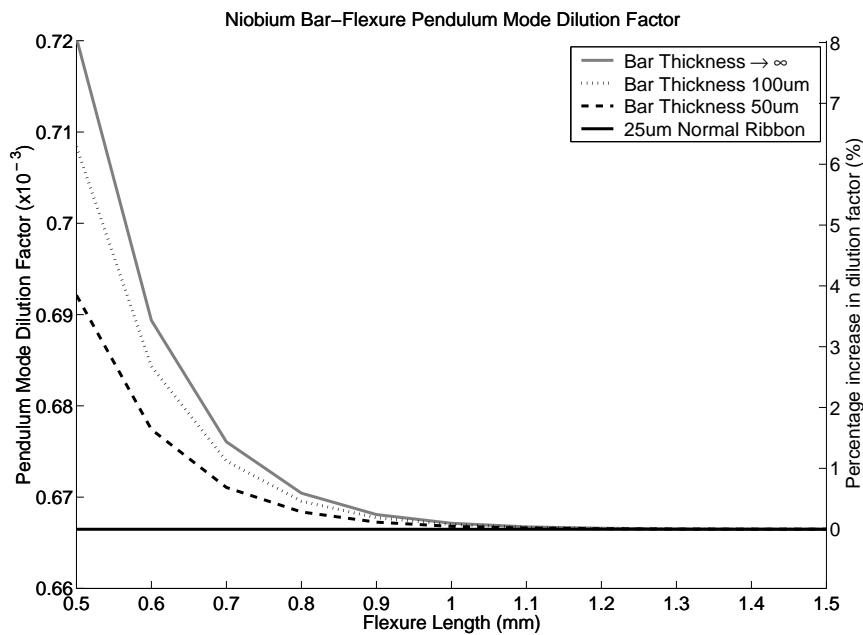


Fig. 4.5: Pendulum mode dilution factor as a function of flexure length for several bar thicknesses. The model consists of four niobium bar/flexure suspensions of width 3mm, with flexure thickness of $25\mu\text{m}$ supporting a 4.2kg test mass. The total suspension length is 30cm.

In this case, it can be seen that even for flexure lengths as small as 0.5mm, the increase in pendulum mode dilution factor will be lower than 8%, regardless of the stiffness of the central section. Thus for flexures as thin as those described for the above model, it will likely be practical limitations that determine the minimum flexure lengths. For comparison, the characteristic bending length for the $25\mu\text{m}$ flexures is approximately 0.20mm. Again, the minimum flexure length required for no more than 10% increase in pendulum mode dilution factor to the equivalent ribbon suspension characteristic bending length is close to a factor of 2.5.

4.2.4 Summary and Conclusion

We have shown through modelling results that it is possible to use triple section suspension elements with thin end flexures for suspending test mass suspensions without significantly degrading the pendulum mode dilution factor. For sufficiently long end flexures, the dilution factor has been shown to increase by less than 10% compared to a typical ribbon suspension with width and thickness dimensions equivalent to the flexures. This result holds regardless of the stiffness, and hence geometry of the central section. The minimum flexure lengths for the three models studied are given in Table 4.1.

Material	Flexure Thickness	Test Mass	Min. Flexure Length
Fused Silica	100 μ m	30kg	1.5mm
Niobium	100 μ m	30kg	2mm
Niobium	25 μ m	4.2kg	0.5mm

Tab. 4.1: The minimum flexure length to ensure less than 10% increase in pendulum mode dilution factor compared to a typical ribbon suspension with the same width and thickness dimensions as the flexure.

Assuming that the end flexures of a triple section suspension are made at least the required length, we are effectively free to alter the geometry of the central section in order to improve the performance of the suspension. The central section bar, as indicated in several figures above, is actually a poor suspension element due primarily to the increased mass of the suspension element. This in turn results in low frequencies for the first two violin modes, and a high amount of coupling of suspension thermal noise to the test mass. More promising central section geometries include the orthogonal ribbon, or the thin tube. The orthogonal ribbon is stiff in the x direction (direction of the laser) and hence provides a lower number of more widely spaced violin modes, while the thin tube provides stiffness and hence more widely spaced violin modes in both x and y direction. Both these ideas are discussed in detail in the following two sections.

4.3 Orthogonal Ribbon Physics Letters A Paper

Orthogonal Ribbons for Suspending Test Masses in Interferometric Gravitational Wave Detectors

B.H.Lee, L.Ju, D.G.Blair, Phys. Lett. A, 339 (2005) 217-223

School of Physics, The University of Western Australia, Crawley 6009, WA, Australia

We show that a simple modification of proposed ribbon suspensions for laser interferometric gravitational wave detectors can substantially reduce the amplitude of violin modes at the expense of a small deterioration of suspension thermal noise. Using low loss fused silica, large amplitude peaks which cause dynamic range problems can be reduced by 21dB. The total number of horizontal longitudinal direction violin modes below 5kHz is reduced to less than half that expected with conventional ribbon suspensions.

4.3.1 Introduction

Thermal noise in interferometric gravitational wave detectors can be separated by distinguishing between two main sources: a) the test mass suspensions and b) the mirror test masses. Suspension thermal noise dominates at low frequencies from a few Hz to a few hundred Hz. With the need for better sensitivity in advanced detectors [107], there has been a large effort to improve test mass suspensions. Much effort has gone into reducing the losses in the suspension elements [79, 108, 109, 78, 84, 110]. Also there has been an extensive study into the use of suspensions with rectangular profiles, i.e. ribbons or flexures in order to further reduce the pendulum mode thermal noise [80, 111]. Cradle suspensions [112] and more elaborate thermal noise readout schemes [113] have also been proposed.

This paper is motivated by concern that the violin string modes in very low loss suspensions have high amplitude and can cause saturation, non-linearity and other dynamic range problems in an advanced interferometer. A large scale interferometer is locked to its maximum sensitivity point through control servos that act on the mirrors. In digital controllers, 20bit A to D converters limit sensors to a sensing range of approximately 120dB. Thus extremely sensitive position sensors require the mirror

to be located within a very small position bandwidth. Excited violin mode vibrations couple to the mirror and can have significantly high amplitudes due to their large Q values. The dynamic motion of the mirror may be larger than the sensing range. This, along with the high ring down time of the oscillations can result in long periods of interferometer down time. It is also possible that feedback actuators drive the violin modes, causing instabilities in high gain length control servos.

Ideally, a suspension would contain no violin modes within the detection band, but since such a solution is not possible, it is likely that notch filters will be required within the length control systems. The number of filters and their Q will depend on the suspension violin modes, and hence these modes have a bearing on the control system complexity. This problem has already led to implementation of special damping schemes [105]. Here, Gossler et. al. report on a method of damping fused silica fibre violin modes such that the fundamental and first harmonic violin modes have Q factor $< 3 \times 10^6$ and $< 2 \times 10^6$ respectively. In this paper we investigate suspension ribbons with a different shape profile as a possibility for use as a test mass suspension element. Our goal is to design a suspension that improves on currently proposed ribbon suspension designs. Thus we aim to lower violin mode Q factors as well as reduce the number of violin modes without compromising the low frequency suspension thermal noise performance. Any improvement in these quantities will ease the problem of length control servo design. The specific implementation is the orthogonal ribbon which is described in detail below.

Our analysis is based on a program by Mark Barton [102, 104] which has been extended and developed to include the contribution to thermal noise due to the violin string modes. To achieve this, we numerically solve the dynamic beam equation [106], given in equation (4.1), relevant to the suspension element.

$$F_T \frac{\partial^2 X(z, t)}{\partial z^2} - EI \frac{\partial^4 X(z, t)}{\partial z^4} = \rho \frac{\partial^2 X(z, t)}{\partial t^2} \quad (4.1)$$

Here F_T is the tension in the beam, E the Young's Modulus, I the area moment of inertia and ρ the linear mass density. $Y(z, t)$ is the displacement of the beam from its equilibrium position at a location along its length z at time t . Solving this equation results in violin mode shapes and frequencies which can be combined with the equation

for thermal noise displacement spectrum, shown by equation (4.2), obtained from the fluctuation dissipation theorem [57].

$$x^2(\omega) = 4k_B T \sum_{n=1}^{\infty} \frac{\psi_n^2(L) \phi_n(\omega) \omega_n^2}{\omega((\omega_n^2 - \omega^2)^2 + \phi_n^2(\omega) \omega_n^4)} \quad (4.2)$$

Here k_B is the Boltzmann constant, T the temperature, ϕ_n the phase angle associated with the loss of the material, ω the angular frequency, ω_n the resonant angular frequency and ψ_n the normalised mode function. The final suspension thermal noise spectrum can then be estimated by summing the thermal noise contributions due to natural modes and violin modes.

4.3.2 The Orthogonal Ribbon

The orthogonal ribbon is essentially a ribbon with the majority of its length rotated 90° around the vertical axis (figure 4.6b). This results in a ribbon orthogonal to a typically orientated ribbon with a short flexure at each end. The length of the flexures are made longer than the characteristic bending length of the ribbon, λ , given by equation (4.11) where E , I and F_T are the Young's modulus, area moment of inertia and tension respectively. This results in pendulum mode flexing of the orthogonal ribbon having almost equal stiffness to the pendulum mode flexing of a typical ribbon. Given equal pendulum bending stiffness, we expect the pendulum mode thermal noise that dominates at low frequencies to be the same.

$$\lambda = \sqrt{\frac{EI}{F_T}} \quad (4.3)$$

With very similar pendulum mode thermal noise, we are free to alter the geometry of the central section (the section between the flexures at each end) in order to increase the violin mode frequency. To study the effect of changing aspects of the central section on the violin mode frequencies we numerically solve the beam equation, given by equation (4.1), for this 3 section beam. We are able to solve for the violin mode frequencies, and the normalised mode shapes.

In the models studied in this article, we aim to compare the thermal noise performance of two sets of suspensions comprising of the following suspension elements:

1. A 30cm long, 100um thick, 5.5mm wide fused silica ribbon compared to an orthogonal fused silica ribbon 30cm long and no dimension less than 100um.

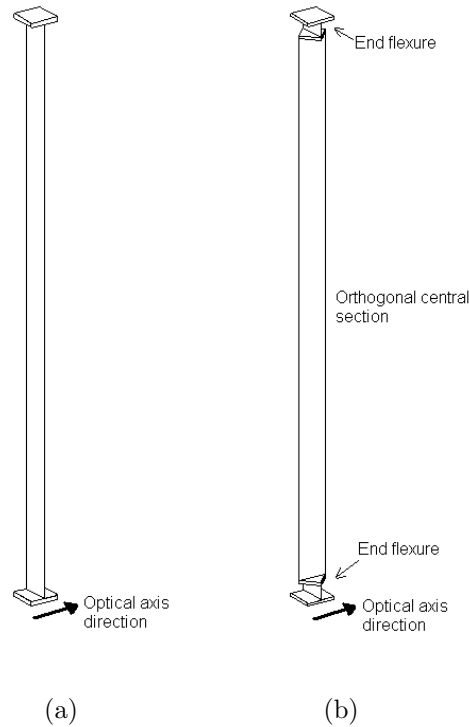


Fig. 4.6: (a) A normal ribbon fixed between two mounting blocks. (b) The orthogonal ribbon consists of a ribbon section orthogonal to the orientation of a normal ribbon, between two flexures of much shorter length. The optical axis direction is indicated by the arrow in each case.

2. A 30cm long, 100 μ m thick 6mm wide niobium ribbon compared to an orthogonal niobium ribbon 30cm long and no dimension less than 100 μ m.

Niobium is chosen because it is the lowest loss metal, and because suspensions can be easily fabricated by electric discharge machining. In the case of fused silica the fabrication could be achieved by welding, silicate bonding or ultrasonic machining. The orthogonal ribbons could be attached to the optic via fused silica standoff plates, or 'ears', bonded directly on the mirror. The mounting blocks can be bonded to the flat horizontal surface presented by these plates. Another possibility is through the use of specially designed pegs replacing the mounting blocks. These pegs fit into small holes located at the test mass 'equator'. This interface relies solely on gravitational force to hold the test mass in place through several well defined high pressure contact points. We are currently investigating this technique.

Our analysis is applied to a four ribbon suspension of a 30kg test mass. For both the fused silica and niobium orthogonal ribbons the flexures at each end are 100 μ m

thick and 2mm long, with the fused silica flexures being 5.5mm wide and the niobium flexures 6mm. The flexure lengths were chosen to be reasonably short to maximise the first violin mode while still being at least twice as long as the characteristic bending length. We then change the geometry of the central section and note its effect on the first violin mode frequency, and on the first violin mode dilution factor. Changing only the aspect ratio whilst keeping a constant cross sectional area will maintain a constant loading.

4.3.3 First Violin mode frequency

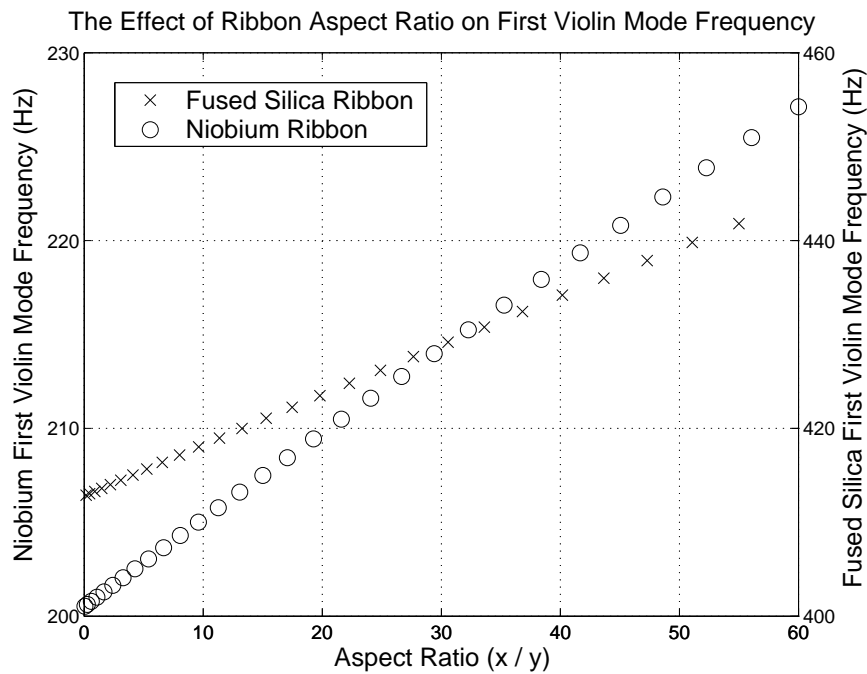


Fig. 4.7: The first violin mode frequency of a fused silica and a niobium orthogonal ribbon as a function of the central section aspect ratio, x/y (x is the horizontal longitudinal dimension and y the horizontal transverse dimension with respect to the laser beam). End flexures are 2mm long, 100 μ m thick and 5.5mm and 6mm wide respectively. The central section is 296mm long.

The simulation result for the first violin mode frequency as a result of changing the aspect ratio of the central section is illustrated in figure 4.7. We define this ratio as the horizontal longitudinal dimension divided by the horizontal transverse dimension with respect to the laser beam. Thus a normal ribbon will exhibit a minimum value for the aspect ratio. For both ribbon types (niobium and fused silica) we see a clear

increase in violin mode frequency as the aspect ratio increases. This implies that the suspension with the highest violin mode frequencies will be the one with maximum aspect ratio value, i.e. an orthogonal ribbon.

For the fused silica ribbon, there is an increase in first violin mode frequency from 413Hz to 442Hz when changing from a typical ribbon to an orthogonal ribbon. This is an increase of 7%. For the niobium ribbon case, the increase in first violin mode frequency is 200Hz to 227Hz, a change of 13%.

There are other geometrical changes that can be made to the central section. Instead of keeping the cross sectional area constant, we could increase the ribbon thickness. In this case there are two competing factors that effect the violin mode frequency, the increase in stiffness of the ribbon and the increase in linear mass density. For a thin central section, the suspension element can be approximated as a zero stiffness ribbon supported at each end by pivots. The violin mode frequencies in this case are related to the tension, F_T and linear mass density, ρ as expressed below:

$$f_n \propto \sqrt{\frac{F_T}{\rho}}. \quad (4.4)$$

By replacing the linear mass density with $\rho = xy\rho_v$, where ρ_v is the material volume density, we obtain:

$$f_n \propto x^{-\frac{1}{2}} \sqrt{\frac{F_T}{y\rho_v}}. \quad (4.5)$$

Here, the only significant effect of increasing the thickness of the central section, y , is to increase the linear mass density, ρ . Thus the violin mode frequencies are proportional to $x^{-\frac{1}{2}}$, and increasing the central section thickness only lowers the violin mode frequency. However, if x is increased to a point that the stiffness of the central section begins to dominate over the tension, the violin mode frequencies can be modelled as that of a stiff bar fixed by a pivot at each end. The frequencies related to E , I and ρ can then be expressed:

$$f_n \propto \sqrt{\frac{EI}{\rho}}. \quad (4.6)$$

Again, by replacing the linear mass density with $\rho = xy\rho_v$ and the area moment of inertia with $I = \frac{1}{12}yx^3$, we obtain:

$$f_n \propto x \sqrt{\frac{E}{12\rho_v}}. \quad (4.7)$$

In this case, the increase in stiffness of the central section dominates over increasing linear mass density. This results in the violin mode frequency being proportional to x . Although these expressions suggest a thick central section as a possibility for increasing the violin mode frequencies, in this letter, we focus only on the rectangular geometry with a constant minimum cross section area. Other geometries will be presented in a future publication.

4.3.4 First Violin mode dilution factor

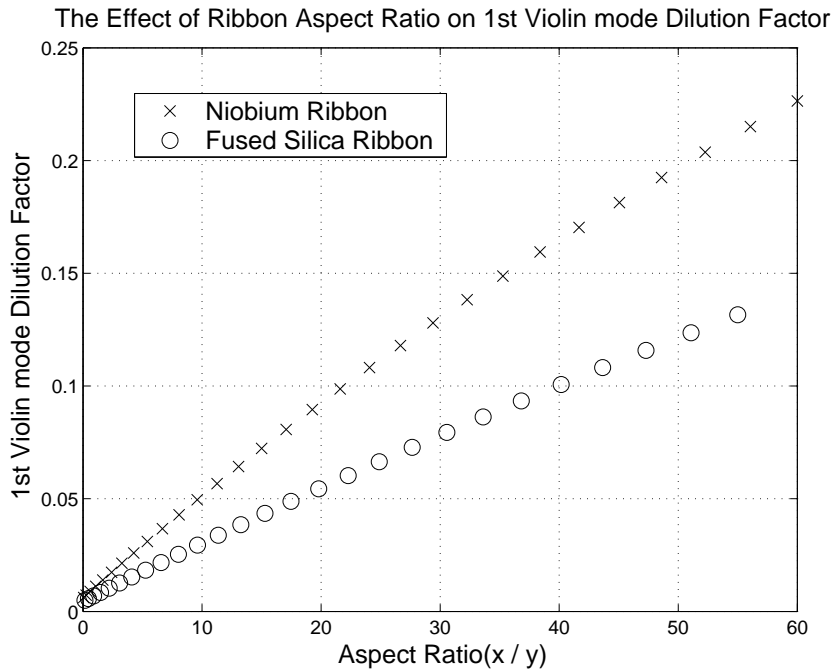


Fig. 4.8: First violin mode dilution factor for a fused silica and a niobium orthogonal ribbon as a function of the central section aspect ratio, x/y (x is the horizontal longitudinal dimension and y the horizontal transverse dimension with respect to the laser beam). End flexures are 2mm long, 100 μ m thick and 5.5mm and 6mm wide respectively. The central section is 296mm long.

The dilution factor of a mode defines the fraction of the intrinsic material loss angle, ϕ , that contributes to the total losses in a normal mode. The reason for this dilution factor is that in most cases, both tension due to gravity and the elasticity of the suspension material contribute to the resonant mode restoring force. Since it is only the restoring force due to the elasticity of the material that contributes to the loss, mode Q-factors are higher than that expected by the intrinsic material loss. Typical

dilution factors are in the range 0.002 to 0.005 for wire suspensions loaded to a fraction of their breaking stress. This is an increase in Q of several hundred.

To obtain the dilution factor, we take the ratio of elastic energy to gravitational energy for the violin mode. The expressions for the energy involved is given by Gonzalez and Saulson [114]. We solve the two expressions numerically for our 3 section orthogonal ribbon to obtain the dilution factors.

We have determined the dilution factor for the same set of aspect ratio values (x/y) as in section 4.3.3 for the central part of an orthogonal ribbon. The results of these values for both the fused silica and the niobium orthogonal ribbon are illustrated in figure 4.8. A clear increase in dilution factor for larger values of aspect ratio can be seen in both cases. In changing from a normal ribbon to an orthogonal ribbon we see a change in dilution factor of 0.005 to 0.13 (a factor of 27) for fused silica and a change of 0.006 to 0.23 (a factor of 37) for niobium. Thus by changing from a normal ribbon to an orthogonal ribbon, our simulations show both an increase in violin mode frequency and in dilution factor. From equation (4.2) we expect the increase in violin mode frequency to improve the suspension thermal noise while the increase in dilution factor (equivalent to an increase in ϕ) to degrade the noise. The question of which will have the largest effect is discussed below.

4.3.5 Comparison of thermal noise spectrums

It is not trivial to determine whether the increase in violin frequency or dilution factor has the dominant effect on the suspension thermal noise spectrum. The expression given by equation (4.2) can be simplified if we assume that the frequency of interest, ω , is much smaller than the resonant frequency, ω_n . The thermal noise spectrum can then be expressed as

$$x^2(\omega) = \frac{4k_B T}{\omega} \sum_{n=1}^{\infty} \frac{\psi_n^2(L) \phi_n(\omega)}{\omega_n^2} \quad (4.8)$$

assuming also that $\phi_n(\omega) \ll 1$. However this simplified equation cannot be used to accurately estimate the effect of violin mode frequency and dilution factor on the thermal noise for two reasons. First, we have assumed $\omega \ll \omega_n$. Although the majority of our interest is in the frequency range where this assumption holds, it is not the violin mode thermal noise that dominates in this region. The violin mode thermal noise only becomes dominant at frequencies close to the violin mode resonant frequencies. Second,

there is another factor, $\psi_n^2(L)$, that will be different between the orthogonal and normal ribbon. Thus to determine whether the orthogonal ribbon will perform better in terms of thermal noise, we use our model to calculate the entire suspension thermal noise spectrum including the effect of violin modes up to 5kHz.

The four suspensions modelled for comparison are the following:

1. Four 300mm long, 100um thick, 6mm wide niobium ribbons suspending a 30kg test mass.
2. Four 296mm long, 100um thick, 6mm wide orthogonal niobium ribbons with 2mm long, 100um thick, 6mm wide flexures suspending a 30kg test mass.
3. Four 300mm long, 100um thick, 5.5mm wide fused silica ribbons suspending a 30kg test mass.
4. Four 296mm long, 100um thick, 5.5mm wide orthogonal fused silica ribbons with 2mm long, 100um thick, 5.5mm wide flexures suspending a 30kg test mass.

We have compared suspensions (1) and (2) in figure 4.9 and suspensions (3) and (4) in figure 4.10. Our assumption is that the horizontal longitudinal to horizontal transverse coupling is 0.1%, (as is also assumed for Advanced LIGO suspensions [100]). The features of the comparison between the normal ribbon and the orthogonal ribbon in both cases are similar.

It can be seen that at low frequency ($< 100\text{Hz}$) when the pendulum mode thermal noise dominates, there is no noticeable difference between the thermal noise of the normal and orthogonal ribbons. The length of the flexures on the orthogonal ribbons are long enough such that pendulum mode stiffness in both cases are almost equal. We also observe that at frequencies approaching the violin mode frequencies ($> 100\text{Hz}$) the orthogonal ribbon has a larger magnitude of thermal noise. In the niobium case (figure 4.9) the thermal noise spectrum for the orthogonal ribbon shows a minimum just below the first violin mode of approximately $5 \times 10^{-21}\text{m}/\sqrt{\text{Hz}}$ at 130Hz. This compares to the niobium normal ribbon minimum of $1.2 \times 10^{-21}\text{m}/\sqrt{\text{Hz}}$ at 100Hz, a difference of a factor of 4.2. Similarly for the fused silica orthogonal suspensions (figure 4.10) a minimum of $4 \times 10^{-22}\text{m}/\sqrt{\text{Hz}}$ at 275Hz is compared to that of the fused silica normal ribbon minimum of $1.5 \times 10^{-22}\text{m}/\sqrt{\text{Hz}}$ at 270Hz, a difference of a factor of 2.7. The orthogonal fused silica ribbon suspension thermal noise is compared to

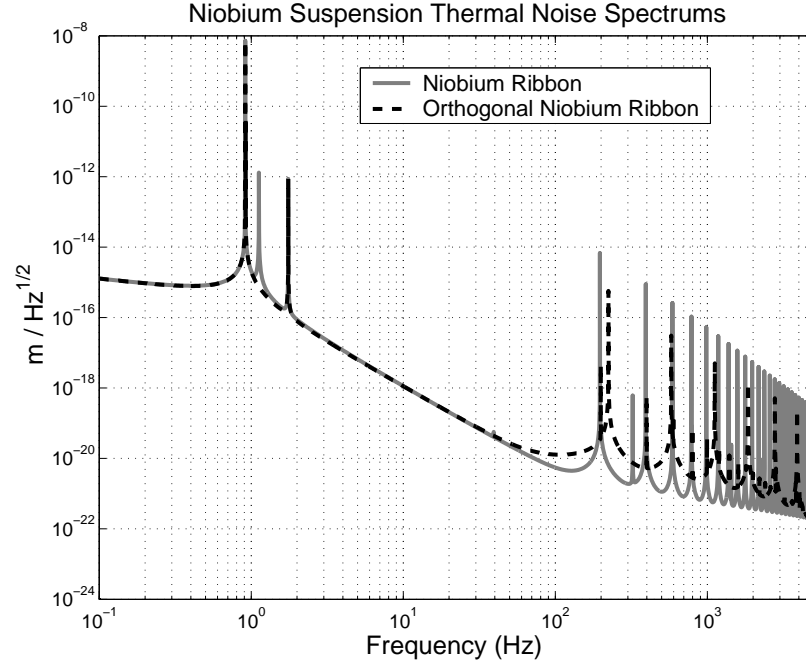


Fig. 4.9: Thermal noise spectrum for a 300mm long, 100 μ m thick, 6mm wide niobium ribbon suspension and a 296mm long, 100 μ m thick, 6mm wide orthogonal ribbon with 2mm long, 100 μ m thick 6mm wide flexures. Both are suspending a 30kg test mass. We have assumed 0.1% horizontal longitudinal to horizontal transverse coupling.

quantum noise and test mass thermal noise between 5Hz to 5kHz in figure 4.11. The illustrated quantum noise and test mass thermal noise is approximately equal to the design goals of Advanced LIGO [67]. It can be seen that although the orthogonal ribbon thermal noise is increased for frequencies > 100 Hz, it is still more than 4 times smaller than the expected quantum noise.

It is also found that in both orthogonal cases, the average peak violin mode thermal noise power is reduced. Considering the niobium normal ribbon, the average peak violin mode amplitude up to 5kHz is $2.7 \times 10^{-16} \text{m}/\sqrt{\text{Hz}}$. However the niobium orthogonal ribbon has an average peak violin mode amplitude of $2.1 \times 10^{-17} \text{m}/\sqrt{\text{Hz}}$. This is a reduction in the average peak violin mode amplitude of 22dB. Similarly for the fused silica normal ribbon, the average peak violin mode amplitude up to 5kHz is $8.6 \times 10^{-16} \text{m}/\sqrt{\text{Hz}}$ compared to the fused silica orthogonal ribbon average of $7.7 \times 10^{-17} \text{m}/\sqrt{\text{Hz}}$. This is a reduction in amplitude of 21dB. For the fused silica orthogonal ribbon, the Q-factors of the first two horizontal longitudinal direction violin modes

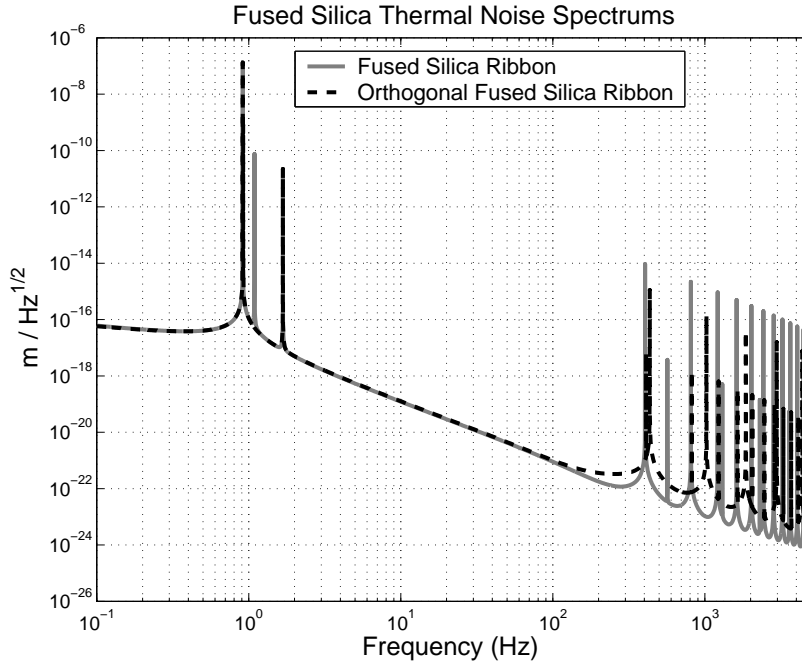


Fig. 4.10: Thermal noise spectrum for a 300mm long, $100\mu\text{m}$ thick, 5.5mm wide fused silica ribbon suspension and a 296mm long, $100\mu\text{m}$ thick, 5.5mm wide orthogonal ribbon with 2mm long, $100\mu\text{m}$ thick 5.5mm wide flexures. Both are suspending a 30kg test mass. We have assumed 0.1% horizontal longitudinal to horizontal transverse coupling.

reduce from 2×10^8 for f_1 and 4×10^8 for f_2 to 9×10^6 and 7×10^6 respectively. This represents Q-factor reductions of more than an order of magnitude.

An analysis of the violin mode peak density shows that the total number of modes for both the normal and orthogonal configurations below 5kHz are similar. Although the orthogonal ribbon demonstrates a lower number of horizontal longitudinal direction violin modes in both cases (12 down to 5 for fused silica and 24 down to 6 for niobium), the transverse direction violin modes have large enough Q values to be significant despite the 0.1% coupling. At high frequencies ($> 2000\text{Hz}$) and for thermal noise spikes greater than approximately $10 \times 10^{-19}\text{m}/\sqrt{\text{Hz}}$, the peaks are dominated by the longitudinal direction violin mode peaks. In this case, the number of interfering violin modes is largely reduced through the use of an orthogonal ribbon. Combined with the Q factor reductions, the use of the orthogonal ribbon allows the number and Q of required notch filters in the length control servo to be reduced, simplifying the feedback control system.

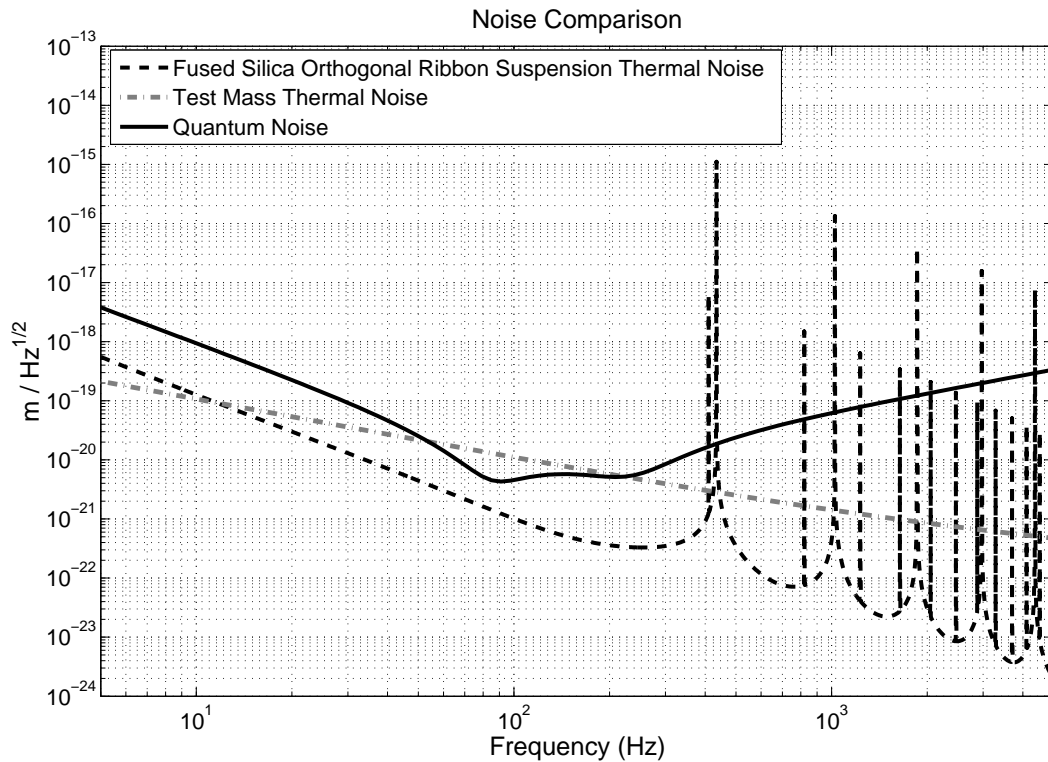


Fig. 4.11: A comparison of the fused silica orthogonal ribbon suspension thermal noise, with quantum noise and test mass thermal noise expected in advanced interferometers.

4.3.6 Conclusion

Through our modelling, we have compared a 3 section orthogonal ribbon to a normal ribbon for use as test mass suspensions in gravitational wave detectors. Analysis of both niobium and fused silica orthogonal ribbons have revealed a reduction in longitudinal direction (with respect to the laser beam) violin modes up to 5kHz, 12 to 5 for fused silica and 24 to 6 for niobium. We also observe a reduction in average peak violin mode thermal noise amplitude of 21dB and 22dB for the two cases respectively. Although this comes at a cost of a maximum increase in thermal noise of a factor of 2.7 above 100Hz for fused silica and 2.4 above 60Hz for niobium, for the fused silica case, the increased thermal noise is still more than four times below the expected interferometer quantum noise.

The reduction in violin mode amplitude and number of horizontal longitudinal violin modes reduce the risk of saturation problems and control system instabilities that may arise from high Q violin mode oscillations. The pendulum mode thermal noise remains

unchanged indicating that in a 3 section ribbon design such as the orthogonal ribbon, the central section can be changed freely as long as the end flexures are sufficiently long. Thus it may be possible to design the central section with a lower number of both longitudinal and transverse violin modes, e.g. a small solid bar, reducing the violin mode density entirely. However this will increase the thermal noise below the violin mode frequencies. We will investigate this geometry in a future publication.

4.3.7 Acknowledgments

This work is supported by the Australian Research Council and is part of the Australian Consortium for Interferometric Gravitational Astronomy (ACIGA). We also acknowledge the help from Mark Barton with regards to the suspension modelling program.

4.3.8 Postscript

At the end of section 4.3.3, it was suggested that a triple section suspension element consisting of a thick central bar may result in higher violin mode frequencies than that expected from a normal ribbon suspension of the same width and thickness as the end flexures. The hypothesis came about from the assumption that the violin modes of a triple section suspension element with short flexures and thick central section bar could essentially be treated as a stiff bar under no tension fixed by a pivot at each end.

In order to test this idea, four fused silica bar/flexure suspensions supporting a 30kg test mass was modelled. The end flexures were fixed at 2mm in length, 5.5mm in width and $100\mu\text{m}$ in thickness, whilst the central section bar was 296mm long, 5.5mm wide and of varying thicknesses. The resulting 1st and 2nd violin mode frequencies of the suspension is given in Figure 4.12.

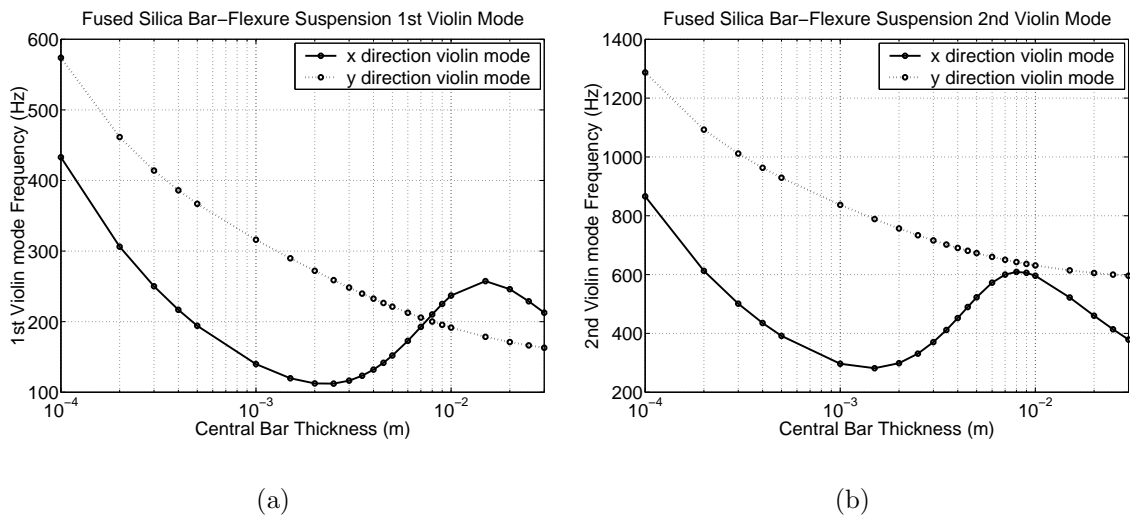


Fig. 4.12: Violin modes of a fused silica bar/flexure suspension versus central section bar thickness. a) 1st x direction and y direction violin mode. b) 2nd x direction and y direction violin mode.

The results show that an increase in central bar thickness from the initial value of $100\mu\text{m}$ results in a reduction in the value of the x direction violin mode frequency. This occurs since for small bar thicknesses, the dominant restoring force occurs from tension. Increasing the central bar thickness simply increases the linear mass density hence lowering the violin mode frequencies. As the bar thickness increases beyond 2mm, it can be seen that the elastic restoring force becomes dominant and hence

further increasing the bar thickness will result in larger violin mode frequencies despite the extra mass. However, the increase in violin mode frequency is limited by the fact that the suspension can no longer be treated as a bar supported by fixed pivots at each end for large central section stiffness. The end flexures begin to act like translational springs and therefore a further increase in the central bar mass will result again in a lowering in the value of frequency. The y direction violin mode decreases for all increases in bar thickness, since the increase in bending stiffness in the y direction is not enough to overcome the reduction in violin mode frequency from the increase in linear mass density.

As such, the hypothesis is not true, due mainly to the fact that the central section changes from acting like a bar between two fixed pivots, to a bar between two springs. It can be seen in Figure 4.12 that the peak violin mode frequency at a bar thickness of approximately 1cm is still much lower than that achieved with an equivalent ribbon suspension. Furthermore, a large suspension element mass results in a larger level of coupling between higher order suspension modes and the test mass. It would be necessary for the resulting violin modes to be significantly higher in frequency to compensate for this increase in coupling factor.

4.4 Thin walled Nb tubes Physics Letters A Paper

Thin walled Nb tubes for suspending test masses in interferometric gravitational wave detectors

B.H.Lee, L.Ju, D.G.Blair, Phys. Lett. A, 350 (2006) 319-323

School of Physics, The University of Western Australia, Crawley 6009, WA, Australia

In a previous letter, we have shown that the use of orthogonal ribbons could provide a better mirror suspension technique in interferometric gravitational wave antennas. One of the key improvements presented by the orthogonal ribbon is the reduction in the number of violin string modes in the direction of the laser. We have considered more elaborate geometries in recent simulations and obtained a suspension that provides further reduction in the number of violin string modes in the direction of the laser, as well as in the direction orthogonal to the laser. This thin walled niobium tube suspension exhibits a reduction in the number of violin modes to 5 in each direction up to a frequency of 5kHz. Furthermore the violin mode thermal noise peaks can be reduced in amplitude by 30dB.

4.4.1 Introduction

Thermal noise currently limits interferometric gravitational wave detectors from a few tens of Hz to several hundred Hz. For advanced detectors [107], the thermal noise must be reduced beyond the shot noise limit in order to achieve optimal sensitivity, i.e. a quantum limited interferometer. Consequently, developments towards improving the suspension thermal noise has been of great interest to researchers in this field. Advances in this area have resulted in the likelihood of suspensions being constructed from very low loss materials such as fused silica and silicon [79, 109, 78]. Fused silica fibres are already being used in the GEO600 detector [82]. It has also been suggested that wires or fibres be replaced by suspensions with rectangular profiles such as ribbons or flexures [80, 111] in order to minimise the thermal noise.

Suspension thermal noise is described by the fluctuation-dissipation theorem [5, 70] and contributes in two ways. In the frequency range from a few Hz to the fundamental violin string mode at several hundred Hz, suspension thermal noise is dominated by the

pendulum mode thermal noise. This noise rolls off at approximately $1/f^{2.5}$ between the pendulum mode frequency and the fundamental violin mode. In the frequency region above several hundred Hz, high Q-factor violin mode thermal noise peaks dominate and are likely to pierce the shot noise level. Therefore the interferometer sensitivity at frequencies close to the violin mode frequencies can be improved by reducing the number and amplitude of the thermal noise peaks.

As well as designing the suspensions to exhibit acceptable levels of thermal noise, issues surrounding the ability to operate the interferometer at its optimum needs to be considered. Achieving the design sensitivity involves periods of ‘noise hunting’, whereby other sources of noise that limits this sensitivity need to be found and either eliminated or reduced to an acceptable level. Control noise, which involves actuation and sensing noise is a very likely candidate. In 20 bit digital controllers, A to D and D to A converters are limited to a dynamic range of approximately 120dB. In order to reduce the contribution to control noise from bit quantisation effects, the maximum actuation force must be limited. Similarly, the dynamic range of the sensors need to be very small in order to achieve the required displacement sensitivities. High Q-factor violin modes may result in oscillations with amplitudes much higher than the sensing dynamic range. Non-linear effects can result from sensor saturation while low amplitude actuation forces make the oscillations difficult to damp. Currently, high amplitude violin mode oscillations can be tolerated with high Q notch filters embedded in the control system, however a notch filter is required for every troublesome violin mode. To avoid further increasing the complexity of the control system, reducing the violin mode Q-factors is desired. A method for damping the Q-factor of fused silica fibre violin modes by coating the fibre in specific areas with a lossy material has been reported by Gossler et. al. [105].

A method for reducing the Q-factor and the number of violin modes whilst having little effect on the pendulum mode thermal noise through the use of an orthogonal ribbon has been previously reported [115]. In this letter, we discuss a new suspension, the niobium tube. This suspension contains reduced violin mode Q-factors in the x direction as does the orthogonal ribbon, however violin mode Q-factors are also reduced in the y direction. In the following sections, we revise the advantages presented by the orthogonal ribbon and present the tube suspension design. The expected thermal noise associated with the suspension is discussed in the final section.

4.4.2 Suspension Modelling

To model the new suspension geometry, we use a program written by Mark Barton [102, 104]. The original code has been modified in order to include the contribution to suspension thermal noise from violin modes up to any desired frequency. Loss mechanisms involving intrinsic material loss and thermoelastic loss are considered in the suspension simulations. The same code is used for modelling the niobium tube suspension as was used for modelling the orthogonal ribbon.

4.4.3 Violin modes and the Orthogonal Ribbon

The orthogonal ribbon is illustrated in Fig. 4.13. It consists of thin flexures located at each end of a ribbon that has been rotated 90 degrees around its vertical axis. As presented in a previous letter [115], the orthogonal ribbon provides a solution to reduce the number of x direction violin modes, whilst having no significant effect on the suspension thermal noise below 40Hz. The term ‘x direction’ describes the motion in line with the laser beam, while the y direction is the direction orthogonal to the laser.

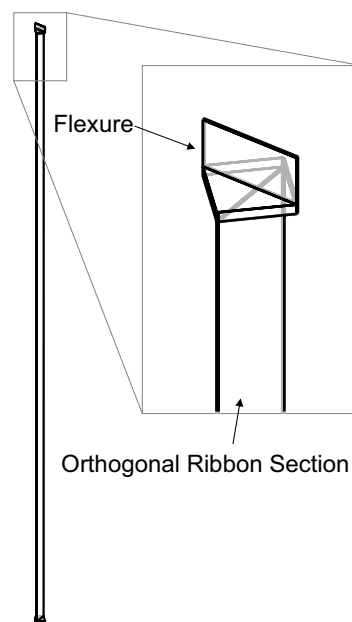


Fig. 4.13: Orthogonal ribbon suspension. This consists of a ribbon rotated 90 degrees around the vertical axis with a flexure at each end.

The stiffness of the orthogonal section in the critical direction, the x direction, results in a lower number of violin modes. This increase in stiffness is achieved without increasing the linear mass density of the suspension element. The higher stiffness reduces the level of dissipation dilution in the violin modes, and hence a reduction of more than 22dB in the violin mode amplitudes. A detailed explanation of dissipation dilution in pendulums is given in [57] while its effect on the orthogonal ribbon violin mode loss is mentioned in [115]. The lower Q-factor of the violin modes also result in a slight increase in thermal noise by a factor of approximately 2.4 between 60Hz to 200Hz.

4.4.4 Improving the Orthogonal Ribbon

The orthogonal ribbon improves the x direction violin modes, however causes an increase in the number and Q-factor of the y direction violin modes. The effect on the y direction violin modes occurs due to the decrease in stiffness and increase in dilution factor in this direction. It was reported by Lee et. al. that a solution could exist where the central section of the orthogonal ribbon is replaced by an alternate geometry that would result in improvements in both the x and y directions [115]. The simplest of such geometries is the solid bar.

In a bar-flexure suspension, thin end flexures result in only a small but tolerable degradation of pendulum mode Q-factor. The reason for using a bar as the central section as opposed to the orthogonal ribbon is to increase the stiffness in both x and y directions. In this scenario, the stiffness of the bar dominates over the tension as the restoring force for the violin mode oscillations. The violin mode frequencies can be related to the Young's modulus, E , area moment of inertia, I , and linear mass density of the bar, ρ as shown below:

$$f_n \propto \sqrt{\frac{EI}{\rho}}. \quad (4.9)$$

Considering x direction bending, linear mass density can be replaced with $\rho = xy\rho_v$ and area moment of inertia with $I = \frac{1}{12}yx^3$. Eq. (4.9) becomes:

$$f_n \propto x\sqrt{\frac{E}{12\rho_v}}. \quad (4.10)$$

Our simulations agree that the frequency of the violin modes can be increased by increasing the thickness (or x dimension) of the bar as is evident in Eq. 4.10. Although

the violin mode density and the violin mode Q-factors are reduced, the increase in linear mass density causes some problems. The frequency of the fundamental violin mode is difficult to increase since the bar acts as a mass resonating between the two end flexures. An increase in the bending stiffness is almost nullified by the effective increase in resonating mass. A simulation of the thermal noise from a suspension of this types illustrates a severe degradation in thermal noise below 100Hz. This occurs due to the low frequency, low Q-factor fundamental violin mode combined with the higher ratio of suspension mass to suspended mirror mass.

To improve on the orthogonal ribbon, a solution is required that increases the stiffness of the x and y bending directions without increasing the linear mass density. This can be achieved by replacing the orthogonal section with a thin walled hollow tube. In the following section, we discuss a niobium tube suspension.

4.4.5 Nb Tube suspension

The tube suspension consists of a hollow tube with thin flexures at each end. As is the case for the orthogonal ribbon, the flexures are designed to be longer than the characteristic bending length of the flexures:

$$\lambda = \sqrt{\frac{EI}{F_T}} \quad (4.11)$$

where E is the Young's modulus, I the area moment of inertia and F_T the tension loaded throughout the suspension element. The tube suspension provides an advantage over the orthogonal ribbon in that it exhibits an increase in stiffness in both the x and y directions. This results in a lower mode density, and lower Q-factors for all violin modes.

We have modelled the suspension of a 30kg test mass by four niobium tube suspensions. Niobium is chosen because it is a very low loss metal and allows the option of using electric discharge machining and diffusion bonding techniques for the manufacturing process. The tube suspensions consist of a 6mm wide, 2mm long, 100 μ m thick flexure at each end of a 7.6mm diameter tube with 25 μ m wall thickness. This is illustrated in Fig. 4.14.

The construction of the niobium tube suspension is simpler than for the orthogonal ribbon. Thin walled niobium tubes of this dimension can be specially made by

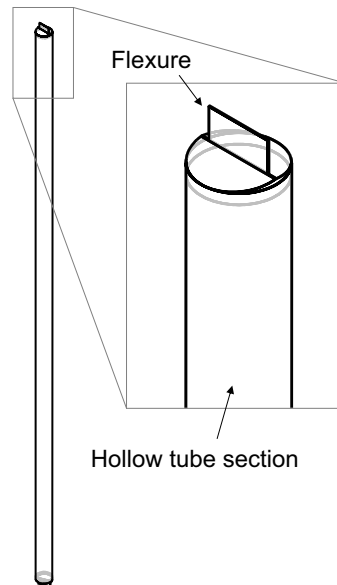


Fig. 4.14: Tube suspension. This consists of a thin hollow tube with a flexure at each end.

GoodFellow¹. By shrink-fitting the discs upon which the flexures are mounted within the tube, the pressure between the contact surfaces for the diffusion bonding process is automatically applied without the need for an external source of force. The use of a $25\mu\text{m}$ wall thickness is possible since the force is evenly distributed around the tube circumference. The advantage that a smaller wall thickness provides is a larger bending stiffness without an increase in linear mass density. This $25\mu\text{m}$ wall thickness and 24.5mm circumference compares to the $100\mu\text{m}$ thickness and 6mm width of the orthogonal ribbon. If $25\mu\text{m}$ thickness was to be used for the orthogonal ribbon, the difficulty would occur in maintaining an even loading across the orthogonal section. This would not be easy to achieve for an orthogonal ribbon 24mm wide.

In our analysis, the niobium tube suspension described above is compared to the following:

1. A niobium orthogonal ribbon of total length 300mm , $100\mu\text{m}$ thick and 6mm wide with end flexures 2mm long as described in [115].
2. A normal niobium ribbon of length 300mm , $100\mu\text{m}$ thick and 6mm wide.

In all three cases, it is assumed that four suspension elements will be used to support a 30kg test mass.

¹GoodFellow is a supplier of small quantities of various metals. See www.goodfellow.com.

Table 4.2 compares the x and y direction pendulum mode frequencies and dilution factors for the three suspensions. In all cases, the x direction pendulum mode frequency and dilution factors are similar, with the tube suspension and orthogonal ribbon dilution factors only 10% larger than for the orthogonal ribbon. This implies a 10% increase in pendulum mode Q-factor and thus only a small increase in pendulum mode thermal noise. There is an increase in y direction pendulum mode frequency and dilution factor for the tube suspension compared to the normal ribbon. However this increase in dilution factor by a factor of 1.7 is insignificant considering the expected y to x coupling of 0.1%.

Pendulum mode frequencies and dilution factors			
		f_{pend} (Hz)	$dilu_{pend}$
Normal Ribbon	x	0.91	2.8×10^{-3}
	y	1.12	0.27
Orthogonal Ribbon	x	0.91	3.1×10^{-3}
	y	0.92	3.0×10^{-3}
Tube Suspension	x	0.91	3.1×10^{-3}
	y	1.27	0.44

Tab. 4.2: A comparison of pendulum mode frequency and pendulum mode dilution factor for the normal ribbon suspension, orthogonal ribbon suspension and the tube suspension.

Tables 4.3 and 4.4 compare the first five violin mode frequencies and dilution factors for the three suspension types. Since there is little difference between the pendulum mode dilution factor for the three cases, the best solution will be the one which exhibits a low number of violin modes and low violin mode Q-factors. The violin mode frequencies of the tube suspension are relatively high and widely spaced in both x and y direction compared to just the y direction for the normal ribbon, and just the x direction for the orthogonal ribbon. Similarly, the dilution factors are relatively high in both x and y direction for the tube suspension, compared to just the y direction for the normal ribbon, and just the x direction for the orthogonal ribbon. These results emphasise the improvements expected in the tube suspension compared to the other suspension types.

The use of a tube as the central section introduces additional modes that may affect the suspension thermal noise spectrum. These ‘ring modes’ consist of symmetric vibrations around the central vertical axis. For a perfectly uniform tube, the symmetry of the ring mode oscillations ensure no coupling to test mass motion in the x or y

Suspension violin mode frequencies (Hz)						
		f_1	f_2	f_3	f_4	f_5
Normal Ribbon	x	196	393	590	787	984
	y	323	784	1436	2292	3356
Orthogonal Ribbon	x	224	579	1119	1854	2781
	y	199	398	598	797	997
Tube Suspension	x	257	763	1564	2639	3933
	y	418	1074	2038	3317	4917

Tab. 4.3: A comparison of violin mode frequencies for the normal ribbon suspension, orthogonal ribbon suspension and the tube suspension.

Suspension violin mode dilution factors						
		f_1	f_2	f_3	f_4	f_5
Normal Ribbon	x	5.9×10^{-3}	6.1×10^{-3}	6.5×10^{-3}	7.1×10^{-3}	7.8×10^{-3}
	y	0.56	0.71	0.82	0.87	0.90
Orthogonal Ribbon	x	0.23	0.54	0.72	0.82	0.86
	y	6.0×10^{-3}	6.2×10^{-3}	6.6×10^{-3}	7.2×10^{-3}	7.8×10^{-3}
Tube Suspension	x	0.41	0.73	0.85	0.88	0.89
	y	0.74	0.85	0.91	0.94	0.96

Tab. 4.4: A comparison of violin mode frequency dilution factors for the normal ribbon suspension, orthogonal ribbon suspension and the tube suspension.

direction. However for the manufacture of the niobium tubes described in this section, the tube wall thickness may vary by $\pm 15\%$. Consequently, asymmetries in the tube wall thicknesses could exist, resulting in ring mode coupling. We have used finite element analysis to simulate the ring modes and find the fundamental ring mode occurs at 1731Hz. Detailed analysis of these modes is complicated and will not be discussed in this letter, however ring mode coupling to x direction test mass motion is expected to be at most 25% lower than the coupling of the x direction violin modes at similar frequencies. Thus ring modes are not likely to induce larger amplitude oscillations than the x direction violin modes and will not appear below 1731Hz.

4.4.6 Thermal noise spectrums

A simulation of the expected suspension thermal noise is shown in Fig. 4.15 and Fig. 4.16. The normal ribbon, orthogonal ribbon and tube suspension refer to the same models described in the previous section. Fig. 4.15 compares the expected suspension thermal noise between the tube suspension and the normal ribbon. In the

frequency band up to 5kHz, the number of x direction violin modes has been reduced from 24 to 5, while the number of y direction violin modes has been reduced from 6 to 5. The peak thermal noise amplitude of the fundamental violin mode has been reduced from $7.0 \times 10^{-15} \text{m}/\sqrt{\text{Hz}}$ to $2.1 \times 10^{-16} \text{m}/\sqrt{\text{Hz}}$. This is an amplitude reduction of 30dB. As is also evident in the orthogonal ribbon spectrum, there is a small increase in thermal noise above 60Hz. This is caused by the lower Q-factor of the fundamental violin mode contributing more to the thermal noise, despite the fact that the violin mode frequency is higher. At 130Hz, the normal ribbon suspension exhibits a minimum thermal noise amplitude of approximately $5.0 \times 10^{-21} \text{m}/\sqrt{\text{Hz}}$ compared to the tube suspension minimum of $1.4 \times 10^{-20} \text{m}/\sqrt{\text{Hz}}$ at 110Hz, an increase by a factor of 2.8.

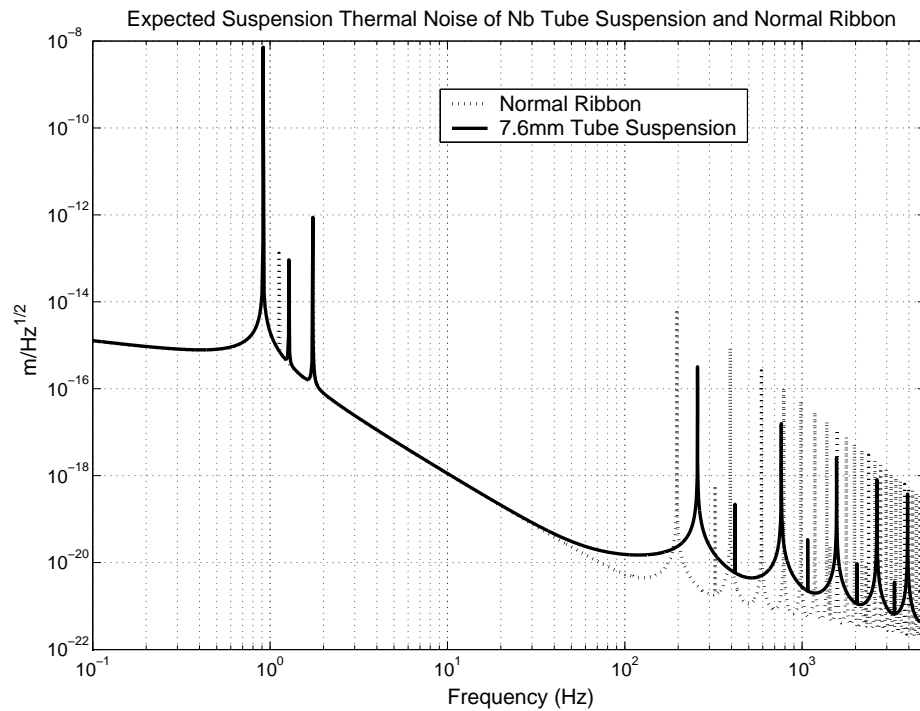


Fig. 4.15: A comparison between expected suspension thermal noise for a $100\mu\text{m}$ thick, 6mm wide 300mm long normal niobium ribbon with the niobium tube suspension.

A comparison of the expected thermal noise between the orthogonal ribbon and the tube suspension is shown in Fig. 4.16. Since the dilution factor for the fundamental x direction violin mode is higher by a factor of 1.7 for the niobium tube suspension (as shown in table 4.4), the Q-factor for this mode is reduced. However, there is little difference between the thermal noise amplitude of the two suspensions between 60Hz and 200Hz because the reduction in Q is compensated by an increase in violin mode frequency. The increase in violin mode frequencies and reduction in violin mode

density up to 5kHz can be seen on the plot, particularly for the y direction where the fundamental violin mode frequency has increased from 199Hz to 418Hz and the number of modes up to 5kHz has been reduced from 20 to 5. Both plots suggest that the tube suspension is a better alternative to the normal ribbon and the orthogonal ribbon suspensions.

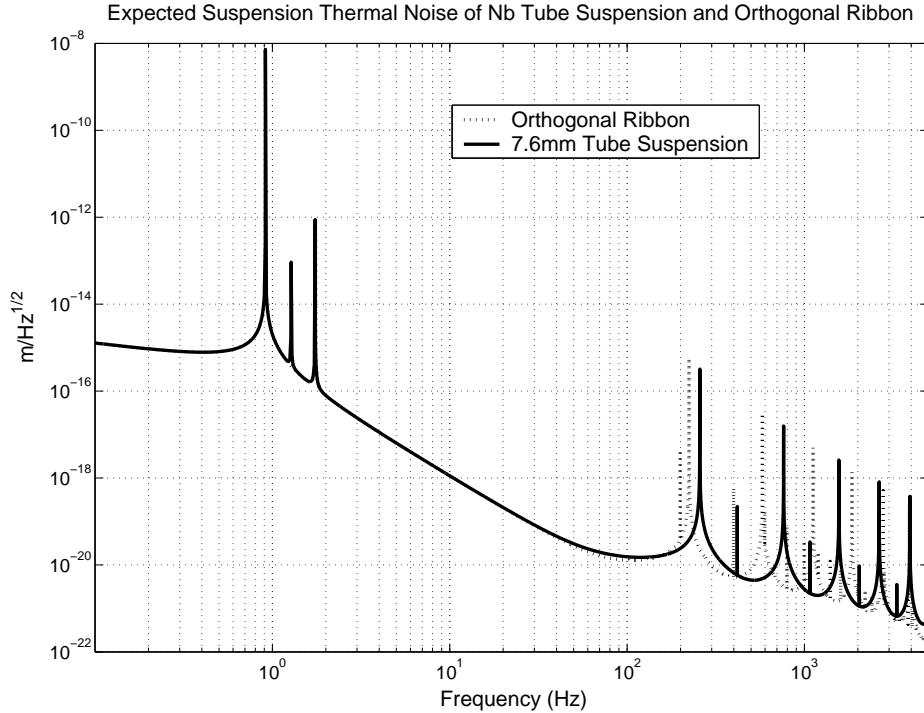


Fig. 4.16: A comparison between expected suspension thermal noise for a $100\mu\text{m}$ wide, 6mm thick 300mm long orthogonal ribbon with the niobium tube suspension.

4.4.7 Conclusion

Through our computer simulations, we have compared the suspension thermal noise performance of three niobium suspensions, the normal ribbon, the orthogonal ribbon and the tube suspension. The orthogonal ribbon has been presented previously as an improvement on a normal ribbon suspension, whereby the number and Q-factor of the violin modes in the x direction is reduced. This was shown to have only a small effect on the thermal noise above 60Hz, an increase in amplitude of no more than 2.4. The niobium tube suspension presented in this letter exhibits a slightly larger reduction in violin mode Q-factor and mode density for the x direction, as well as a significant improvement for these values in the y direction. Compared to the orthogonal

ribbon, the tube suspension contains higher x direction and y direction fundamental violin mode frequencies (257Hz from 224Hz and 418Hz from 199Hz respectively), higher fundamental violin mode dilution factors (0.41 from 0.23 and 0.74 from 6.0×10^{-3}) and hence lower Q-factors and a lower total number of violin modes up to 5kHz (5 from 6 and 5 from 20).

The tube suspension provides a better alternative to the normal ribbon than the orthogonal ribbon for reducing the possibility of saturation problems and servo instabilities caused by high Q violin mode oscillations. Although the method of constructing the tube suspension from niobium can be achieved, it is likely to require advances in bonding techniques before suspensions with this geometry can be made from very low loss materials such as fused silica or silicon.

4.4.8 Acknowledgments

This work is supported by the Australian Research Council and is part of the Australian Consortium for Interferometric Gravitational Astronomy (ACIGA). We also acknowledge the help from Mark Barton with regards to the suspension modelling program.

4.4.9 Postscript

The author acknowledges the fact that in order to fully benefit from the advantages that a thin walled tube suspension may provide, these suspensions will need to be constructed from very low loss materials such as fused silica. However, the use of fused silica tube suspensions is currently limited by practical issues in constructing the required geometry. It is likely that the end flexures can be pulled from silica rods in a similar fashion that a silica ribbon is currently created. Small mounting discs would need to be left attached to each end of the flexure for bonding to both the central tube and attachment to the test mass or intermediate mass (or test mass support structure). The greatest difficulty however may be the process required to pull the fused silica hollow tubes with wall thickness in the order of $100\mu\text{m}$. With the on going improvement in silica welding, pulling and handling techniques, it does not seem impossible that such suspensions could be constructed for advanced detectors. Therefore the results of fused silica tube suspensions (shown below) have also been studied and show similar improvements as discussed for the niobium case.

Four fused silica tube suspensions supporting a 30kg test mass is modelled and the resultant thermal noise compared to that of a typical 5.5mm wide, $100\mu\text{m}$ thick fused silica ribbon suspension. This is illustrated in Figure 4.17. The end flexures of the tube suspension are 5.5mm wide, $100\mu\text{m}$ thick and 2mm long, while the central tube is 7mm in diameter and $25\mu\text{m}$ thick. The total length of both suspensions is 30cm.

Again, a vast reduction in the number of violin modes up to 5kHz can be observed. The number of x direction violin modes is reduced from 12 to 4 while the number of y direction violin modes is reduced from 4 to 3 when compared to a typical ribbon suspension. The amplitude of the violin modes is also smaller, due partly to the increase in dilution factor for the tube suspension, and partly to the reduction in loss value ϕ for the central section resulting from the increase in surface loss. The cost however is a small increase in thermal noise above about 100Hz. Despite this increase, the suspension thermal noise is still expected to be below the quantum noise predicted in an advanced detector. Thus the result is essentially a reduction in number and amplitude of violin spikes piercing the detector shot noise limit at high frequencies.

When compared to the fused silica $100\mu\text{m}$ orthogonal ribbon, there is only a small improvement in the number of x direction violin modes up to 5kHz. The number of

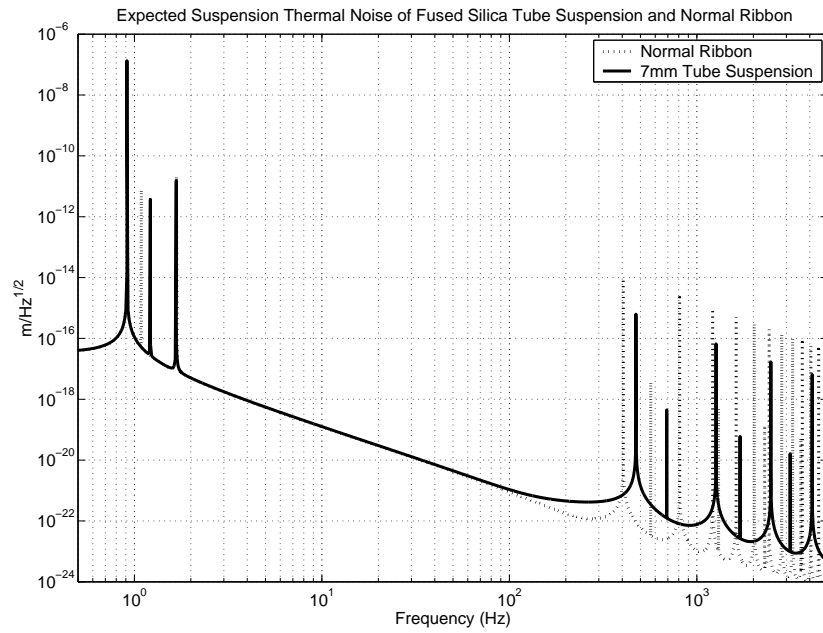


Fig. 4.17: A comparison between expected suspension thermal noise for a $100\mu\text{m}$ thick, 5.5mm wide 300mm long normal fused silica ribbon with a 7mm fused silica tube suspension.

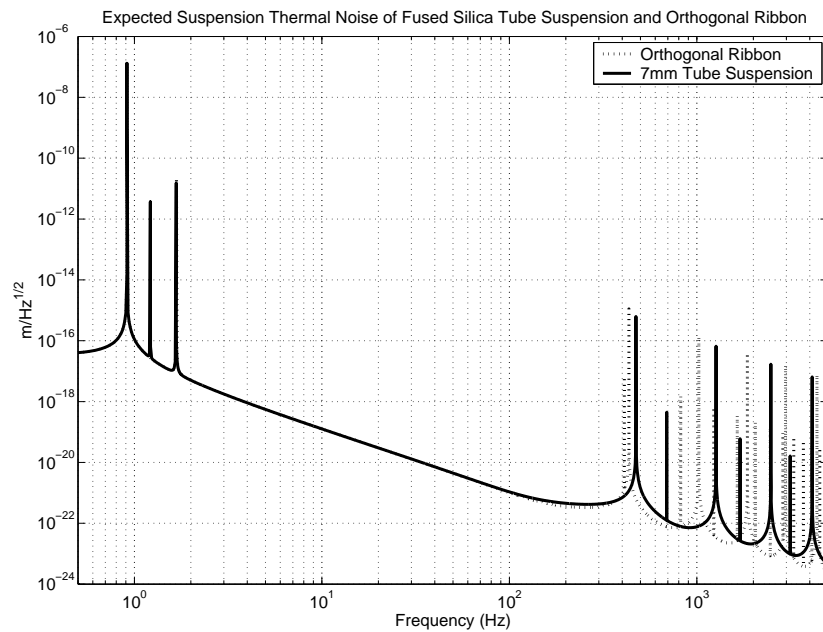


Fig. 4.18: A comparison between expected suspension thermal noise for a $100\mu\text{m}$ thick, 5.5mm wide 300mm long normal fused silica orthogonal ribbon with a 7mm fused silica tube suspension.

modes is reduced from 5 to 4. The amplitude of the tube suspension violin modes are only very slightly smaller. There is significant improvement in the y direction violin modes however, with the number of violin modes reducing from 11 to 3 and

a considerable reduction in violin mode amplitude. This comparison is illustrated in Figure 4.18.

4.5 Removable Modular Suspension Elements for AIGO

The Fabry Perot mirrors to be suspended at AIGO are 4.2kg sapphire optics, with a diameter of 150mm and thickness of 60mm. One of the goals of the facility is to test the performance and feasibility of the orthogonal ribbon and tube suspension geometries discussed earlier. To achieve this, the use of removable modular suspensions is being employed. Such suspensions can be removed and exchanged with suspensions of different geometry without the need to change the optic itself. Another advantage is that this method avoids the need for permanent bonding of suspensions to the optic. Problems associated with bonding, in particular the stresses resulting from the different thermal expansion coefficients of bonded objects, are avoided.

To avoid the introduction of thermal noise due to the slip-stick phenomena at the point where the suspension element makes contact with the optic, it is important that well defined high pressure contact points are created. To achieve this, a ‘pin-in-hole’ interface has been designed, where pins connected to the suspension element slot into small holes machined into the optic. It is solely the gravitational force acting on the test mass that induces the pressure on the contact points.

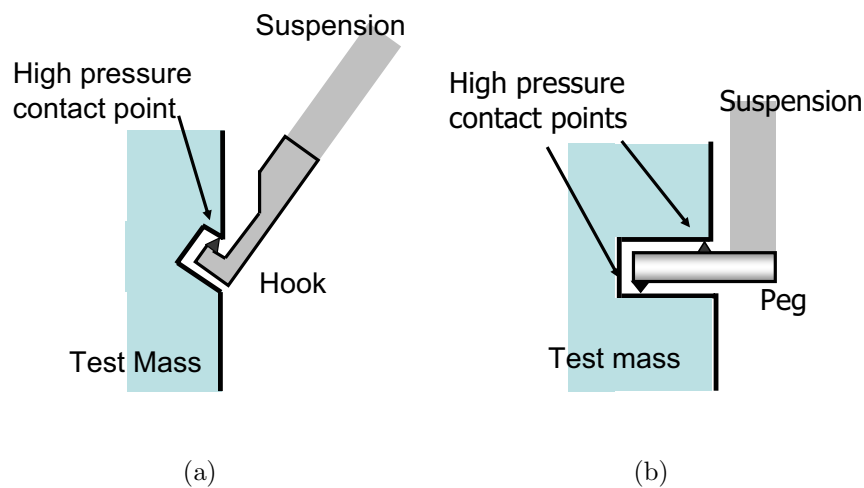


Fig. 4.19: a) Removable modular hook suspension. b) Removable modular peg suspension.

Ideally, only one high pressure contact point per suspension element would be desired. This method of suspension is a little difficult to engineer, however a possible solution is through the use of a hook suspension. This is illustrated in Figure 4.19(a). The need for the suspension elements to be angled in the yz plane of the suspension

is a deterrent. This means that the suspensions are stressed to a value greater than that required from vertical suspensions. The need for greater tensile strength when using the hook suspensions will more than likely result in worse violin mode performance. A better solution is the use of pegs connected to each end of the suspension, resulting in two high pressure contact points with the test mass. This is illustrated in Figure 4.19(b). In order to connect the ribbon to the peg, either a clamping mechanism with a well defined high pressure contact ‘tooth’ be constructed as part of the peg, or a permanent bond be established between the peg and the ribbon. The same method is used to mount the top of the suspension elements to the preceding isolation stage.

One concern of this method of suspension is the increase in test mass thermal noise contributed by the loss at the surface of the equatorial holes. Four holes of depth 6mm and diameter 3mm are required in the test mass for this system. This is illustrated in Figure 4.20. This issue has been studied in depth by Gras et. al. [116] and it has been

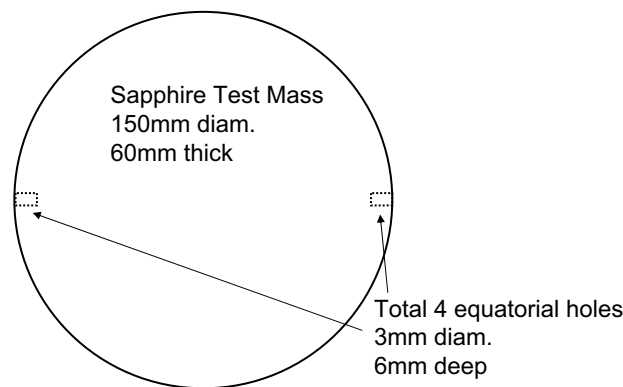


Fig. 4.20: 3mm diameter, 6mm deep equatorial holes required in the test mass to support the pin-in-hole interface.

found that for the AIGO beam radius of 20mm, equatorial losses, ϕ_{hole} , can be as high as 4×10^{-3} without the test mass thermal noise increasing by more than 10%. We are confident that the losses at the surface of the equatorial holes can be kept below this value.

At AIGO, niobium modular suspensions will be tested first, since the facilities to machine and bond (through diffusion bonding) this metal are readily available. Although the loss of niobium is not as good as fused silica or silicon, the results of these suspensions will allow the feasibility and reliability of the technique to be tested. Furthermore, the accuracy of the triple section suspension modelling program can be

experimentally verified. If in the future the need for low loss suspensions is required, the modular nature of the suspension elements allows them to be easily replaced.

Design of the niobium pins essentially involves determining the correct contact point surface area, such that the contact pressure approaches the yield strength of niobium. Assuming that the pin itself does not significantly deform when placed under load, it is trivial to determine the force applied by each contact point. The force diagram for the pin when supporting the 4.2kg test mass is illustrated in Figure 4.21. Applying

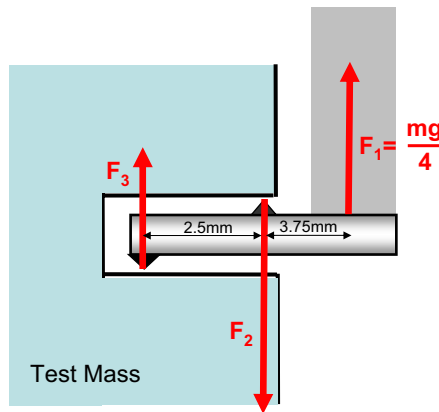


Fig. 4.21: Force diagram for pin-in-hole interface supporting the 4.2kg sapphire test mass.

the requirements of static equilibrium, $\sum F = 0$ and $\sum M = 0$, and the yield strength of niobium, 105Mpa, it is possible to calculate the inner and out contact areas as 1.3×10^{-7} and 2.3×10^{-7} respectively. This is equivalent to an area approximately 0.4mm by 0.4mm, which can easily be machined.

Structural modelling of the AIGO suspension pin was used to fine tune the design. Using an ANSYS finite element model the stress and deformation exhibited by the pin when placed under load could be approximated. A contour plot of the deformation of the loaded pin is shown in Figure 4.22. It can be seen that the maximum deformation, which occurs at the end of the pin is $36\mu\text{m}$. Similarly, the stress is indicated in a log contour plot in Figures 4.23. It can be seen that the maximum stress occurs at the two contact points, where the value of stress approaches the yield strength of niobium. These pins are designed to fit into 3mm diameter holes located in the test mass and in a location on the preceding stage designed to support the final stage suspension. The larger diameter section of the pin, which is 4mm diameter by 4mm length is the section to which the suspension element is to be bonded to the pins. In order to make this connection, a small slit in the vertical direction will be cut into this section, through

which a niobium flexure or ribbon will be inserted and bonded using diffusive bonding techniques.

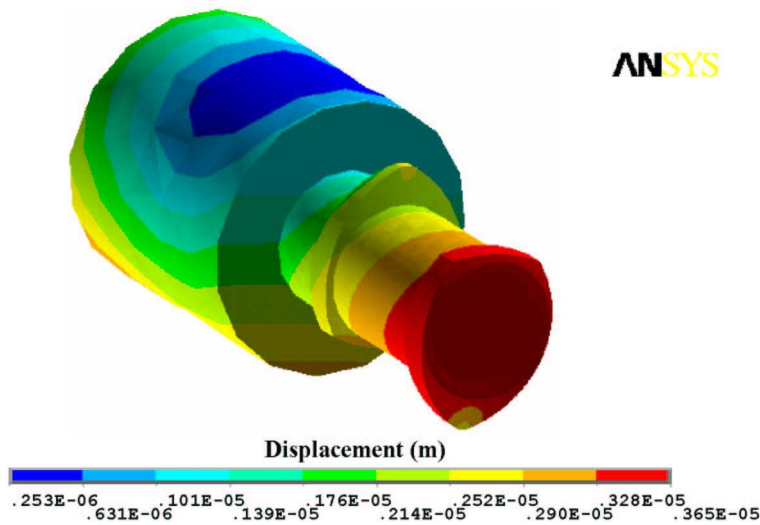


Fig. 4.22: A contour plot of the vector displacement magnitude of a Nb contact pin used for an AIGO removable modular suspension element.

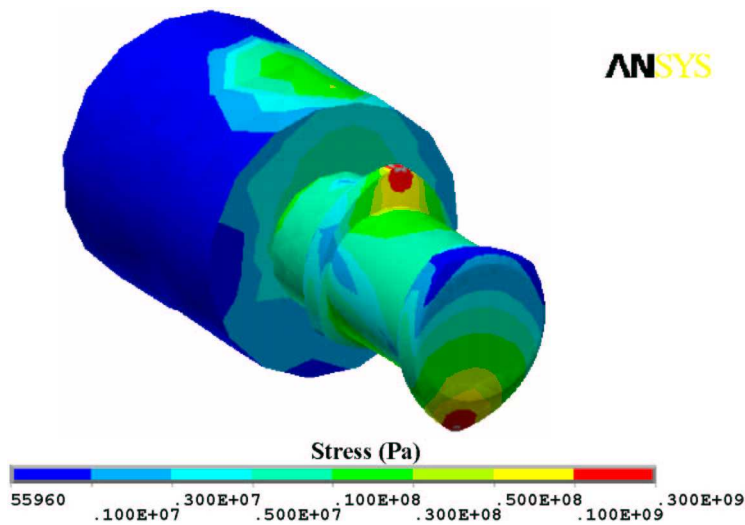


Fig. 4.23: A contour plot of the total stress intensity of a Nb contact pin used for an AIGO removable modular suspension element.

CHAPTER 5

ISOLATION SYSTEM CONTROL

5.1 Introduction

The high power test facility located at AIGO in Western Australia will incorporate the use of compact advanced vibration isolation systems that have been developed at the University of Western Australia (UWA). Although the use of vibration isolation systems for suspending mirrors in interferometric gravitational wave detectors is not a new idea and in fact is currently being used in every detector in varying forms, the system being finalised at UWA comprises of several advantages and unique features. Each isolation system (designed to support an end mirror, input mirror or beam splitter) is more compact compared to the VIRGO superattenuator [46], with total height being 2.5m compared to 7m. This provides the advantage of being cheaper to manufacture, as well as requiring smaller vacuum tanks to house the isolations systems. A primarily passive vibration isolation system is also a cheaper and generally less complex alternative compared to the active system proposed for Advanced LIGO [52]. The use of newly developed ideas such as self damped pendulums [117], double pre-isolation [118] and euler springs for improved vertical isolation performance [119, 49] are included in the AIGO vibration isolation systems. These improvements allow the use of a more compact system without a significant degradation in performance.

The use of an advanced vibration isolation system to support optics allows the detection window of an interferometric gravitational wave detector to be extended to frequencies approaching several Hz. When optimally tuned, the AIGO vibration isolation system is expected to be completely compatible with proposed second generation interferometric gravitational wave detectors. Although the required performance of the isolation system can be easily achieved above 10Hz, it is inevitable in passive isolation

systems that there be some amplification of seismic noise at lower frequencies. The highest displacement sensitivity is required in the frequency range from a few Hz to several kHz. Such high sensitivities, (close to $10^{-20}\text{m}/\sqrt{\text{Hz}}$ at 100Hz), can only be achieved within a very small displacement bandwidth and hence demand very low levels of RMS mirror motion. We discuss how this can be accomplished with sophisticated methods of active control.

5.2 AIGO Isolation system requirements

The vibration isolation systems for each optic to be installed in the high power test facility at AIGO are designed to be compatible with second generation interferometric gravitational wave detectors. The most stringent requirements are those related to the mirrors that form the multi km scale fabry perot cavities.

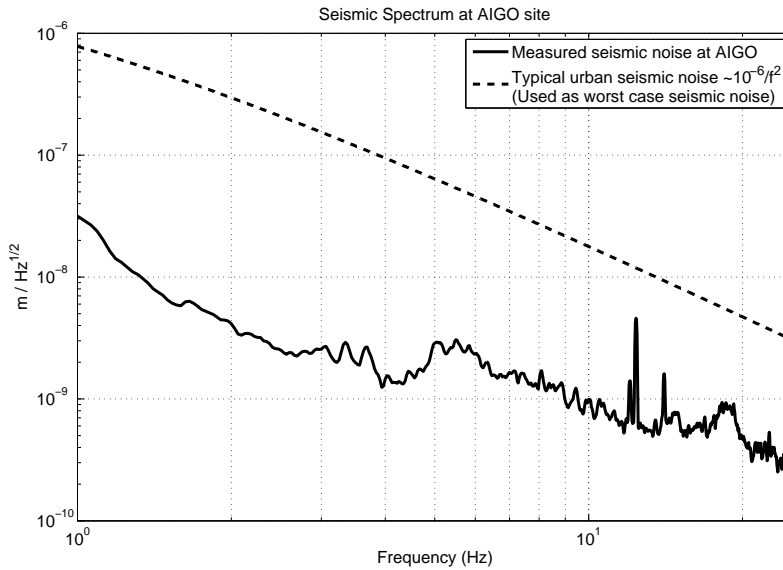


Fig. 5.1: Seismic noise measured at the AIGO site in September 2000.

Typically, urban seismic noise rolls off at 40dB/decade from approximately $10^{-6}\text{m}/\sqrt{\text{Hz}}$ at 1Hz [101]. Figure 5.1 illustrates this noise spectrum and compares it to seismic noise measured at the AIGO site during September 2000. It can be seen that the seismic noise obtained from the AIGO site is between one and two orders of magnitude lower than typical urban seismic noise. Similar or better seismic noise measurements have been obtained at other detector sites [120, 83]. In the calculations that follow in this chapter, typical urban seismic noise is used to model the AIGO scenario and will be

here after be referred to as worst case seismic noise. This allows us a safety margin of at least a factor of 10 between 2 and 20Hz. It is obvious that the level of seismic noise, even at a relatively quiet location such as AIGO, must be attenuated by many orders of magnitude. This requirement, including the restrictions that must govern any active control loops are discussed in the following with respect to two frequency bands; within the detection band and below the detection band.

5.2.1 Within the detection band

The detection band of second generation interferometric gravitational wave detectors lies between several Hz and several kHz. This is illustrated in Figure 5.2 by the expected noise budget of Advanced LIGO [67]. Attenuating the seismic noise below the sensitivity level requires that the differential mirror displacement be reduced below $10^{-19}\text{m}/\sqrt{\text{Hz}}$ at 10Hz [51]. This is approximately 200dB attenuation and has been achieved by many researchers.

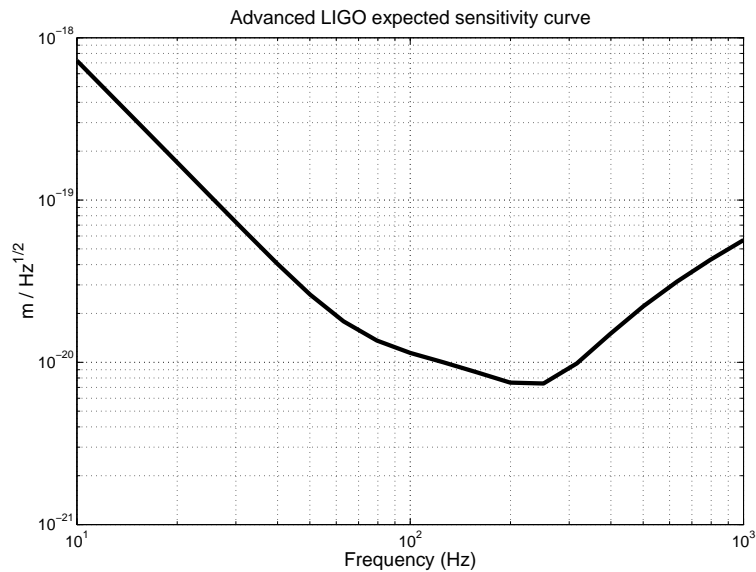


Fig. 5.2: Principal noise sources for Advanced LIGO as estimated in August, 2004. Sapphire test masses assumed. Response optimized for NS-NS inspiral.

The other requirement stems from the need for control loops to keep the interferometer locked on a dark fringe. Limited dynamic range of actuators and sensors, where currently the dynamic range of these components are at best 200dB, may result in a reduction of interferometer sensitivity. In fact in all first generation detectors that have recently begun science runs or commissioning phases, there has been a need to

reduce ‘control noise’ in order for the current sensitivity to approach the design sensitivity. Actuation noise usually results from electronic noise causing small random fluctuations in actuation forces, accelerating the suspended mirrors in a manner that is indistinguishable from a passing gravitational wave. Sensor noise results in signals that are introduced into the control loop and hence incorrectly compensated for by applying forces to the mirrors via the actuators. As for the seismic noise, control noise must be kept below the design sensitivity level of the detector. In fact the efficiency at which seismic noise can be attenuated by passive means for frequencies above 10Hz, and the steep roll off that can be achieved by cascading multiple suspensions means that control noise is almost certainly going to be more significant than seismic noise in this frequency region. However below the detection band seismic noise is dominant and active means of reducing this noise is necessary.

5.2.2 Below the detection band

Prior to the interferometer being locked, the RMS residual motion of the suspended optics should be kept as low as possible. Reduction of residual velocities of the mirrors reduces the force required to initially lock the cavity. At AIGO, we intend to obtain a cavity lock using electrostatic actuators capable of applying 1mN of force. Given a laser wavelength of $\lambda = 10^{-6}\text{m}$ and a finesse $F = 3000$, the RMS residual velocity must be kept below $5 \times 10^{-7}\text{ms}^{-1}$.

Once cavity lock has been acquired, the total differential RMS motion of the mirrors that make the large scale fabry perot cavities must be kept below 10^{-14}m . Such accurate low frequency positioning of the mirrors is necessary to maintain the extremely sensitive global control signals. Since the vibration isolation system attenuates seismic noise very steeply above approximately 1Hz, the majority of the contribution toward the total differential RMS motion of the mirrors occurs in this frequency regime below the detection band. It is for this reason that feedback control forces are required, resulting in the presence of control noise in the detection band.

Large amplitude low frequency motion, in the order of millimeters, must also be compensated. This motion results from the thermal expansion of the earth from daily temperature changes, and hence has a time constant in the order of hours. Such low

frequency motion bypasses passive isolation techniques. As a consequence, means of actively compensating this motion must be incorporated.

5.2.3 Requirement Summary

Listed below is a summary of the requirements for the vibration isolation system to be used at AIGO.

1. Approximately 200dB of seismic isolation is required within the detection band. More specifically, seismic noise must be kept below $10^{-20}\text{m}/\sqrt{\text{Hz}}$ at 10Hz, and roll off steeper than 20dB per decade
2. Control noise must be kept below the anticipated detector sensitivity level for all frequencies within the detection band.
3. Prior to lock acquisition, the total RMS differential residual velocity should be kept below $5 \times 10^{-7}\text{ms}^{-1}$.
4. Once locked, the total RMS differential residual motion of the fabry perot mirrors must not exceed 10^{-14}m .
5. Active techniques capable of compensating for low frequency millimetre level motions, due to daily temperature fluctuations, needs to be incorporated.

As well as these criteria, all control loops need to be stable and relatively robust in order to prevent unwanted mechanical oscillations causing interferometer downtime as well as damage to delicate components. In the following sections, we present the best method of applying control loops to the AIGO suspension in order to achieve the goals presented above.

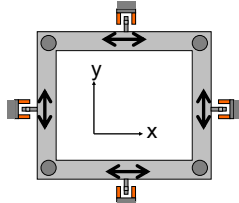
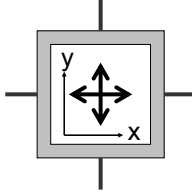
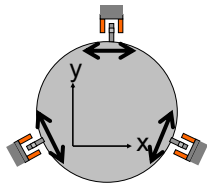
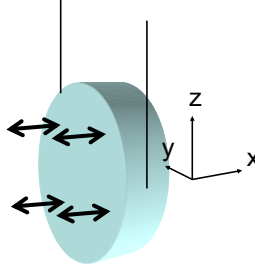
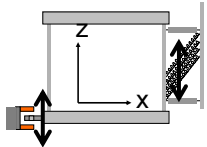
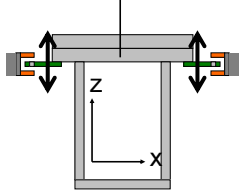
5.3 Local Control Systems

The difference between local and global control systems in an interferometric gravitational wave detector lies primarily in the feedback error signal. Global error signals, as the name suggests, links the status of multiple parts of the interferometer. These signals are used to keep the interferometer working at its peak sensitivity and involve information such as relative differential mirror positions and alignments. Local control

signals usually provide information about the status of a single suspended optic independent of the other optics in the interferometer. Feeding back local control signals to the mirror suspensions allows the positioning of the mirrors in such a manner to minimise the difficulty of obtaining a global interferometer lock.

There are several aspects of the AIGO isolation system that are unique, and hence will be briefly explained. Firstly the Roberts Linkage stage forms a second pre-isolator after the inverse pendulum. This stage essentially consists of a frame suspended in such a manner that a particular point on that frame traverses a very shallow arc in both horizontal directions. The shallow arc traversed by this point is a result of the geometrical constraints of the system, and by attaching the isolation chain to this point, such a system acts as an effective pre-isolator. The Roberts Linkage is discussed in detail in [121]. Secondly, the LaCoste stage is a vertical pre-isolator. This system makes use of similar concepts as an inverse pendulum rotated on its side, such that motion is constrained in the vertical direction. Springs are arranged to apply the negative spring force that would normally be applied by gravity in a inverse pendulum. This stage is discussed in detail in [101]. Finally, the suspension chain that links the pre-isolators to the control mass suspension consists of three self damped pendulums. The term ‘self damped’ is used because the pendulums exhibit damped Q factors without any external coupling. This is achieved by coupling the pendulum motion with the rocking motion of the pendulum masses through viscous magnetic damping. Further detail can be found in [117].

The local control system used for the AIGO vibration isolation system consists of six points for actuation and sensing. Four of these points can be used for the horizontal local control loops, as illustrated in Figure 5.3, while two points can be used for the vertical control loops, as illustrated in Figure 5.4. The distribution of actuator/sensor pairs throughout the isolation system is given in Table 5.1. The IP loop, CM loop and LaCoste loop use magnet/coil actuation and shadow sensors for sensing. IP stands for inverse pendulum while CM stands for control mass, reflecting the mechanical stage to which the control loops are directly linked. Each magnet/coil actuator consists of a Maxwell pair of coils in order to provide an almost position independent force. The coils are attached to the isolator support frame, (i.e. the mechanical ground) and act on a magnet which is attached to the moving part. A position independent force transducer is important in order not to inject seismic noise into seismically isolated

Location	No. of Actuators	Distribution	Degrees of Freedom
Inverse Pendulum -Horizontal	4		3: x-direction y-direction yaw
Roberts Linkage -Horizontal	2		2: x-direction y-direction
Control Mass -Horizontal	3		3: x-direction y-direction yaw
Test Mass -Horizontal	4		3: x-direction yaw pitch
LaCoste Stage -Vertical	2		1: z-direction
Control Mass -Vertical	2		2: z-direction pitch

Tab. 5.1: The number of actuators and actuation degrees of freedom associated with the AIGO vibration isolation system. The plane of the interferometer coincides with the xy plane of the axes indicated in the diagrams. The x direction is the direction of the laser field relative to each isolator. Yaw and pitch refer to the standard directions of rotation about the z and y axes respectively.

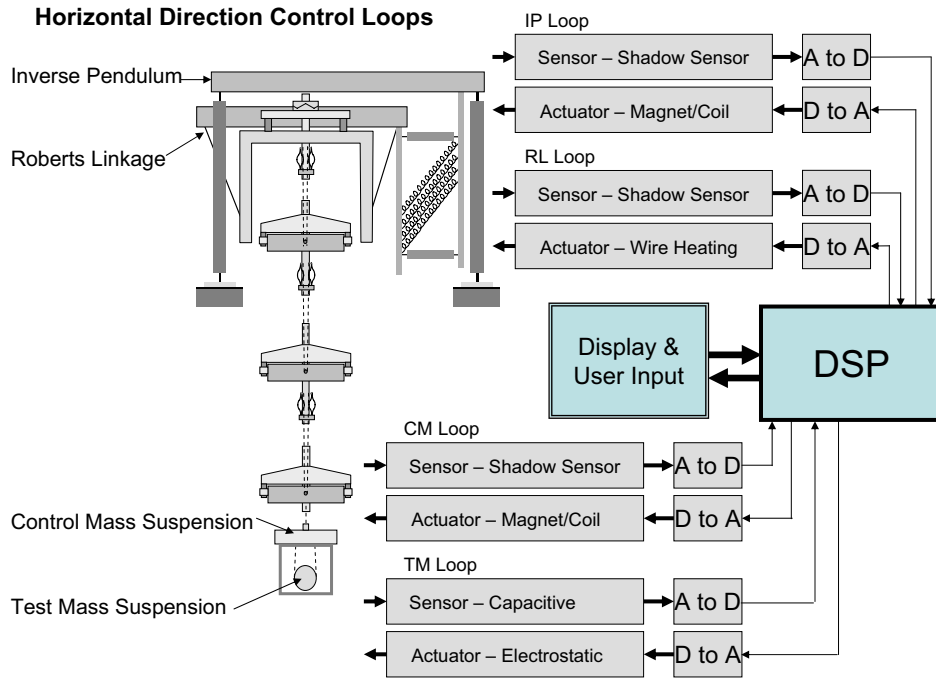


Fig. 5.3: There are four horizontal direction control loops accessible in the AIGO vibration isolation system.

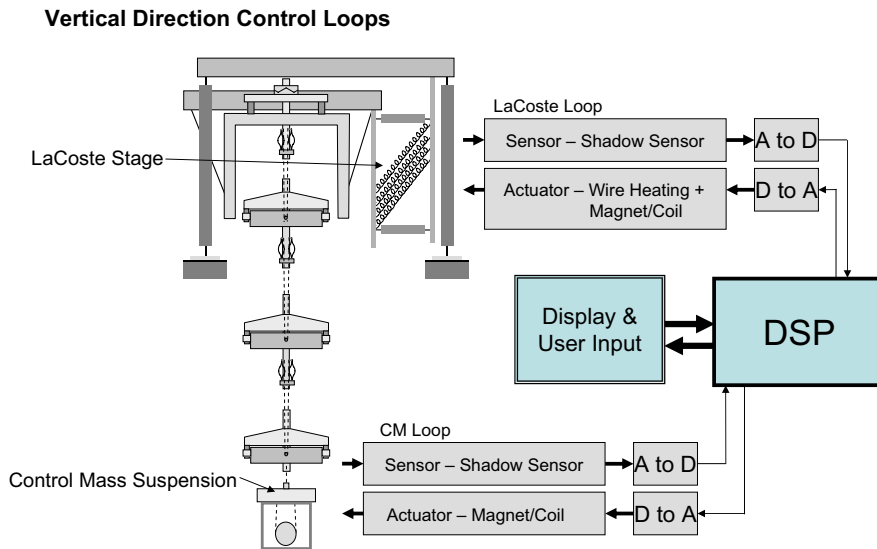


Fig. 5.4: There are two vertical direction control loops accessible in the AIGO vibration isolation system.

parts. Each coil is able to apply forces in one dimension in line with the coil axis. The shadow sensors are typical split photodiode sensors, where a shadow piece attached to the moving part, (in this case the magnet) partially blocks the light emitted from a nearby LED, thereby changing the currents generated by the split photodiodes. The

RL loop makes use of shadow sensors for sensing, and heating of the Roberts Linkage wires for actuation. Passing an electrical current through the RL wires causes them to heat up. This process slightly changes the wire lengths, allowing a low frequency change in the equilibrium position of the RL stage. The TM loop makes use of non-contact electrostatic actuation and capacitive sensing proposed by [122] and further researched by [123, 124]. Electrostatic actuators have been implemented at GEO600 [125]. The actuator and sensor in this loop is not referenced to ground, but the control mass stage. Electrostatic forces act on the control mass from the nearby electrodes. Test mass motion relative to these electrodes changes their capacitance, which is used to sense the relative test mass displacement.

Using these actuators and sensors, the local control system must achieve the following:

1. Allow for remote control of DC mirror positioning and alignment.
2. Reduction of low frequency torsion mode of the suspension chain.
3. Minimisation of the RMS differential mirror velocity.

5.3.1 Remote Mirror Positioning and Alignment

The ultra high vacuum system that houses the suspended interferometer of a gravitational wave detector may take days to pump down to the required vacuum levels of 10^{-7} torr [67]. For this reason, it is highly undesirable if the isolators require manual adjustments after the initial vacuum pump-down. It is very unlikely that once the vibration isolators are balanced, tuned and isolated in vacuum tanks, the suspended mirror will be aligned and positioned as desired. Thus there is the need for a remote mirror positioning and alignment system.

A digital local control system is ideal for remote positioning and alignment. At AIGO, a digital system will be used in conjunction with the actuators and sensors to form the local control loops. Each DSP (digital signal processor) will be linked to a remote processor where user inputs can adjust loop gain values and set points, thus allowing the remote control of DC mirror positioning and alignment. The state of the suspended mirror obtained from the local sensor signals will also be observable remotely via the communication link between the remote processor and control DSPs.

5.3.2 Low Frequency Torsion Mode

Optical cavities of lengths up to 4km in advanced interferometric detectors mean that small angular displacements of the end mirrors result in large changes of laser spot position on the test mass surface. The angular requirement for Advanced LIGO is 10^{-9} rad rms [67] during interferometer operation. This stringent requirement is achieved through the auto alignment system which becomes operational once the cavity is locked. The requirement of the local control system is therefore to reduce the angular motions of the mirrors enough to obtain this locked condition. For a spot size of 6cm, spot position variations of 10% can be tolerated. Thus for a cavity length of 4km, an angular amplitude of less than 1.5μ rad rms is needed.

The AIGO vibration isolation system consists essentially of two pre-isolators followed by a chain of suspended pendulums of total length approximately 2.5m. The relatively large pendulum masses (40kg and dimensions 40cm width by 40cm length by 10cm height) coupled with highly stressed suspension wires results in a low frequency torsion mode with a significant amplitude. A measurement of the rotation period gives a torsion frequency of 0.016Hz. In Sections 5.5, the effect of control mass actuation noise on the interferometer sensitivity is discussed. It is found that with the current AIGO coil drivers, the maximum force range that can be employed by the control mass actuators is 100μ N. A force range beyond this level results in intolerable levels of force noise. Using this force range, the maximum level of yaw compensation can be estimated.

A block diagram of the $\theta_{yaw,CM}$ compensation method is shown in Figure 5.5(b). Here G represents the yaw transfer function of the entire suspension chain to the control mass and H represents the feedback path transfer function. Figure 5.5(a) shows that the block diagram representation of the yaw feedback system does not exactly illustrate the compensation process. In reality, a compensation force is applied to the control mass via the CM actuators, whereas the block diagram shows a compensation angular displacement being applied at the beginning of the isolation system. The block diagram representation is completely valid so long as a $\frac{\theta_{yaw,in}}{\Gamma_{CM}}$ transfer function (input angular displacement to control mass torque transfer function) is included in the feedback transfer function H. The compensation force is therefore converted to a hypothetical compensation input angular displacement ($\theta_{yaw,in}$) as represented by the

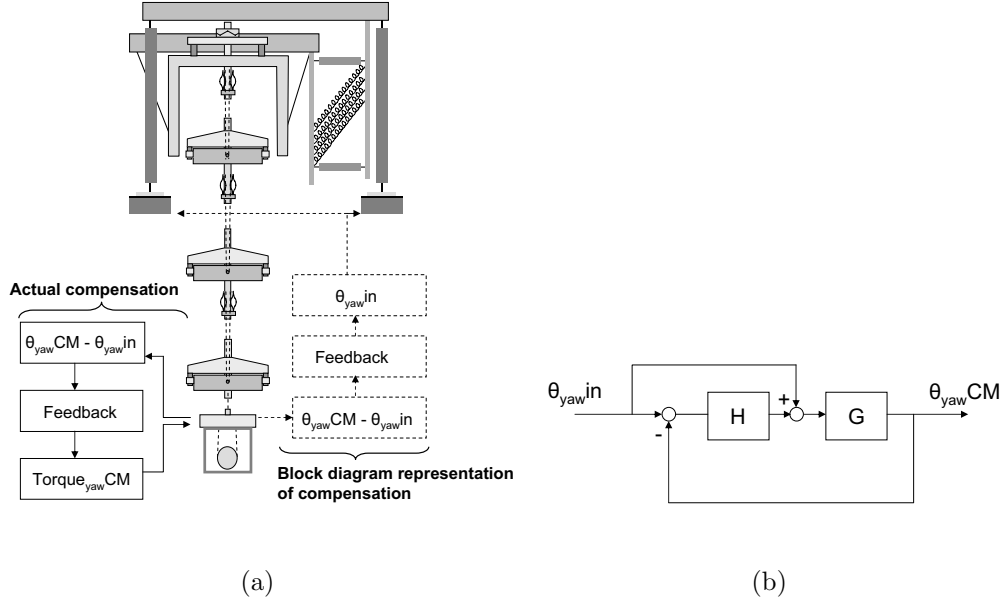


Fig. 5.5: a) Actual feedback path and feedback path represented by the block diagram for yaw compensation. b) Feedback block diagram for yaw compensation.

block diagram. The closed loop transfer function G_{closed} is given by $\frac{G+GH}{1+GH}$. It can be seen that for high gain ($H \rightarrow \infty$), $G_{closed} \rightarrow 1$, since the control mass will essentially be locked to ground. For small gain ($H \rightarrow 0$), $G_{closed} \rightarrow G$, i.e. the case of no torsion mode feedback. Therefore we require high gain around the torsion resonant frequency in order to suppress the oscillation magnitude, and low gain at other frequencies to preserve the isolating properties of the suspension.

The transfer function H can be represented as follows:

$$H = KR \frac{\theta_{yaw,in}}{\Gamma_{CM}} \quad (5.1)$$

Here K has units of N/rad since it represents the amount of force generated due to an input angular displacement. R is the effective moment arm length in m and $\frac{\theta_{yaw,in}}{\Gamma_{CM}}$ is the transfer function of CM torque to input angular displacement. The closed loop yaw transfer function is therefore given by:

$$G_{closed} = \frac{G + KR \frac{\theta_{yaw,in}}{\Gamma_{CM}} G}{1 + KR \frac{\theta_{yaw,in}}{\Gamma_{CM}} G} \quad (5.2)$$

To obtain the above transfer function, the fact that $G = \frac{\theta_{yaw,CM}}{\theta_{yaw,in}}$ has been used such that the ratio is defined as a function of K and transfer function $\frac{\theta_{yaw,CM}}{\Gamma_{CM}}$. The value of K is defined by the maximum force that can be applied by the actuators and the

desired closed loop CM angular motion (i.e. $1.5\mu\text{rad}$ RMS). Assuming the maximum absolute force of each of the three CM actuators to be $50\mu\text{N}$, the maximum allowable value of K is $100\text{N}/\text{rad}$. Given that we know the transfer function $\frac{\theta_{yaw,CM}}{\Gamma_{CM}}$, the value of G_{closed} at the torsion resonant frequency can be determined and thus the level of closed loop yaw.

All pendulum masses except for the control mass consist of double wire suspensions, with the two suspension wires separated by approximately 1cm . The control mass however is suspended by a single wire, thereby making its yaw mode spring constant significantly softer than the other isolator stages. Therefore the $\frac{\theta_{yaw,CM}}{\Gamma_{CM}}$ transfer function can be approximated by considering only the control mass suspension.

The suspended control mass yaw mode theoretical transfer function is given below.

$$\frac{\theta_{yaw,CM}}{\Gamma_{CM}} = \frac{\frac{1}{I}}{s^2 + s\frac{1}{Q}\sqrt{\frac{\kappa}{I}} + \frac{\kappa}{I}} \quad (5.3)$$

Here I (kgm^2) is the rotational inertia of the control mass in the yaw direction and κ (Nm/rad) is the torsional spring constant of the control mass suspension wire. The value Q is the quality factor of the mode, giving an indication of the loss associated with the twisting of the suspension wires. We assume $Q = 100$. For the values $I = 1.32\text{kgm}^2$, $\kappa = 0.014\text{Nm}/\text{rad}$ and $r = 0.25\text{m}$, the yaw on force transfer function gives a value $\frac{\theta_{yaw,CM}}{\Gamma_{CM}} \simeq 6400$ at 0.016Hz . By substituting this value along with $K = 100$ and $R = 0.25$ into Equation 5.2, we obtain $G_{closed} \simeq 1.001$ at the the resonant mode frequency of 0.016Hz . Sufficient low pass filtering of the feedback gain beyond this frequency will ensure that $G_{closed} \ll 1$ and thus higher frequency torsion mode noise will remain filtered passively by the suspension chain. With the isolator frame consisting of four legs separated by approximately 1m , differential seismic motion between the legs results in seismic yaw of approximately $1\mu\text{rad}$ RMS. Thus the use $100\mu\text{N}$ range CM actuators for locking the control mass to the isolator frame at 0.016Hz by means of feedback should result in mirror yaw less than the required level of $1.5\mu\text{rad}$ RMS.

5.3.3 Low Frequency Pitch Mode

Similar to the low frequency torsion mode, the pitch mode of the mirror must be maintained within $1.5\mu\text{rad}$. The reason for this requirement is identical to that for torsion (or yaw) control. Over a cavity length of 4km , angular displacements of $1.5\mu\text{rad}$

are equivalent to approximately 10% in laser spot displacement on the opposite mirror. Spot displacements of greater than 10% of the 6cm spot size cannot be tolerated.

There are essentially two choices for pitch mode actuation; actuation at the TM or actuation at the CM stages. This is indicated in Figure 5.6. A differential in force between top and bottom TM actuators will cause a small amount of pitch to be induced in the mirror. Similarly, a differential force between the front and rear vertical control mass actuators will induce a small amount of pitch in the control mass, which will couple directly to the test mass via the double ribbon suspension.

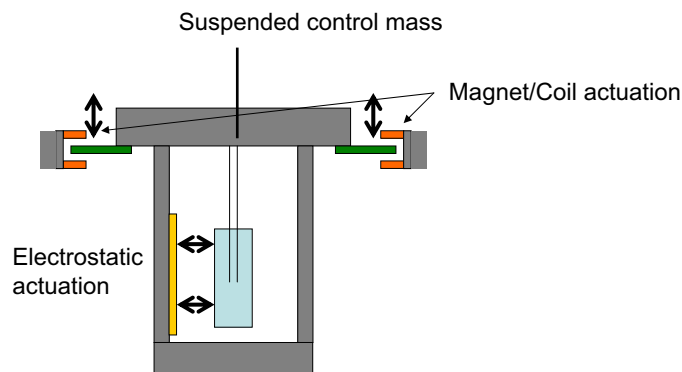


Fig. 5.6: Pitch mode actuation at the test mass stage and at the control mass stage.

For AIGO, pitch mode actuation will occur through the use of the vertical control mass actuators. This is mainly due to the fact that the TM actuators will be used in the global control system. Although it would still be possible to share the TM actuators between both local pitch control and global cavity locking, use of the CM actuators provides the simplest solution.

It is expected that the dominant pitch mode resonance will correspond to the rocking mode of the control mass. The frequency of this resonance will depend on how closely the control mass suspension point is tuned to its centre of mass, however it is likely that a rocking period of greater than 5 seconds will be obtained. The seismic induced pitch noise will be much smaller than that for the torsion mode, resulting in a lower feedback gain. Thus the same actuators used for torsion control (with force up to $\pm 50\mu\text{N}$) will be more than sufficient.

There is a small amount of coupling between pitch and translation of the test mass along the direction of the laser path when CM induced pitch actuation is applied. This is caused by the slight change in distance between the test mass and the electrostatic actuator due to the rocking of the control mass and the non-linearity between force

and displacement of the actuator. With the test mass located 1mm from the actuator, a maximum force to distance derivative $\frac{dF}{dx}$ of approximately 0.84N/m is obtained. For a 4.2kg test mass suspended from the control mass by 300mm length suspension elements, the effective pendulum mode spring constant in the direction of the actuator is approximately 196N/m. Thus for a control mass angular displacement of $1.5\mu\text{rad}$, a maximum change in test mass displacement of approximately 1.9nm will result. The electrostatic actuator is discussed in more detail in Chapter 6. Given that the major pitch mode resonance will be much lower than 1Hz, pitch mode actuation and hence translation coupling will not be significant within the detection band. For frequencies below 1Hz, the 1.9nm of coupled translation is much lower than the level of seismic noise. Therefore the mirror displacement coupled from the pitch mode local control system will not affect interferometer operation. If measurements show that coupling is indeed a problem, more advanced diagonalization techniques, such as that described at the end of Section 6.3.2 may need to be applied.

5.3.4 Minimisation of Horizontal RMS Residual Velocity

The differential RMS residual velocity of the cavity mirrors determines the amount of force required to obtain an initial lock. At AIGO, a cavity finesse of approximately 1000 and a laser wavelength of $1\mu\text{m}$ allows a locking displacement bandwidth of 1nm. In other words, the cavity mirrors must be located within about 0.5nm of a resonant position. It is only while the mirrors are within this range that a global error signal is available.

The differential RMS residual velocity of the mirrors determine the force required to stop the mirrors within the resonant range, as well as the time within which the stopping force must be transmitted. In reality, locking forces are only induced on one of the mirrors, stopping it with respect to the other mirror, i.e. minimising the differential displacement. Reduction of the residual velocity is only effective if it is achieved for all mirrors, thus being a task for the local controls. In section 5.4.1 we show that a differential RMS residual velocity of $\leq 2 \times 10^{-7}\text{ms}^{-1}$ is acceptable.

The theoretical horizontal transfer function of the AIGO vibration isolation system is shown in Figure 5.7. When multiplied by the worst case seismic noise (Figure 5.1), the filtered seismic noise spectrum that can be expected at the suspended mirror is

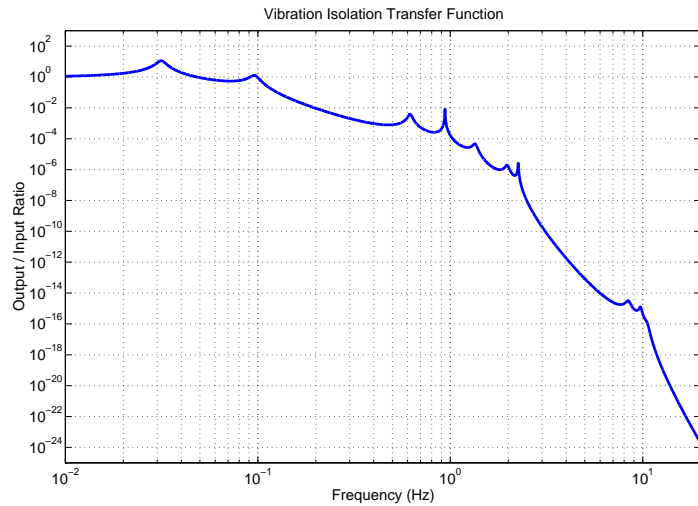


Fig. 5.7: The expected horizontal transfer function of the AIGO vibration isolation system. The input is taken as the point where the isolation system makes contact with the earth while the output is the motion of the mirror.

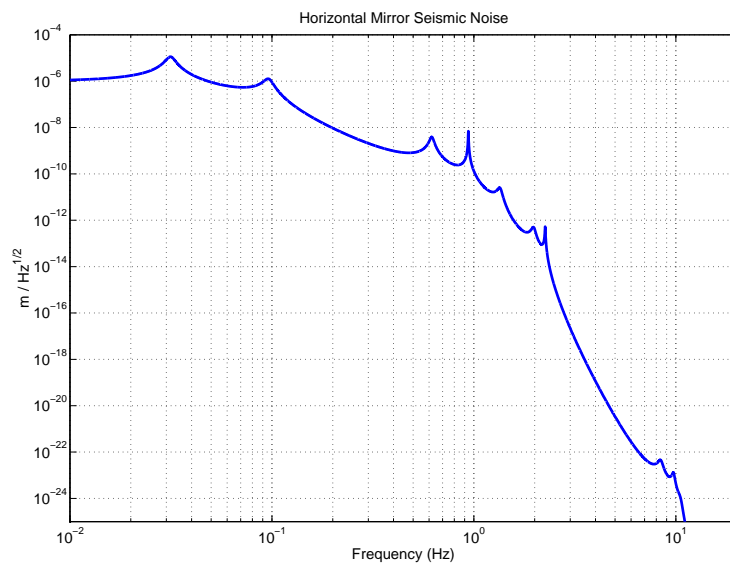


Fig. 5.8: The expected horizontal seismic noise seen at the suspended mirror when supported by the AIGO vibration isolation system.

illustrated in Figure 5.8. The RMS motion and velocity is usually dominated by the largest peaks in the seismic spectrum. In this case the peaks at 0.03Hz and 0.1Hz, corresponding to the pre-isolator and Roberts Linkage, dominate the spectrum and present the largest contribution to the RMS displacement and velocity.

The RMS residual motion can be obtained from the displacement spectrum using the formula given in Equation 5.4. Here, $\tilde{x}(v)$ is the displacement spectrum amplitude

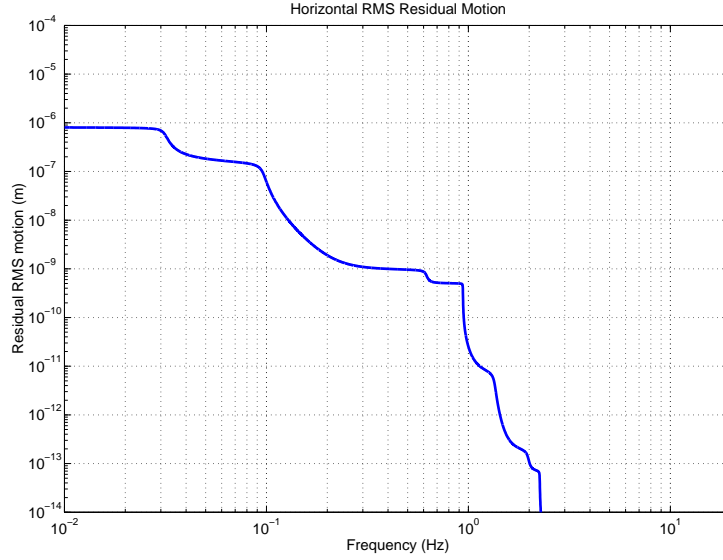


Fig. 5.9: The RMS residual motion of the mirror suspended by the AIGO vibration isolation system.

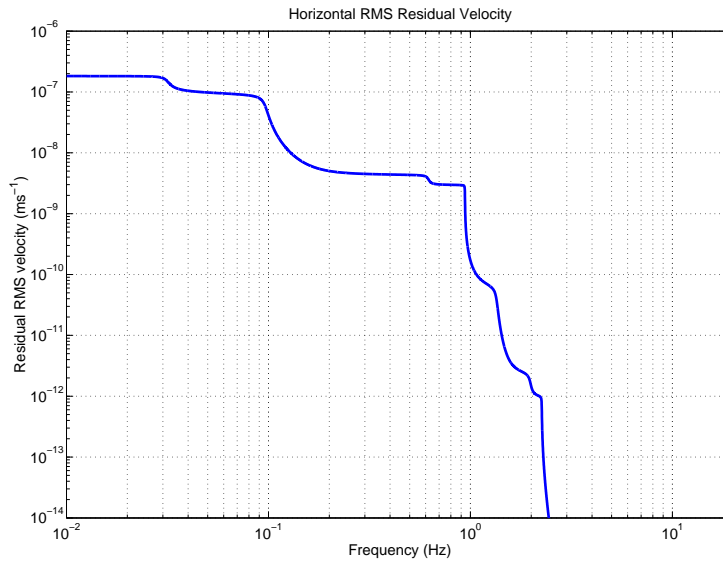


Fig. 5.10: The RMS residual velocity of the mirror suspended by the AIGO vibration isolation system.

in $\text{m}/\sqrt{\text{Hz}}$ as a function of frequency, v .

$$x_{rms}(f) = \sqrt{\int_f^{\infty} \tilde{x}^2(v) dv} \quad (5.4)$$

Similarly the RMS residual velocity can be obtained by applying Equation 5.4 to the velocity spectrum. Plots of the RMS residual motion and velocity obtained in this manner is shown in Figure 5.9 and Figure 5.10 respectively. The RMS residual velocity plot shows a maximum value of $2 \times 10^{-7} \text{ms}^{-1}$. As mentioned earlier, this is about the

limit of acceptable mirror velocity. The RMS residual motion is close to 1 μ m. This value becomes important once cavity lock has been achieved, since it determines the range of force that is required. Given that a global control signal will be available once the cavity is locked, the RMS residual motion is not of major concern to the local control system given that it is no larger than about 1 μ m.

The possibility of actively reducing the mirror velocity relies on sensing and actuating at either the pre-isolator, Roberts Linkage, control mass or test mass stage. The wire heating method of actuation for the Roberts Linkage and hence the large amount of phase lag results in a relatively complex feedback path if actuation at this point is used. Velocity damping at the test mass is also difficult, since the test mass sensor is mounted relative to the control mass rather than the isolator frame, meaning the two dominating peaks at 0.03Hz and 0.1Hz as mentioned previously cannot be damped. This leaves the control mass and pre-isolator actuators and sensors as the best means for active velocity damping. Since one of the major peaks in the seismic noise spectrum is due to the pre-isolator, and the control mass is likely to be used for low frequency torsion mode control, reducing the mirror velocity at the pre-isolator stage seems to be the best choice.

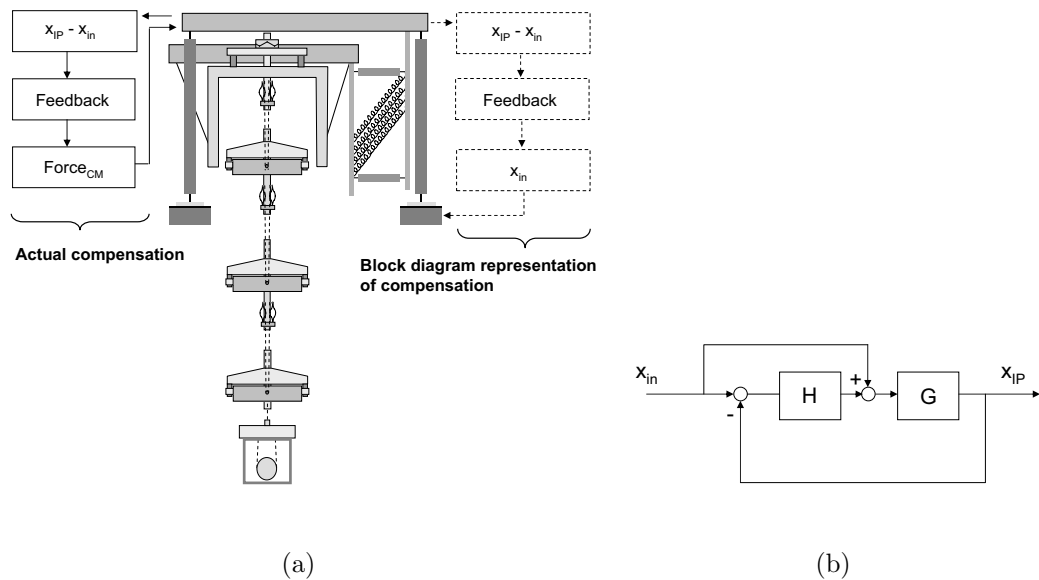


Fig. 5.11: a) Actual feedback path and feedback path represented by the block diagram for local horizontal compensation. b) Feedback block diagram for local horizontal compensation.

Figure 5.11(a) and 5.11(b) show the feedback block diagram to be used for the AIGO horizontal direction local control. The block G represents the displacement transfer function of the isolation system from ground to the IP stage, while H is the feedback transfer function. Similar to torsion mode compensation, the actual feedback process is different to the represented feedback process in that a force is fed back to IP stage rather than a displacement. Again this is valid as long as the $\frac{x_{in}}{F_{IP}}$ transfer function (inverse pendulum force to displacement transfer function) is considered within the feedback gain H . In this manner, the feedback gain H can be determined as is represented in the block diagram 5.11(b), i.e. as if the output of H was an input displacement signal. To apply H to the actual case where the output is a force signal, it simply needs to be multiplied by $\frac{x_{in}}{F_{IP}}$.

To design a suitable local horizontal control method, loop gain and phase margins are studied with various feedback filter transfer functions, H . A phase margin larger than 30° and gain margin of at least 10dB should provide a sufficiently robust control system. Figure 5.12 shows the loop gain bode plot of the system with a simple feedback gain of 1, and a more complicated feedback transfer function H , consisting of various lead, notch and low pass filters. It can be seen that with a feedback gain of 1 (illustrated

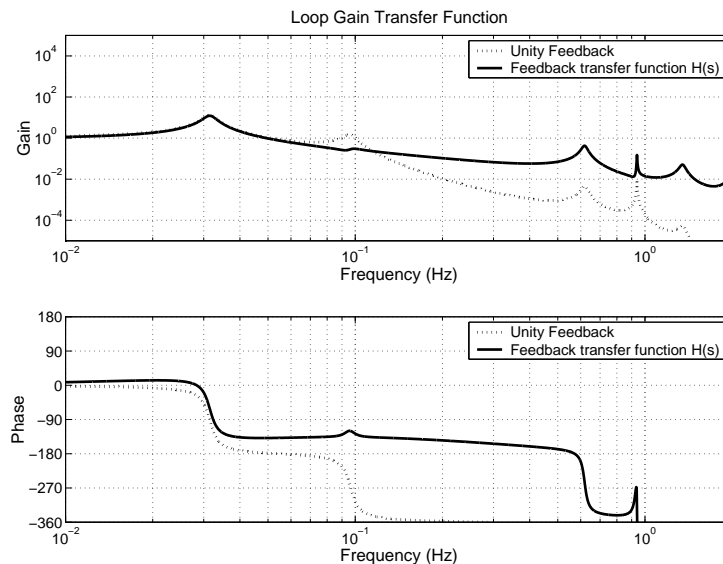


Fig. 5.12: Loop gain bode plot of the local control loop with: 1) Unity feedback. 2) A feedback transfer function $H(s)$.

by the dotted line), a unity gain frequency of approximately 0.1Hz results in an unstable system due to the negative phase margin at this point. In order to make this ‘simple

feedback' system stable, the gain must be reduced such that the unity gain frequency is less than 0.05Hz. With this level of gain, very little compensation is achieved and the system still exhibits a lower phase margin than the desired 30°. Instead, a more sophisticated feedback transfer function H is used. The loop gain bode plot of this closed loop system is shown in Figure 5.12 by the solid line. A unity gain frequency of approximately 0.04Hz with phase margin close to 45° and gain margin of about 20dB both lie within the desired specifications. The design of the filter H in order to achieve this is described below.

Firstly a lead filter is employed with a zero at $s=0.28$ (0.04Hz) and a pole at $s=1.41$ (0.22Hz). This acts to increase the loop gain phase response, and hence the phase margin at frequencies close to the unity gain frequency. The cost however is higher gain at higher frequency, resulting in a reduction in gain margin. Secondly two notch filters are used to suppress the gain from two resonant modes, and at the same time increasing the phase at higher frequencies by 180°. The expected isolator resonant modes are given in Table 5.2. It is found that the 0.095Hz and 0.93Hz modes need to be notched in order to provide sufficient gain margin. Although the phase increase at higher frequencies provided by the notch filters act to further stabilise the system, the high pass nature of the notch filters must be considered in order that a reduction of phase margin or amplification of high frequency noise does not result. The notch filter zeros are $-0.030 \pm 0.60i$ and $-0.097 \pm 5.84i$ respectively, although will need to be tuned to the measured frequencies of the corresponding modes. Finally a fifth order low pass filter with corner frequency at 300Hz is included. The low pass filter will reduce the effect of high frequency amplification caused by the notch filters, whilst the corner frequency is high enough that the phase lag from the filter does not effect the stability of the closed loop system. This is summarised in Table 5.3.

The DC gain of 1 is approximately the largest feedback gain that can be applied whilst maintaining a stable system. The loop gain bode plot of Figure 5.12 shows that a higher gain would result in the resonant mode peak at 0.62Hz crossing the unity gain axis, and thus resulting in a negative phase margin. It is also difficult to use a notch filter on this mode due to the high pass nature of the filter increasing the amplitude from the higher frequency modes. The DC gain of 1 corresponds to the displacement to displacement feedback represented by the block diagram. In reality however a force is fed back to the IP stage, and hence the DC gain of the $\frac{x_{in}}{F_{IP}}$ must be considered. Since

Poles	f (Hz)	Q
$-0.0098 \pm 0.1977i$	0.03	10.1
$-0.0301 \pm 0.6051i$	0.10	10.0
$-0.0879 \pm 3.8896i$	0.62	22.1
$-0.0102 \pm 5.8974i$	0.94	289.0
$-0.1978 \pm 8.4753i$	1.35	21.4
$-0.2685 \pm 12.429i$	1.98	23.1
$-0.0364 \pm 14.164i$	2.25	194.8
$-1.3216 \pm 52.900i$	8.42	20.0
$-0.8490 \pm 61.220i$	9.74	36.1
$-1.6570 \pm 66.429i$	10.58	20.1

Tab. 5.2: The theoretical poles for the AIGO isolation system and the equivalent mode frequencies and Q factors.

Filter	Transfer Function
DC Gain	1
Lead Filter	$\frac{1+aTs}{1+Ts}$, $a = 5$, $T = 0.71$
Notch Filter 1	$\frac{s^2+s\frac{\omega_0}{Q}+\omega_0^2}{\omega_0^2}$, $\omega_0 = 2\pi 0.095$, $Q = 10$
Notch Filter 2	$\frac{s^2+s\frac{\omega_0}{Q}+\omega_0^2}{\omega_0^2}$, $\omega_0 = 2\pi 0.93$, $Q = 30$
Low Pass Filter	$\left(\frac{\omega}{s+\omega}\right)^5$, $\omega = 2\pi 300$

Tab. 5.3: A summary of the filters connected in series to produce the feedback filter H.

the DC gain of the $\frac{x_{in}}{F_{IP}}$ transfer function is approximately 0.023, then the required DC gain to be used with the H filter when the actual case of force feedback is used is

$\frac{1}{0.023} = 43$. Thus the maximum force required by the IP actuators for local horizontal control is approximately $43\mu\text{N}$.

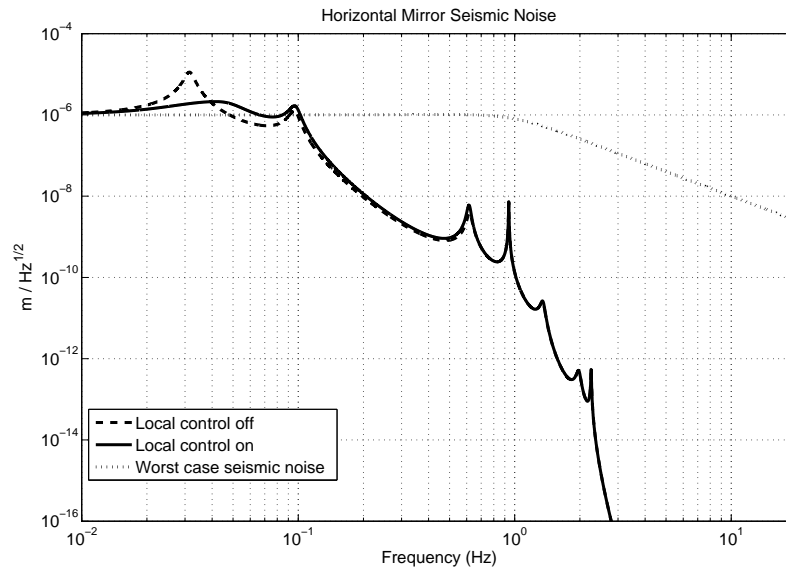


Fig. 5.13: The horizontal seismic noise with the local control loop closed.

The seismic noise that would result at the suspended mirror given a closed horizontal local control loop is indicated in Figure 5.13. Since we are only considering a local control loop, the best that can be achieved is a reduction in seismic noise amplitude to the worst case seismic noise level, also indicated on the plot. Therefore the only frequency band where gain is useful is within the frequency range of the lowest pre-isolator peak, i.e. DC and 0.05Hz. The closed loop seismic noise indicates that the original seismic noise has been reduced somewhat around the 0.03Hz peak. The effectiveness of the local control loop is easily visualised when considering the resulting RMS residual motion and velocity plots.

A comparison between the RMS residual motion of the closed and open loop systems is indicated in Figure 5.14. Similarly, the RMS residual velocity is shown in Figure 5.15. A reduction in RMS residual velocity is most important when aiming to reduce the required locking force. As mentioned earlier, the goal of the AIGO suspension is to achieve an RMS residual velocity of $\leq 2 \times 10^{-7} \text{ms}^{-1}$. Figure 5.15 shows that there is little improvement in the RMS residual velocity for the closed loop system, despite there being a reduction in RMS residual displacement of more than a factor of 2. This is because a significant contribution to the RMS residual velocity comes from the inverted pendulum at the 0.09Hz peak. Although Figure 5.13 indicates a larger amplitude peak

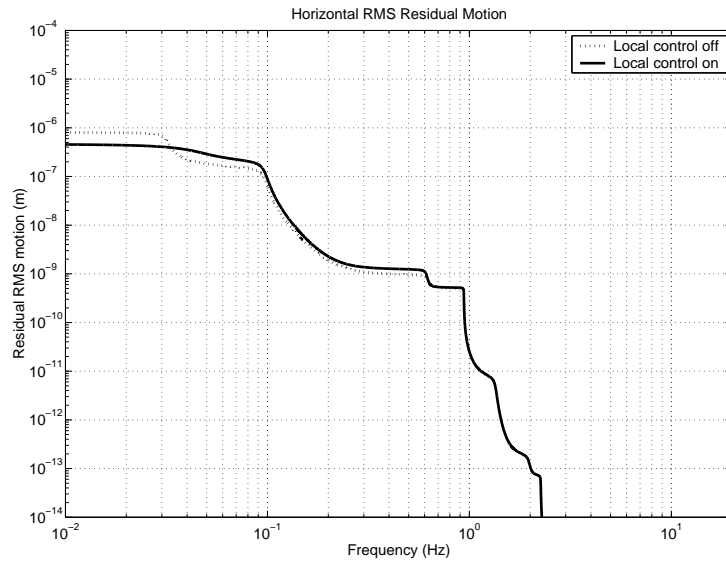


Fig. 5.14: The RMS residual motion of the mirror with the local control system closed.

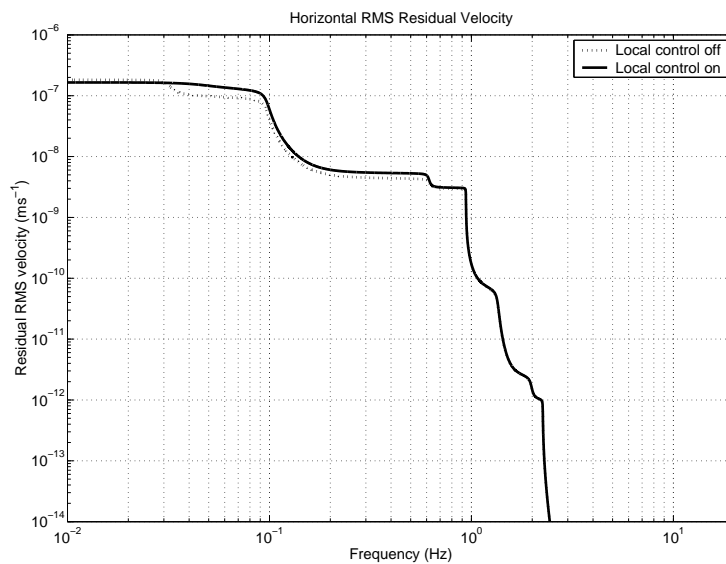


Fig. 5.15: The RMS residual velocity of the mirror with the local control system closed.

at 0.03Hz, the lower frequency means that the velocity contribution of this peak is not dominant. The amplitude of seismic noise at 0.09Hz peak is close to the ground seismic noise level, hence the inability of the local servo to suppress. This indicates that the AIGO suspension, when sufficiently tuned, already exhibits very close to minimal differential RMS residual velocity. Furthermore, this velocity level is acceptable for the proposed AIGO control strategy.

5.3.5 Vertical RMS Residual Velocity

Ideally, vertical seismic motion that is coupled through the isolation chain to the suspended mirror would be completely independent to any horizontal direction motion (motion in the direction of the laser field). In reality however, there always exists a level of coupling between vertical and horizontal motion and thus a small proportion of the transmitted vertical seismic noise would be observed as horizontal seismic motion. It is accepted that the lowest level of coupling that can be achieved between vertical and horizontal is 1 to 1000. Since the vibration isolation chain consists of single wire pendulums, there are no obvious locations where asymmetries could spoil the expected 1 to 1000 coupling. However, asymmetries in the four ribbon suspension of the test mass could lead to a higher coupling factor. Modelling of this suspension has shown that differential ribbon lengths of up to 1mm (for 300mm suspensions) can be tolerated if the suspension point is located at the test mass equator to within 0.5mm. Machining to within these tolerances can be reasonably expected. A larger problem may be the extra vertical to horizontal coupling resulting from a small dc tilt due to the slightly different ribbon lengths. This should be compensated by the pitch control actuators as part of the cavity alignment requirement. Therefore, by using this expected vertical to horizontal coupling factor of 1 to 1000, the effect of vertical residual velocity, and the need for any vertical motion local compensation can be analysed.

Figure 5.16 compares the expected horizontal mirror seismic noise to the coupled motion expected from the vertical direction. With the 1 to 1000 coupling factor, seismic noise coupled from the vertical direction is always smaller than the horizontal direction for low frequencies, i.e. below 1Hz where seismic noise is a significant noise source.

Figure 5.17 and Figure 5.18 compare the horizontal and coupled vertical RMS motion and RMS velocity respectively. In both cases it can be seen that the coupling factor greatly dilutes the impact of the vertical motion.

Therefore vertical direction local control is not necessary for the AIGO isolation system. The 1 to 1000 vertical to horizontal coupling factor ensures that the coupled vertical motion is always significantly smaller than the horizontal motion. Thus the vertical actuators located within the isolation system are only needed for remote mirror positioning and local compensation for vertical mirror motion induced by temperature variations, both of which are low frequency operations. This is satisfied through the

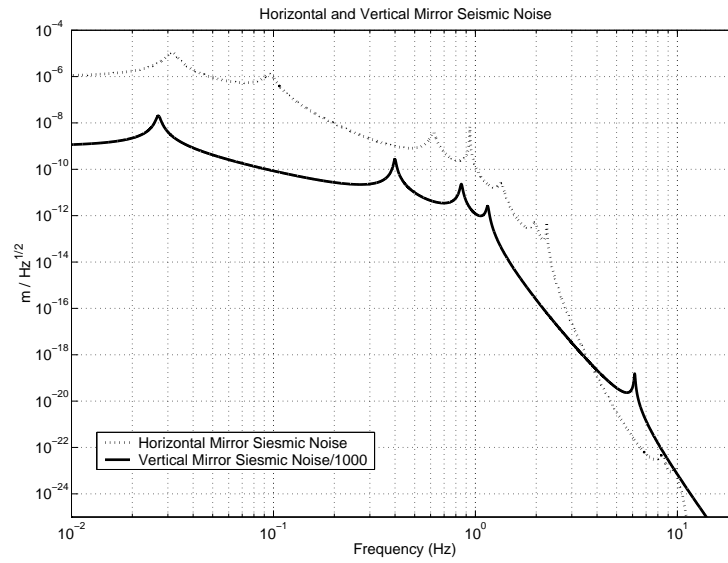


Fig. 5.16: A comparison between the expected horizontal and vertical seismic noise seen at the suspended mirror when supported by the AIGO vibration isolation system. A vertical to horizontal coupling factor of 1 to 1000 is assumed.

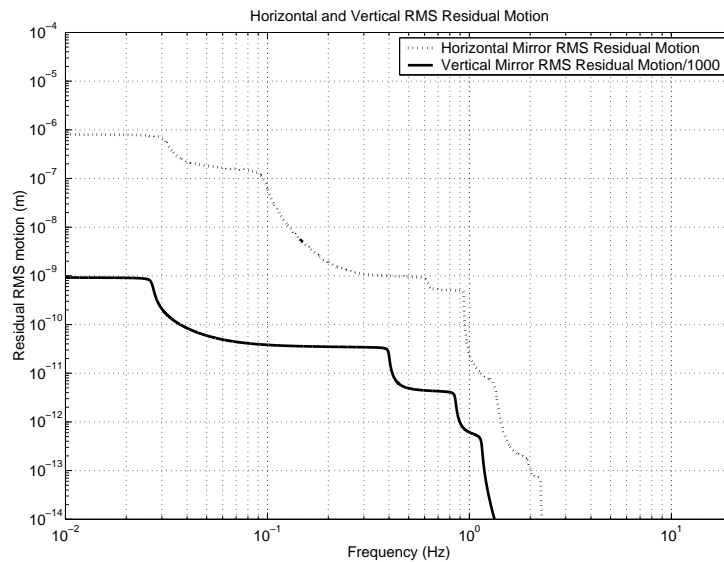


Fig. 5.17: A comparison between the horizontal and vertical RMS residual motion of the mirror suspended by the AIGO vibration isolation system. A vertical to horizontal coupling factor of 1 to 1000 is assumed.

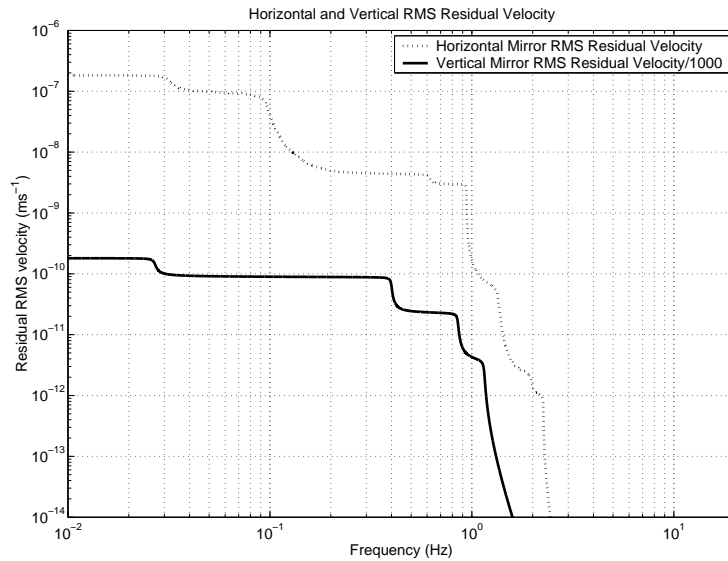


Fig. 5.18: A comparison between the horizontal and vertical RMS residual velocity of the mirror suspended by the AIGO vibration isolation system. A vertical to horizontal coupling factor of 1 to 1000 is assumed.

use of the LaCoste stage wire heating actuation method, where a total vertical range of approximately 5mm is available. Furthermore, vertical actuation noise that is present at this location is heavily filtered by the 3 stages of Euler Spring vertical isolation that follow.

5.4 Global Control Systems

In an interferometric gravitational wave detector, the global control signals are the very low noise signals that allow the interferometer to be maintained at its optimum operating condition. One of the global signals is that relating to the cavity length. This signal is proportional to the differential displacement between the two end mirrors that form the km scale optical cavities. By feeding this signal back into actuators that apply forces on the suspended mirrors, the cavity can be maintained at resonance.

The difficulty with the cavity length global control signal is the very small position bandwidth within which the signal exists. What this means is that the mirrors have to be positioned very close to resonance in order for the mirror differential error signal to be available. The size of the position bandwidth depends on optical parameters, but can be approximated with knowledge of the cavity finesse and laser wavelength. At

AIGO, the laser wavelength is 1024nm with a maximum cavity finesse of approximately 3000. This results in a position bandwidth of close to 0.3nm.

With mirror RMS residual motion in the order of 1 μ m and RMS residual velocity of several $\times 10^{-7}\text{ms}^{-1}$, the global feedback signal will initially be observed as pulses. This corresponds to the instant when the freely swinging mirrors happen to pass through a resonant condition. In order to obtain a useable global signal, the mirrors must be locked on resonance within the time frame of one of these pulses. We describe this procedure as initial cavity locking.

5.4.1 Initial Cavity Locking

This simplest way to lock a suspended optical cavity in length is to apply forces on one mirror, ensuring that it mimics the motion of the other mirror. This is equivalent to assuming that one mirror is perfectly still, while forces act on the other mirror, reducing the seismic induced motion to zero. The convenience of this method, is that we can consider the cavity as a single suspended mirror and that the error signal is referenced to a seismically still ground. In the following sections, we make use of this simplification.

Initial cavity locking simply involves locking the mirrors while they move through a resonant condition. The amount of force needed for initial locking can be approximated by assuming the mirrors are free and moving with differential velocity of $2 \times 10^{-7}\text{ms}^{-1}$. This free mirror assumption is valid since an impulse being applied to the mirror occurs in a time much small than the resonant period of the mirror suspension. By knowing the mirrors are to be 4.2kg in mass, the necessary change in momentum of the mirrors can be calculated.

Solving Newton's second law allows us to determine the velocity of the mirror over time.

$$\frac{F(t)}{m} = \frac{dv(t)}{dt} \quad (5.5)$$

In Equation 5.5, $m = 4.2\text{kg}$ is the mass of the mirror, $F(t)$ is the force applied to the mirror over time, while $v(t)$ is the velocity of the mirror as a function of time. Assuming $v(0) = 2 \times 10^{-7}\text{ms}^{-1}$, $F(0) = 0$, and that $F(t)$ has an exponential time constant of $3 \times 10^{-4}\text{s}$ associated with it, the trajectories for $F(t)$, $v(t)$ and also the mirror displacement, $x(t)$ can be obtained.

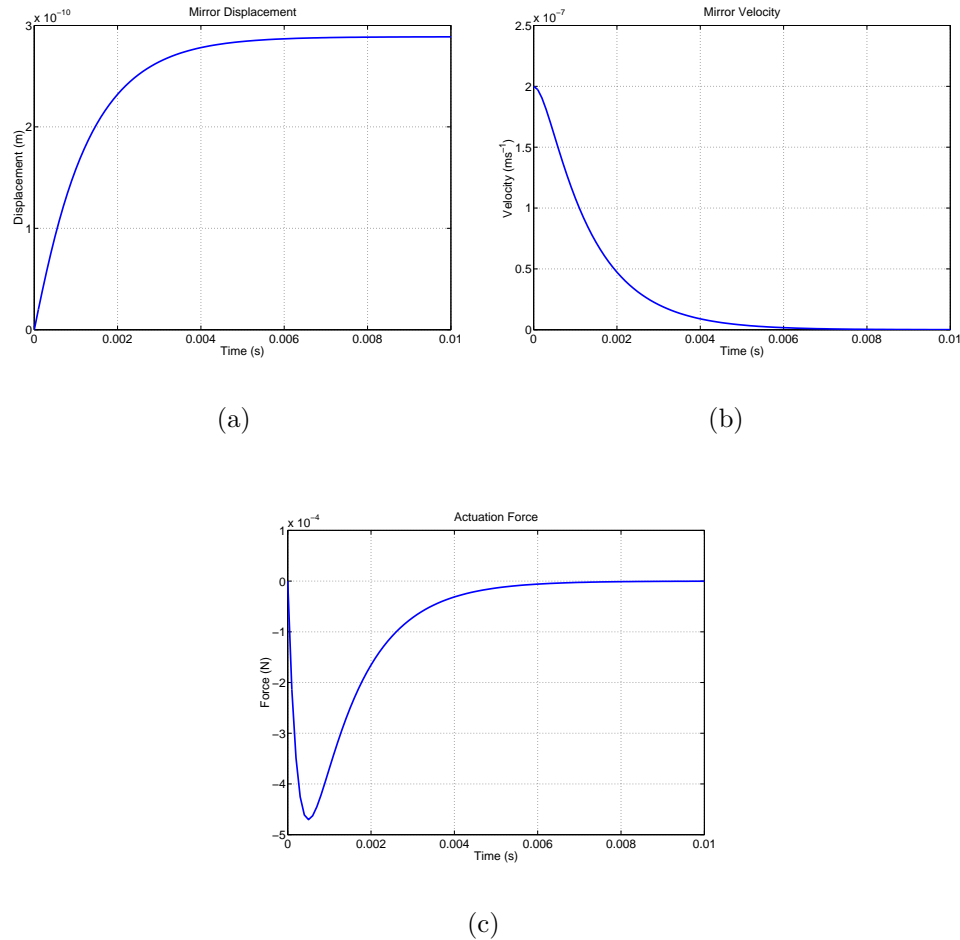


Fig. 5.19: A simulated mirror stop resulting from an initial velocity of $2 \times 10^{-7} \text{ms}^{-1}$. (a) Mirror displacement. (b) Mirror velocity. (c) Actuation Force.

In Figure 5.19 a simulation of mirror locking given an initial velocity of $2 \times 10^{-7} \text{ms}^{-1}$ and an initial force of 0N is illustrated. The mirror displacement trajectory shows that the mirror will not travel more than 0.3nm before its momentum (or mirror velocity) is reduced to zero. The force trajectory shows that the maximum force induced during the lock is 460uN. The exponential time constant that was included in the force output is equivalent to the dynamic response of the electrostatic actuator being built for AIGO. The design of this actuator is discussed in Chapter 6.

Once stopped, the cavity must be locked and held in the locked position by feeding back the global cavity length error signal. This is illustrated schematically in Figure 5.20. The locked cavity can only be maintained if the differential RMS residual motion of the mirrors is very small. The reason for this is that the global error signal provides the information about the possibility of mirror motion due to a passing grav-

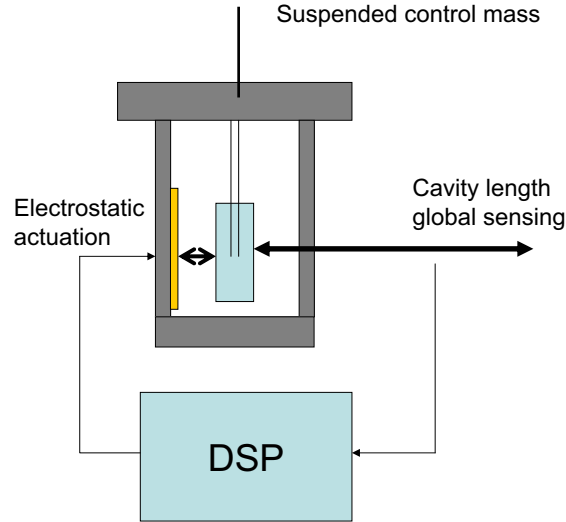


Fig. 5.20: Feedback loop of the initial cavity locking strategy. The global cavity length signal is fed directly into the DSP through the A to D converter, processed by a digital filter, then fed via a D to A converter to the actuators.

itational wave. Thus the signal needs to exhibit minimum noise within the detection bandwidth (10Hz to several kHz) and as a result is easily saturated by excessive mirror motion. For Advanced LIGO, the locked cavity must exhibit a differential RMS residual motion of below 10^{-14} m [67]. We have assumed the same level of mirror motion while developing the AIGO control strategy.

The closed loop noise spectrum of the locked cavity is shown in Figure 5.21. This illustrates clearly that the majority of the gain is required at low frequency. This is because the most significant contributions to the RMS residual motion occurs at the low frequency region, particularly at the resonant modes of the two pre-isolators. Above 10Hz however, no gain is needed since the passive vibration isolation performance of the system is more than adequate. By minimising any gain above 10Hz, it is possible to minimise control noise injected in the detection band due to unwanted actuation forces.

The closed loop block diagram of this system is illustrated in Figure 5.22. The transfer function $G(s)$ represents the force to cavity length transfer function of the suspended mirror, where the force is applied through the electrostatic actuators. The feedback filter $H(s)$ has the following transfer function:

$$H(s) = 10^{12} \left(\frac{\omega_1}{s + \omega_1} \right)^9 \left(\frac{s + \omega_2}{\omega_2} \right)^{10} \left(\frac{\omega_3}{s + \omega_3} \right)^5 \quad (5.6)$$

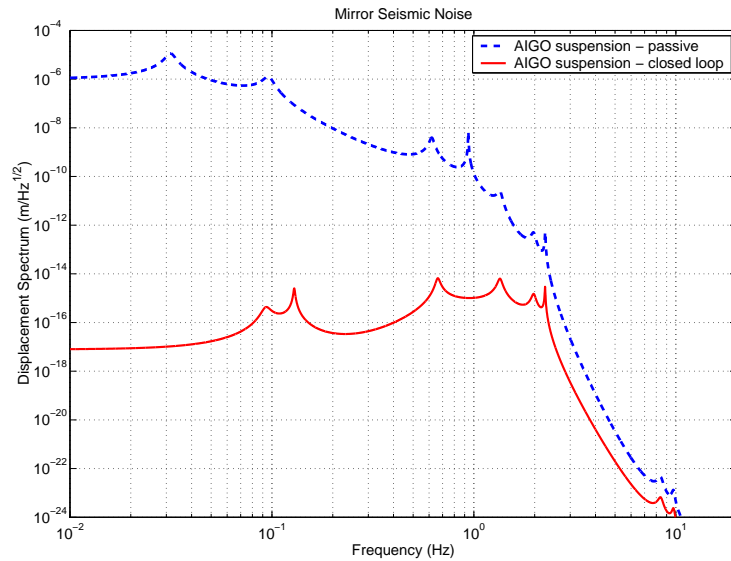


Fig. 5.21: A comparison between the closed loop and open loop seismic spectrum. The closed loop spectrum uses feedback of the global cavity length signal to the electrostatic actuators that apply forces directly to the test mass.

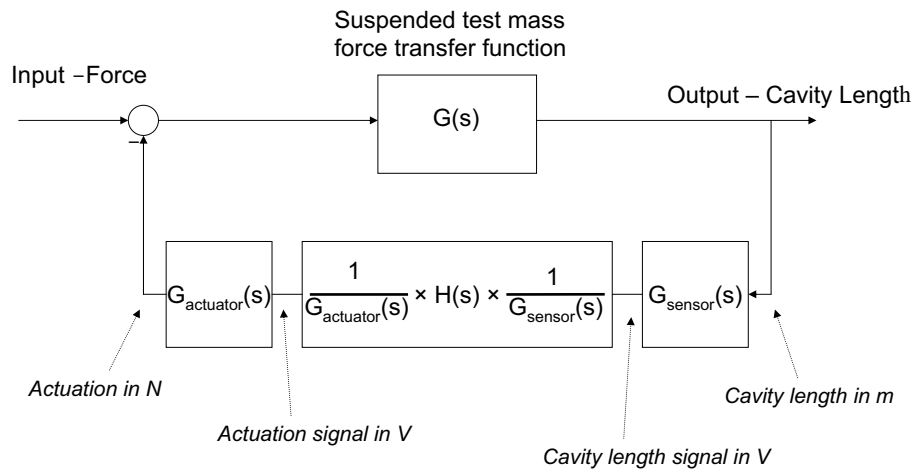


Fig. 5.22: A block diagram illustrating the feedback loop for initial locking of the AIGO optical cavities.

for $\omega_1 = 2\pi \times 0.2$, $\omega_2 = 2\pi \times 1.5$ and $\omega_3 = 2\pi \times 500$. The transfer functions for cavity length sensing (metres to volts), and for the actuators (volts to newtons) is made unity by incorporating the reciprocal of these functions digitally in series with the feedback filter $H(s)$. These are transfer functions represented in the block by $G_{sensor}(s)$ and $G_{actuator}(s)$ respectively. It can be seen that the feedback loop in the diagram can be reduced to the filter $H(s)$. Thus analysis of the control system can be done without prior knowledge of the transfer functions $G_{sensor}(s)$ and $G_{actuator}(s)$.

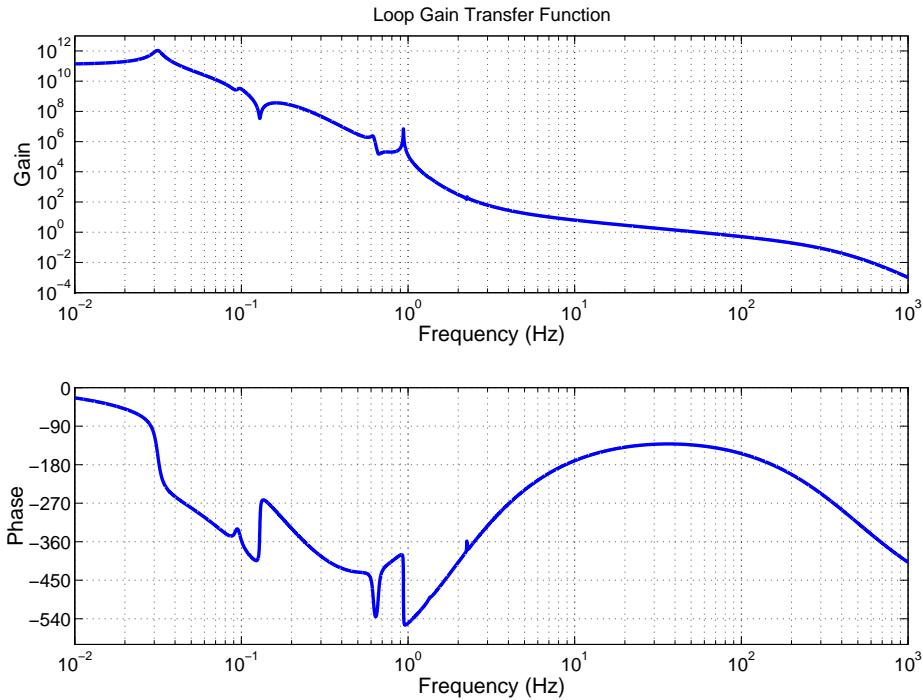


Fig. 5.23: The loop gain transfer function of the global cavity length feedback to the electrostatic actuators.

The loop gain transfer function is given by $G(s) \times H(s)$. This is plotted in Figure 5.23 and illustrates the necessity of the different components forming $H(s)$ as shown in Equation 5.6. The 9th order low pass filter defined by ω_1 provides the attenuation necessary for high gain at low frequency, while having minimal gain at frequencies within the detection band, i.e. above 10Hz. The 10th order high pass filter given by ω_2 is required to keep the closed loop system stable. This filter provides the positive phase slope between 1Hz and 30Hz, in order to obtain a phase margin of close to 45° at the unity gain frequency of 40Hz. The 5th order low pass filter at ω_3 prevents the high pass filter from amplifying high frequency noise and injecting it into mirror motion. Although a higher order filter or a lower corner frequency would be better for reducing high frequency noise, the third low pass filter is already limited by its effect on the phase margin and hence closed loop stability. This filter also gives the bandwidth requirement of the actuator. The electrostatic actuator design for AIGO has a bandwidth of approximately 3000Hz, which is much larger than the 500Hz bandwidth requirement.

The resulting differential RMS residual motion is shown in Figure 5.24. The closed loop motion is the result of the global cavity length signal being fed back through the

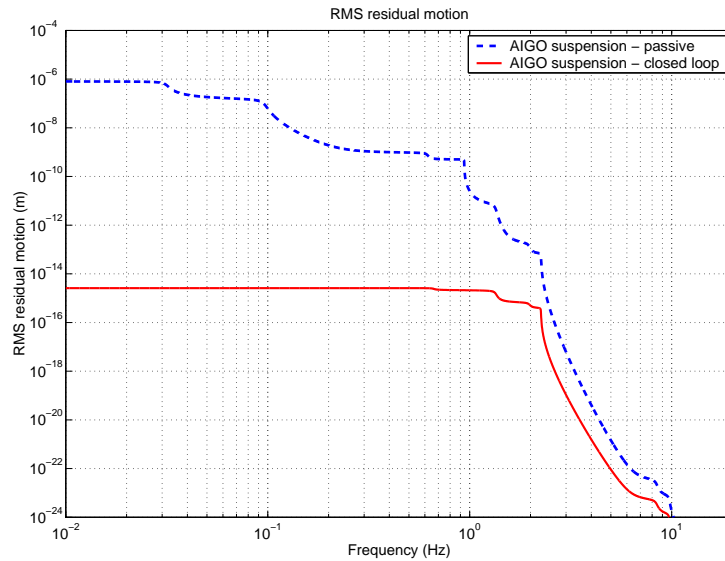


Fig. 5.24: A comparison between the closed loop and open loop differential RMS residual motion. The closed loop system uses the global cavity length signal fed back to the electrostatic actuators applying forces directly on the mirror.

filter with transfer function given by Equation 5.6 and actuation with the electrostatic actuators. It can be seen that the closed loop system exhibits the desired amount of motion of less than 10^{-14} m. Once initial lock is achieved, the expected force spectrum that is fed through the electrostatic actuators is given by Figure 5.25. This spectrum is obtained by multiplying the closed loop seismic noise by the feedback transfer function $H(s)$. Thus in order to hold this initial lock, the actuators must have a maximum force range of $500\mu\text{N}$ at approximately 0.1Hz. This force spectrum results in an RMS force of approximately $50\mu\text{N}$.

With the initial cavity lock achieved, a cavity length global signal will be available for gravitational wave detection. In fact there is no reason why an optical cavity in this state cannot be used to take scientific data. The sensitivity of the instrument however, will most likely be limited by the actuation noise (given that the other main sources of noise are relatively close to their design specifications). This is shown in Figure 5.26, where the actuation noise is compared to the expected seismic noise of the AIGO vibration isolator and the expected broadband sensitivity of Advanced LIGO [67]. The actuation noise usually results from one of two places. The first is the output noise of the voltage amplifier. Being an electrostatic actuator, the magnitude of force is varied by changing the amount of voltage across the capacitive electrodes (see Chapter 6 for more details). This is typically due to the amplification of input voltage noise intrinsic

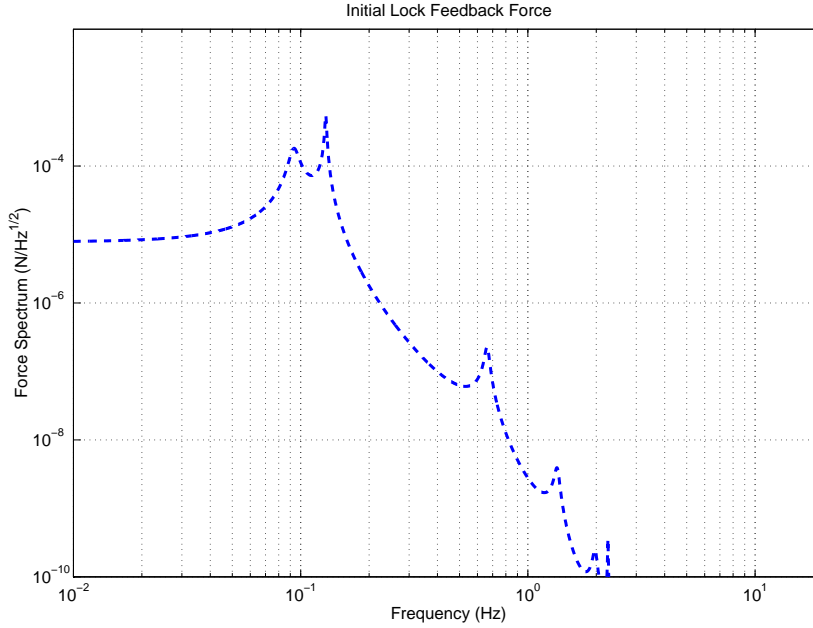


Fig. 5.25: The feedback force spectrum required to hold the initial lock. This is given by the closed loop seismic spectrum multiplied by the transfer function .

to the amplifier. The second is the output noise of the D to A converter. Signal to noise ratio of an analogue circuit is typically 10^9 , and thus the noise level of the signal output from the D to A converter results in actuation noise. The D to A converters used for VIRGO superattenuator inertial damping [126] consist of a signal level of $\pm 10\text{V}$ and a noise level of about $300\text{nV}/\sqrt{\text{Hz}}$. Since the current intention for the AIGO site is to use a digital control system at least equivalent to the current VIRGO system, we have used supplied VIRGO DSP boards for our measurements and analysis presented in this chapter. It should also be noted that the actuation noise plotted in Figure 5.26 has been calculated for electrostatic actuators capable of inducing $\pm 0.5\text{mN}$ of force over the required actuation bandwidth. This level of initial locking actuation has been designed for AIGO considering approximately ten times larger seismic noise than that measured at the Gingin site.

At 100Hz , the actuation noise level is approximately 1000 times larger than the desired sensitivity. The initial locking technique is a first generation detector locking method, the simplest method of positioning suspended mirrors with forces acting directly on the mirror itself. To reduce the actuation noise beyond the level set by the desired sensitivity, advanced control techniques need to be implemented to spread the mirror control force over the different actuation regions on the isolator. This has

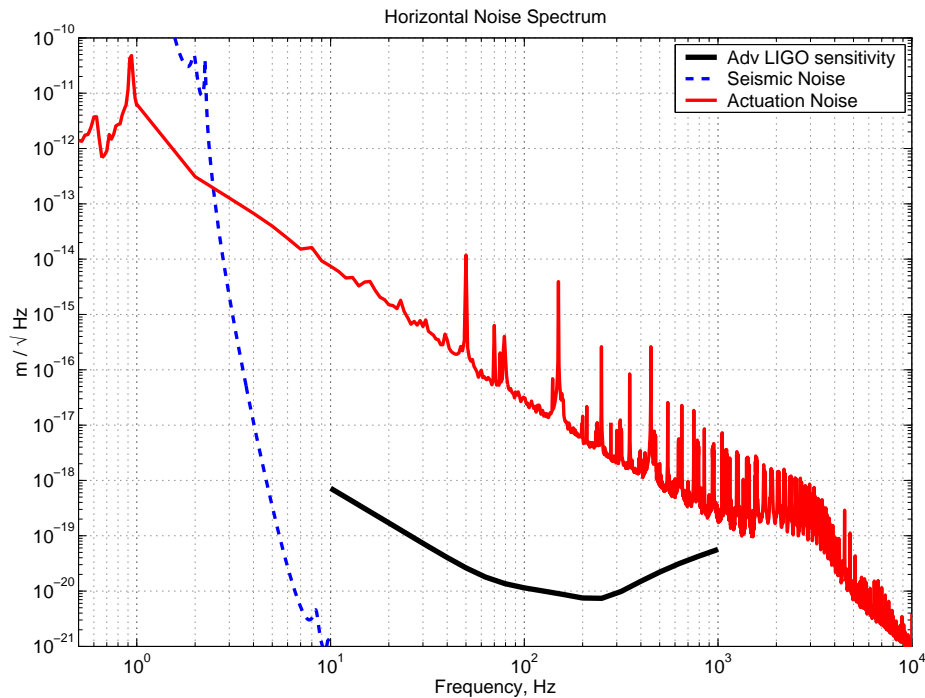


Fig. 5.26: A comparison of actuation noise with the expected AIGO seismic noise, and broad-band sensitivity of an advanced interferometric gravitational wave detector.

the effect of minimising the amount of force needed at the electrostatic actuators, and hence allows the signal noise to be reduced. This type of control is termed Hierarchical control and is discussed in the following section.

Although hierarchical control techniques will be necessary to achieve the desired interferometer sensitivity, initial locking still needs to be achieved to obtain a global cavity length error signal. This error signal can then be applied to the hierarchical control scheme. The initial lock only needs to remain as long as is required to switch over to the hierarchical control. The switching task itself is not trivial and requires a smooth merge from one system to the other. Therefore the initial lock needs to be stable for at least several tens of seconds. The initial lock procedure described above should be more than capable of remaining locked for this amount of time, and will only lose lock when large low frequency millimetre length movements cause the electrostatic actuators to saturate. These motions result from thermal expansions and contractions and are due to daily temperature changes. The frequencies are much lower than the few tens of seconds required for switching and are thus not a concern. If it is desired that the initial lock be kept for longer than a day, it is then a matter of feeding back the low frequency components of the cavity length error signal to the pre-isolator actuators.

These actuators are capable of compensating the low frequency millimetre amplitude motions.

5.4.2 Switching to Hierarchical Control - General Case

The general idea of hierarchical control is simple and is based on the ability to feedback a control signal via separate frequency bands. Since the mirror is suspended from a high performance isolation chain, the seismic displacement experienced by the mirror is dominated by low frequency components. By avoiding direct feedback of the low frequency seismic displacement to the mirror, only small compensation forces are required, thereby reducing the level of actuation noise. These larger amplitude feedback forces can be applied higher up in the isolation chain, where the higher level of actuation noise is mechanically filtered.

Although the idea may be simple, the practise of applying a global hierarchical control system is not trivial. We analyse the stability of a hierarchical system by simple manipulations of block diagrams. Consider Figure 5.27 which illustrates a simple single input, single output feedback control system. The output Y of the system (or plant)

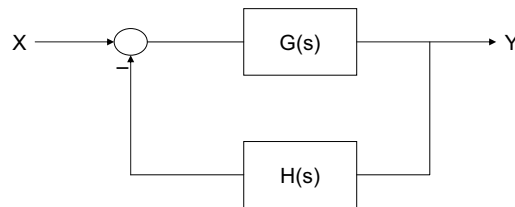


Fig. 5.27: A block diagram illustrating a simple control system. The plant $G(s)$ is controlled via feedback through the gain filter $H(s)$.

$G(s)$ is controlled by feedback through a gain filter $H(s)$. There are many methods of choosing the appropriate gain filter including gain phase margins, nyquist plots, pole zero placements etc, and an abundant supply of literature discussing these topics, so we will not repeat any of this here. However for the purpose of this analysis, we will assume an appropriate gain filter $H(s)$ is chosen for the desired and stable control of the output Y .

Converting this system into a hierarchical feedback system would involve multiple feedbacks of the error signal into $G(s)$ via band pass filters. This system could then be simplified to the block diagram shown in Figure 5.28. Given that $T_1(s) + T_2(s) + \dots +$

$T_n(s) = 1$, the hierarchical system simplifies further to the general feedback system indicated in Figure 5.27.

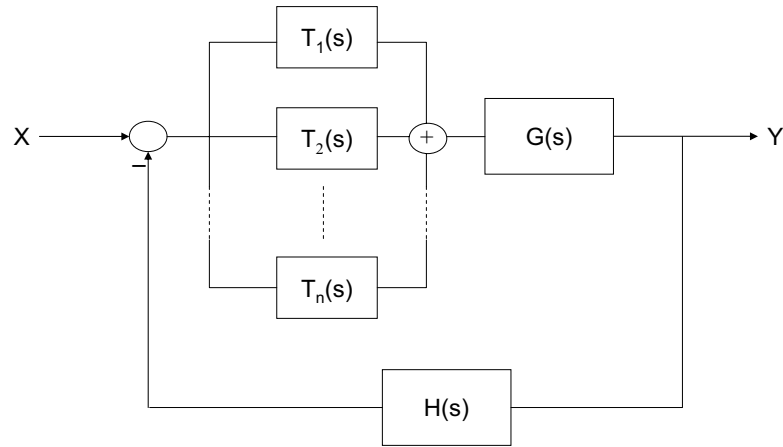


Fig. 5.28: A block diagram illustrating a general process of splitting the error signal and feeding back via separate filters, $T_n(s)$ to form a hierarchical feedback system.

This result tells us that for an appropriate choice of filters $T_n(s)$, the task of ensuring system stability is greatly simplified. If $T_1(s) + T_2(s) + \dots + T_n(s) = 1$, then the overall system performance is defined by the $H(s)$ filter, and independent of the hierarchical splitting of the feedback signal.

5.4.3 Switching to Hierarchical Control - AIGO

In order to apply controlling forces on the test mass for the AIGO suspension, we aim to split the feedback through the IP (inverse pendulum stage), CM (control mass stage) and the TM (test mass stage). Given that initial locking has been successful and a global length signal exists, a fade in/fade out method of switching the control forces from initial locking to hierarchical control should ensure a smooth transition.

With the length signal split and fed to the three stages of actuation as mentioned above, the feedback loop can be simplified as illustrated in Figure 5.29. The mechanical transfer functions have been included in the block diagram, whilst the actuator and sensor transfer functions are accounted for indirectly in the definition of the filters $LP(s)$, $BP(s)$ and $HP(s)$. These filters represent the combined series combination of the sensing transfer function, digital filter transfer function and the actuation transfer function.

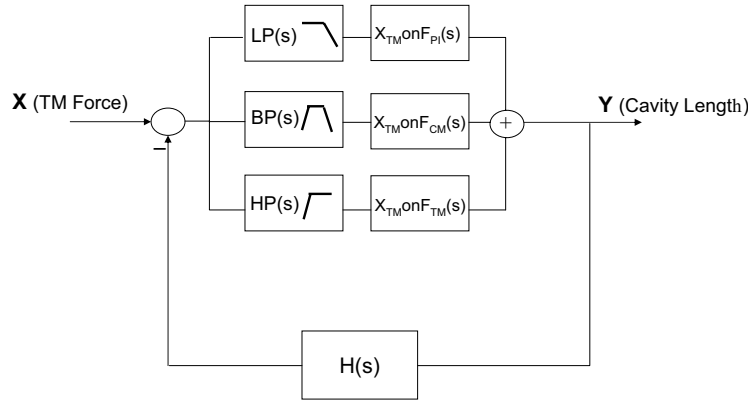


Fig. 5.29: Block diagram of the proposed hierarchical feedback for the AIGO cavity length control system.

The block diagram of Figure 5.29 can be rearranged to that shown in Figure 5.30. It can be seen that the form of this feedback is the same as that of Figure 5.28.

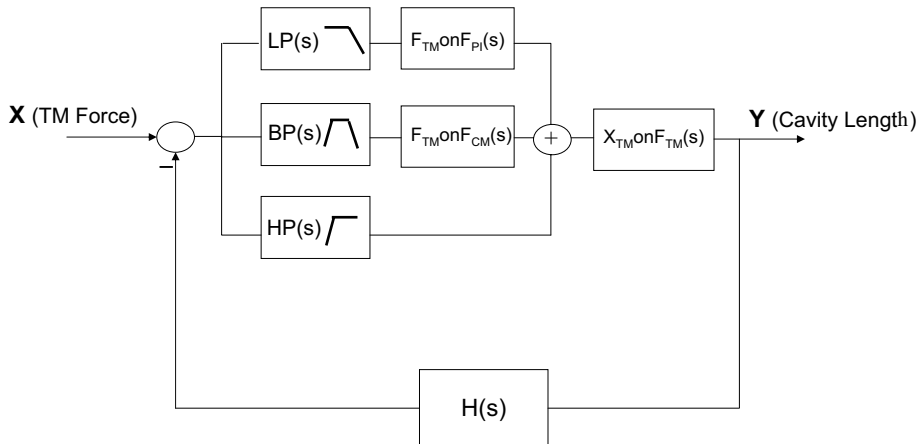


Fig. 5.30: Rearranged block diagram of the proposed hierarchical feedback for the AIGO cavity length control system.

Therefore the specifications of $H(s)$ can be chosen by considering only the transfer function $X_{TM}onF_{TM}(s)$, and independently of the ‘split’ feedback components, given that $LP(s).F_{TM}onF_{IP}(s) + BP(s).F_{TM}onF_{CM}(s) + HP(s) = 1$. Thus, solving the specifications of the feedback filter $H(s)$ is in fact the same problem as that for the initial cavity locking feedback, as described in section 5.4.1.

This implies that there is no difference between the controlled length of the optical cavity, whether it be in initial locking phase, or hierarchical control. This is true from an external point of view, when one only observes the cavity length. However, the sensitivity of the detector is significantly influenced by the actuation noise, which is

reduced through the hierarchical technique. It is also unlikely that the split path will have an overall transfer function of exactly 1. The effect that this difference from unity will have on stability will be discussed below.

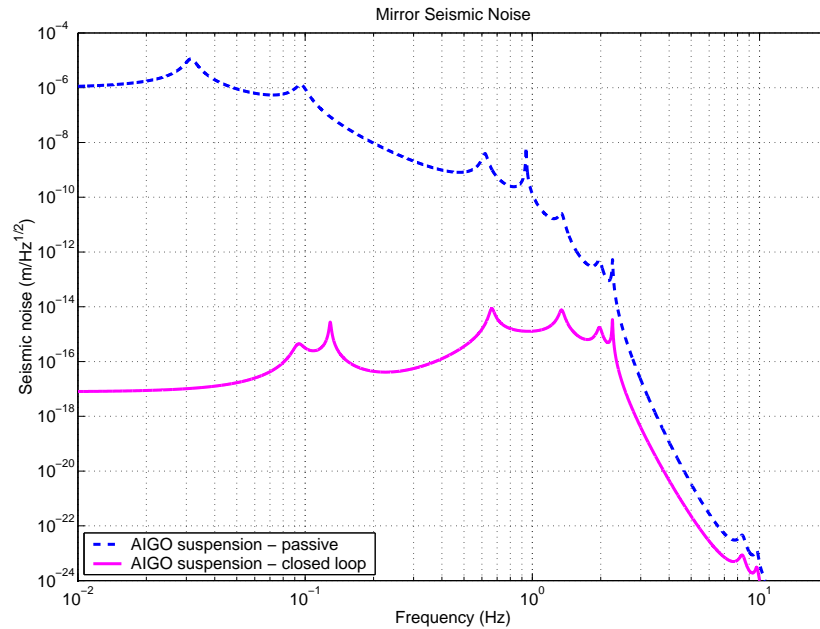


Fig. 5.31: Seismic induced cavity length spectrum of the open and hierarchical closed loop system.

The resultant closed loop seismic spectrum of the hierarchical controlled cavity is illustrated in Figure 5.31. This is through the use of the same feedback filter $H(s)$ as discussed in section 5.4.1. However the stability analysis used for this feedback filter, i.e. the open loop gain/phase margins obtained in section 5.4.1, is only relevant if the parallel combination of the split path has a transfer function of 1.

The open loop gain and phase plots of the parallel combination of the chosen split paths as described above is illustrated in Figure 5.32. The phase remains between -10 and 10 degrees throughout the entire frequency range of interest (DC to 10kHz), while the gain remains between 0.75 and 1. From Figure 5.23, the unity gain frequency of the initially locked cavity is 40Hz, with a phase margin close to 45° . The combined gain of the split paths at 40Hz, as illustrated in Figure 5.32 is approximately 0.8, and therefore the unity gain frequency of the hierarchical feedback system will be only slightly lower, but still approximately 40Hz. The extra phase delay at this frequency is 7.5° , and given that a phase margin of 45° was established for initial locking, the extra delay caused by the combined split filters does not adversely affect the system.

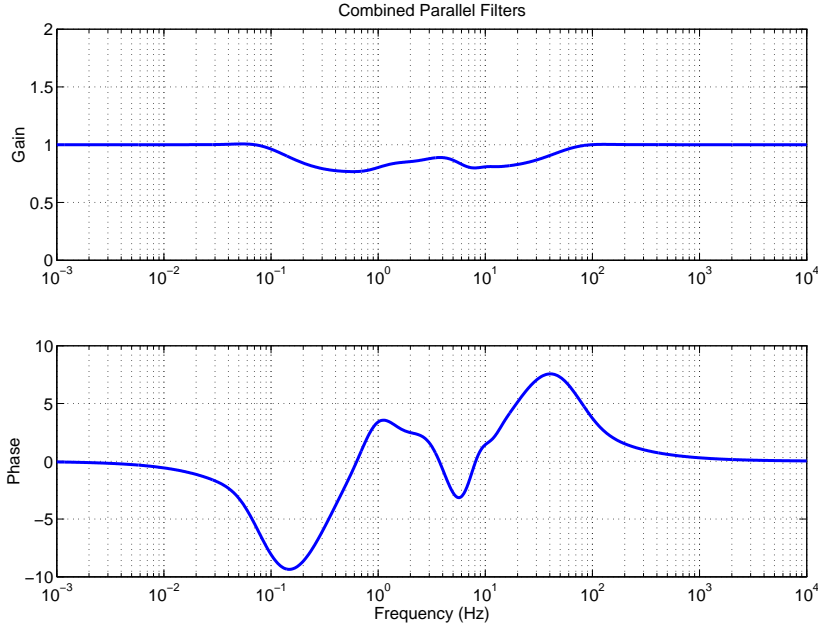


Fig. 5.32: The open loop gain and phase plots of the parallel combination of the split paths.

Consequently, the described method of hierarchical feedback to the isolation system for maintaining cavity lock can be applied without significantly affecting the stability.

The RMS residual motion of the hierarchical controlled cavity length signal is plotted in Figure 5.33. As mentioned earlier, it is required that the RMS residual motion be less than 10^{-14} m in order for the high Q optical cavities not to saturate any photodiodes. The plot of the expected RMS residual motion of the cavity length signal illustrates that the AIGO optical cavity can be sustained to the requirements of advanced gravitational wave detectors when under the control of the hierarchical system as described above.

Of course the whole idea of hierarchical suspension control is to increase the instrument sensitivity by reducing the control noise that is seen at the detector output. Actuation noise is likely to dominate this family of noise sources, and hence the desire to minimise the required actuation forces through hierarchical feedback methods. The actuation force spectrums for each of the IP, CM and TM locations within the AIGO hierarchical scheme is illustrated in Figure 5.34. These are the closed loop feedback force spectrums induced by seismic noise.

The resulting residual force for each actuation point is plotted in Figure 5.35. These plots indicate the required actuation force magnitudes of the hierarchical system. The maximum actuation force at the TM has been reduced to 20nN compared to 500uN as

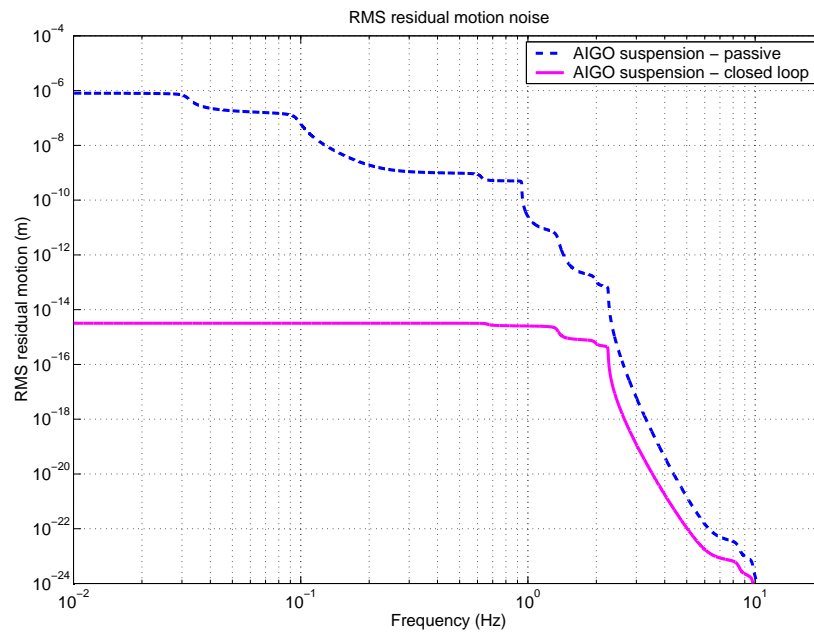


Fig. 5.33: Seismic induced cavity length RMS residual motion of the open and hierarchical closed loop system.

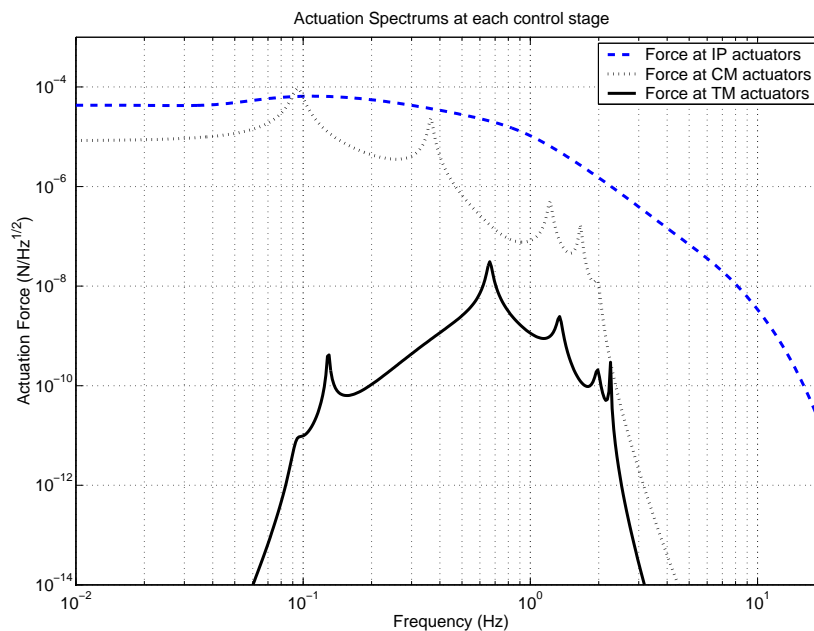


Fig. 5.34: Closed loop actuation force spectrum for each actuation point, IP, CM, TM while under hierarchical feedback length control.

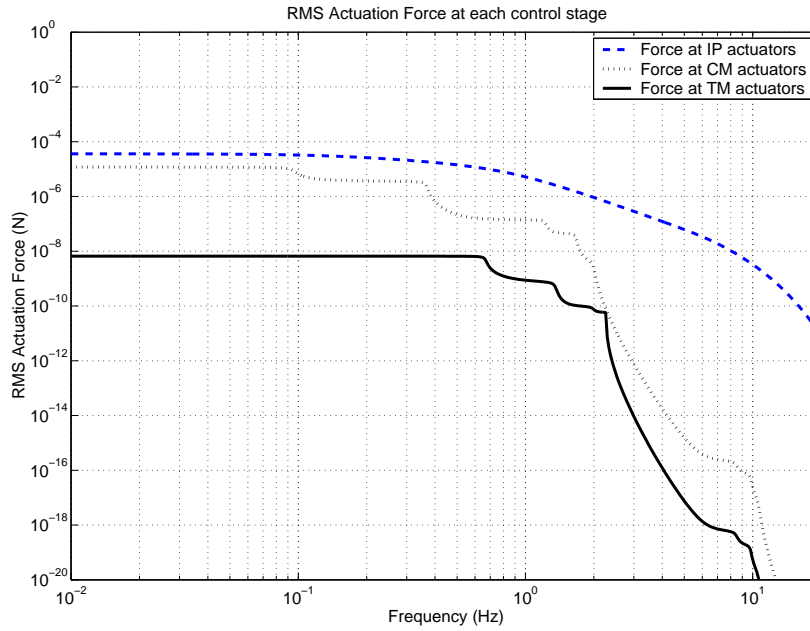


Fig. 5.35: Closed loop actuation residual force for each actuation point, IP, CM, TM while under hierarchical feedback length control.

estimated in section 5.4.1. Actuation at the CM point should not exceed approximately 100uN while actuation levels required at the IP cannot be predicted using the residual force plot, since this does not take into account the low frequency millimetre scale motion that must be compensated. However IP actuators with a force range capacity of 0.25N are able to shift the fully loaded isolator several millimeters, sufficiently covering the hierarchical lock requirements as well as the low frequency millimeter motion requirements.

The effective feedback gain that is contributed by each of the actuation points is illustrated in Figure 5.36. It is interesting to note the frequency bands within which each actuation point dominates the mirror positioning. Above 5Hz, it is the TM actuators that dominate. Between 0.3Hz and 5Hz, the CM actuators dominate and motion below 0.3Hz are applied mainly through the IP actuators. This plot summarises nicely the concept of splitting feedback to form a hierarchical system.

As was done at the end of section 5.4.1, the actuation noise of the locked cavity can be approximated. Again, the output noise of the D to A converters ($300\text{nV}/\sqrt{\text{Hz}}$) was used to approximate the contribution of actuation noise from the TM electrostatic actuators. The reduction of the maximum force required by the electrostatic actuators from 500uN to approximately 20nN due to the hierarchical feedback method reduces

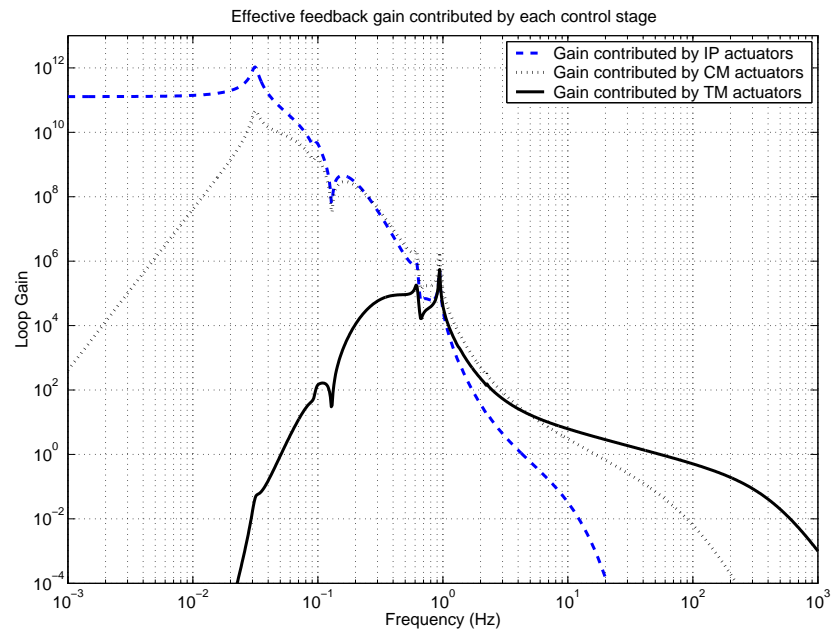


Fig. 5.36: Feedback gain that is contributed to each of the actuation locations within the hierarchical system.

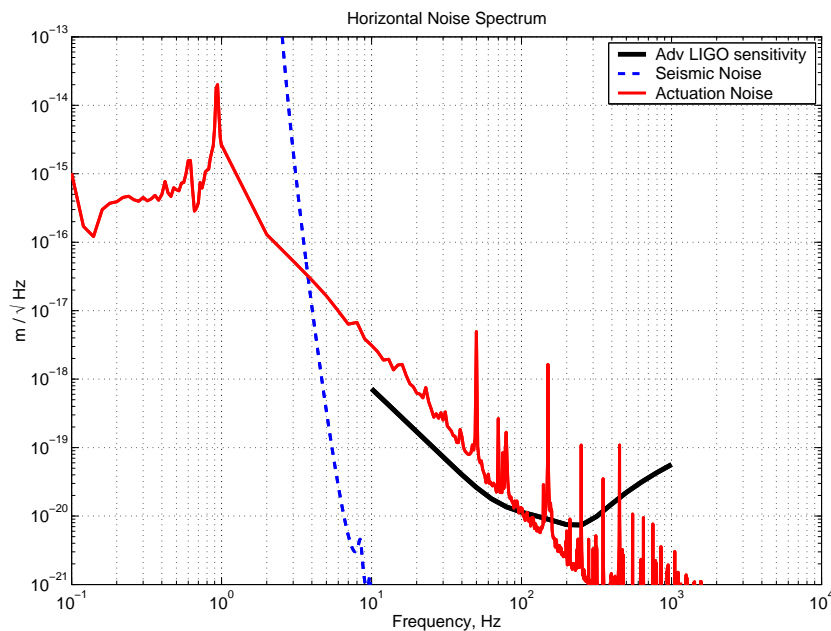


Fig. 5.37: A comparison of actuation noise during hierarchical feedback with the expected AIGO seismic noise, and broadband sensitivity of an advanced interferometric gravitational wave detector.

the voltage range to be applied to the actuating electrodes. As a result, the maximum actuating force of the electrostatic actuator is designed to be reduced from $\pm 0.5\text{mN}$ to $\pm 210\text{nN}$ when switching from initial locking to hierarchical control mode. This will reduce the actuation noise by more than a factor of 1000 to an acceptable level (as discussed below). The $\pm 210\text{nN}$ force range of the actuator also provides an extra ten times safety margin over the estimated requirement of up to 20nN . This also leaves room for future improvements in sensitivity whilst maintaining the same cavity locking technique.

The actuation noise is illustrated in Figure 5.37 and is compared to the expected seismic noise and advanced gravitational wave detector sensitivity requirements. It can be seen that above 100Hz , the actuation noise can be reduced below the required sensitivity. However for frequencies below 100Hz , further reduction in noise is required. A method of further reducing the actuation noise through the clever use of analogue and digital filters is discussed in the following section. It must also be mentioned that the actuation noise from the TM actuator is in general the most dominant source of this type of noise. For this reason, the plot above is not crowded with extra noise curves. A curve of all actuation noise is presented in section 5.5.

5.4.4 Noise Improvement through Emphasis Filtering

As mentioned earlier, actuation noise at the test mass stage is dominated by DAC voltage noise. For TM electrostatic actuation, this DAC noise level of approximately $300\text{nV}/\sqrt{\text{Hz}}$ is amplified through a High Voltage amplifier with a gain of about 20 for initial locking. Figure 5.38 illustrates actuation noise in a block diagram. Of course sensing noise would also be present through the actuation path, but it has been assumed that motion sensing will be a comparatively low noise signal obtained from the global cavity length signal. For this reason, sensing noise has been omitted in this study.

The block diagram shows that it should be possible to reduce the noise at the High Voltage amplifier input to approximately $10\text{nV}/\sqrt{\text{Hz}}$ over a limited frequency band. This corresponds to the input noise of the PA85 High Voltage amplifier, given in the PA85 datasheet [127]. The frequency band that is of interest is of course the gravitational wave detection band of approximately audio frequencies, 10Hz to 10kHz . The obvious solution to reduce noise would be to insert a low noise analogue filter

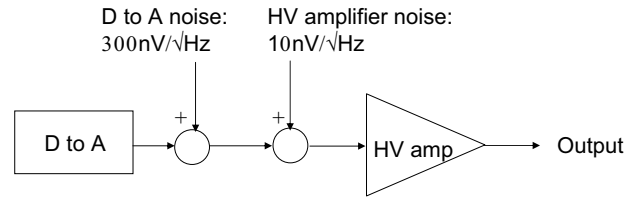


Fig. 5.38: A block diagram showing the source of the dominant electrostatic actuation noise. Without additional filtering, noise at the output is a result of amplified D to A (DAC) output noise.

between the DAC output and the HV amplifier. The purpose of this filter would be to reduce the DAC output noise level within the detection band such that it falls below $10\text{nV}/\sqrt{\text{Hz}}$. However the phase lag associated with the filter will likely cause instabilities in the control system.

In fact the phase lag can be removed through the use of another filter, known as the preemphasis filter. The preemphasis filter, along with the low noise analogue filter, (the deemphasis filter) can be used to reduce the output electronic noise without jeopardising the stability of the high gain control system. The use of emphasis filters in this situation is illustrated in Figure 5.39

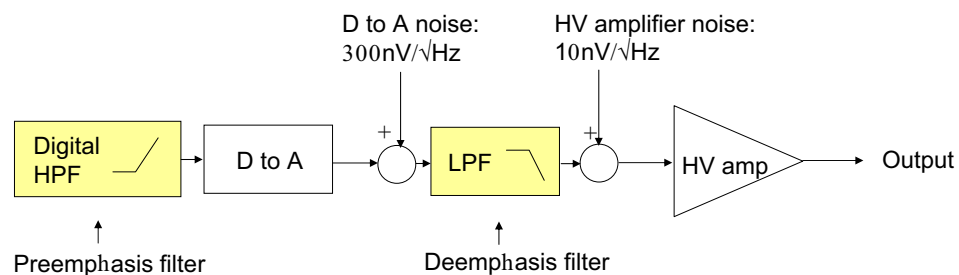


Fig. 5.39: A block diagram showing the inclusion of preemphasis and deemphasis filters to reduce actuation noise. In principle, the output noise can be reduced to the output noise level of the HV amplifier over the desired frequency band.

The block diagram shows the use of a low pass deemphasis filter between the DAC and the HV amplifier. By designing this filter such that the corner frequency is below the detection band, the amount of DAC noise within the detection band should be reduced. The preemphasis filter is to be implemented digitally, and is designed to be

the inverse of the deemphasis filter. The two filters combined should exhibit negligible phase lag and hence have no significant effect on the control system performance.

Figure 5.40 shows the magnitude response of the two emphasis filters. Second order filters have been modeled which flatten off at approximately 100Hz. The corner frequency of both filters is located at 0.8Hz with a second order roll off. This allows the deemphasis filter to sufficiently filter DAC noise within the detection band (beginning at approximately 10Hz). The high pass preemphasis filter is necessary to cancel the

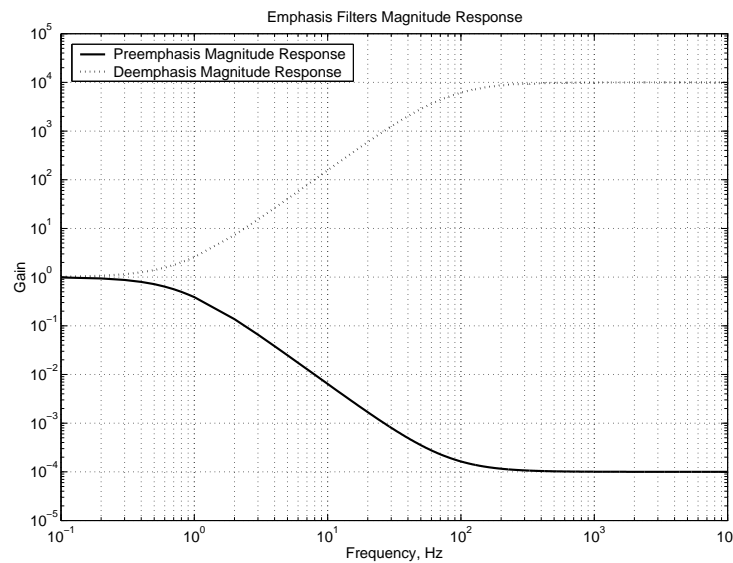


Fig. 5.40: Magnitude response of the Preemphasis and Deemphasis filters. Second order filters have been modelled with corner frequencies at 0.8Hz and 100Hz.

phase lag exhibited by the deemphasis filter. However, one must be careful that the high pass filter does not saturate the DAC. In the case of the electrostatic actuator for AIGO, the feedback signal that will be passed through the preemphasis filter consists primarily of heavily filtered seismic noise. Therefore the DAC will not be saturated despite the signal being amplified by a second order high pass filter at frequencies above 0.8Hz. Since the mirror is mechanically isolated by 5 pendulum stages and 2 preisolator stages, sufficient tuning and pendulum mode damping of the isolation system implies that a 16th order high pass filter (and hence 16th order deemphasis filter) could be used without DAC saturation problems. However in reality, pendulum and higher order modes of the suspension chain would cause such a system to saturate. Given that second order emphasis filters will be sufficient and that electronic noise can only be reduced to the HV amplifier noise level, emphasis filters with order greater than 2 are unnecessary.

The effect of emphasis filtering on the control system noise is illustrated in Figure 5.41. The deemphasis transfer function is given by

$$H_{de}(s) = \left(\frac{5}{s+5}\right)^2 \left(\frac{500+s}{500}\right)^2 \quad (5.7)$$

where the magnitude response is that plotted in Figure 5.40. The preemphasis filter has a transfer function equal to the inverse of $H_{de}(s)$, i.e. $H_{pe}(s) = 1/H_{de}(s)$.

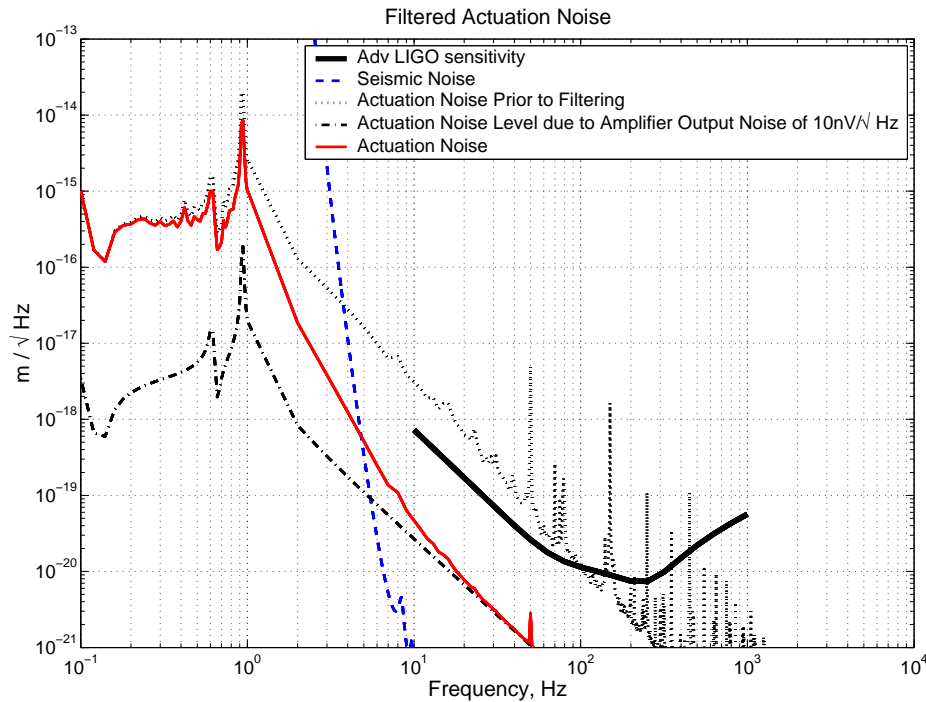


Fig. 5.41: The improvement in sensitivity that can be achieved with emphasis filtering techniques.

Again, the measured DAC noise has been used to compute its contribution to the cavity length displacement noise spectrum. This is labeled as ‘Actuation Noise Prior to Filtering’, as it is the same actuation noise that is expected without emphasis filtering. The actuation noise expected from the HV amplifier input noise is also plotted and labeled ‘Actuation Noise Level due to Amplifier Input Noise’. It can be seen that the filtered actuation noise has improved by close to two orders of magnitude above 10Hz, as the contribution from the DAC noise is removed.

5.5 Noise Analysis and Comparison

Figures 5.42 and 5.43 compare the expected test mass actuation noise with the other sources of actuation noise as well as seismic noise and the expected sensitivity of Ad-

vanced LIGO. In Figure 5.42 the test mass actuation noise for initial locking is displayed, while in Figure 5.43 we show the test mass actuation noise during hierarchical control.

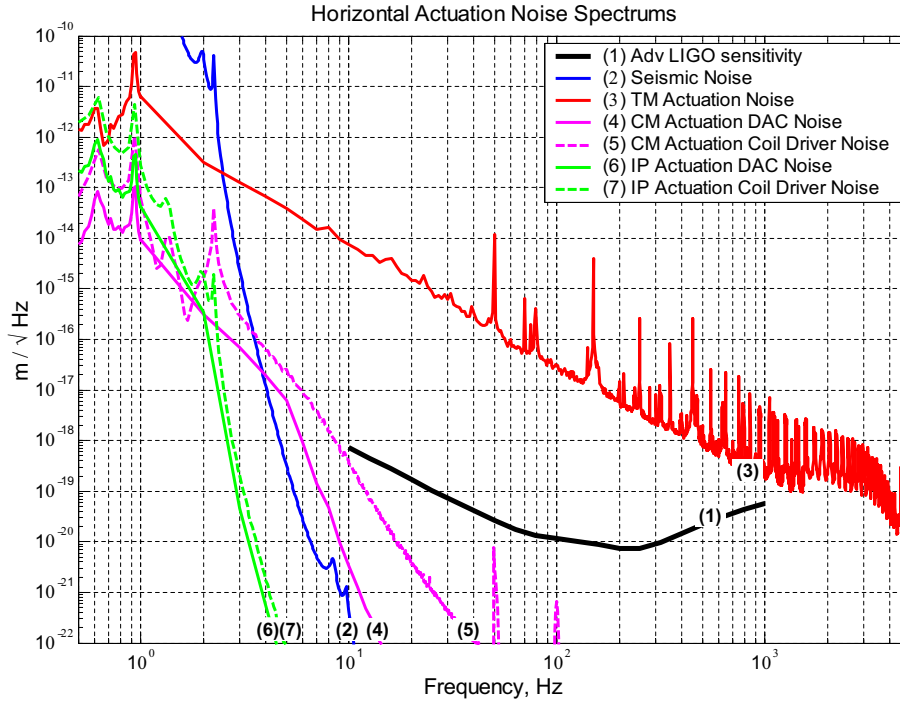


Fig. 5.42: Actuation noise sources in comparison to seismic noise and the expected sensitivity of Advanced LIGO. (3) Actuation noise from the electrostatic actuator, dominated by DAC noise. (4) DAC noise from the CM actuators. (5) Current noise from the CM coil drivers. (6) DAC noise from the IP actuators. (7) Current noise from the IP coil drivers.

For each of the IP and CM control noises, two noise curves have been plotted and labeled as either DAC noise or coil driver noise. These spectrums represent the actuation noise that is seen at the test mass, i.e. having passed through the relevant stages of vibration isolation. The DAC noise corresponds to DAC voltage noise driving the pre-isolator or control mass, and the resultant vibration filtering through to the test mass. This is the same curve that is plotted for the test mass electrostatic actuation noise. The coil driver noise results from the current noise due to the coil driver exerting forces on the pre-isolator and control mass. For both the IP case and the CM case, it is observed that the coil driver noise is likely to dominate. Since the RL actuation stage will only be used for very low frequency compensation, the actuation noise is heavily low pass filtered and hence falls below any of the noise spectrums shown. For this reason, the RL actuation noise curve was not included in these figures.

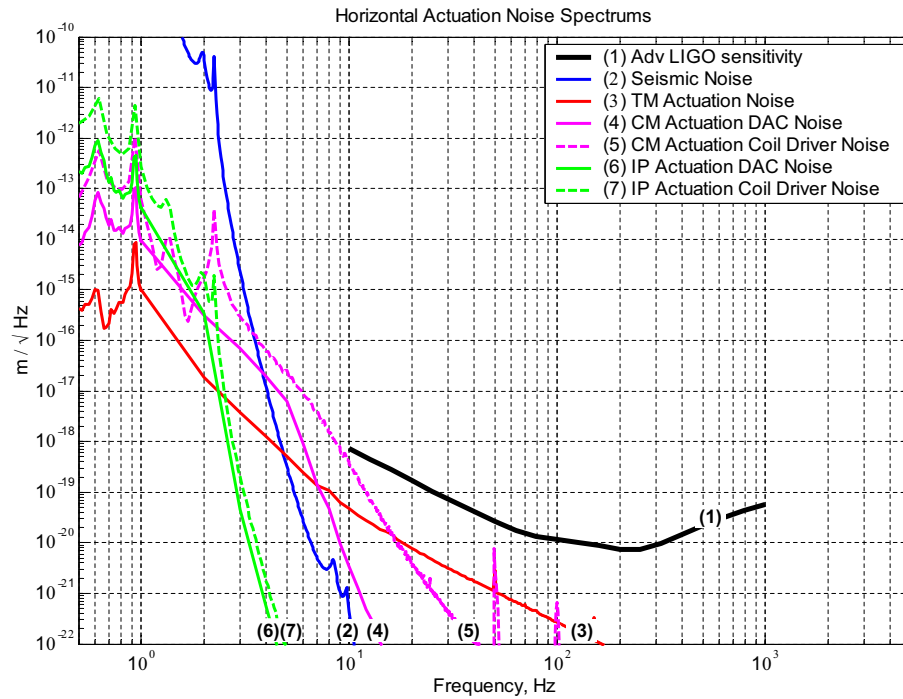


Fig. 5.43: Actuation noise sources in comparison to seismic noise and the expected sensitivity of Advanced LIGO. (3) Actuation noise from the electrostatic actuator, dominated by HV amplifier noise. (4) DAC noise from the CM actuators. (5) Current noise from the CM coil drivers. (6) DAC noise from the IP actuators. (7) Current noise from the IP coil drivers.

For the initial locking actuation noise curves, it can be seen that all actuation noise is dominated by the test mass electrostatic actuation noise. This is due to the large force required by the actuator, and the lack of mechanical filtering since the force is applied directly on the test mass. The optimised hierarchical actuation curves are shown to be compatible with expected advanced detector sensitivity. In this case, the hierarchical feedback reduces the force required at the test mass level and hence also the amount of test mass actuation noise. It can be seen that this electrostatic actuation noise only becomes dominant at 30Hz, but is still an order of magnitude better than the required sensitivity. Below 2Hz, seismic noise dominates whilst in between 2Hz and 30Hz, the control mass coil driver noise is most significant. The high level of control mass coil driver noise results from the need to compensate the low frequency rotation mode of the entire suspension chain as discussed earlier. If low frequency sensitivity is to be improved, it is possible to achieve this through the use of emphasis filtering techniques on the control mass actuators.

5.6 Summary

Table 5.4 summarises the force range required by the actuators at various stages; Inverse Pendulum stage (IP), Control Mass stage (CM) and the Test Mass stage (TM). The actual range of the actuators to be implemented within the AIGO isolation system is also shown, displaying a significant safety margin in most cases. This is already on top of the ‘worst case’ seismic noise that was used in the study. With the force range of the actuators set at the levels shown, the expected control noise is given previously in Figure 5.42 and Figure 5.43 in Section 5.5.

	IP	CM	TM
Force Range Available	0.25N	100μN	500μN
Local Horizontal	43 μ N	-	-
Local Torsion (Yaw)	-	100 μ N	-
Local Pitch	-	< 100 μ N	-
Very Low Freq	0.25N	-	-
Initial Mirror Stopping	-	-	460 μ N
Initial Lock Hold	-	-	500 μ N
Hierarchical Hold	100 μ N	100 μ N	20nN

Tab. 5.4: Actuation force required at various stages on the AIGO isolation system.

Local Horizontal Control

Local horizontal control is discussed in Section 5.3.4. The purpose of this control loop is to minimise the RMS residual velocity of the suspended mirror in order to ease the process of initially stopping the mirror and locking the cavity. The best location for this compensation to occur is at the IP, where it is the three lowest resonant modes of the isolation system that contribute most to mirror velocity. Due to the various resonant modes of the entire suspension chain, a non trivial feedback filter is required, which includes the use of notch and lead filters. The result however is only a small reduction in RMS residual velocity. The mechanical design of the isolation system has already resulted in almost minimal mirror velocity, and thus this control loop may currently be omitted in order to simplify the control system.

Local Torsion Control

Local torsion control is discussed in Section 5.3.2 and refers to the 0.016Hz torsion mode of the entire suspension chain. The requirement of this control loop is to reduce the yaw motion of the mirror to within $1.5\mu\text{rad}$ such that cavity locking can be achieved and the auto alignment system can operate. It is found that the $100\mu\text{N}$ range of the CM actuators will be enough to compensate the 0.016Hz torsion mode.

Local Pitch Control

Local pitch control is discussed in Section 5.3.3. This refers to the low frequency pitch oscillations with period expected to be greater than 5 seconds due primarily to the pitch mode of the suspended control mass. The level of pitch motion is likely to be very small since there is very little tilt coupling through the isolation chain. The CM vertical actuators with force up to $\pm 50\mu\text{N}$ are more than capable for the compensation of this mode. It is likely that these pitch mode actuators will be used primarily for initial mirror alignment.

Very Low Frequency Compensation

Very low frequency compensation refers to the need to compensate for millimetre range motions caused by daily changes in temperature affecting the distance between two suspended mirrors. Actuators with range of 0.25N can translate a fully loaded isolation system approximately 5mm. This displacement range is enough to compensate these low frequency motions.

Initial Mirror Stopping

Initial mirror stopping refers to the task of reducing to zero the relative velocity between the two mirrors that form the optical cavity. The relative velocity must be reduced to zero within an optical fringe, corresponding to a distance of approximately 0.3nm. This is discussed in Section 5.4.1. It is found that a maximum actuation force of $460\mu\text{N}$ is required with a time constant of 0.27ms. This can be achieved with the electrostatic actuators at the TM stage.

Initial Lock Hold

Initial lock hold is also discussed in Section 5.4.1 and refers to the process of holding the optical cavity in lock once an initial lock is achieved. Further more, the relative RMS residual motion between the two mirrors must be kept below 10^{-14}m in order not to saturate the photodiodes measuring light intensity outside of the cavity. This can be done using the TM actuators with an actuation range of $500\mu\text{N}$.

Hierarchical Hold

Hierarchical hold is similar to Initial lock hold in that it refers to the force required to keep the two mirrors locked to within a relative RMS displacement of 10^{-14} m. In this case however, the force is not applied entirely at the TM stage but rather distributed throughout the IP, CM and TM stages in a hierarchical feedback manner. This method is discussed in Section 5.4.2 and Section 5.4.3. The use of this method allows the same feedback signal to be applied to the suspended mirror with a significantly smaller force requirement on the TM actuators. This results in a lower level of control noise within the detection frequency band. It is found that the required level of force on the IP, CM and TM actuators for this feedback method is satisfied with force ranges of $100\mu\text{N}$, $100\mu\text{N}$ and 20nN respectively.

CHAPTER 6

AIGO TEST MASS CONTROL

6.1 Introduction

In this chapter, the current test mass suspension at AIGO is presented. The initial task is to characterise the vibration isolation system with an optical cavity as soon as possible, and hence more emphasis is placed on the construction of a simple reliable mirror suspension method over extremely low thermal noise performance. The discussion of such a suspension is given below, including the expected suspension thermal noise. The basic design of the electrostatics that has been implemented to sense and actuate directly on the test mass is also discussed, with more detail shown in the circuit diagrams given in Appendix B. Finally, some initial results involving the control and positioning of the test mass currently suspended at AIGO is presented.

6.2 The Suspension

Currently, the AIGO suspension consists of a 50mm diameter, 30mm thick sapphire mirror supported in an aluminium and stainless steel cylindrical structure that forms a ‘dummy mass’. This dummy mass replicates closely the mass and dimensions of the full sized 150mm diameter, 4.2kg sapphire mirrors that will form the Fabry Perot mirrors in east arm at AIGO. The purpose of the dummy suspension is to allow the characterisation of the high performance vibration isolation chain developed at UWA, using an optical cavity.

The dummy mass is suspended from a control mass of approximately 30kg and within a control cage which provides both mechanical safety stops for the optic, and a low noise reference from which actuation and local sensing of the test mass can be performed. The control mass, which is suspended from the vibration isolation system

also contains actuators and sensors from which 5 degrees of freedom (translation in all 3 dimensions, yaw and pitch) can be accessed. Illustrations of the control mass are shown in Figure 6.1.

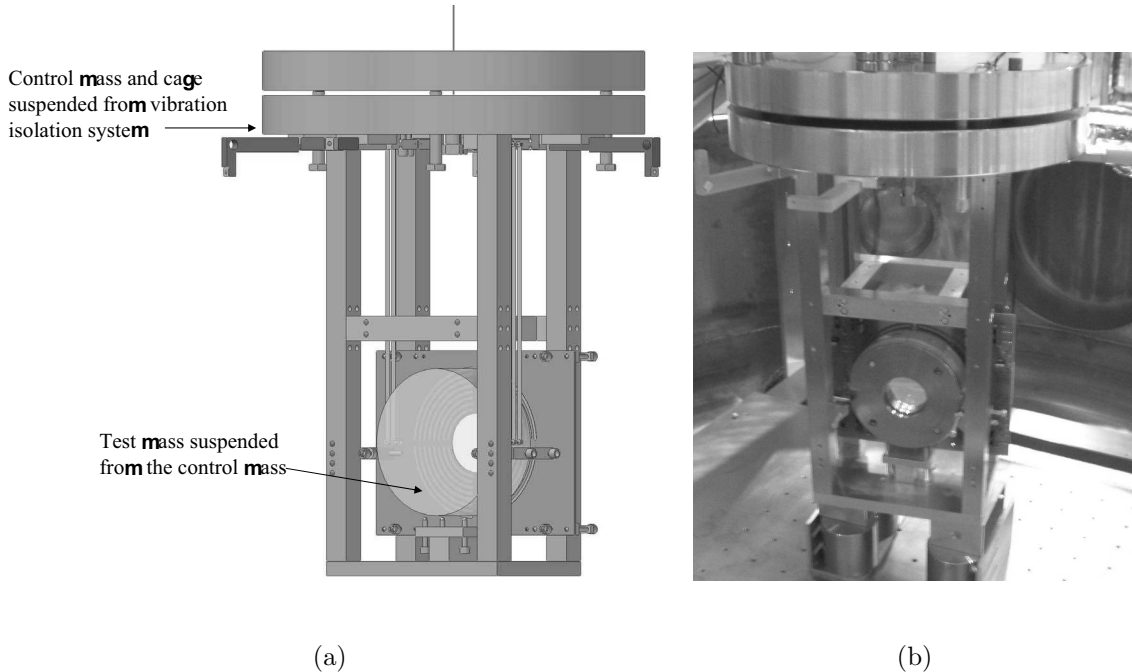


Fig. 6.1: a) AIGO control mass drawing. b) A Photo of the suspended AIGO control mass.

The optic is suspended from the control mass using $25\mu\text{m}$ niobium ribbon removable modular suspension elements. For the initial dummy suspension, we have not bonded niobium high pressure contact pins to the ends of the ribbon, instead we have used temporary brass pins that clamp to the suspension ribbons through a high pressure contact tooth. Modelling of the niobium high pressure contact pins when under load is given at the end of Chapter 4. The same pin design has been used for the initial brass pins, and therefore the contact points will be stressed at about 40% of yield strength. Although a slightly higher contact pressure is desired for the brass design, the extra thermal noise that may be induced is not of major importance for this test. Currently, priority lies in testing of the performance of the vibration isolation system. For this reason, a temporary brass/niobium suspension at the expense of a possible increase in thermal noise is acceptable. The ribbon clamping mechanism, as opposed to a permanent bond, is also not ideal. However, the current design provides high enough contact pressure (approaching the yield strength of niobium) to minimise slip

stick friction, whilst not weakening the suspension ribbon at the point of clamping. Illustrations of the brass pin and its connection to the control mass and the test mass is shown in Figure 6.2.

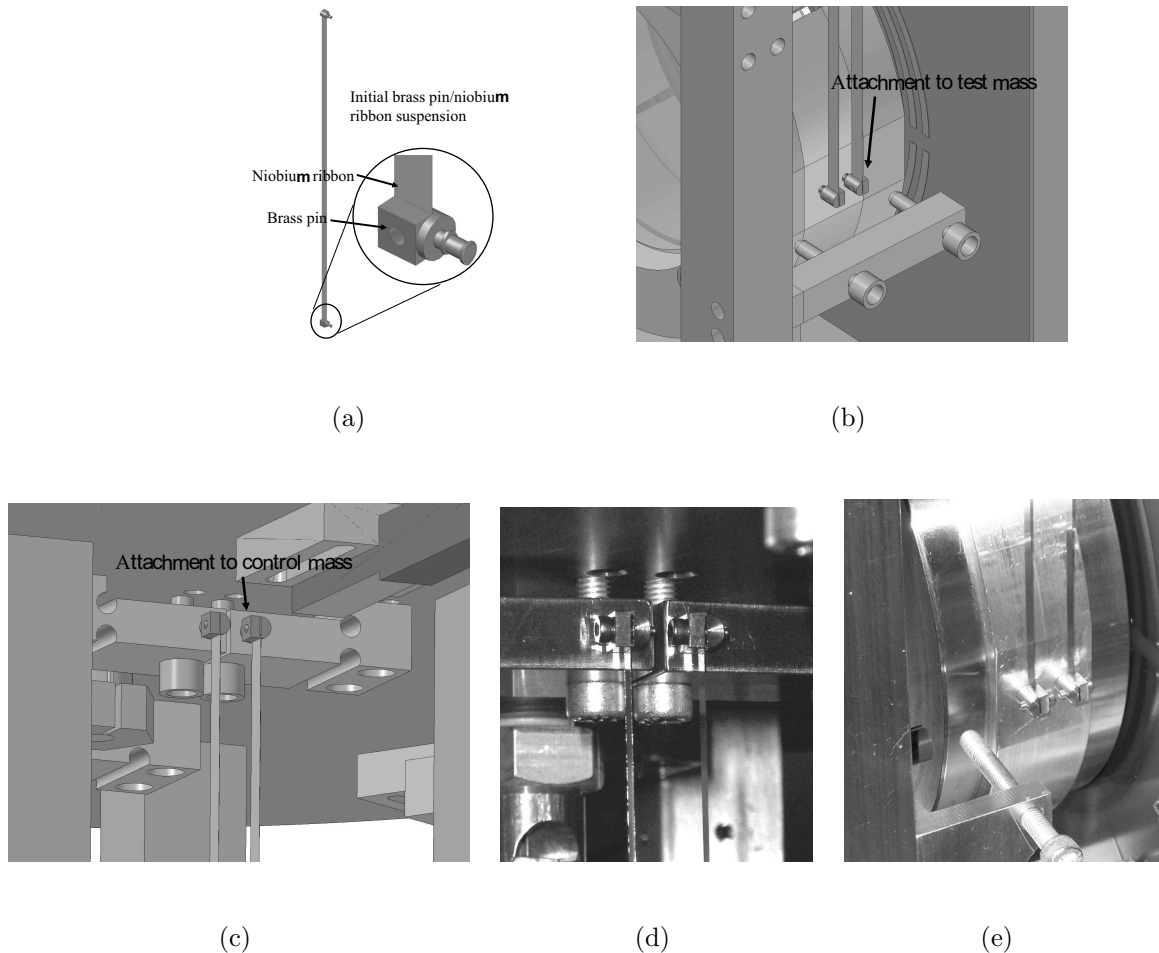


Fig. 6.2: a) The brass/niobium suspension currently being used. b) Pin connection to the test mass. c) Pin connection to the control mass. d) Photograph of the brass pins connected to the dummy mass. e) Photograph of the brass pins connected to the control mass.

Replacement of the brass/niobium suspension to the full niobium suspension is expected when the dummy mirrors are replaced with the full sapphire optics. For properly treated niobium [97, 76], we expect that a loss angle approaching a few times 10^{-5} can be achieved for the $25\mu\text{m}$ thick ribbons. With such loss, the expected suspension thermal noise spectrum for $25\mu\text{m}$ thick, 3mm wide, 300mm long niobium ribbons is given in Figure 6.3. For this model, we have assumed that four such ribbons support a 4.2kg optic. An assumption has also been made that the laser is probing the center of the optic.

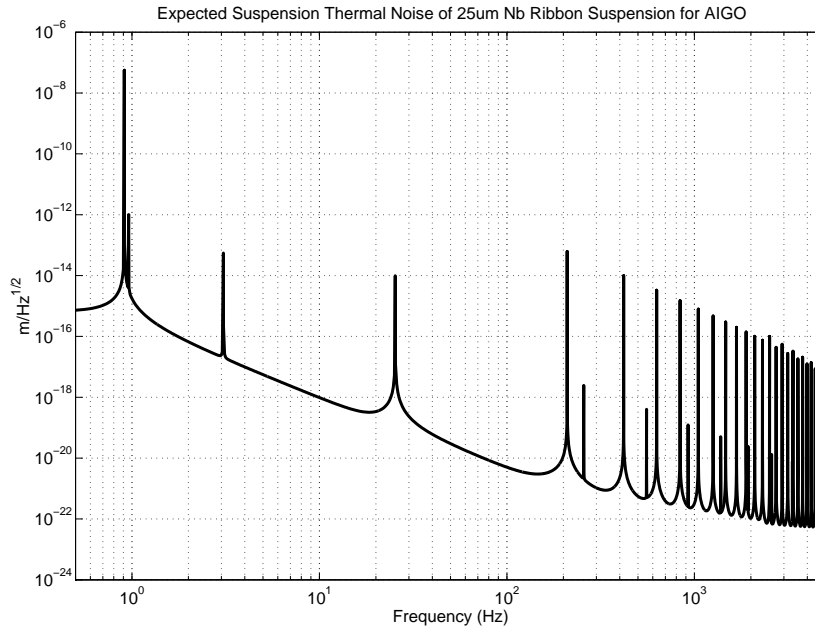


Fig. 6.3: Expected suspension thermal noise from the AIGO four ribbon niobium suspension. Each ribbon is 300mm long, 3mm wide and $25\mu\text{m}$ thick.

The peak at 25Hz results from 0.1% coupling from suspension thermal noise in the vertical direction. It can be seen that the vertical mode contributes a small amount to the horizontal direction thermal noise particularly around 25Hz. The first violin mode occurs just above 200Hz, while below about 5Hz, it is expected that seismic noise will dominate.

If the laser spot is not centered on the optic, the thermal noise level will increase due to coupling with the pitch and yaw modes. This is illustrated in Figures 6.4(a) and 6.4(b), where the x direction suspension thermal noise at 100Hz is plotted against vertical spot displacement and horizontal spot displacement respectively. The plots show that the suspension thermal noise is much more sensitive to vertical spot misalignments than horizontal spot misalignments. The vertical misalignment causes x direction coupling to the pitch mode oscillation and the horizontal spot misalignments cause coupling to the yaw mode. The higher frequency of the pitch mode oscillation compared to the yaw mode results in a higher contribution to thermal noise at higher frequencies, and hence the larger sensitivity of suspension thermal noise on the vertical spot position.

A comparison of the suspension thermal noise observed at the centre of the optic compared to a point 5mm from the centre of the optic in both horizontal and vertical

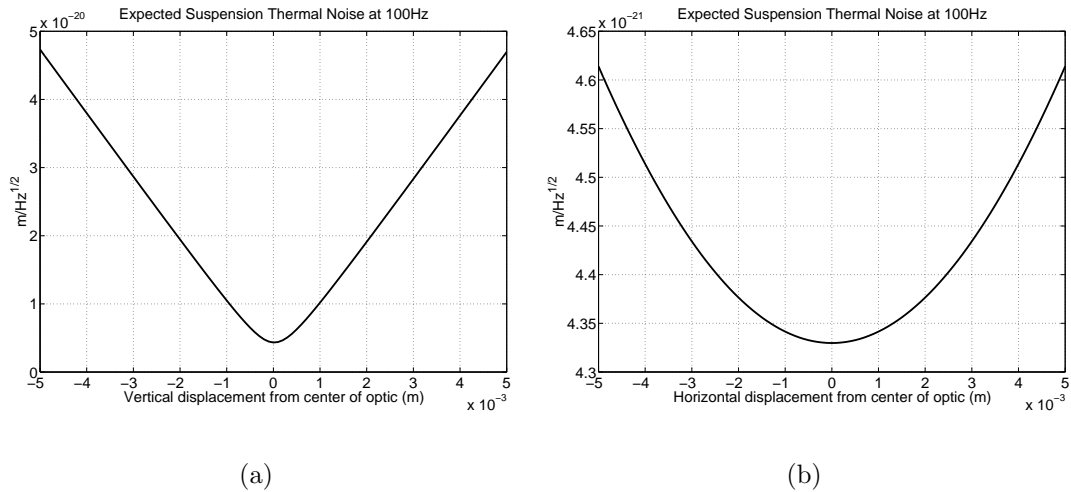


Fig. 6.4: Expected contribution of suspension thermal noise at 100Hz as a function of laser spot position in the; a) vertical (z) direction and, b) horizontal (y) direction.

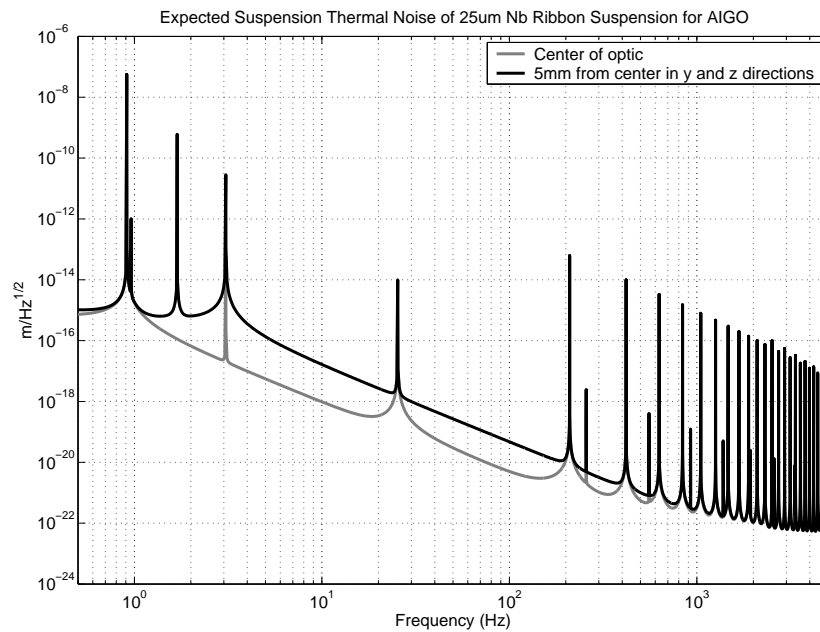


Fig. 6.5: A comparison of expected AIGO suspension thermal noise for a centred laser spot, and a laser spot located located 5mm from the centre of the optic in both horizontal and vertical direction.

(y and z) directions is shown in Figure 6.5. It can be seen that the suspension thermal noise amplitude is larger by about an order of magnitude if the laser spot is misaligned in the vertical direction by 5mm. This is due to coupling with the pitch mode of approximately 3Hz. The 5mm misalignment in the horizontal direction also results in

the appearance of a 1.7Hz yaw peak. This contribution to x direction thermal noise however is minimal compared to that resulting from the pitch mode.

6.3 The Electrostatic Actuator

6.3.1 Basic Design

Test mass actuation and local sensing is achieved via a four quadrant capacitor with electrode layout as illustrated in Figure 6.6. The capacitor design is very similar to that suggested by almost all who thought of using non-contact electrostatic actuation on suspended gravitational wave detector mirrors. It consists of electrodes of width 3mm separated by a 3mm gap in a concentric pattern as illustrated in Figure 6.6. The electrodes are designed to locate between 2 and 3mm from the face of the suspended optic. The diameter of the outer electrodes is 160mm, just larger than the 150mm diameter of the AIGO optics, while the inner electrode diameter is 60mm, sufficiently large enough for the proposed 20mm beam radius.

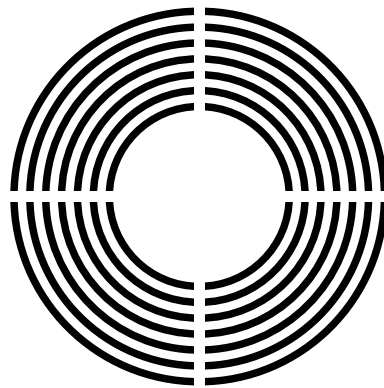


Fig. 6.6: The electrode layout for the four quadrant capacitor used at AIGO. Each quadrant has a capacitance of between 20pF to 30pF, depending on the location of the test mass. This diagram shows the physical layout of the electrodes only, and does not show the electrical connection of each electrode that is achieved via tracks on the reverse side of the electrostatic actuator plate. This can be found in Appendix B.

It was decided early that the four quadrant capacitors were to be designed as both positions sensors as well as actuators. The need for electrostatic actuation is obvious, as it provides the high frequency forces required to lock the optical cavity. It also allows direct actuation on the test mass for the purpose of mirror positioning

and alignment and damping of mirror suspension oscillations. The inclusion of mirror sensors stems from the need for local sensing of mirror position in order to ease the task of local control and reduction in residual mirror velocity. Although it was discussed in Chapter 5 that sufficiently low residual mirror velocity is expected without the need for active intervention, the capacitive sensors will be available if necessary. The capacitive sensors also provide feedback during mirror positioning and alignment.

To achieve both sensing and actuation using the same capacitor, the circuit as illustrated in Figure 6.7 is constructed. The sensing circuit simply incorporates the

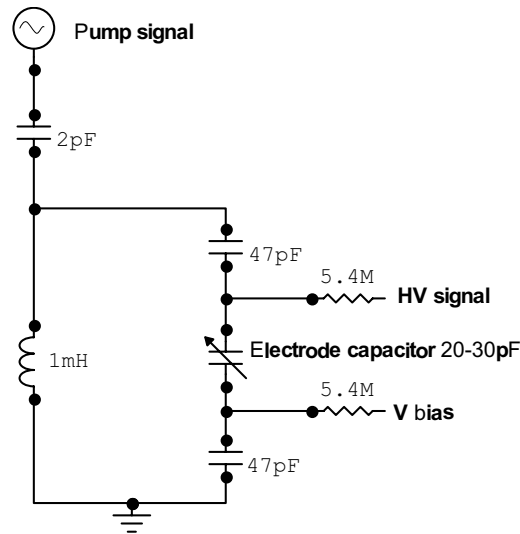


Fig. 6.7: Basic circuit constructed around the electrode capacitor used to allow both actuation and position sensing.

electrode capacitance (represented as the variable capacitor) into a resonant LRC circuit, with resonant frequency dependant on the choice of inductor. Changes in the test mass position result in changes in the circuit capacitance and thus changes in resonant frequency. In the usual manner, a comparison between the phase of the reference signal (pump signal) and the resonant signal produce an output signal that is dependant on the mirror position. We have used an analogue mixer (MPY634KP) to achieve the phase comparison. Actual circuit diagrams are given in Appendix B.

The actuation signal is supplied through the 5.4M coupling resistors as indicated in Figure 6.7. Large impedance coupling resistors are required in order not to reduce the Q of the resonant circuit to maintain high position sensitivity. High voltage signals with range $\pm 220\text{V}$ and bandwidth up to 3000Hz is achieved using a pa85 high voltage

power operational amplifier. A DC bias signal of approximately 500V is also being used.

The use of the quadrant capacitors as both sensors and actuators results in some disadvantages. Firstly, the large coupling resistors essentially result in a very high impedance high voltage amplifier. This impedance damps the motion of the suspended mirror. The effective Q factor of the damped mirror can be approximated using Equation 6.1 as discussed by Grote [125].

$$Q_{damped} = \frac{2mM\omega d^3}{C^2RU^2} \quad (6.1)$$

Here m is the mass of the test mass, M the effective mass of the actuator, ω the oscillation frequency, d the average distance between electrodes and the suspended test mass, C the capacitance of the electrodes, R the real part of the impedance of the high voltage amplifier and U the permanent bias voltage. Assumptions have been made that the amplitude of oscillation is much smaller than d , and that the bias voltage U is constant. By substituting relevant values for the AIGO suspension, with $R=10.8M$ as indicated in Figure 6.7, it is found that the effective pendulum mode Q factor is approximately 1.2×10^4 . This is a lower pendulum mode Q factor than would be desired for high sensitivity performance, and hence it is likely that the capacitive position sensing technique will need to be removed or altered before minimal thermal noise performance is required. It is possible that eventually, no local sensing at the test mass level will be required. For the initial testing of the vibration isolation system however, the ability to locally sense the test mass position may be very useful as we become more familiar with the control and dynamics of the system.

Secondly, intensity fluctuations in the sensing pump signal may introduce test mass displacement noise. Although the pump frequency will be between 500kHz to 1.2MHz, voltage fluctuations within the detection band will displace the suspended test mass and affect interferometer sensitivity. Ideally, the intensity fluctuations within the detection band should be lower than the noise of the high voltage actuation signal. The high voltage amplifier is based on an Apex pa85 high voltage power operational amplifier. It has an input voltage noise of approximately $6nV/\sqrt{Hz}$ at 100Hz as given in [127]. To supply sufficient force, a gain of 20 is required with a bandwidth up to approximately 3000Hz, and thus the output noise will be limited by about $120nV/\sqrt{Hz}$ for a voltage range of $\pm 220V$. Of course, the assumption has been made that the input signal to the

high voltage amplifier has lower voltage noise than the amplifier input noise. If this is not the case, e.g. if the output noise of the D to A converter is higher than $6\text{nV}/\sqrt{\text{Hz}}$ at 100Hz, then the high voltage output noise will also be higher. However, if the intensity fluctuations of the pump signal is kept below $120\text{nV}/\sqrt{\text{Hz}}$ at 100Hz, we can be certain that the pump signal will not significantly add to the test mass displacement noise. The other solution is of course to turn off the capacitive sensing during high sensitivity operation. When the optical cavity is locked, the local capacitive displacement signal is not needed due to the existence of the global cavity length signal.

The electrostatic actuator described above has been designed specifically for use at AIGO, and hence for integration with the AIGO suspension system and for applying forces to a 4.2kg test mass. The author sees no reason why a similar system could not be used for actuation on larger masses of size expected in advanced detectors (say 30kg). For use in such a system, a larger electrostatic plate will likely be needed in order to apply greater amounts of force. The larger surface area presented by the face of the test mass should allow for this. The precise force that will be needed (and thus the voltage bias required) will need to be re-calculated depending on issues involving the suspension system, desired sensitivity and available space for the electrodes.

6.3.2 Pitch Mode Coupling

In section 5.3.3 of Chapter 5, we discussed the coupling of control mass pitch to test mass x direction displacement due to the change in distance between the electrodes and the mirror. Similarly, electrostatic actuation on the test mass will result in coupling of test mass translation and pitch motion. This occurs due to the location of the electrostatic plate within the control mass as indicated in Figure 6.8(b). The lack of a seismically clean suspended reference mass within the AIGO suspension to which an actuation force can react means that the test mass actuation forces must be applied against the preceding stage, i.e. the control mass. With the electrostatic plate located within the control mass cage approximately 300mm below the control mass suspension point, reaction forces will tilt the control mass and hence result in test mass pitching. This is indicated in Figure 6.8(a).

With a control mass pitch frequency of 0.2Hz, (which can be obtained with simple mechanical tuning of the suspension point) the relationship between electrostatic

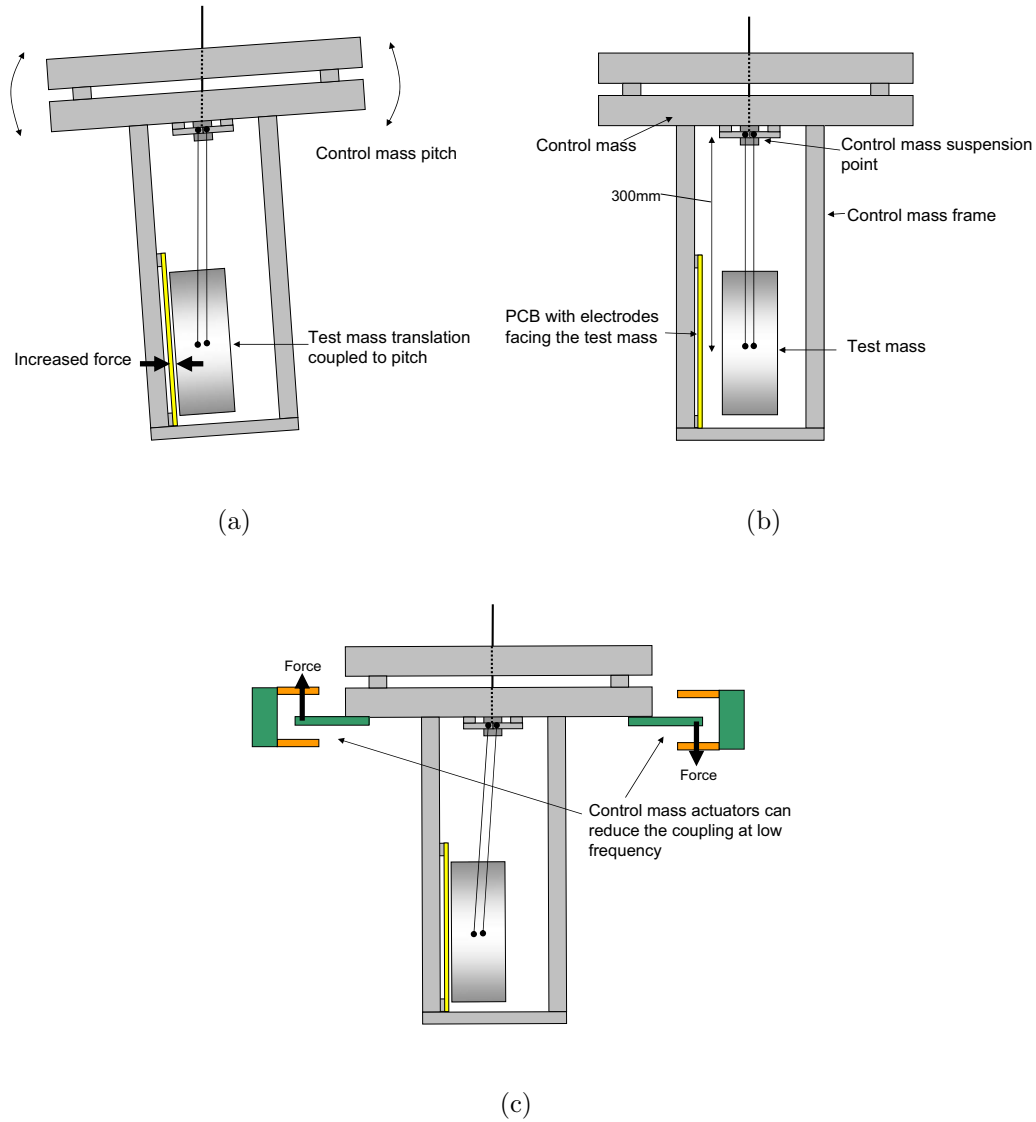


Fig. 6.8: a) Coupling of test mass translation to pitch when a force is applied by the electrostatic actuator. b) Location of the electrode capacitor within the control cage. c) Control mass vertical actuators can reduce the coupled pitch at low frequencies.

actuation force and test mass pitch can be approximated. The rotational moment of inertia of the control mass about the y direction axis, I_y , is about 1.2kg/m^2 . Therefore the pitch mode spring constant of the control mass about the y axis is given by $\kappa = (2\pi f_0)^2 I_y$. By substituting in the values given above, we obtain $\kappa \approx 1.9\text{Nm/rad}$.

Using the relationship $\Gamma = \kappa\theta$ and that the generated torque around the control mass suspension point is given by the electrostatic force multiplied by the moment arm length of approximately 300mm , the relationship between electrostatic force and test mass pitch displacement at DC is given by $F = \frac{\kappa}{0.3}\theta$. Therefore in order to keep the

pitch displacement within about $1.5\mu\text{rad}$ (necessary for auto-alignment systems to take place) an electrostatic force no greater than $9.5\mu\text{N}$ can be applied. At low frequencies however (up to a few Hz) the control mass vertical actuators can compensate for this induced pitch. This is illustrated in Figure 6.8(c) and thus low frequencies electrostatic force can be applied with negligible pitch coupling, since the control mass actuator force range $100\mu\text{N}$ will be larger than that of the electrode capacitor.

At higher frequencies, the level of control mass pitch coupling will roll off at 40dB per decade above the resonant frequency of 0.2Hz. Therefore at 20Hz, an electrostatic force range up to 95mN in amplitude will be required before a pitch range of $1.5\mu\text{rad}$ is seen. Since this actuation level is much larger than that expected from the electrostatics, it seems unlikely that the force to pitch coupling of the electrostatic actuation system will be a significant problem.

If coupling between the two modes of motion is observed to be significant, decoupling can be achieved with a frequency dependant diagonalization driving matrix. The driving matrix calculates the correct amount of force to apply through the translation and pitch actuators in order to only move the suspended test mass about the desired degree of freedom. Although this process is far from trivial, it has been effectively implemented at Virgo [126].

6.3.3 Sensor Calibration

Calibration of the electrodes as a position sensor was achieved using a micrometer to position the test mass a known distance from the capacitor surface. The results of this calibration for all four quadrants is illustrated in Figure 6.9. In this measurement, the absolute value of the distance may be out by up to $20\mu\text{m}$, due to the difficulty in determining the actual position of zero distance. However for the purpose of approximating the signal to distance calibration, it is the relative distance between points of measurement that is important. This was achieved to within an error of $\pm 1\mu\text{m}$. Additionally, the calibration was also done with a metallic test mass. This will give a higher sensitivity than would be achieved with a sapphire test mass by about a factor of about 2. Output voltage signals were measured to within an accuracy of $\pm 5\text{mV}$. A pump signal amplitude of 5Vpp was used.

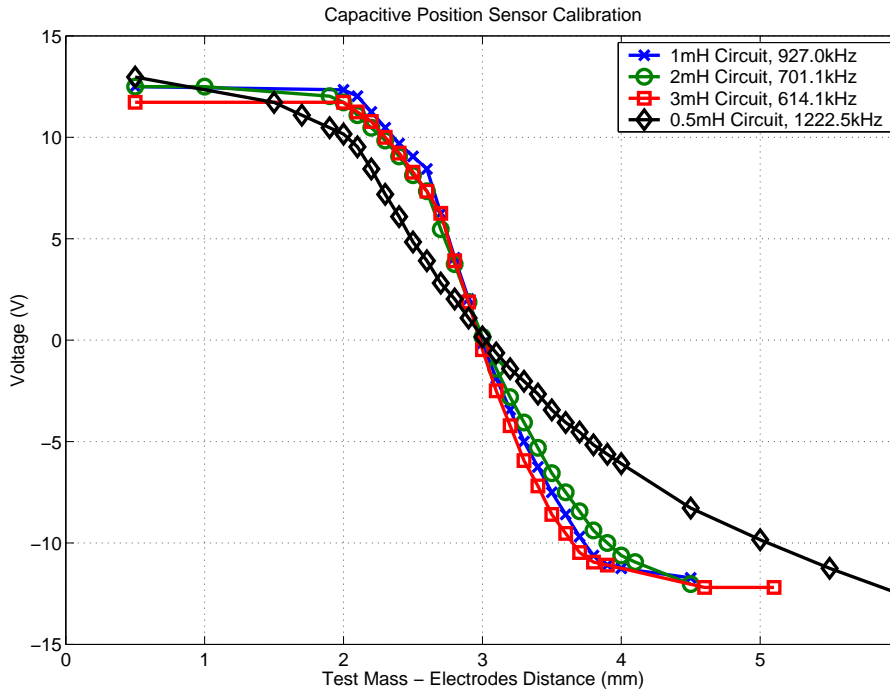


Fig. 6.9: Capacitive position sensor calibration for the four quadrants. Relative distance measurements were obtained to within $\pm 1\mu\text{m}$ while voltage signals were measured within $\pm 5\text{mV}$.

Each quadrant pump signal was adjusted in frequency such that resonance and hence maximum sensitivity would occur at a test mass to electrode distance of 3mm. From the measured data, the resulting calibration values range from approximately 20000V/m to 8000V/m around the nominal position of 3mm.

By measuring the voltage noise of the output signal (mixer output noise through a low pass filter) the sensor noise floor was obtained as a displacement sensitivity. This was done by dividing the output voltage noise spectrum by the worst sensitivity calibration value of 8000V/m . This spectrum is illustrated in Figure 6.10, and shows a displacement sensitivity of around $2\text{nm}/\sqrt{\text{Hz}}$ at 1Hz. For the purpose of aiding with local control and positioning of the mirror, we believe that this sensitivity is adequate.

6.3.4 Actuator Calibration

Initially, an estimation of the achievable actuation force using this particular electrode array design was calculated by measuring the capacitance of the electrodes as a function of test mass to electrode separation. An aluminium dummy mass was used. The result of this measurement is shown in Figure 6.11. An LCR meter with a resolution of

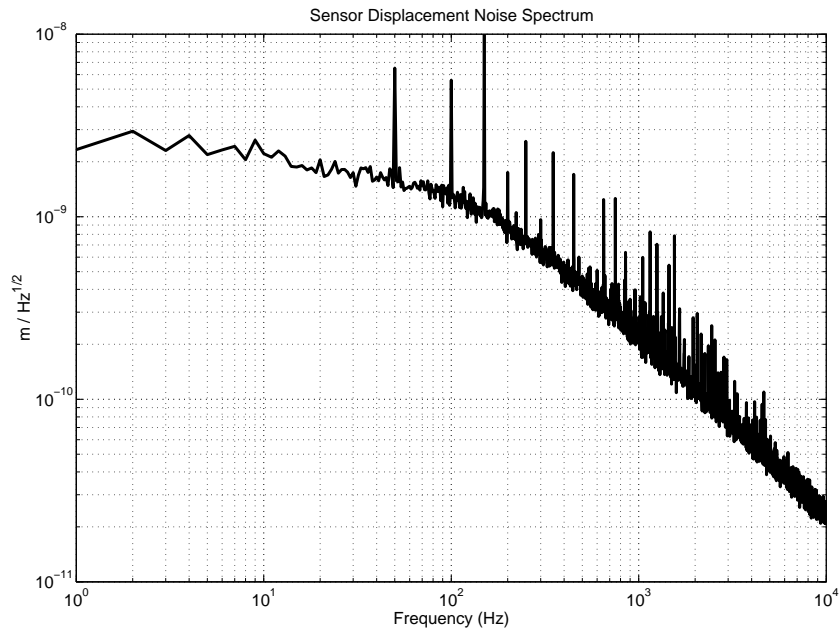


Fig. 6.10: The noise floor of the capacitive sensor obtained by measuring the output voltage noise of the displacement signal, and converting to a displacement noise through a calibration of 8000V/m.

0.1pF was used to obtain the capacitance readings, however each reading was seen to fluctuate by ± 0.3 pF. This is indicated by the error bars in the graph.

A rough estimate of the derivative, $\frac{dC}{dx}$ gives values of -3×10^{-9} F/m and -6×10^{-10} F/m at distances of 1.5mm and 3mm respectively. Using the relationship between electrostatic force and electrode voltage, $F = \frac{1}{2} \frac{dC}{dx} V^2$, we find that for a voltage of 500V, a force magnitude of 0.38mN and 75μ N can be applied at 1.5mm and 3mm separation.

A better method to characterise the force vs voltage relationship of the electrode layout was achieved through the use of a magnetic actuator and shadow sensor with known calibrations within a feedback control system. The purpose of the control loop is to hold the suspended test mass at a constant position. This is indicated in Figure 6.12 Using this setup, the electrostatic force can be obtained from the magnetic actuator signal. Therefore the electrostatic force as a function of voltage can be measured without the test mass to electrode distance changing for changing electrostatic force values. The electrostatic force of a single quadrant as electrode voltage varies from 0 to 2.5kV DC is plotted in Figure 6.13.

It can be seen that the pull force generated by the electrostatic actuator is related very closely to V^2 . For an input voltage range of 2.5kV DC, the force range generated

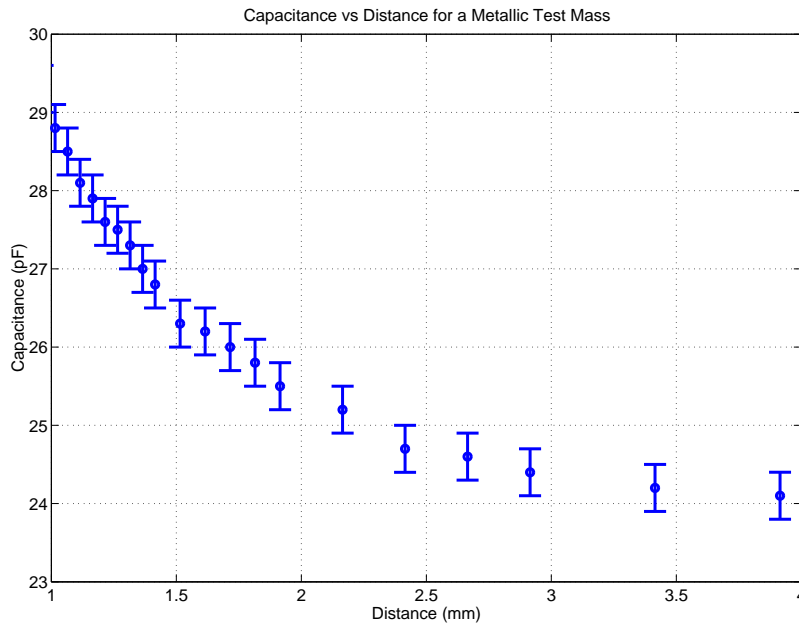


Fig. 6.11: A measurement of the capacitance of one electrode quadrant vs test mass distance.

by the actuator is 9mN when the test mass is located 1.5mm from the electrodes and 3.5mN when the test mass is located at 3mm. For use at AIGO, the requirement of an electrostatic actuation bandwidth of approximately 3000Hz means that control voltages with range in the order of kV is difficult to obtain. Instead, a high voltage operational amplifier is used with an output range of $\pm 220\text{V}$. A high voltage bias signal of 500V is also used to increase the achievable force range.

Figure 6.14 presents a closer view of the electrostatic force vs electrode voltage for lower voltage values. With a bias DC voltage supply of 500V and a high voltage actuation signal with range $\pm 220\text{V}$, the electrode voltage will vary between 280V and 720V. From Figure 6.14, it can be seen that this voltage range corresponds to a force range of just over $250\mu\text{N}$ when the test mass is located at a distance of 3mm. With all four quadrant actuators acting simultaneously, a total force range close to 1mN can be achieved. This is larger than the expected force range required to initially lock the AIGO cavity ($500\mu\text{N}$) as discussed in Chapter 5. With a sapphire test mass, the electrostatic force may be smaller by a factor of two. In this case, a larger force range can be achieved by either using a larger bias voltage, or a smaller test mass to electrode separation. Similarly, it may be found that a smaller force range is desired in order to reduce the amount of actuation force noise. Again, the bias voltage level or test mass separation distance can be altered to cater for this.

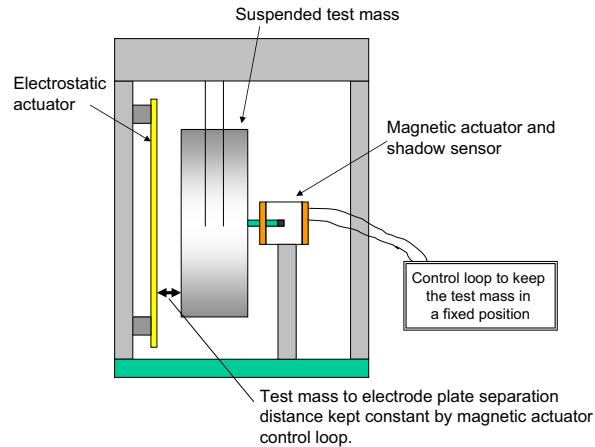


Fig. 6.12: Force calibration of the electrostatic plate using a magnetic actuator with known calibration to keep the test mass to electrostatic plate distant constant.

6.4 Local Test Mass Positioning

6.4.1 Basic Layout

As discussed earlier, a 50mm diameter, 30mm thick sapphire mirror within a 150mm diameter aluminium and stainless steel holder is currently suspended within a control mass. The control mass itself is suspended at the bottom of the AIGO vibration isolation system. The setup used to initially test the electrostatic design for control and positioning of the suspended test mass is illustrated in Figure 6.15. For clarity, only a single quadrant is illustrated. Currently the vacuum tanks are not pumped down and thus the system is being tested in air within a clean room environment.

To be located within the vacuum are the electrodes, which together with the suspended test mass effectively produce a variable capacitor. The LRC resonant circuit components and the MPY634KP mixer and low pass filter are also to be located within the vacuum. These components are needed for the position sensing circuit and must be located close to the electrode capacitor such that stray capacitances are kept minimal. A prototype has successfully been tested in a separate vacuum chamber to confirm that components will not overheat and that there are no problems with changes in breakdown voltages. Outgassing of the components however has not been tested. The in vacuum electronics has been cleaned using the required AIGO cleaning procedure [128], however vacuum baking at high temperature is not possible due to the limited temperature range of some of the components. For this reason vacuum baking was done

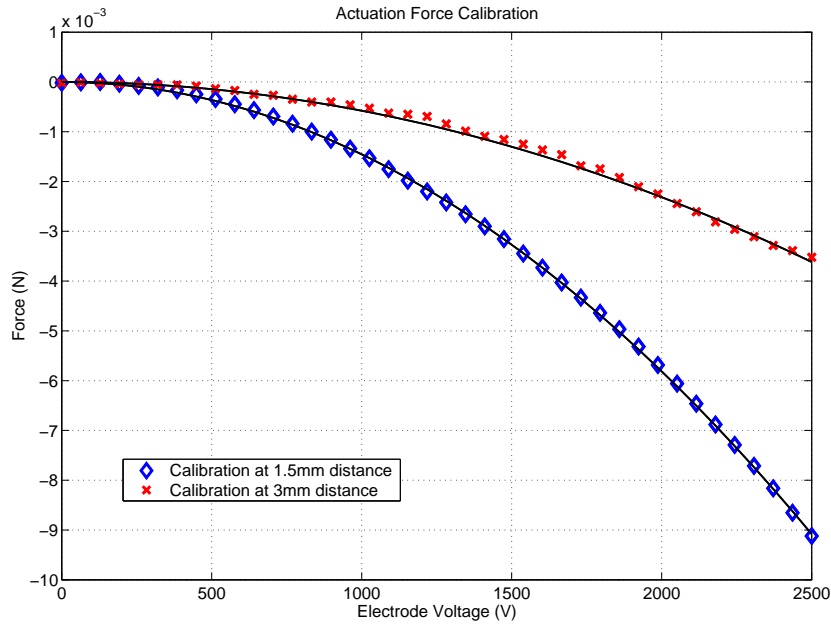


Fig. 6.13: Electrostatic force vs electrode voltage up to 2.5kV for the AIGO electrode array layout acting on an aluminium test mass.

at room temperature. If desired vacuum pressure of 10^{-7} torr cannot be achieved due to excessive outgassing of the electrostatic components, a re-design may be necessary. This may involve hermetically sealing the troublesome components.

Since the suspension is currently in air, coupling of the suspended dummy mass with air currents results in much larger motions than that anticipated if the system were under vacuum. Similarly, no control of the suspended control mass at this stage means that the residual motion between the dummy mass and control mass frame is large. For this reason, a larger electrostatic force range is required for this test. To achieve this, a dummy mass to electrostatic plate separation of 1.5mm is used as well as a 1000V DC bias signal. The high voltage amplifiers have been replaced by DC to HV DC converters (EMCO G25), with a voltage range of approximately 600V. These voltage converters have a much larger range than the Apex power operational amplifier circuit, however have a lower bandwidth (about 50Hz) and worse noise performance. As such they cannot be used to lock a cavity, but for the initial test involving the damping and positioning of a suspended dummy mass in air, they provide the larger voltage range required.

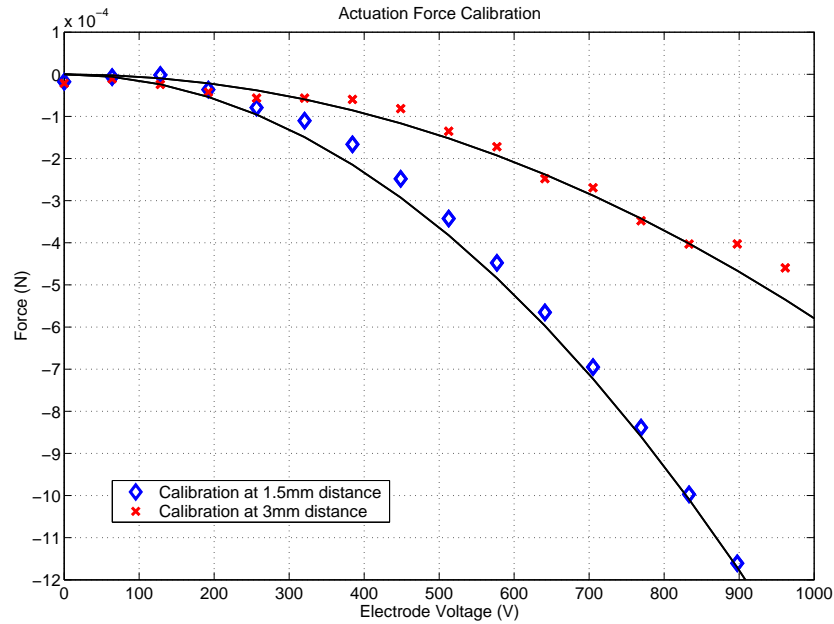


Fig. 6.14: Electrostatic force vs electrode voltage up to 1kV for the AIGO electrode array layout acting on an aluminium test mass.

6.4.2 Initial Tuning

Initially, a test mass to electrostatic plate separation distance was mechanically adjusted to be approximately 1.5mm. A 1000V DC bias voltage was then applied which should result only in a small DC shift in the test mass central position (in the order of $10\mu\text{m}$). The pump signal, currently supplied by a signal generator for each quadrant is manually adjusted to provide a 5Vpp signal with frequency corresponding to the resonant frequency of the relevant quadrant LRC circuit. Once the pump signal frequency is tuned, the test mass position signal sensed by each quadrant is available and can be read by the DSP. The required frequencies are approximately 600kHz for the 3mH circuit, 700kHz for the 2mH circuit, 900kHz for the 1mH circuit and 1.2MHz for the 0.5mH circuit. These frequencies were chosen such that they are separated enough to avoid coupling between each of the quadrant signals, and low enough to avoid interference with any optical modulation frequencies.

6.4.3 Results

A digital PID control loop was programmed in LabView in order to control the suspended dummy mass. The DSP is manufactured by Sheldon Instruments Inc. and uses a Texas Instruments TMS320C33 150MHz processor. The A to D and D to A

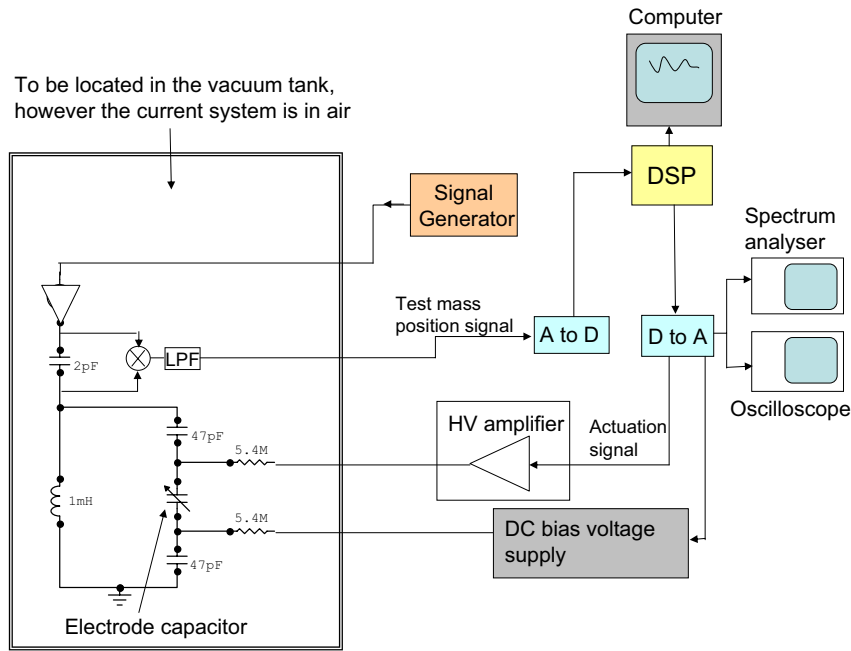


Fig. 6.15: The experimental layout used to initially control the suspended dummy test mass using only the electrostatic sensor and actuator. Here we have only drawn one of the four quadrant sensors/actuators.

converters consist of 16bit resolution with up to 100kHz sampling rate. More information on the hardware is given in [129]. For the initial test, PID gains were essentially determined on a trial and error basis. It was found that sufficient results could be obtained using mostly derivative feedback at low frequencies (up to a few Hz) and some proportional feedback over a higher frequency band (a few tens of Hz). Integral feedback to compensate DC drifts was not implemented since the electrostatic actuator will not be needed for any large amplitude low frequency control.

The result of the x direction feedback loop on the dummy mass displacement is shown in Figure 6.16. With the feedback control off, several modes of the system can be identified. The largest amplitude peak at 0.21Hz corresponds to the control mass pitch mode. The 0.91Hz mode and 1.1Hz mode are the dummy mass pendulum modes in the x and y directions respectively while the 1.6Hz mode is the dummy mass yaw mode. The other modes are slightly harder to identify, but are possibly related to the roll mode of the control mass and the combined pendulum mode of the control mass and dummy mass.

It can be seen that with the control loop on, the x direction motion is significantly damped. All of the modes can be sufficiently suppressed with the electrostatic actuator.

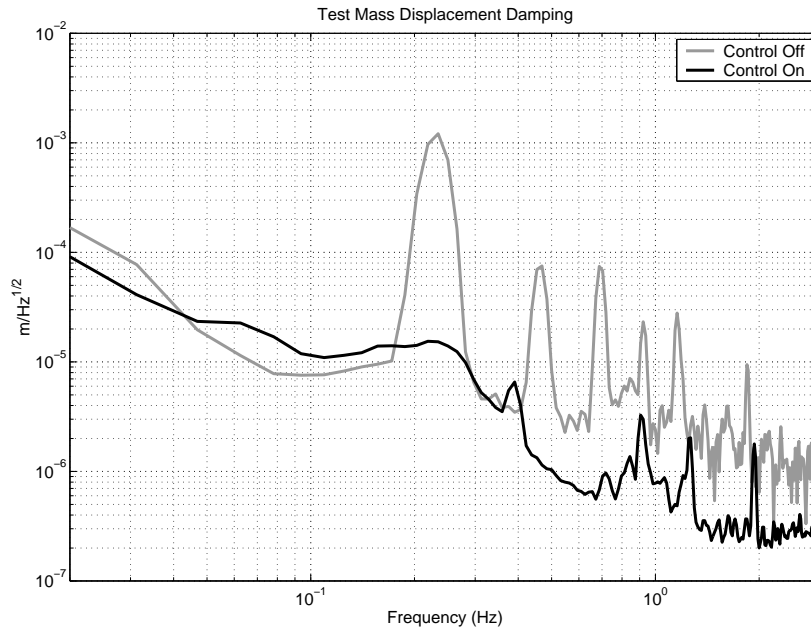


Fig. 6.16: Measured displacement spectrum of the suspended dummy mass.

Thus if required, the electrostatic actuator may be useful in reducing the residual velocity of the suspended mirror. The time domain response of the undamped and damped system is shown in Figure 6.17. It can be seen that the $150\mu\text{m}$ amplitude oscillation, due primarily to the control mass pitch mode is successfully damped after the control loop is closed at approximately $t=-2\text{sec}$. It should be noted that in the complete AIGO suspension, the control mass pitch will be heavily suppressed by the control mass actuators, and hence much smaller amplitude motions will be seen by the capacitive sensors.

Use of the electrostatic actuator to position the test mass to a new DC position is illustrated in Figure 6.18. It can be seen that a DC shift of about $30\mu\text{m}$ is achieved with the actuator. Although possible, it is unlikely that the electrostatics will be used to position the test mass. This is due mainly to the limited range of the actuator, and that DC positioning can be achieved by other actuators located elsewhere on the isolation chain.

Figure 6.19 shows the yaw spectrum of the suspended dummy mass for both the closed loop and open loop case. Yaw direction angular displacement is approximated by determining the differential dummy mass distance measured by the left and right pair of capacitive sensors, and dividing by the average separation of the left and right pairs, i.e. $\sim 10\text{cm}$. The spectrum shows that most modes are damped except for those

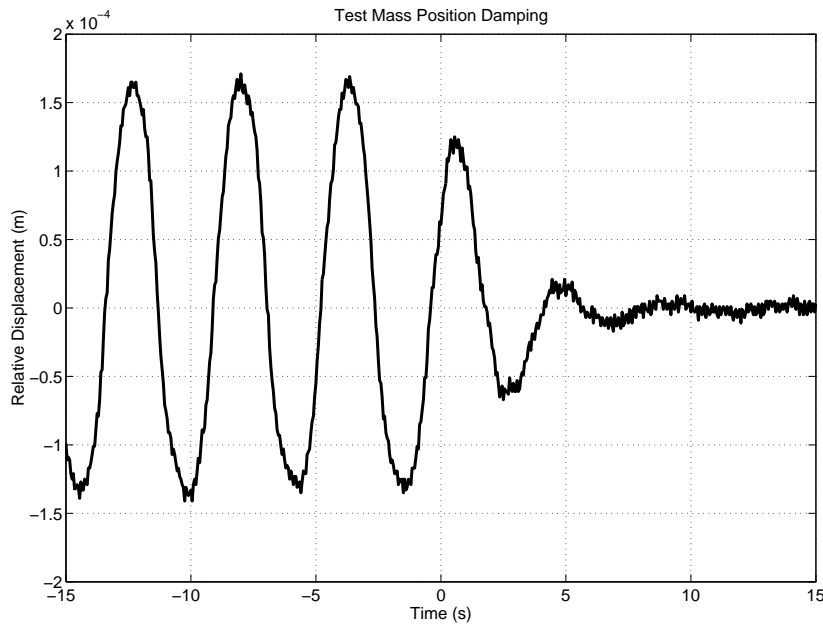


Fig. 6.17: Time domain response of both the undamped and damped x direction motion of the suspended mirror. The control loop was switched on at approximately $t = -2$ sec.

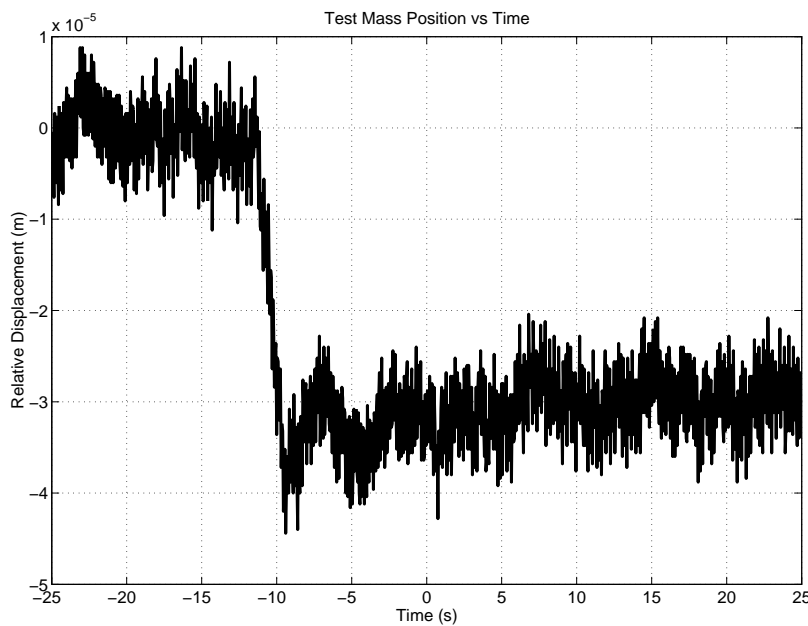


Fig. 6.18: Dummy mass position control using the electrostatic actuator.

at 0.91Hz and 0.4Hz. The 0.91Hz mode corresponds to the dummy mass pendulum mode in the x direction, while the 0.4Hz mode may correspond to the control mass roll mode. The reason that these modes occur is because only two high voltage converters were available for this initial testing. Therefore only two degrees of motion could be controlled at one time. For yaw control, pitch mode control was also necessary to prevent yaw mode feedback from exciting the pitch mode at 3Hz. This coupling

is likely caused by slightly different sensitivities exhibited by each quadrant sensor. It should be possible to reduce this coupling by tuning the sensitivity of each sensor by either adjusting the pump signal amplitude, or digitally adding gain to the necessary signals. With no x direction control during the measurement, x direction motion is coupled into the yaw sensing.

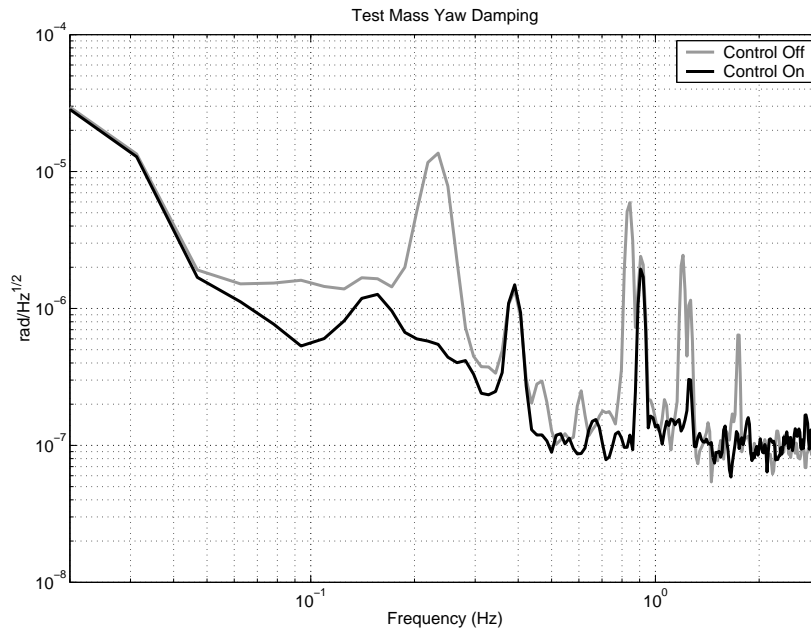


Fig. 6.19: Measured yaw spectrum of the suspended dummy mass.

Figure 6.20 shows the time domain response of test mass yaw displacement when the control loop is closed at around -1sec. Significant damping of the 0.2Hz signal is seen, however a relatively strong 0.9Hz signal is still observed in the time trace. This reflects the discussion made about the closed loop spectrum of Figure 6.19.

The use of the electrostatic actuator to apply a DC yaw displacement on the suspended control mass is shown in Figure 6.21. Large angular displacements will not need to be achieved using the electrostatic actuator since such displacements can be generated using the control mass actuators. Lower amplitude angles however may be required to help fine tune the alignment of the cavity.

Finally the measured pitch spectrum for both control on and control off is given in Figure 6.22. It can be seen that all modes are significantly damped except for the yaw mode at 1.6Hz. In this case, the two degrees of freedom that were controlled with the two available HV converters were the pitch mode and x direction pendulum mode. This was necessary due to the small amount of pitch to x direction coupling through

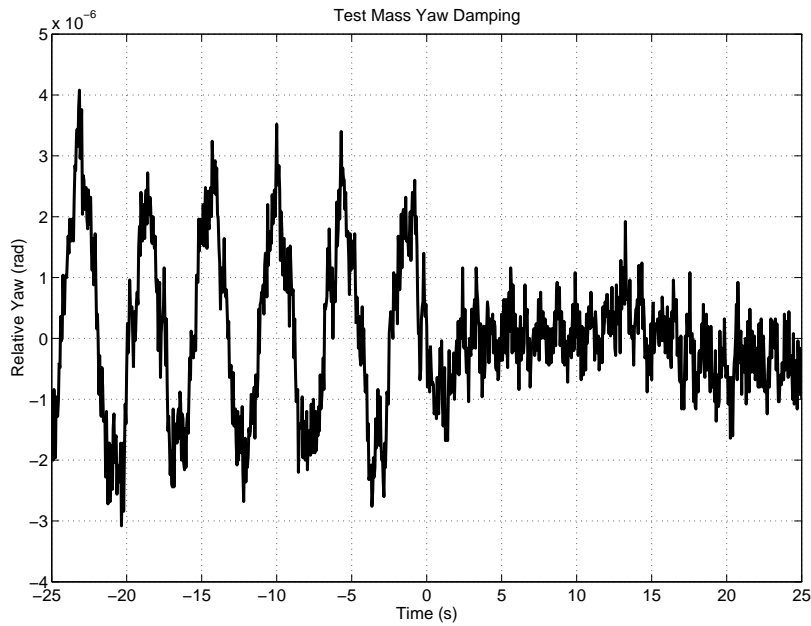


Fig. 6.20: Time domain response of both the undamped and damped yaw direction motion of the suspended mirror. The control loop was switched on at approximately $t=-1$ sec.

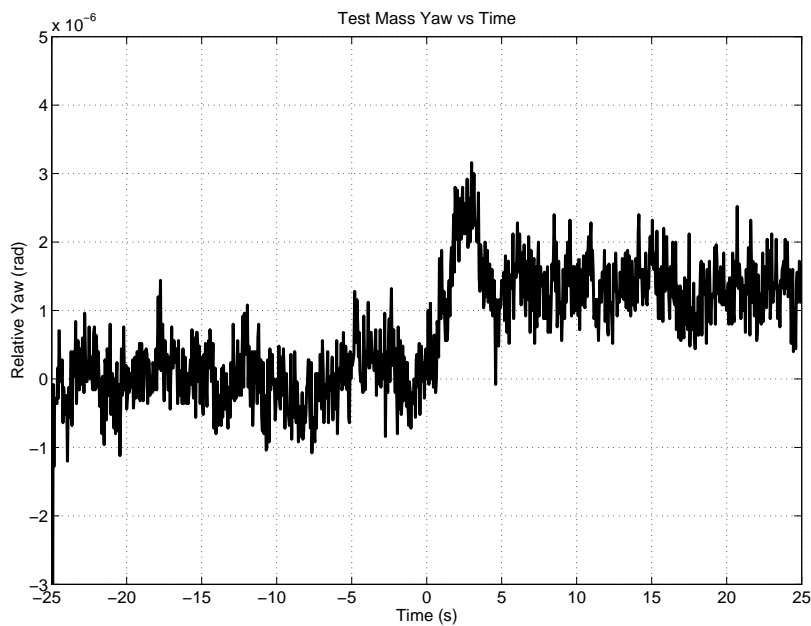


Fig. 6.21: Dummy mass yaw position control using the electrostatic actuator.

the control mass as discussed in section 6.3.2. For this reason, the closed loop pitch spectrum shows a peak at 1.6Hz, corresponding to undamped yaw motion coupling through the pitch mode sensing.

A time domain response illustrating the pitch mode damping is shown in Figure 6.23. Again it shows a significant improvement in the level of pitch mode motion once the feedback loop is closed.

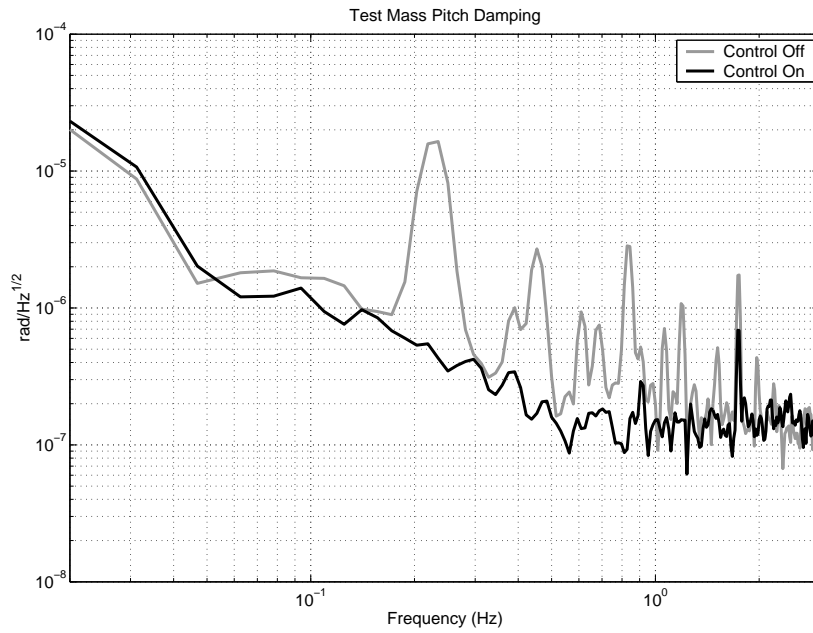


Fig. 6.22: Measured pitch spectrum of the suspended dummy mass.

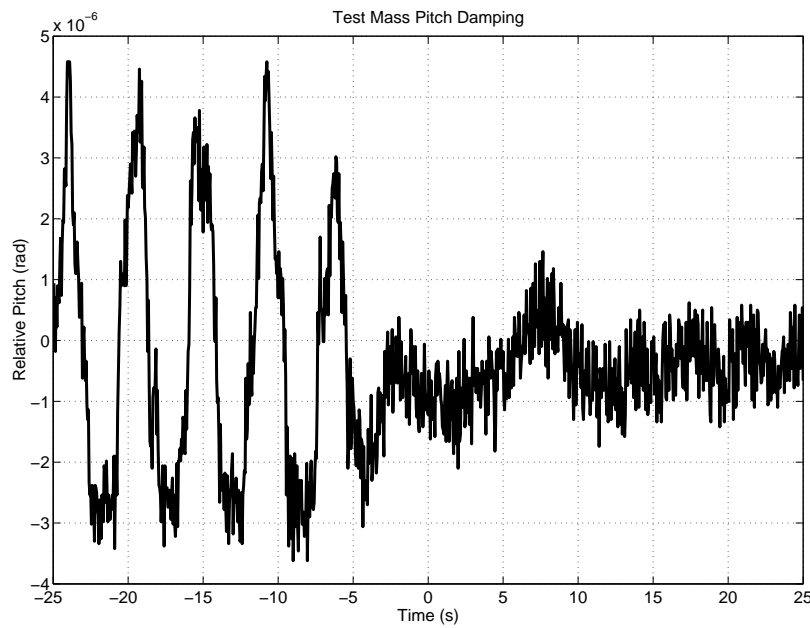


Fig. 6.23: Time domain response of both the undamped and damped pitch direction motion of the suspended mirror. The control loop was switched on at approximately $t=-5$ sec.

Pitch mode angular displacement can also be generated as indicated in Figure 6.24. As is the case for yaw displacement, only a small pitch range is likely to be required through electrostatic actuation in order to fine tune cavity alignment. Larger pitch mode angular displacements can again be achieved using the control mass actuators.

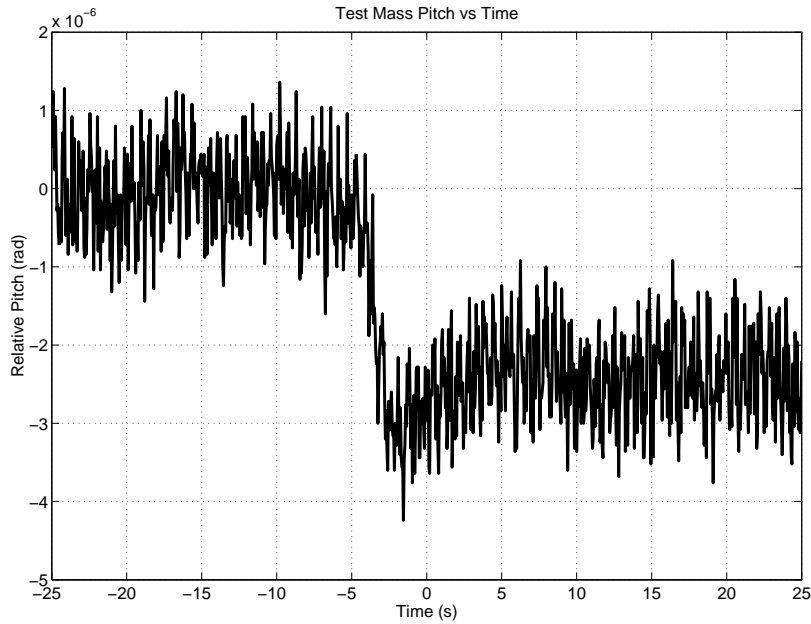


Fig. 6.24: Dummy mass pitch position control using the electrostatic actuator.

6.4.4 Discussion

The results presented above show that the electrodes connected as both a position sensor and an actuator can provide some degree of local control on the suspended test mass. This accessibility to the final stage of the suspension may be very useful during initial alignment and reduction in residual velocity of the suspended cavity mirrors. Sensing coupling between different degrees of freedom due to varying sensitivities of different quadrants may cause some problems, particularly control loop instabilities in the coupled directions. However it is expected that this coupling can be minimised by tuning the various quadrant sensitivities.

Importantly, the results indicate that the location of the electrostatic plate within the control mass cage does not significantly hinder the ability to actuate cleanly on the test mass. Therefore it seems possible to avoid the need for a reaction mass through which test mass actuation is normally referenced. Secondly, the lack of y direction actuation at the test mass level did not pose problems. Even in the relatively noisy environment within which the tests were carried out, y direction pendulum mode oscillations were not excited.

CHAPTER 7

CONCLUSIONS

7.1 Thesis Summary

In Chapter 2, we presented some of the issues involved with the design of mirror suspensions in gravitational wave detectors with a goal to minimise suspension thermal noise. A comparison of mechanical properties (internal loss angle, tensile strength and density) and physical properties (thermal expansion coefficient, thermal conductivity and specific heat) demonstrated that fused silica and silicon are likely to provide the best room temperature suspensions. At cryogenic temperatures, significant increases in the value of thermal conductivity and reductions in the value of loss angle and thermal expansion coefficient result in large improvements in suspension thermal noise for sapphire and silicon suspensions. Improvements in loss angle within the detection band of over two orders of magnitude ($\phi \rightarrow 10^{-9}$) has been predicted.

A study of four materials; fused silica, silicon, sapphire and niobium for use as ribbon suspensions of a 30kg test mass was also presented. The effect of changing the aspect ratio on the predicted suspension thermal noise (similar to the study of fused silica ribbons by Gretarsson et. al. [80]) is plotted. It shows that for fused silica and silicon ribbons, a reduction of ribbon thickness beyond about $50\mu\text{m}$ results in little thermal noise improvement. For niobium however and more so, sapphire, ribbon thickness down to $10\mu\text{m}$ still results in steady thermal noise improvements. Considerations such as practical issues and ribbon internal torsion modes however are likely to set the limit on the thickness of niobium and sapphire suspension ribbons. Coupled thermal noise from the y and z direction were also considered as a function of ribbon thickness. For all four materials, it was found that coupling of the z direction thermal noise to the x direction through a coupling factor of 0.1% will become the dominant source of

thermal noise for thin enough ribbons. This occurs due to the increase in surface loss for thinner ribbons with no z direction dilution factor improvement. Ribbons thinner than $40\mu\text{m}$ are needed before the z direction thermal noise become significant.

The extension of a suspension modelling program is presented in Chapter 3. Using this program, the analysis of a triple section suspension element is presented in Chapter 4. Study of the pendulum mode thermal noise of such suspension elements supporting a 30kg test mass showed that short end flexures combined with a stiff central section will result in an increase in thermal noise when compared to a typical ribbon suspension with thickness and width the same as the end flexures. However, if the end flexures are made at least 2mm long, pendulum mode thermal noise was shown to increase by no more than 10%, regardless of the central section geometry. This result lead to the design of the orthogonal ribbon and the thin tube suspension. This is essentially a suspension that consists of two end flexures and a central section that is either a ribbon with the thin dimension in the y direction, or a thin hollow tube. For the orthogonal ribbon suspension, violin mode amplitudes were shown to reduce by 21dB while the number of x direction violin modes up to 5kHz is reduced by half. For the tube suspension, it was found that the number of violin modes below 5kHz in both directions could be reduced to 5, while the thermal noise peak amplitudes can be reduced in amplitude by 31dB. The cost however is a small increase in pendulum mode thermal noise above 60Hz by a factor of about 2.4. The idea to construct removable modular suspensions was also presented at the end of this chapter. The design and finite element analysis of suitable pins is given.

In Chapter 5, a theoretical hierarchical cavity locking scheme suitable for the current AIGO isolators and compatible with advanced detector sensitivities is presented. It was approximated that all local control and locking requirements could be achieved with actuator force ranges of 0.25N, $100\mu\text{N}$ and $500\mu\text{N}$ for actuators located at the inverse pendulum, control mass and test mass respectively. When switching to hierarchical feedback to keep the optical cavity locked, the test mass electrostatic actuators need to be reduced in range to about 420nN in order for the actuator noise to fall below the sensitivity requirement of an advanced detector.

Finally, the current dummy mass suspension and electrostatic design to be implemented at AIGO is discussed in Chapter 6. Calibrations of the electrostatic position sensor showed a displacement sensitivity in the order of $2\text{nm}/\sqrt{\text{Hz}}$ around 1Hz while

a force calibration showed that an actuation range of 1mN can easily be obtained. Experimental results of the suspended dummy mass in air demonstrated the ability to damp and position three degrees of freedom of the suspended mass (x translation, yaw and pitch) using the electrostatic plate located on the control mass cage. No problems associated with the excitation of y direction pendulum mode oscillations were observed.

7.2 Future Work

The next logical step towards achieving a locked optical cavity suspended by the AIGO vibration isolation system is to extend the experimental work done in Chapter 6. Decoupling of the modes x, yaw and pitch as much as possible through the tuning of the capacitive sensor gains should provide cleaner control of the suspended dummy mass. Installation of the control mass actuators and sensors will also allow us to test more elaborate methods of positioning the dummy mass. It may be found that test mass control at the control mass stage and levels of test mass residual motion is low enough that test mass position sensing using the electrode capacitor is not necessary. In this case, vacuum compatibility and capacitive sensor noise will no longer be an issue.

Other future work includes extending the suspension modelling program to include the effect of higher order torsion modes. These modes are likely to become significant as the suspension aspect ratios increase. Currently all of the programming exists to allow one to compute the contribution to thermal noise from the torsion modes, however the results (the torsion mode frequencies) differ from that obtained through finite element modelling by a factor up to about 2. Currently the author does not know the reason for this discrepancy and for this reason it was not presented in the main body of the thesis. Finally, experimental verification of some of the results of the triple section suspensions will confirm some of the simulation outcomes. Therefore the construction of such suspension geometries is also a task to be completed.

APPENDIX A

ELECTROSTATIC MODELLING

A.1 Introduction

The idea to use electrostatic fields to apply control forces on a suspended mirror was initially developed by Lindsay et. al. [122]. Grasso et. al. [123] provide an in depth analysis of two types of electrode geometries, including the electrode comb array, of which is currently in use at GEO600 and is proposed for use in Advanced LIGO. The idea of the comb electrode array is to arrange both positively and negatively charged electrodes on the same surface, such that the mirror to be actuated upon is within close vicinity of the comb array and penetrates the resulting electric fields. This is indicated in Figures A.1(a) and A.1(b). Due to the fringing effects of the fields, calculation of the capacitance of such a system is difficult. For this reason, a method for characterising such a capacitor using finite element techniques is being developed.

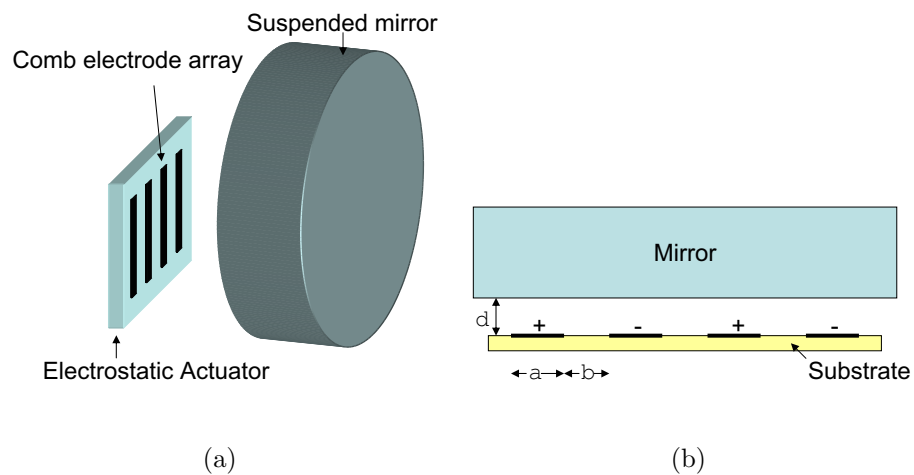


Fig. A.1: a) Comb electrode array for electrostatic actuation of a suspended dielectric. b) Two dimensional representation of the electrostatic system.

Currently, the modelling technique is based on a 2D representation of the system as indicated in Figure A.1(b). Using the pre-processor tools provided by ANSYS, the two dimensional model is drawn based on the geometric parameters supplied by the user. After sufficient meshing with 2D PLANE121 electromagnetic elements, capacitance is calculated by determining the energy, U , stored by the electrostatic fields when the electrodes are held at a particular potential difference V . This energy is equivalent to the work required to charge the electrodes to the given potential and is given by:

$$U = W_e = \frac{1}{2} \int_v (\vec{D} \cdot \vec{E}) dv = \frac{1}{2} \epsilon_r \epsilon_0 |E|^2 \int_v dv \quad (\text{A.1})$$

Of course in our model, the integral is a two dimensional integral over area. Knowing the value of U , the capacitance can then be calculated through the relation $U = \frac{1}{2} CV^2$. ANSYS also allows one to calculate the electrostatic force induced on any interface. A plot of the meshing for a sapphire sample (darker mesh located at the top of the model) located 1mm from the electrode substrate is illustrated in Figure A.2(a). A

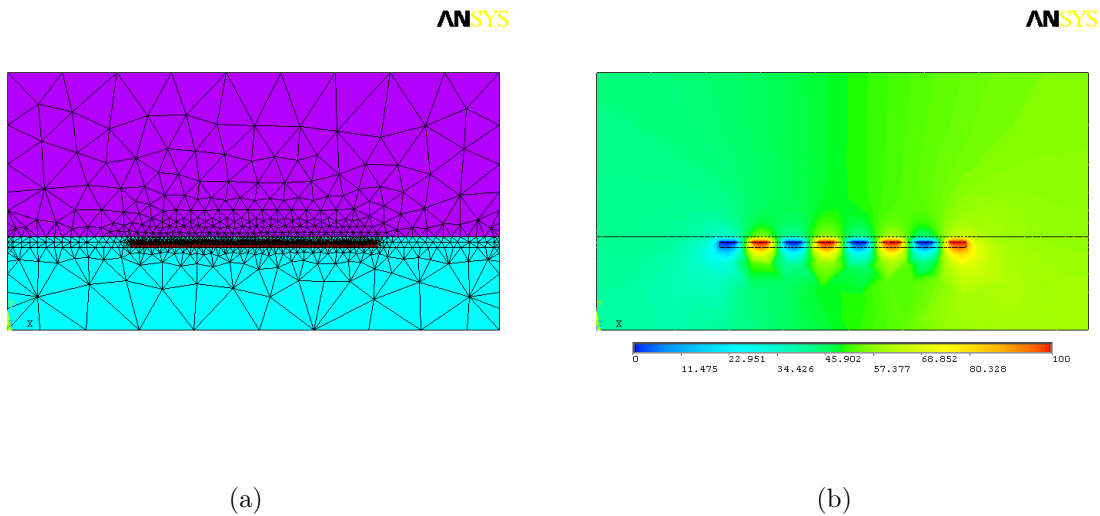


Fig. A.2: a) The mesh generated from the model of a sapphire sample located 1mm from the electrodes. The electrodes are located on a 1mm thick FR4 substrate. b) The resulting contour plot of potential, when the electrodes are held at a potential difference of 100V.

contour plot of the resulting potential is shown in Figure A.2(b). This process can be looped to calculate the capacitance and force for variation in any parameter, and therefore capacitance vs distance plots can be created. In this particular model, there are 8 electrodes of width 3mm and separated by 3mm on a FR4 (typical PCB material)

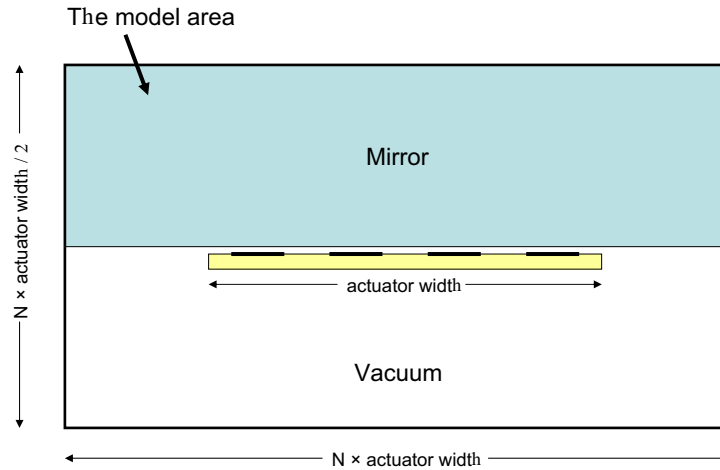


Fig. A.3: The total area of the model must be much larger than the actuator in order to obtain reasonable results.

substrate, ($\epsilon_r = 4.5$). The capacitance was calculated for a total actuator length of 80mm.

It was found that the total size of the model compared to the actuator width was important in order to generate reliable results. To determine the adequate model size, the actuator described above was simulated using models of various sizes as illustrated in Figure A.3. For an actuator to mirror separation distance of 1mm and a sapphire mirror with $\epsilon_r = 9.4$, the simulated capacitance as a function of N (from Figure A.3) was calculated. The result is illustrated in Figure A.4. Compared to the measured capacitance for this system of 25.9pF, the plot shows that for small model areas compared to the actuator width, inaccurate results are obtained. This is likely due to the fact that regions with small but significant electric field strength have been truncated, and hence the electrostatic energy determined in the model through an area integration similar to that shown in Equation A.1 is incorrect. For larger model areas (i.e. $N > 15$), it is seen that the model more closely matches that measured result. The difference here between the modeled result and the measured result of approximately 6% is likely due to the fringing effects at the ends of the actuator that are not modeled (i.e the actuator ends perpendicular to the electrodes).

The simulated capacitance as a function of distance for this actuator was modelled using this method for both a sapphire and an aluminium test mass. This result is shown in Figure A.5 and is also compared to measured values of capacitance. It can be seen that the simulated values are correct to within 10%. Similarly, the model analysed

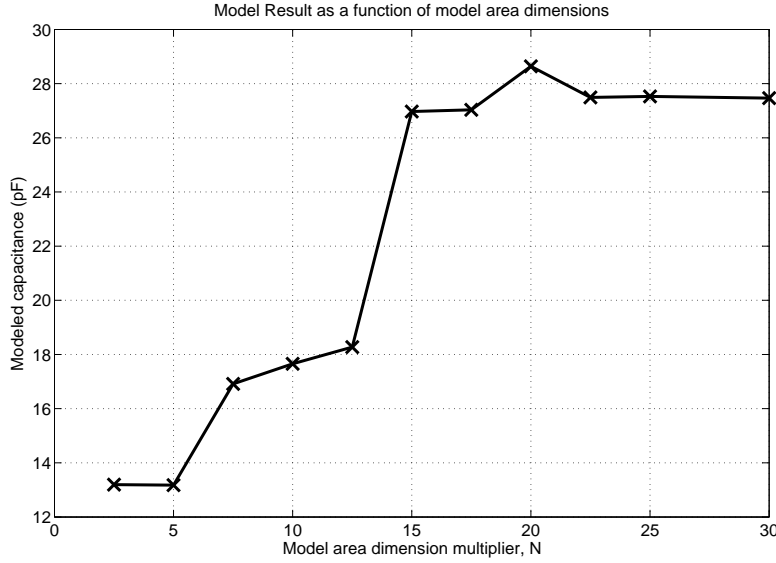


Fig. A.4: Modelled capacitance of 8 $a=3\text{mm}$, $b=3\text{mm}$ electrodes on a FR4 substrate for sapphire test mass separated from the actuator by 1mm. The total model area was changed by changing the value N (given in Figure A.3).

by Grasso et. al. [123] which consisted of 20 electrodes with $a=3.2\text{mm}$, $b=4\text{mm}$, total length $L=80\text{mm}$ on a vetronite substrate with $\epsilon_r = 4.2$ probing a quartz test mass with $\epsilon_r = 4$ was modelled using the same finite element technique and produced the capacitance vs distance plot shown in Figure A.6. In this case the result also match those measured by Grasso et al to within 10%.

The author believes that the discrepancy between the measured results and the simulated results using this finite element modeling technique can be mainly attributed to the fact that the fringing effects on the ends of the actuator perpendicular to the electrodes are not modelled. With a 2 dimensional model of the system, these fringing effects must be ignored in order to model the fringing fields between electrodes. The use of a 3 dimensional finite element model would enable one to model all fringing fields in the system and possibly solve this discrepancy. The existence of 3 dimensional electromagnetic elements within ANSYS allows this to be achieved in principle.

Although some result discrepancies still exist, the two dimensional electrostatic modelling techniques still produces reasonable estimations of capacitance and force values. In the following two sections, possible applications of such a model are presented. These include characterisation of an electrostatic actuator to act orthogonally on a test mass and electrode spacing optimisation.

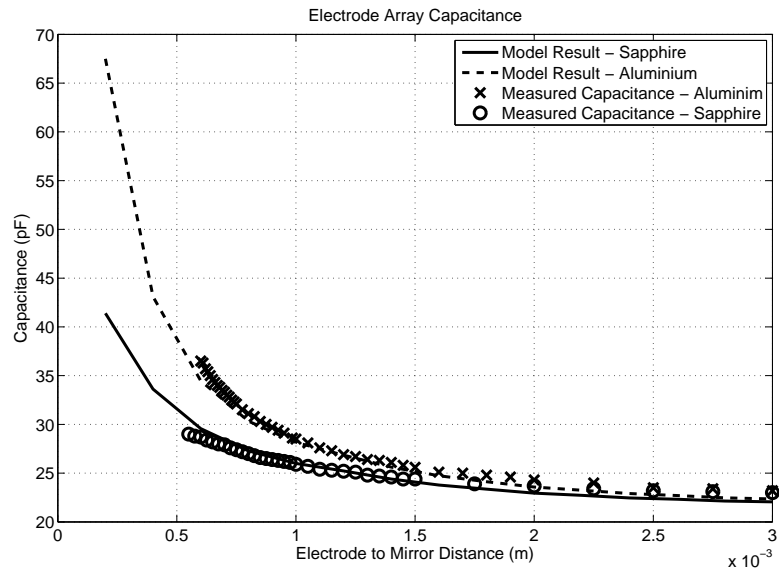


Fig. A.5: Modelled capacitance vs distance plots of 8 $a=3\text{mm}$, $b=3\text{mm}$ electrodes on a FR4 substrate for both sapphire and aluminium test masses. The measured values of capacitance are also shown.

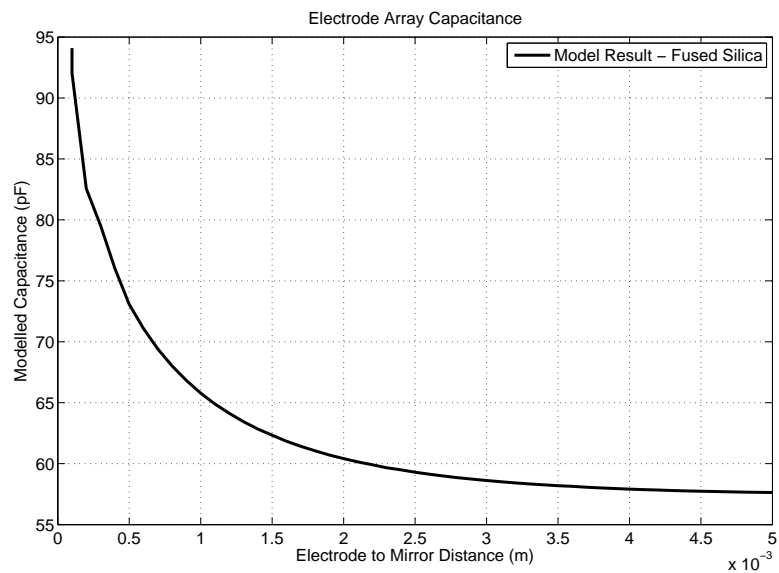


Fig. A.6: Modelled capacitance vs distance plots of 20 $a=3.2\text{mm}$, $b=4\text{mm}$ electrodes on a vetronite substrate for a quartz test mass.

A.2 Orthogonal Direction Actuation

Currently the model can also be used to characterise the force generated when an electrode array acts on the circumferential surface of the test mass. This may be useful if non-contact control forces in the y -direction (direction orthogonal to the direction of the laser) is required. The modelling procedure is exactly the same as that which is used when the electrode array is characterised in the presence of a flat surface, with the only difference being a change in geometry. Again, induced force and capacitance can be determined as a function of any geometrical parameter. The mesh and contour plot of a set of electrodes acting on a mirror of diameter 150mm is shown in Figures A.7(a) and A.7(b).

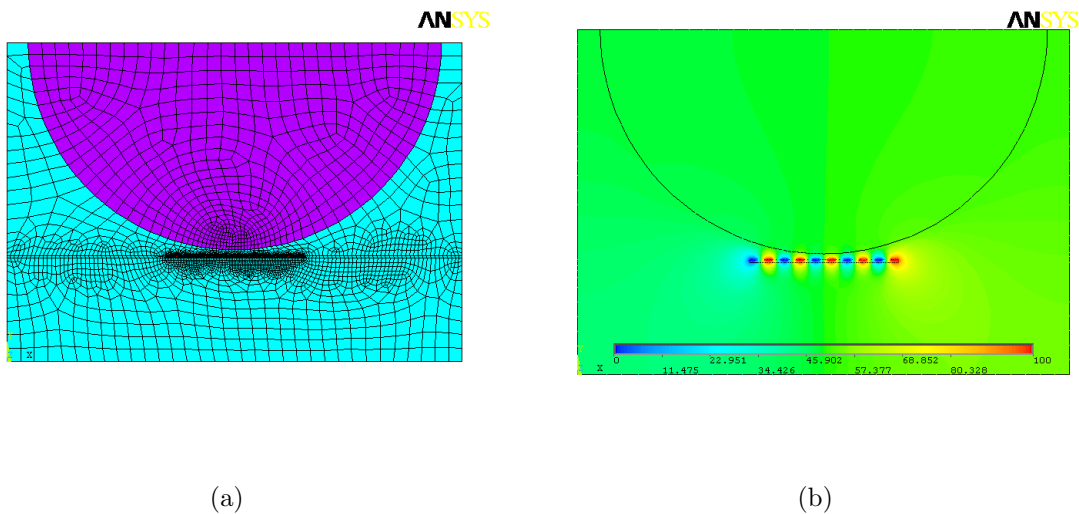


Fig. A.7: a) The mesh generated from the model of a 150mm diameter sapphire mirror located 1mm tangentially from the electrodes. The electrodes are located on a 1mm thick FR4 substrate. b) The resulting contour plot of potential, when the electrodes are held at a potential difference of 100V.

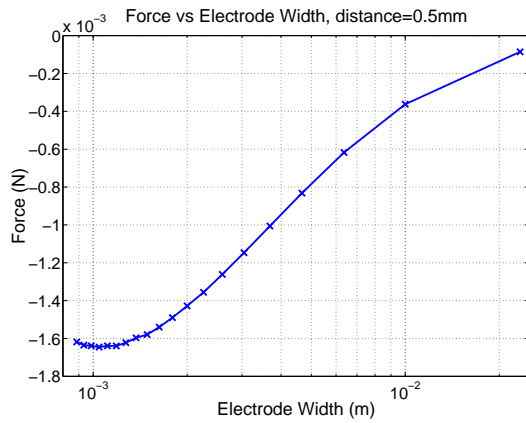
A.3 Electrode Spacing Optimisation

It was also found that the spacing and dimensions of the electrodes has a bearing on the amount of force that is induced. With reference to Figure A.1(b), various combinations of electrode width, a , electrode spacing, b , and total number of electrodes, N , were

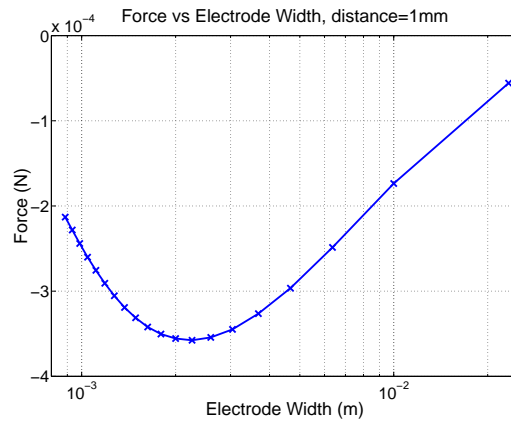
analysed with the goal being to find the parameters that allow one to induce the largest amount of force.

The results displayed in Figure A.8 show the electrostatic force for increasing electrode width, a , for six different electrode-mirror separation distances, d . These results are obtained for a sapphire test mass, with $\epsilon_r = 9.4$ and a 1mm thick FR4 substrate ($\epsilon_r = 4.2$) on which the electrodes reside. Other fixed parameters include a voltage potential across the electrodes of 100V, and an actuator size of 70mm in width and 70mm in length. The electrode width to electrode separation ratio (a/b) is also held constant at 1. The negative values of force are due to the orientation of the axis and simply mean that the force on the dielectric is in the direction towards the electrodes.

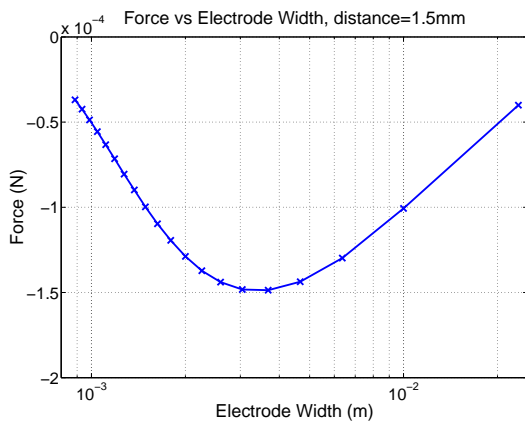
The simulated results indicate that for each of the six test mass separation values, a clear maximum in the amount of force that can be induced is visible for a particular electrode width value (or electrode separation value). This maximum force seems to occur for electrode widths of approximately twice the test mass to electrodes separation. Thus for an electrostatic actuator designed to be located approximately 3mm from the surface of the test mass, electrodes with width and separation of approximately 6mm will most likely provide the largest amount of force. This result already contradicts slightly the actuator design for GEO600 and proposed design for Advanced LIGO, where an electrode width and electrode spacing dimension of approximately equal value to the mirror separation distance is used. Obviously the electrostatic finite element modelling procedure will need to be fine tuned before such results can be confirmed.



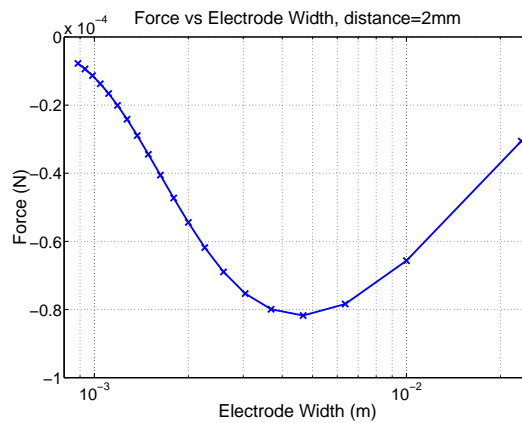
(a)



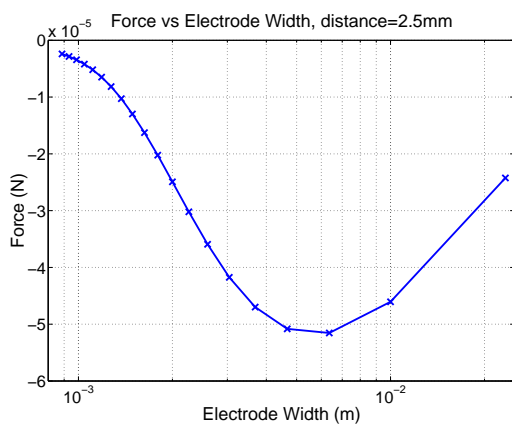
(b)



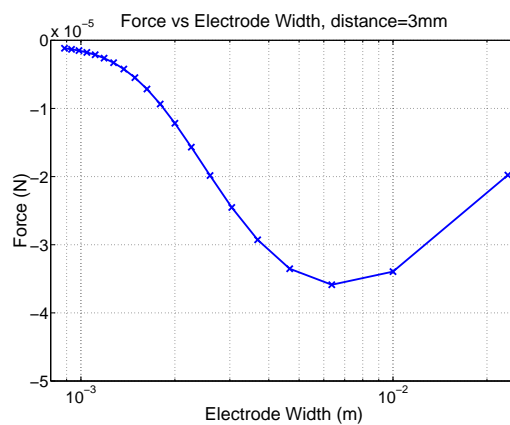
(c)



(d)



(e)



(f)

Fig. A.8: Modelled electrostatic force vs electrode width a for different electrode to mirror separation distance, d . A fixed actuator area of 70mm by 70mm is assumed, with a fixed voltage potential across the electrodes of 100V.

APPENDIX B

ELECTRONIC CIRCUITS

This appendix contains the circuit diagrams discussed in this thesis.

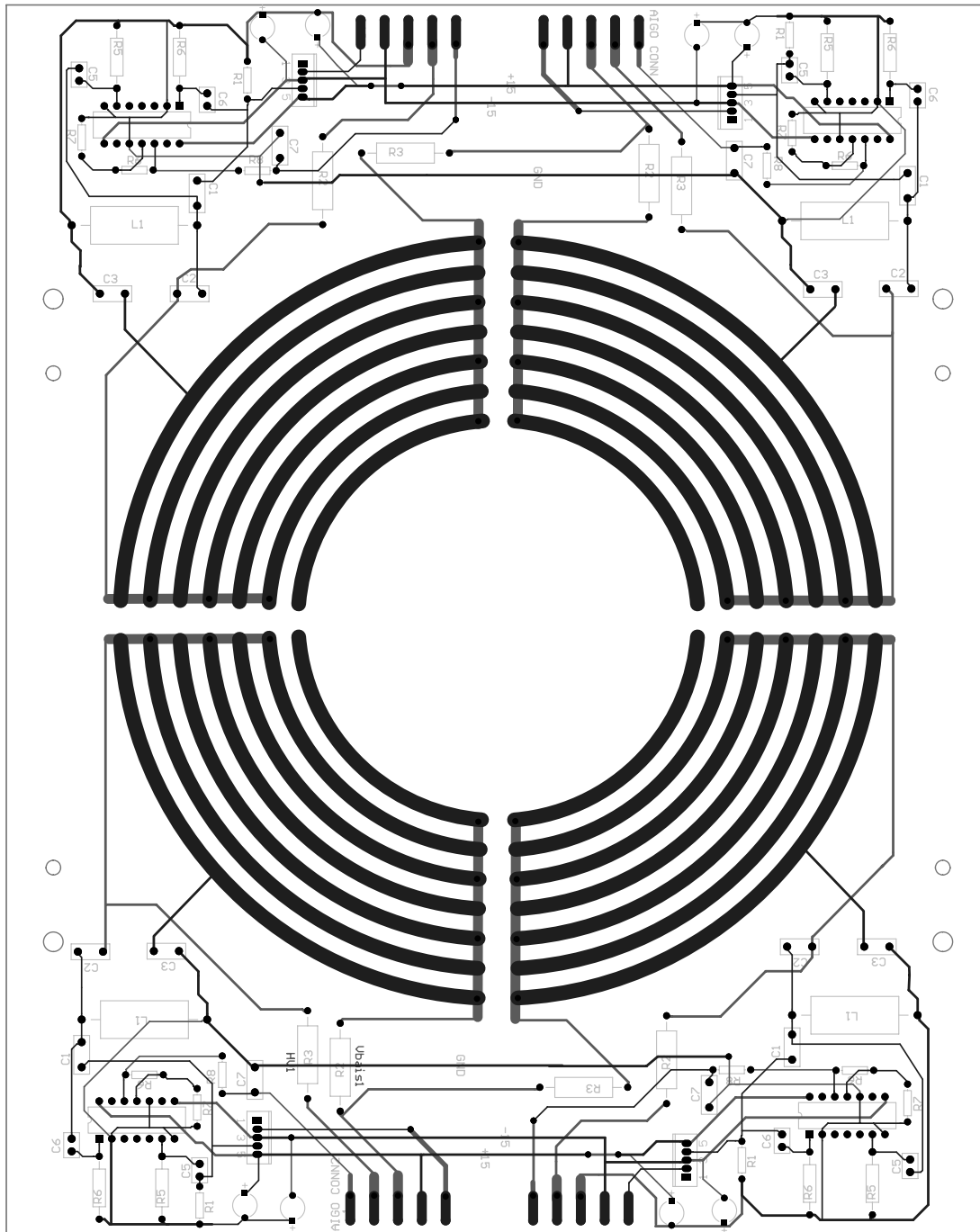


Fig. B.1: Printed circuit board design of the electrostatic plate. The PCB shown here is double sided with tracks on the top side shown in black and the tracks on the bottom side shown in grey. The electrodes exist on the top side, while the tracks connecting the electrodes exist on the bottom side. Every alternate electrode is connected, such that each electrode is adjacent to one that will be of opposite polarity.

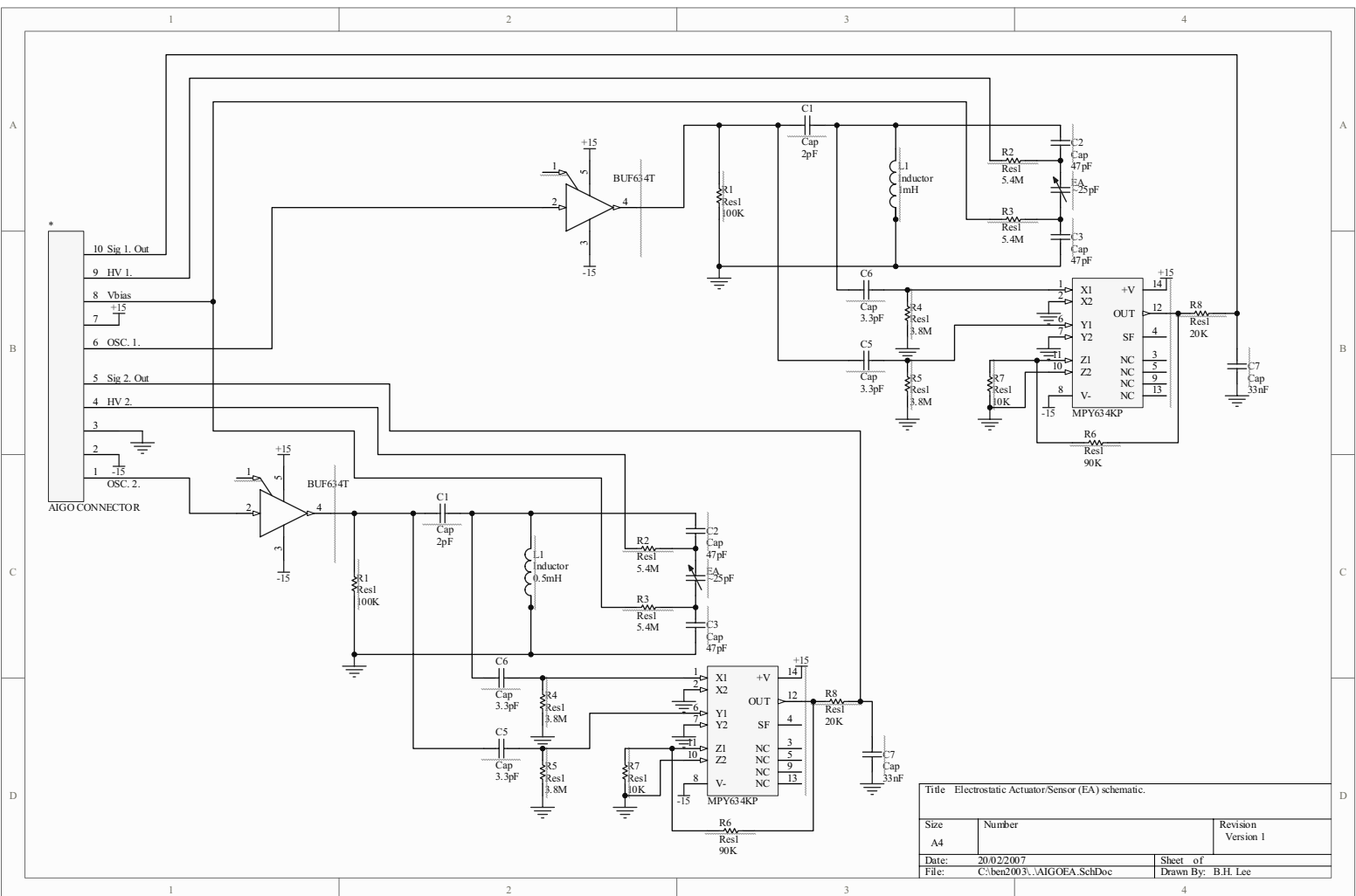


Fig. B.2: Schematic of the electrostatic sensing circuit for the north quadrants.

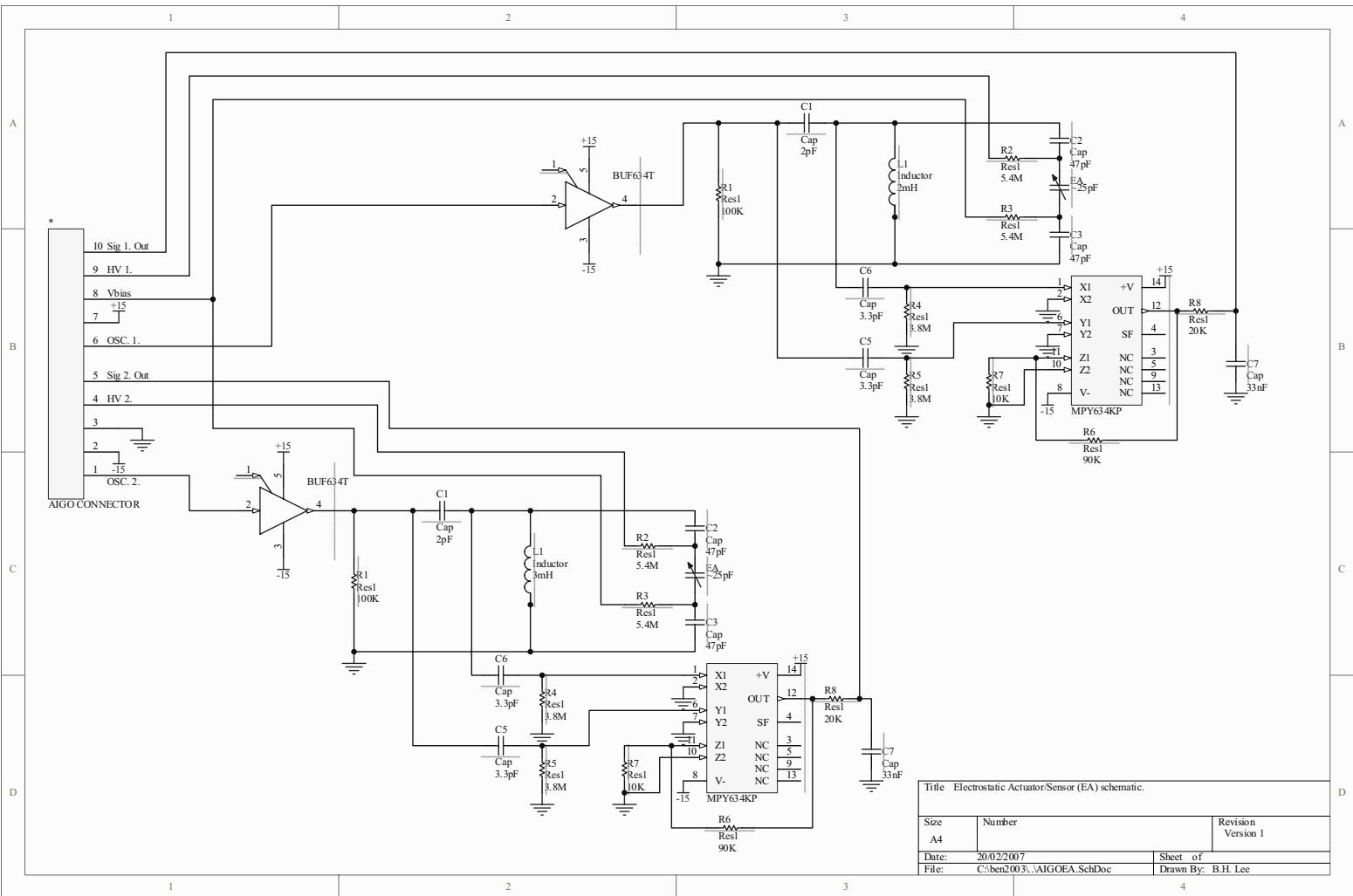


Fig. B.3: Schematic of the electrostatic sensing circuit for the south quadrants.

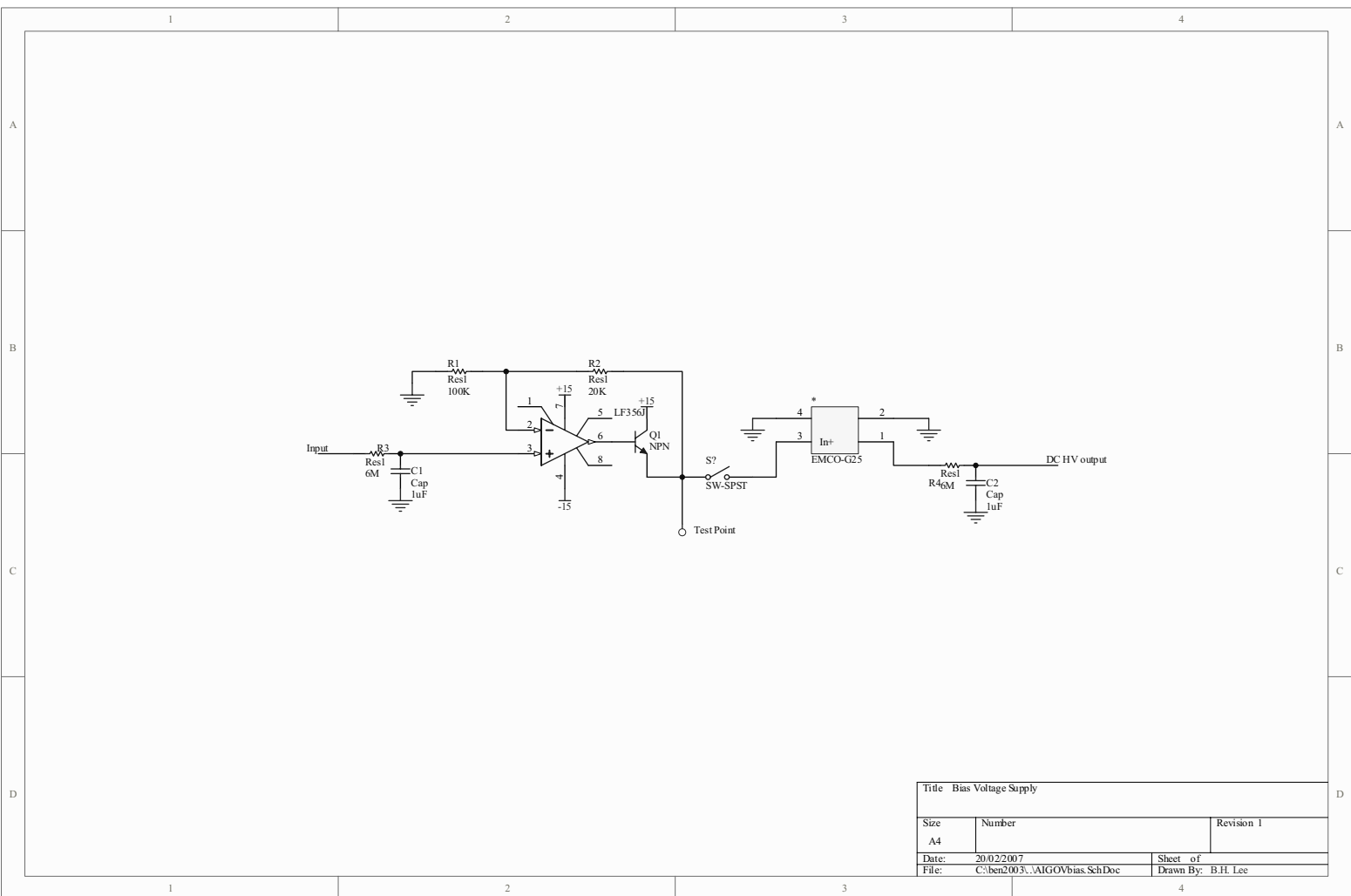


Fig. B.4: Schematic of the bias voltage supply circuit.

Title: Bias Voltage Supply		
Size: A4	Number:	Revision 1
Date: 20/02/2007	Sheet of	
File: C:\ben2003\AIGOVbias.SchDoc	Drawn By: B.H. Lee	

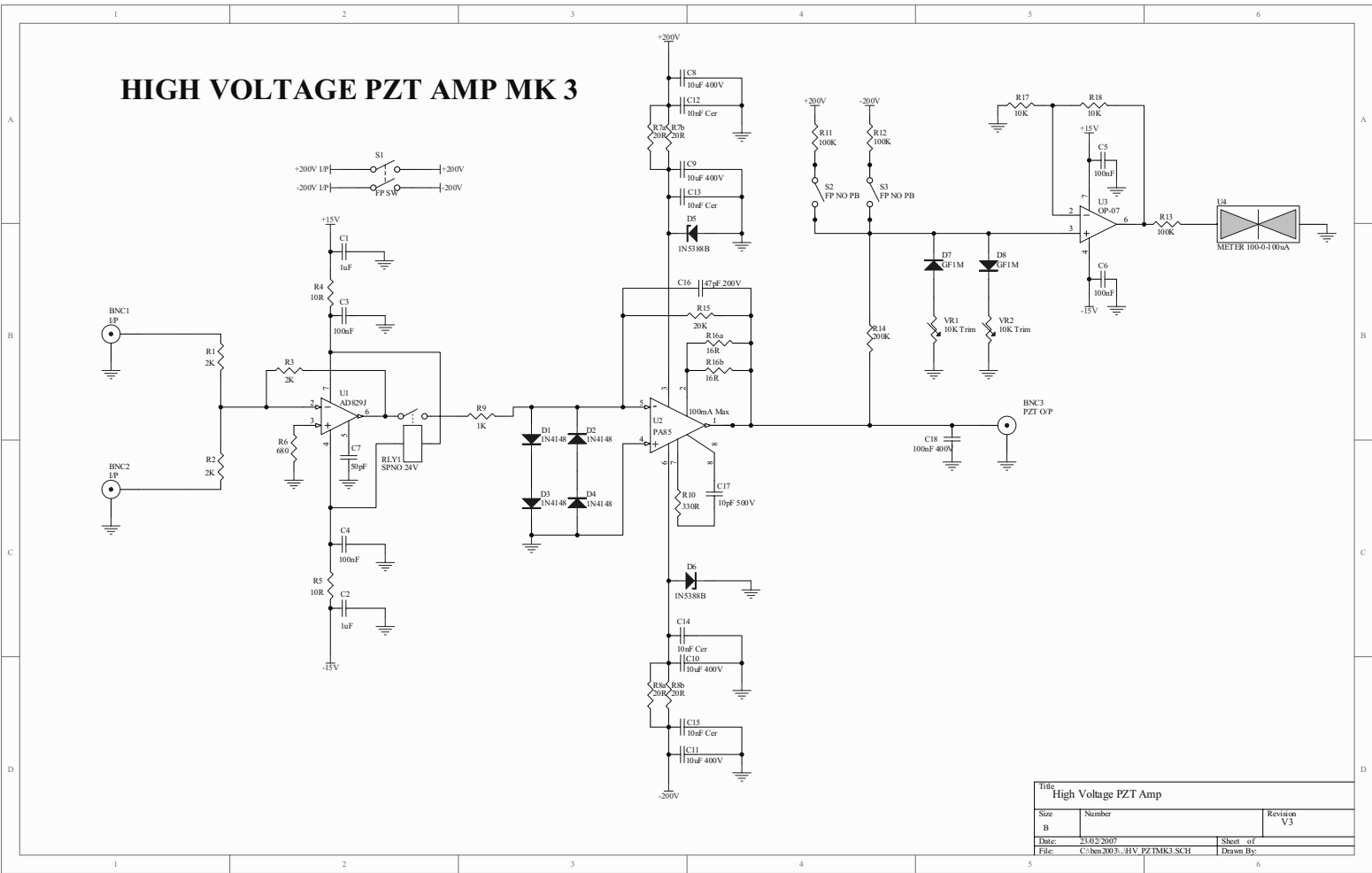


Fig. B.5: Schematic of the high voltage amplifier.

BIBLIOGRAPHY

- [1] K. S. Thorne. *Gravitational Radiation, in 300 years of Gravitation, edited by S.Hawking and W.Israel*. Cambridge U. Press, Cambridge, UK, 1987.
- [2] C. W. Misner, K. S. Thorne, and J. A. Wheeler. *Gravitation*. W. H. Freeman and Company, San Francisco, 1973.
- [3] L. Ju, D. G. Blair, and C. Zhao. Detection of gravitational waves. *Rep. Prog. Phys*, 63:1317, 2000.
- [4] J. Weber. *Phys. Rev.*, 117:306, 1960.
- [5] H. B. Callen and R. F. Green. *Phys. Rev.*, 86:702, 1952.
- [6] P. Astone et. al. *Phys. Rev. D*, 47:2, 1993.
- [7] E. Mauceli et al. *Phys. Rev. D*, 54:1264, 1996.
- [8] D. G. Blair et al. *Phys. Rev. Lett.*, 74:1908, 1995.
- [9] P. Astone et. al. *Astropart. Phys.*, 7:231, 1997.
- [10] G. Prodi et al. *Proc. 2nd Edoardo Amaldi Conf. (CERN, Switzerland, 1-4 July 1997)*. Singapore: World Scientific, Singapore, 1999.
- [11] H. J. Paik and R. V. Wagoner. *Phys. Rev. D*, 13:2694, 1976.
- [12] G. W. Gibbons and S. W. Hawking. *Phys. Rev. D*, 4:2191, 1971.
- [13] X. H. Douglas and V. B. Braginsky. *General Relativity, An Einstein Centenary Survey, edited by S.W. Hawking and W. Israel*. Cambridge: Cambridge University Press, Cambridge, 1979.
- [14] H. J. Paik. *J. Appl. Phys.*, 47:1168, 1976.
- [15] P. Astone et. al. *Phys. Rev. D*, 47:362, 1993.

- [16] N. P. Linthorne et al. *Physica. B*, 165:9, 1990.
- [17] T. Aldcroft et al. *Rev. Sci. Instrum.*, 63:3815, 1992.
- [18] D. G. Blair et al. *Proc. 6th Marcel Grossmann Meeting, edited by H. sato and T. Nakamura*. Singapore: World Scientific, Singapore, 1992.
- [19] E. Coccia. *Rev. Sci. Instrum.*, 55:1980, 1984.
- [20] A. de Waard et al. *Class. Quant. Grav.*, 20:S143, 2003.
- [21] O. D. Aguiar et al. *Class. Quant. Grav.*, 21:S457, 2004.
- [22] M. Bassan et al. *Proc. VIRGO conf. edited by F. Fidecaro and I. Ciufolini*. Singapore: World Scientific, Singapore, 1997.
- [23] J. L. Melo et al. *Class. Quant. Grav.*, 21:S999, 2004.
- [24] M. Cerdonio et al. *Phys. Rev. Lett.*, 87:031101, 2001.
- [25] M. Bonaldi et al. *Class. Quant. Grav.*, 21:S1155, 2004.
- [26] R. L. Forward. *Phys. Rev. D*, 17:379, 1960.
- [27] D. Sigg. Status of the ligo detectors. *Class. Quant. Grav.*, 23:S51–S56, 2006.
- [28] H. Lück et al. Status of te geo600 detector. *Class. Quant. Grav.*, 23:S71–S78, 2006.
- [29] R. Takahashi et al. *Class. Quant. Grav.*, 21:S403, 2004.
- [30] N. Nakagawa et al. Influence of radio frequency harmonics to tama300 sensitivity. *Journal of Physics: Conference Series*, 32:432–438, 2006.
- [31] F. Acernese et al. The status of virgo. *Class. Quant. Grav.*, 23:S63–S69, 2006.
- [32] F. Nocera. *Class. Quant. Grav.*, 21:S481, 2004.
- [33] R. W. Drever et al. *J. Appl. Phys. B*, 31:97, 1983.
- [34] R. V. Pound. *Rev. Sci. Instrum.*, 17:490, 1946.
- [35] A. Freise et al. *Class. Quant. Grav.*, 19:1389, 2002.

- [36] C. M. Caves. *Phys. Rev. Lett.*, 45:75, 1980.
- [37] C. M. Caves. *Phys. Rev. D*, 23:1693, 1981.
- [38] R. W. Drever et al. *Proc. 9th Int. Conf. on General Relativity and Gravitation, edited by E. Shmutzer*. Cambridge: Cambridge University Press, Cambridge, 1983.
- [39] B. J. Meers et al. *Phys. Rev. D*, 38:2317, 1988.
- [40] G. Heinzel et al. *Phys. Rev. Lett*, 81:5493, 1998.
- [41] A. Freise et al. *Phys. Lett. A*, 277:135, 2000.
- [42] H. Grote et al. Dual recycling for GEO600. *Class. Quant. Grav.*, 21:S473–S480, 2004.
- [43] A. Buonanno et al. Laser-interferometer gravitational-wave optical-spring detectors. *Class. Quant. Grav.*, 19:1569–1574, 2002.
- [44] B. S. Sheard et al. *Phys. Rev. A*, 69:051801, 2004.
- [45] T. Corbitt et al. Measurement of radiation-pressure-induced optomechanical dynamics in a suspended Fabry-Perot cavity. *Phys. Rev. A*, 74:021802, 2006.
- [46] G. Ballardini et al. Measurement of the virgo superattenuator performance for seismic noise suppression. *Rev. Sci. Instrum*, 72:3643, 2001.
- [47] L. Ju et al. *Meas. Sci. Technol.*, 3:463, 1992.
- [48] S. Braccini et al. Seismic vibrations mechanical filters for the gravitational waves detector VIRGO. *Rev. Sci. Instrum.*, 67:2899–2902, 1996.
- [49] E. J. Chin et al. Low frequency vertical geometric anti-spring vibration isolators. *Phys. Lett. A*, 336:97, 2005.
- [50] N. Robertson, R.W.P Drever, I. Kerr, and J. Hough. Passive and active seismic isolation for gravitational radiation detectors and other instruments. *J. Phys. E:Sci. Instrum.*, 15:1101–1105, 1982.

- [51] N. Robertson et al. *Proceedings of SPIE – Volume 5500*, edited by James Hough, Gary H. Sanders. 2004.
- [52] R. Abbott et al. Seismic isolation enhancements for initial and advanced ligo. *Class. Quant. Grav.*, 21:S915–S921, 2004.
- [53] M. Pinoli et al. *Meas. Sci. Technol.*, 4:995, 1993.
- [54] P. R. Saulson and et.al. *Rev. Sci. Instrum.*, 65:182, 1994.
- [55] G. Losurdo et al. *Rev. Sci. Instrum.*, 70:2507, 1999.
- [56] J. Winterflood et al. *Proc. 3rd Edoardo Amaldi Conf. on Gravitational Waves*, edited by S. Meshkov. New York: AIP, New York, 1999.
- [57] P. R. Saulson. Thermal noise in mechanical experiments. *Phys. Rev. D*, 42:2437, 1990.
- [58] S. Rowan et al. *Proc. 3rd Edoardo Amaldi Conf. on Gravitational Waves*, edited by S. Meshkov. (New York: AIP), New York, 1999.
- [59] B. W. Barr et al. Silica research in glasgow. *Class. Quant. Grav.*, 19:1655, 2002.
- [60] P. Amico et al. Monocrystalline fibres for low thermal noise suspension in advanced gravitational wave detectors. *Class. Quant. Grav.*, 21:S1009, 2004.
- [61] V. B. Braginsky et al. *JETP. Lett.*, 55:432, 1992.
- [62] S.D. Penn et al. Frequency and surface dependence of the mechanical loss in fused silica. *Phys. Lett. A*, 352:3–6, 2006.
- [63] Y. Levin. Internal thermal noise in the LIGO test masses: a direct approach. *Phys. Rev. D*, 57:659–663, 1998.
- [64] S. Rowan, J. Hough, and D.R.M. Crooks. Thermal noise and material issues for gravitational wave detectors. *Phys. Lett. A*, 347:25–32, 2005.
- [65] G. M. Harry et al. Thermal noise from optical coatings in gravitational wave detectors. *Applied Optics*, 45:1569–1574, 2006.

- [66] D.R.M Crooks et al. Experimental measurements of coating mechanical loss factors. *Class. Quant. Grav.*, 21:S1059–S1065, 2004.
- [67] D. Shoemaker. Advanced LIGO: Context and overview (proposal to the NSF). *LIGO Document*, M030023-0-M, 2003.
- [68] T. Uchiyama et al. *Class. Quant. Grav.*, 21:S1161, 2004.
- [69] D. E. McClelland et al. Status of the Australian consortium for interferometric gravitational astronomy. *Class. Quant. Grav.*, 23:S41–S49, 2006.
- [70] H. B. Callen and T. A. Welton. *Phys. Rev.*, 83:34, 1951.
- [71] K. Kuroda et al. Current status of large-scale cryogenic gravitational wave telescope. *Class. Quantum Grav.*, 20:S871, 2003.
- [72] W. Winkler et al. Heating by optical absorption and the performance of interferometric gravitational wave detectors. *Phys. Rev. A*, 44:7022, 1991.
- [73] S. Reid et al. Mechanical dissipation in silicon flexures. *Phys. Lett. A*, 351:205, 2006.
- [74] T. Uchiyama et al. Mechanical quality factor of a sapphire fiber at cryogenic temperatures. *Phys. Lett. A*, 273:310, 2000.
- [75] T. Tomaru. Maximum heat transfer along a sapphire suspension fiber for a cryogenic interferometric gravitational wave detector. *Phys. Lett. A*, 301:215, 2002.
- [76] L. Ju et al. The quality factor of niobium flexure pendulums. *Phys. Lett. A*, 254:239, 1999.
- [77] A. Gillespie and F. Raab. Thermal noise in the test mass suspensions of a laser interferometer gravitational-wave detector prototype. *Phys. Lett. A*, 178:357, 1993.
- [78] P. Willems et al. Investigations of the dynamics and mechanical dissipation of a fused silica suspension. *Phys. Lett. A*, 297:37, 2002.

- [79] P. Amico et al. Thermal noise reduction for present and future gravitational wave detectors. *Nucl. Instrum. and Meth. A*, 518:240, 2004.
- [80] A. M. Gretarsson et al. Pendulum mode thermal noise in advanced interferometers: a comparison of fused silica fibers and ribbons in the presence of surface loss. *Phys. Lett. A*, 270:108, 2000.
- [81] D. H. Santamore and Yuri Levin. Eliminating thermal violin spikes from LIGO noise. *Phys. Rev. D*, 46:042002, 2001.
- [82] B. Willke et al. The GEO600 gravitational wave detector. *Class. Quant. Grav.*, 19:1377–1388, 2002.
- [83] M.V. Plissi et al. Aspects of the suspension systems for GEO600. *Rev. Sci. Instrum.*, 69:3055–3061, 1998.
- [84] P. Amico et al. Thermal noise limit in the virgo mirror suspension. *Nucl. Instrum. and Meth. A*, 461:297, 2001.
- [85] G. Cagnoli et al. Low-frequency internal friction in clamped-free thin wires. *Phys. Lett. A*, 255:230, 1999.
- [86] L. Ju. Private communication, 2006.
- [87] Goodfellow. Material properties, niobium, 2006.
- [88] V. B. Braginsky and V. P. Mitrofanov. *Systems with small dissipation*. University of Chicago Press., Chicago, 1985.
- [89] Goodfellow. Material properties, sapphire monofilament, 2006.
- [90] A. M. Gretarsson and G. M. Harry. Dissipation of mechanical energy in fused silica fibers. *Rev. Sci. Instrum*, 70:4081, 1999.
- [91] K. Y. Yasumura et al. *IEEE trans*, Electron Devices 9:119, 2000.
- [92] P. J. Veitch. Development and preliminary operation of a cryogenic gravitational wave antenna. *PhD Thesis, University of Western Australia*, 1986.
- [93] C. Zener. Internal friction in solids. *Phys. Rev.*, 52:230, 1937.

- [94] C. Zener. Internal friction in solids. *Phys. Rev.*, 53:90, 1938.
- [95] G. Cagnoli et al. Silica suspension and coating developments for advanced ligo. *J. Phys.: Conf. Ser.*, 386:32, 2006.
- [96] C. R. Locke, M. E. Tobar, and E. N. Ivanov. Monolithic sapphire parametric transducer operation at cryogenic temperatures. *Rev. Sci. Instrum.*, 71:2737, 2000.
- [97] J. Ferreira. Low temperature internal friction in niobium. *PhD Thesis, University of Western Australia*, 1986.
- [98] Purdue University. Thermophysical Properties Research Center. *Thermophysical properties of matter : [the TPRC data series; a comprehensive compilation of data / Y.S. Touloukian, series editor]*. IFI/Plenum, New York, 1970.
- [99] A. Giazotto and G. Cella. Some considerations about future interferometric GW detectors. *Class. Quant. Grav.*, 21:S1183, 2004.
- [100] P. Willems et al. Cavity optics suspension subsystem design requirement document. *LIGO Internal Document*, pages LIGO010007–01–R, 2001.
- [101] J. Winterflood. High performance vibration isolation for gravitational wave detectors. *PhD Thesis, University of Western Australia*, 2001.
- [102] M. Barton. Models of the advanced ligo suspensions in mathematica. *LIGO Internal Document*, pages LIGO020205–00–D, 2003.
- [103] M. E. Husman et al. Modeling of multistage pendulums: Triple pendulum suspension for GEO600. *Rev. Sci. Instrum.*, 71:2546, 2000.
- [104] M. Barton and C. Torrie. Suspension model comparison. *LIGO Internal Document*, pages LIGO020011–00–D, 2003.
- [105] S. Gossler et al. Damping and tuning of the fibre violin modes in monolithic silica suspensions. *Class. Quant. Grav.*, 21:923, 2004.
- [106] P. M. Morse. *Vibration and Sound*. McGraw-Hill Book Company, Inc., New York and London, first edition, 1936.

- [107] G. M. Harry et al. Comparison of advanced gravitational wave detectors. *Phys. Rev. D*, 65:082001, 2002.
- [108] J.R. Smith et al. Mechanical loss associated with silicate bonding of fused silica. *Class. Quant. Grav.*, 20:5039–5047, 2003.
- [109] P. Amico et al. Monolithic fused silica suspension for the Virgo gravitational wave detector. *Rev. Sci. Instrum.*, 73:3318, 2002.
- [110] S. Rowan et al. Q factor measurements on prototype fused quartz pendulum suspensions for use in gravitational wave detectors. *Phys. Lett. A*, 233:303–308, 1997.
- [111] D. G. Blair et al. Ultrahigh Q pendulum suspension for gravitational wave detectors. *Rev. Sci. Instrum.*, 64:1899, 1993.
- [112] J. E. Logan et al. Thermal motion associated with monolithic fused silica cradle suspensions for gravitational wave detectors. *Phys. Lett. A*, 218:181, 1996.
- [113] V. B. Braginsky et al. How to reduce suspension thermal noise in ligo without improving the q of the pendulum and violin modes. *Meas. Sci. Technol.*, 10:598, 1999.
- [114] G. I. Gonzalez and P. R. Saulson. Brownian motion of a mass suspended by an anelastic wire. *J. Acoust. Soc. Am.*, 96:207, 1994.
- [115] B. H. Lee et al. Orthogonal ribbons for suspending test masses in interferometric gravitational wave detectors. *Phys. Lett. A*, 339:217, 2005.
- [116] S. Gras, D. G. Blair, and L. Ju. Thermal noise dependence on equatorial losses in the mirrors of an interferometric gravitational wave detector. *Phys. Lett. A*, 333:1, 2004.
- [117] J. C. Dumas et al. Testing of a multi-stage low-frequency isolator using euler spring and self-damped pendulums. *Class. Quant. Grav.*, 21:S965–S971, 2004.
- [118] J. Winterflood et al. Tilt suppression for ultra-low residual motion vibration isolation in gravitational wave detection. *Phys. Lett. A*, 277:143, 2000.

- [119] E. J. Chin et al. Techniques for reducing the resonant frequency of euler spring vibration isolators. *Class. Quant. Grav*, 21:S959, 2004.
- [120] R. Abbott et al. Seismic isolation for Advanced LIGO. *Class. Quant. Grav*, 19:1591–1597, 2002.
- [121] E. Chin. High performance vibration isolation techniques for the aigo gravitational wave detector. *PhD Thesis, University of Western Australia*, 2007.
- [122] P. S. Linsay and D. H. Shoemaker. Low-noise rf capacitance bridge transducer. *Rev. Sci. Instrum.*, 53:1014, 1982.
- [123] S. Grasso et al. Electrostatic systems for fine control of mirror orientation in interferometric gw antennas. *Phys. Lett. A*, 244:360, 1998.
- [124] V. P. Mitrofanov et al. Damping of the test mass oscillations caused by multistrip electrostatic actuator. *Phys. Lett. A*, 278:25, 2000.
- [125] H. Grote. Making it work: Second generation interferometry in GEO600! *PhD Thesis, University of Hannover*, 2003.
- [126] G. Losurdo et al. Inertial control of the mirror suspensions of the Virgo interferometer for gravitational wave detection. *Rev. Sci. Instrum.*, 72:3653, 2001.
- [127] Apex Microtechnology Corp. Data sheet - high voltage power operational amplifier, pa85, pa85a, 1998.
- [128] B.J.J. Slagmolen, T. Slade, and C. Mow-Lowry. Aigo vacuum parts cleaning process. *Internal ACIGA report ver 1.2*, 2004.
- [129] C. Y. Lee and C. Zhao et al. Control of pre-isolators for gravitational wave detection. *Class. Quant. Grav.*, 21:S1015, 2004.

APPENDIX C

LIST OF PUBLICATIONS

B.H. Lee, L. Ju and D.G. Blair, *Thin walled Nb tubes for suspending test masses in interferometric gravitational wave detectors*, PAPER 4.4, Phys., Lett. A, 350, 319-323 (2006)

D E McClelland, S M Scott, M B Gray, A C Searle, S Goler, B J J Slagmolen, J Dickson, J H Chow, G de Vine, K McKenzie, C M Mow-Lowry, A Moylan, D S Rabeling, B S Sheard, J Cumpston, K Wette, D G Blair, L Ju, R Burman, D Coward, C Zhao, P Barrigo, E Chin, J Degallaix, Y Fan, S Gras, E Howell, **B Lee**, S Schediwy, Z Yan, J Munch, P J Veitch, D Mudge, A Brooks and D Hosken, *Status of the Australian Consortium for Interferometric Gravitational Astronomy*, Class. Quantum Grav. 23, S41-S50 (2006)

B. H. Lee, L. Ju and D.G. Blair, *Suspensions with reduced violin string modes*, Journal of Physics: Conference Series-Proceedings of the Sixth Edoardo Amaldi Conference on Gravitational Waves. Ed. N Mio, 353-361 (2006)

B.H. Lee, L. Ju, D.G. Blair, *Orthogonal Ribbons for Suspending Test Masses in Interferometric Gravitational Wave Detectors*, PAPER 4.3, Phys. Lett. A 339, 217-223 (2005)

P. Barriga, M. Barton, D. G. Blair, A. Brooks, R. Burman, R. Burston, E. J. Chin, J. Chow, D. Coward, B. Cusack, G. de Vine, J. Degallaix, J. C. Dumas, M. Feat, S. Gras, M. Gray, M. Hamilton, D. Hosken, E. Howell, J. S. Jacob, L. Ju, T. L. Kelly, **B. H. Lee**, C. Y. Lee, K. T. Lee, A. Lun, D. E. McClelland, K. McKenzie, C.

Mow-Lowry, A. Moylan, D. Mudge, J. Munch, D. Rabeling, D. Reitze, A. Romann, S. Schediwy, S. M. Scott, A. Searle, B. S. Sheard, B. J. J. Slagmolen, P. Veitch, J. Winterflood, A. Woolley, Z. Yan and C. Zhao, *Technology Developments for ACIGA High Power Test Facility for Advanced Interferometry*, Class. Quantum Grav. 22:199-208, (2005).

B Lee, E Howell, D Coward and D Blair, *Gravitational waves-concepts, sources, signals and detection*, in Cosmology and Gravitation: XI Brazilian School of Cosmology and Gravitation: Eds. M. Novello and S.E Perez-Bergliaffa 128-165 (2005).

L Ju, M Aoun, P Barriga, D G Blair, A Brooks, R Burman, R Burston, X T Chin, E J Chin, C Y Lee, D Coward, B Cusack, G de Vine, J Degallaix, J C Dumas, F Garoi, S Gras, M Gray, D Hosken, E Howell, J S Jacob, T L Kelly, **B Lee**, K T Lee, T Lun, D McClelland, C Mow-Lowry, D Mudge, J Munch, S Schediwy, S Scott, A Searle, B Sheard, B Slagmolen, P Veitch, J Winterflood, A Wooley, Z Yan and C Zhao, *ACIGA's high optical power test facility*, Class. Quantum Grav., 21, S887-S893 (2004)

B. Lee, D. G. Blair, L. Ju, C. Zhao, "Implementation of electrostatic actuators for suspended test mass control", Class. Quantum Grav., 21, S977 - S983, (2004).

P. Barriga, M. Barton, D. G. Blair, A. Brooks, R. Burman, R. Burston, E. J. Chin, J. Chow, D. Coward, B. Cusack, G. de Vine, J. Degallaix, J. C. Dumas, M. Feat, S. Gras, M. Gray, M. Hamilton, D. Hosken, E. Howell, J. S. Jacob, L. Ju, T. L. Kelly, **B. H. Lee**, C. Y. Lee, K. T. Lee, A. Lun, D. E. McClelland, K. McKenzie, C. Mow-Lowry, A. Moylan, D. Mudge, J. Munch, D. Rabeling, D. Reitze, A. Romann, S. Schediwy, S. M. Scott, A. Searle, B. S. Sheard, B. J. J. Slagmolen, P. Veitch, J. Winterflood, A. Woolley, Z. Yan and C. Zhao, *Status of ACIGA High Power Test Facility for Advanced Interferometry*, Proc. Society of Photo-Optical Instrumentation Engineering 5500:70-80, (2004).

noindent L. Ju, M. Aoun, P. Barriga, D. G. Blair, A. Brooks, R. Burman, R. Burston, X. T. Chin, E. J. Chin, C. Y. Lee, D. Coward, B. Cusack, G. de Vine, J. Degallaix, J. C. Dumas, F. Garoi, S. Gras, M. Gray, D. Hosken, E. Howell, J. S. Jacob, T. L. Kelly,

B. H. Lee, K. T. Lee, T. Lun, D. McClelland, C. Mow-Lowry, D. Mudge, J. Munch, S. Schediwy, S. Scott, A. Searle, B. Sheard, B. Slagmolen, P. Veitch, J. Winterflood, A. Woolley, Z. Yan, C. Zhao, *ACIGA's High Optical Power Test Facility*, *Class. Quantum Grav.* 21:887-893, (2004).

J. S. Jacob, P. Barriga, D. G. Blair, A. Brooks, R. Burman, R. Burston, L. Chan, X. Chan, E. J. Chin, J. Chow, D. Coward, B. Cusack, G. de Vine, J. Degallaix, J. C. Dumas, A. Faulkner, F. Garoi, S. Gras, M. Gray, M. Hamilton, M. Herne, C. Hollitt, D. Hosken, E. Howell, L. Ju, T. Kelly, **B. Lee**, C. Y. Lee, K. T. Lee, A. Lun, D. McClelland, K. McKenzie, C. Mow-Lowry, D. Mudge, J. Munch, D. Paget, S. Schediwy, S. Scott, A. Searle, B. Sheard, B. Slagmolen, P. Veitch, J. Winterflood, A. Woolley, Z. Yan, C. Zhao, *Australia's Role in Gravitational Wave Detection*, *Publications of the Astronomical Society of Australia* 20:223-241, (2003).